Aix*Marseille université
Socialement engagée

NNT : 0000AIXM0000

# THÈSE DE DOCTORAT

Soutenue à Aix-Marseille Université
le 7 Novembre 2024 par

**Junlong WANG**

## Surface functionalization of gold by self-assembled monolayers of novel push-pull chromophores: synthesis, characterization of the structural and electrical properties

**Discipline**
PHYSIQUE ET SCIENCES DE LA MATIERE

**Spécialité**
Matière Condensée et nanosciences

**École doctorale**
ED352

**Laboratoire/Partenaires de recherche**
IM2NP UMR 7334 (Institut Matériaux Microélectronique Nanosciences de Provence)

**Composition du jury**

Phillipe LANG — Rapporteur
Directeur de Recherche
CNRS ITODYS, UMR 7086 Université Paris Cité

Phillipe LECLERE — Rapporteur
Professeur
Directeur de Recherches honoraire du F.R.S. - FNRS Service de Physique des Nanomatériaux et Energie, Université de Mons

Pascal CARRIERE — Examinateur
Maître de Conférences
HDR Université de Toulon, MAPIEM-UR 4323

Jean-Manuel RAIMUNDO — Président du jury
Professeur
AMU – CINAM UMR 7325 Dpt. Ingénierie Moléculaire et Matériaux Fonctionnels

Lionel PATRONE — Directeur de thèse
Chargé de Recherche
CNRS HDR IM2NP UMR 7334

Virginie GADENNE — Co-directrice de thèse
Enseignant-chercheur
ISEN Méditerranée IM2NP UMR 7334

im2np

ISEN

# Affidavit

Je soussigné, Junlong WANG, déclare par la présente que le travail présenté dans ce manuscrit est mon propre travail, réalisé sous la direction scientifique de Lionel Patrone et Virginie Gadenne, dans le respect des principes d'honnêteté, d'intégrité et de responsabilité inhérents à la mission de recherche. Les travaux de recherche et la rédaction de ce manuscrit ont été réalisés dans le respect à la fois de la charte nationale de déontologie des métiers de la recherche et de la charte d'Aix-Marseille Université relative à la lutte contre le plagiat.

Ce travail n'a pas été précédemment soumis en France ou à l'étranger dans une version identique ou similaire à un organisme examinateur.

Fait à Marseille, le 10 septembre 2024



Cette œuvre est mise à disposition selon les termes de la Licence Creative Commons Attribution - Pas d'Utilisation Commerciale - Pas de Modification 4.0 International.

# Liste de publications et/ou brevets et participation aux conférences

1) Liste des publications et/ou brevet réalisées dans le cadre du projet de thèse :

    1. Self-Assembled Monolayers of Push–Pull Chromophores as Active Layers and Their Applications
    Wang, J.; Gadenne, V.; Patrone, L.; Raimundo, J.-M. Self-Assembled Monolayers of Push–Pull Chromophores as Active Layers and Their Applications. *Molecules* 2024, *29*, 559. https://doi.org/10.3390/molecules29030559

2) Participation aux conférences[1] et écoles d'été au cours de la période de thèse :

    1. Surface functionalization by self-assembled monolayers of novel push-pull chromophores: photoelectric properties and application to bio-sensors
    Poster in 2022 Annual IM2NP meeting, Marseille
    2. Surface functionalization by self-assembled monolayers of novel push-pull chromophores: photoelectric properties and application to bio-sensors
    Poster in 2023 Annual IM2NP meeting, La Londe-les-Maures
    3. Synthesis of new push-pull chromophore and its functionalization on gold surface
    Presentation in 2023 PHANO (department of IM2NP) meeting, Marseille
    4. Toward the development of self-assembled monolayers with modulated polarization for the controlled detection of biomarkers
    Oral presentation in CNRS GDR NEMO meeting, Lille 16-18th October 2023
    5. Self-assembled monolayers of push-pull chromophores for the potential modulation for selective detection of biomolecules
    Poster in 2024 Annual IM2NP meeting, Aix-en-Provence
    6. Self-assembled monolayer of push-pull chromophore on gold: towards the modulated polarization for the controlled detection of biomolecules
    Oral presentation in international conference Nanosea, Marseille 16-19th July 2024

[1] Le terme « conférence » est générique. Il désigne à la fois « conférence », « congrès », « workshop », « colloques », « rencontres nationales et/ou internationales » … etc.
Indiquer si vous avez fait une présentation orale ou sous forme de poster.

# Résumé

Cette thèse s'intéresse au greffage et à l'organisation de chromophores push-pull sur un substrat d'or pour bénéficier de leur dipôle orienté sur la surface afin de pouvoir moduler de manière contrôlée le potentiel d'activation permettant de déployer un oligopeptide chargé déposé au-dessus pour la détection des espèces cibles dans la perspective d'une application aux biocapteurs. Pour cela, la première partie de ce travail a été consacrée à l'étude d'un système modèle constitué de monocouches auto-assemblées (SAMs) à base de ferrocène adsorbé soit directement sur l'or, soit au-dessus de SAMs intermédiaires de cystéamine ou d'aminothiophénol afin de mettre en évidence leur effet sur la modulation de polarisation du ferrocène. Une fois cet effet confirmé, des chromophores push-pull originaux non chargés spécifiques ont été synthétisés par les méthodes de chimie organique et la structure moléculaire des chromophores push-pull obtenus a été caractérisée par spectroscopie de résonance magnétique nucléaire, spectroscopie infrarouge à transformée de Fourier et spectroscopie de masse à ionisation par électrospray. Différentes unités de groupements attracteurs d'électrons (acide cyanoacrylique (acide carboxylique + nitrile), acide rhodanine-N-acétique (dithiocarbamate + amide) et aldéhyde) ont été testés. Les propriétés photophysiques des chromophores push-pull ont été étudiées par spectrophotométrie UV-visible. Les monocouches auto-assemblées (SAM) ont été obtenues par adsorption spontanée des molécules en solution sur le substrat dans le but de les greffer chimiquement via le groupement d'ancrage à base de thiol. Tout d'abord les SAMs de push-pull ont été étudiées et analysées. Il a été démontré que la concentration du chromophore push-pull et le choix du solvant exercent une influence sur la qualité de la monocouche auto-assemblée. Ensuite, les monocouches auto-assemblées d'oligo(éthylène glycol) et d'oligopeptide 4KC ont été préparées et caractérisées pour agir respectivement comme matrice inerte et comme un oligopeptide chargé. Enfin, j'ai étudié la formation de SAMs binaires afin d'isoler les chromophores push-pull et les 4KC à l'intérieur d'une matrice inerte. Les monocouches auto-assemblées ont été caractérisées par la mesure des angles de contact de l'eau, la microscopie à effet tunnel, la microscopie à force atomique, la spectroscopie XPS, la spectroscopie Raman exaltée par la surface, la spectroscopie infrarouge et la voltamétrie cyclique.

Mots clés : chromophore push-pull, ferrocène, oligopeptide, poly(éthylène glycol) monocouche auto-assemblée

# Abstract

This thesis is focused on the grafting and the organization of push-pull chromophores on a gold substrate for benefiting from their oriented dipole on the surface to be able to tune the activation potential enabling to unfold a charged oligopeptide deposited on top for the target species detection in a biosensor application. For this purpose, the first part of this work has been dedicated to study a model system made of ferrocene-based self-assembled monolayers (SAMs), adsorbed either directly on gold or on top of an intermediate SAM of cysteamine or aminothiophenol to evidence their effect on potential modulation on ferrocene. Once this effect has been confirmed, specific non-charged original push-pull chromophores have been synthesized by organic chemistry methods and their molecular structure has been characterized by nuclear magnetic resonance spectroscopy, Fourier-transform infrared spectroscopy and electrospray ionization mass spectroscopy. Various electron-withdrawing group (cyanoacrylic acid (carboxylic acid + nitrile), rhodanine-N-acetic acid (dithiocarbamate + amide), and aldehyde) have been tested. The photophysical property of the push-pull chromophore has been studied by UV-visible spectrophotometry. Self-assembled monolayers (SAMs) have been obtained by the spontaneous adsorption of the molecules in the solution on the substrate with the aim to chemically graft them through an anchoring unit. First push-pull SAMs have been studied and analysed. The concentration of the push-pull chromophore and the choice of the solvent have been shown to have an influence on the quality of the self-assembled monolayer. Then, self-assembled monolayers of thiol based on the chain of oligo (ethylene glycol) mPEG12SH and 4KC and gold substrate have been prepared and characterized to act respectively as an inert matrix and the charged oligopetide. Finally, I have studied binary SAM formation to isolate the push-pull chromophores and the 4KC inside an inert matrix. The self-assembled monolayers have been characterized by the measurement of the water contact angles, scanning tunnelling microscopy, atomic force microscopy, X-ray photoelectron spectroscopy, surface-enhanced Raman spectroscopy, infrared spectroscopy, and cyclic voltammetry.

Keywords : push-pull chromophore, ferrocene, oligopeptide, oligo(ethylene glycol), self-assembled monolayer

# Résumé en français du manuscrit de thèse

Les chromophores push-pull permettent d'obtenir une séparation de charge intramoléculaire entre un donneur et un accepteur via un espaceur (Fig. 1).

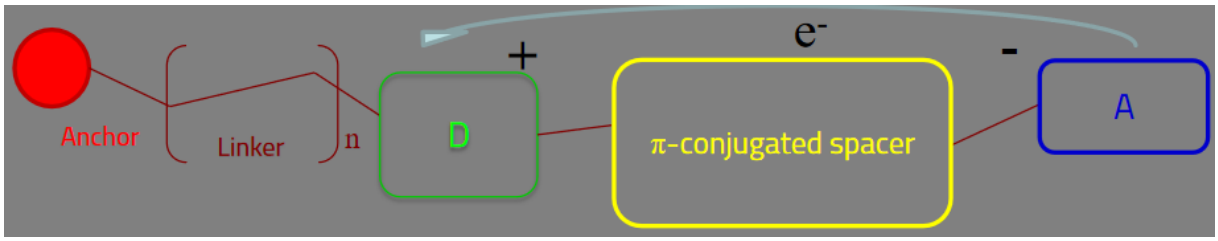


Figure 1 : Structure d'un chromophore push-pull

Un tel effet peut être mis à profit dans différents domaines tels que l'optique non linéaire, les cellules solaires[1,2], la modification du travail de sortie et l'interface avec des électrodes, ou encore la formation d'une couche à haute permittivité diélectrique[3,4] bénéfique en micro-nanoélectronique ou pour minimiser les recombinaisons d'excitons photo-générés dans le domaine du photovoltaïque. Pour cela il est indispensable d'orienter tous les dipôles dans le même sens et d'éviter qu'ils se positionnent tête-bêche. Le dépôt sous forme de monocouches auto-assemblées[5] des chromophores greffés sur la surface se révèle très bien adapté à cet objectif tout en permettant une organisation des chromophores nécessaire à l'obtention de phénomènes collectifs contrôlés. Les travaux existants sur les push-pull chromophores traitent de molécules chargées ce qui peut nuire à l'organisation par l'effet de répulsion entre charges. Dans ce travail, on propose de s'attacher à la formation de SAMs ordonnées de chromophores push-pull chromophores originaux non chargés sur la base de l'expertise développée au laboratoire[1,6]. Ainsi on a travaillé en étroite collaboration avec les chimistes du CINaM à Marseille pour mettre au point les chromophores push-pull non chargés qui assurent une bonne organisation des monocouches auto-assemblées et une séparation de charges efficace. Une fois maîtrisée l'organisation des monocouches auto-assemblées, l'idée est de réaliser des couches

binaires de chromophores complémentaires dilués dans une matrice inerte d'oligo(éthylène glycol) pour une application vers les biocapteurs avec une détection sélective. Pour cela on a travaillé sur substrats d'or avec des chromophores chacun présentant un dipôle qui lui est propre et qui servira à activer le déploiement hors de la matrice inerte d'un oligomère chargé de oligopeptide 4KC permettant ainsi la détection d'espèces cibles au sein d'un biocapteur[7] (Fig. 2).

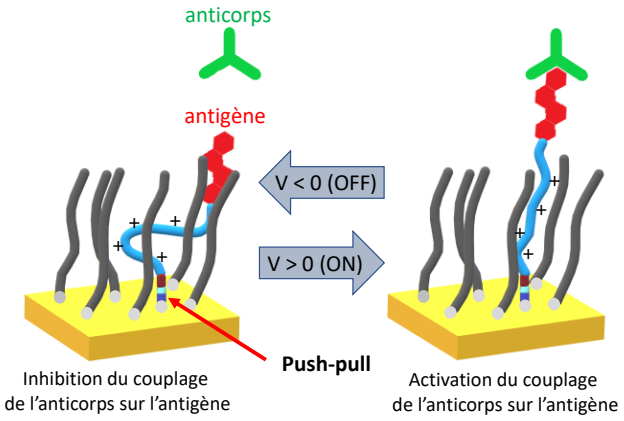


Figure 2 : Principe de la détection des anticorps par la tension appliquée sur la surface.

Le premier chapitre traite de la recherche bibliographique sur le sujet. Une très grande variété de thèmes est résumée à partir des articles de journaux scientifiques et des livres de thème scientifique. La première partie se rapporte aux chromophores push-pull : les aspects fondamentaux du chromophore push-pull (donneur d'électrons, attracteur d'électrons et l'espaceur π-conjugué), et les chromophores push-pull linéaires (le type de chromophore push-pull utilisé dans la thèse). Quelques réactions chimiques dans la chimie organique sont présentées en tant qu'une petite introduction. Elles sont les réactions pour former des liaison C=C (la réaction de Wittig pour former la double liaison C=C à partir de sel de triphénylphosphonium, la réaction de l'aldolization-crotonization à partir de l'énolisation et la réaction de Knovenagel pour former la double liaison C=C en activant le carbonyl par pipéridine) et les réaction de couplage croisé en utilisant les catalyseurs à base de palladium (la réaction de Heck pour former liaison $C(sp^2)$-$C(sp^2)$ en liant un groupement arylique et un groupement allylique, la réaction de Sonogashira pour former la liaison $C(sp^2)$-C(sp) en liant

un groupement arylique et un alkyne terminal et la réaction de Suzuki-Miyauna pour former la liaison $C(sp^2)$-$C(sp^2)$ en liant un groupement arylique et un autre groupement arylique via une autre réaction de couplage croisé en transformant Ar-X (X=Br ou I) à $Ar\text{-}B(OR)_2$). La deuxième partie est consacrée aux monocouches auto-assemblées sur différents substrats par diverses molécules organosoufrées : le modèle fondamental de la monocouche auto-assemblée de thiol sur l'or, les différentes molécules organosoufrées (différents groupements fonctionnels de soufre incluant disulfure, acide dithiocarbamique, acide dithiocarboxylique, etc, et différentes denticités telles que monodenté, bidenté, tridenté, etc) et différents substrats sont présentés. La troisième partie introduit la notion de la cristallinité et la notion de matériaux 2D à base de cristaux moléculaires : naphtalène, biphényl, chaîne alkyle, molécule organométallique comme ferrocène etc. de façon à aborder les différents types d'interactions intermoléculaires structurantes qui peuvent intervenir dans la compacité des monocouches auto-assemblées. La dernière partie est consacrée aux différents applications directes des monocouches auto-assemblées de chromophores push-pull, en particulier les cellules solaires (Graetzel, pérovskites en tant que couches interfaciales,…) et les nanodiélectriques qui mettent à profit l'orientation de dipôles dans la couche organisée sur surface.

Le deuxième chapitre présente toutes les méthodes de caractérisations utilisées au cours de la synthèse organique des chromophores push-pull, et pour analyser les monocouches auto-assemblées de chromophores push-pull sur le substrat d'or : les microscopies à sondes locales pour la monocouche auto-assemblée, les spectroscopies optiques pour la synthèse organique et la monocouche auto-assemblée, les méthodes électroanalytiques pour la chimie de la solution et la monocouche auto-assemblée, la spectroscopie de masse pour la synthèse organique, la mesure d'angle de contact, et les techniques de spectroscopie XPS, infrarouge, et Raman en mode SERS pour la monocouche auto-assemblée.

Les techniques de microscopie à sondes locales utilisées sont au nombre de trois : la microscopie à effet de tunnel, la microscopie à force atomique, la microscopie à force électrostatique. Dans la thèse, la microscopie à l'effet de tunnel est utilisée pour sonder la structure à l'échelle nanométrique grâce à sa bonne résolution latérale et pour faire la spectroscopie électrique à l'échelle nanométrique pour regarder l'effet de rectification. La microscopie à force atomique nous renseigne sur la structure à l'échelle nanométrique grâce à sa bonne résolution verticale. La microscopie à force électrostatique est une méthode intéressante pour sonder les charges électrique grâce à sa plus longue portée que la force de Van der Waals.

Six techniques différentes de spectroscopie optique sont présentées. Pour l'utilisation, elles peuvent être divisées en deux parties : la spectroscopie optique pour la molécule et la spectroscopie pour la monocouche auto-assemblée.

Trois méthodes de spectroscopie optique ont été utilisées pour caractériser la molécule. La spectroscopie infrarouge à transformée de Fourier, qui est une méthode courante pour caractériser un composé chimique, est utilisée pour extraire les informations des liaisons chimiques. La spectroscopie UV-visible est une technique utilisée en chimie analytique pour le titrage. Mais elle peut aussi être utilisée pour caractériser les propriétés photo-physiques des chromophores push-pull. Le phénomène de transfert interne de charge confère au chromophore push-pull une bande d'absorption dans la région UV-visible. La spectroscopie de résonance magnétique nucléaire est un outil puissant pour caractériser la structure moléculaire grâce à sa très bonne sensibilité et très bonne résolution, ce qui en fait une étape de caractérisation indispensable pour un composé chimique. Le fonctionnement de la spectroscopie de résonance magnétique nucléaire (RMN) est présenté. En RMN, comme le décalage de niveau d'énergie est très petit, les spins nucléaires absorbent les rayons de radiofréquence. Enfin, pour caractériser les molécules synthétisées, la spectroscopie de masse a été utilisée pour obtenir des informations sur la

structure des molécules en mesurant la masse molaire et/ou en analysant les fragments de molécules. Cette méthode est surtout très utile pour les molécules qui ne comportent pas beaucoup d'atomes hydrogène.

Il y a aussi trois méthodes de spectroscopie optique qui ont été mises en œuvre pour caractériser les monocouches auto-assemblées. La spectroscopie Raman exaltée par les plasmons de surface (SERS) est une méthode de spectroscopie bien adaptée pour sonder les informations de composition chimique pour les molécules qui sont greffées sur la surface. Le substrat pour la spectroscopie de Raman exaltée est nanostructuré pour avoir un très bon effet de plasmons de surface. Ces plasmons de surface vont exalter le signal Raman par la voie électromagnétique à laquelle peut s'ajouter la voie électrochimique. La spectroscopie infrarouge à transformée de Fourier va non seulement fournir des informations sur la composition chimique de la molécule adsorbée sur la surface, mais aussi fournir de l'information structurale de la monocouche auto-assemblée. La spectroscopie d'émission de photoélectrons émis par excitation par rayons X (XPS) est une spectroscopie qui sonde la structure électronique des électrons de cœur des différents éléments à la base de l'effet photoélectrique. Cette spectroscopie peut aussi donner une information sur la composition chimique de la molécule adsorbée sur la surface, et sur la structure de la monocouche auto-assemblée.

Les méthodes électroanalytiques sont très intéressantes dans beaucoup de domaines. Elles peuvent être divisée en deux parties : les méthodes électroanalytiques pour sonder des réactions électrochimiques et les méthodes électroanalytiques pour sonder des constantes physiques comme dans un circuit électrique. La voltamétrie cyclique est une méthode électroanalytique fondamentale qui sonde la réaction électrochimique. Tout comme l'XPS, la voltamétrie cyclique peut aussi fournir des informations sur la composition chimique de la molécule adsorbée sur la surface et sur la structure de la monocouche auto-assemblée. En effet, il y a deux parties de courant dans le courant de la voltamétrie cyclique

: le courant faradique et le courant de couche double. Seul le courant faradique est le courant causé par la réaction électrochimique. Enfin, la mesure de l'angle de contact est une mesure essentielle pour caractériser la qualité (complétude et organisation de la couche) de monocouche auto-assemblée. En effet un groupement terminal donné détermine une valeur d'angle de contact. Sa valeur couplée aux résultats de l'imagerie par microscopie à sondes locales nous aide à déterminer si la couche est complète et ordonnée, ou non. De plus, dans le cas des couches binaires l'utilisation de la loi de Cassie donne une évaluation de la composition respective des deux composants sur la surface.

En ce qui concerne mon travail expérimental je me suis d'abord attaché à démontrer l'effet de la nature de la molécule interfaciale entre le substrat la molécule électro-active sur la réponse électrique de cette dernière. Cela constitue le chapitre trois. Pour cela, j'ai travaillé sur un système modèle en remplaçant l'oligopeptide par une molécule à base de ferrocène terminée par un acide carboxylique. Les molécules intermédiaires choisies sont la cystéamine et l'aminothiophénol. Toutes deux se greffent sur l'or via leur groupement d'ancrage et comportent un groupement amine terminal permettant le greffage du composé de ferrocène grâce à son groupement acide carboxylique. Après l'étude des couches de cystéamine, de para-aminothiophénol, et de 3-amino-5-mercapto-1,2,4-triazole, trois systèmes ont été préparés, étudiés, et comparés : les monocouches des molécules à base de ferrocène sur or, sur cystéamine sur or, et sur aminothiophénol sur or. Le 3-amino-5-mercapto-1,2,4-triazole a été abandonnée car ses monocouches montrent une grande dispersion. La qualité des monocouche auto-assemblée a été examinée par la mesure de l'angle de contact de l'eau, la microscopie à la force atomique, la microscopie à l'effet tunnel au balayage, la spectroscopie XPS, la spectroscopie Raman exaltée par la surface, et la voltamétrie cyclique. Une fois le greffage de la molécule basée sur ferrocène prouvé, cette dernière technique nous a permis d'atteindre le but recherché. L'analyse des cycles d'oxydo-réduction des trois types de monocouches de la molécule basée sur ferrocène a permis d'identifier des décalages de polarisation en fonction des couches

intermédiaires cystéamine ou aminothiophénol. Cela montre que la nature des molécules des monocouches sous-jacentes, qui peuvent être identifiées également comme des chromophores push-pull sièges d'un dipôle, permet en effet de modifier la tension d'activation de la couche supérieure. Ainsi dans ce qui suit on s'intéressera aux monocouches à base des chromophore push-pull spécifiques qu'il a fallu au préalable synthétiser.

Dans ce chapitre, un autre objectif est de montrer la faisabilité de modulation de potentiel en utilisant la monocouche auto-assemblée de molécules d'aminothiol en raison de leur dipôle électrique intrinsèque. Cystéamine, para-aminothiophénol et 3-amino-5-mercapto-1,2,4-triazole sont adopté pour préparer la monocouche auto-assemblée. L'effet de modulation de potentiel peut être vu à partir de résultat de la voltamétrie cyclique. La première couche de cystéamine et para-aminothiophénol a un effet de modulation de potentiel de 0.05 V et 0.25 V pour le shift de signal de la réaction électrochimique vers une value plus haute. Ce phénomène montre la faisabilité de monocouche auto-assemblée constituée par des molécules comprenant un dipole comme chromophore push-pull pour réussir la modification de propriété électrique.

La synthèse des chromophores push-pull est abordée dans le chapitre quatre. La voie de synthèse est présentée. Puis, un chromophore push-pull spécial est utilisé pour une étude de la propriété photophysique en détail en utilisant la spectrophotométrie UV-visible. Une grande quantité de molécules de chromophore push-pull a été synthétisée. Il y a cinq parties dans la structure de chromophore push-pull, ce sont le groupement greffant, le lien aliphatique, le groupement électrodonneur, le groupement électroattracteur et le pont de structure conjuguée. Dans ce chapitre, le groupement électrodonneur est toujours N,N-dialkylamine. Au cours de la synthèse, il y a trois groupements organosoufrés qui peuvent être greffés sur le substrat d'or : le thiocyanate, le disulfure, et le thioacétate. Il y a aussi trois groupements électroattracteur différents, ce sont acide cyanoacrylique (acide

carboxylique + nitrile), aldéhyde et acide rhodanine-N-acétique (dithiocarbamate + amide) (Fig. 3). Toutes les informations de la synthèse organique, y compris tous les spectres (spectroscopie infrarouge à transformée de Fourier, spectroscopie de résonance magnétique nucléaire et spectroscopie de masse avec l'ionisation en électro-spray), sont détaillées à l a fin du quatrième chapitre.

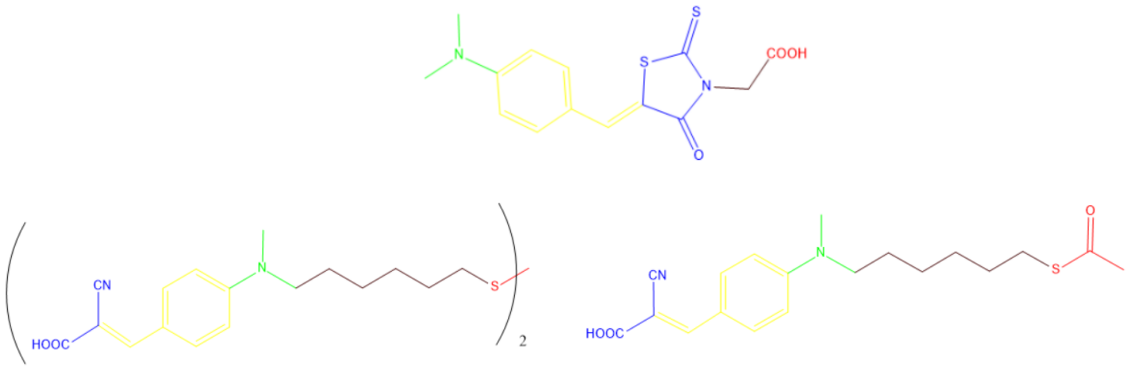


**Figure 3** : Les trois chromophores push-pull synthétisés.

Une fois les chromophores push-pull synthétisés, leur monocouches auto-assemblées ont ensuite été préparées sur or via un greffage de type thiol et étudiées. Plusieurs séries d'échantillons de monocouche auto-assemblées de chromophore push-pull ont été réalisées avec différentes concentrations et dans différents solvants. D'après les mesures d'angle de contact de l'eau, les images de microscopie à effet tunnel et à force atomique, ainsi que leurs analyses de section, la qualité de la monocouche auto-assemblée peut être directement influencée par la concentration de chromophore push-pull et la nature du solvant. Ces caractérisations ont été complétées par les techniques de spectroscopie infrarouge à transformée de Fourier, Raman en mode SERS, et XPS, permettant d'obtenir une signature des chromophores push-pull sur la surface et des informations sur leur interaction avec l'or. Une fois identifiés les paramètres de solvant et de concentration assurant les monocouches de push-pull de meilleure qualité, on s'est attelé à la fonctionnalisation de surface par la monocouche auto-assemblée d'oligomère de poly (éthylène glycol) 'PEG) et d'oligopeptide à partir d'aminoacide naturel (4KC). Ce choix a été inspiré par un article dans lequel une interface binaire est créée pour suivre l'interaction

antigène-anticorps en appliquant différentes tensions pour contrôler l'activation et l'inhibition de changement de conformation de chaîne chargée d'oligopeptide dispersée dans la matrice inerte de PEG. Ces monocouches auto-assemblées ont été caractérisées par les techniques de microscopie à effet tunnel et à force atomique, ainsi que par la spectroscopie infrarouge à transformée de Fourier pour le PEG. Une fois la préparation de ces monocouches validée, on s'est alors intéressé à la fonctionnalisation de surface par des monocouche auto-assemblées binaires afin d'isoler les chromophores push-pull au sein d'une matrice inerte. Pour cette dernière on a utilisé d'abord le dodécanethiol, l'acide 12-mercaptododecanoïque, et bien sûr le PEG. Tout à bord, nous avons fait un essai de la co-adsorption de l'oligomère de poly (éthylène glycol) (mPEG12SH) et de l'acide 12-mercaptododecanoïque. La réalisation de plusieurs monocouches auto-assemblée de ces deux composés avec différentes proportions montre que la co-adsorption marche bien. En appliquant la loi de Cassie après les mesures des angles de contact, la fraction molaire pour ces deux molécules sur la surface est presque la même que la fraction de ces deux composants dans la solution. Cela montre que la taille de la molécule n'a pas trop d'impact pour la cinétique d'adsorption si le groupement organosoufré des molécules est le même. Cela étant, afin de mieux contrôler l'adsorption isolée des molécules actives de push-pull, on a finalement opté pour l'obtention de monocouches auto-assemblées binaires par la méthode en deux étapes utilisant l'échange via l'équilibre dynamique du complexe thiolate-or. Pour cela, on a fait plusieurs essais à partir de l'insertion de chromophore push-pull dans les matrices de dodécanethiol et d'acide 12-mercaptododecanoïque, ainsi que d'acide 12-mercaptododecanoïque dans la monocouche de push-pull. Une fois ces insertions étudiées on a pu passer aux systèmes finaux obtenus par l'insertion dans la matrice de PEG d'une part des chromophores push-pull, d'autre part du 4KC. Les images de microscopie à effet tunnel, mais aussi de microscopie à force électrique pour le 4KC, et les mesures de l'angle de contact montrent une évolution de la fraction des différents composants sur la surface.

A la fin, les monocouches auto-assemblées binaires sont préparées avec succès par la réaction d'échange or-thiolate. Ces monocouches auto-assemblées sont caractérisées par angle de contact, la microscopie à effet de tunnel, la microscopie à force atomique et la microscopie à force électrostatique. Ce genre d'étude est intéressants pour le développement de l'électronique organique (dodécanethiol + chromophore push-pull) et biocapteur (oligo(éthylène glycol) + oligopeptide).

# Remerciements

Je tiens à remercier M. Lionel Patrone et Mme Virginie Gadenne pour les articles à lire et leur encadrement de thèse et M. Jean-Manuel Raimundo pour m'avoir accueilli au CINaM, donné des articles à lire et encadré sur mes travaux de synthèse chimique. Je tiens également à remercier les personnes suivantes qui ont contribué au contenu de la thèse : Mme Gaëlle Hisler et Mme Valérie Monier à Spectropole d'Université Aix-Marseille pour la spectroscopie de masse avec ionisation d'électrospray, M. Grégory Excoffier pour l'analyse élémentaire de CHNS/O à Spectropole d'Université Aix-Marseille, M. Frédéric Brunel pour la formation de spectroscopie de résonance magnétique nucléaire, Madame Gadenne pour préparer le substrat et la mesure pour la spectroscopie de Raman exalatée par la surface, la formation de la mesure de l'angle de contact et la formation de microscope à force atomique, Monsieur Jean-Christophe Valmalette pour le montage de la spectroscopie de Raman, Monsieur Patrone pour la préparation de substrat de l'or sur arsenide de gallium pour les mesures de l'angle de contact, la formation et quelques images pour la microscope à effet tunnel, Monsieur Guillaume Monnier de l'Institut Pascal pour les mesures et la mise en forme des résultats de spectroscopie de photo-électrons sous excitation par rayons X (XPS), Mme Ariana Villarroel Marquez pour son aide sur les expériences de voltamétrie cyclique et beaucoup de résultats au CINaM, M. Pascal Carrière du MAPIEM pour les mesures de spectroscopie infrarouge, et M. Premek Fitl et Ján Lančok, pour m'avoir accueilli dans leurs laboratoires de l'UCT et de l'Institut de Physique à Prague ainsi que et M. Martin Vondráček pour les mesures XPS qu'il a effectuées sur mes premiers échantillons. A la fin, je dois dire merci à M. Frédéric Brunel, Mme Virginie Gadenne, M. Lionel Patrone et M. Jean-Manuel Raimundo pour toutes les maintenances de laboratoire.

Je souhaite aussi remercier M. Frédéric Brunel et M. Marcos Aurelio Dahlem Junior pour les discussions constructives et m'avoir mis à disposition les équipements nécessaires pour la synthèse chimique au CINaM.

# Contents

**Introduction** **1**

**1. Bibliography** **4**

A. Push-pull chromophores ....4

I. Fundamental aspects ....4

II. Push-pull chromophore elaboration ....10

III. Typical reactions to synthesize push-pull chromophore....14

B. Surface functionalization by molecular self-assembled monolayer ....21

I. Surface functionalization of the substrate by self-assembled molecules ...21

II. Surface functionalization of gold by self-assembled molecules with thiol functional group ....26

III. Surface functionalization of gold by self-assembled multidentate organosulphur molecules....30

C. Potential applications using self-assembled monolayer of push-pull chromophore....37

I. Solar cell ....37

II. Nanodielectric material based on ferroelectric push-pull chromophore.42

III. Biosensors....46

**2. Characterization methods** **53**

A. Electrospray ionisation mass spectroscopy (ESI-MS)....53

B. Nuclear magnetic resonance spectroscopy (NMR) ....56

C. UV-visible spectroscopy (UV-vis)....59

D. Attenuated Total Reflection-Fourier Transform Infrared spectroscopy (ATR-FTIR) 62

E. Surface-enhanced Raman spectroscopy (SERS)....65

F. X-ray photoelectron spectroscopy (XPS) ....68

G. Cyclic Voltammetry ....70

H. Contact angle measurement....74

I. Scanning probe microscopy (SPM)....77

I. Scanning tunneling microscopy (STM) ....78

II. Atomic force microscopy (AFM)....80

III. Electrostatic force microscopy (EFM) ....82

**3. Self-assembled monolayer of push-pull chromophore using ferrocene as the electron donating group on different surfaces for the potential modulation** **84**

A. Self-assembled monolayer of different aminothiols on gold....85

I. Self-assembled monolayer preparation ....86

II. Contact angle measurement ....87

III. Scanning probe microscopy ....87

IV. Conclusion ....94

B. Ferrocene derivative molecule on the aminothiol self-assembled monolayer for the effect of potential modulation ....95

I. Self-assembled monolayer preparation ....95

II. Atomic force microscopy ....96

III. Scanning tunnelling microscopy....99

IV. X-ray photoelectron spectroscopy....101

V. Surface-enhanced Raman spectroscopy ....106

VI. Cyclic voltammetry ....107

VII. Conclusion ..... 112
C. Conclusion ..... 113
**4. Push-pull chromophore 114**
A. Synthesis of the push-pull chromophore ..... 114
B. Push-pull chromophore characterization by UV-vis spectroscopy ..... 120
C. Conclusion ..... 125
D. Experimental part ..... 126
**5. Self-assembled monolayer of push-pull chromophore and oligomers on gold 149**
A. Self-assembled monolayer of synthesized push-pull chromophore on gold 149
I. Self-assembled monolayer preparation ..... 149
II. Contact angle measurement ..... 152
III. Scanning tunnelling microscopy ..... 153
IV. Atomic force microscopy ..... 161
V. Surface-enhanced Raman spectroscopy ..... 168
VI. Attenuated total reflection-Fourier Transform Infrared Spectroscopy ..... 169
VII. X-ray photoelectron spectroscopy ..... 172
VIII. Statistical analysis of the I-V curves of the adsorbed push-pull chromophore molecule on the surface ..... 174
IX. Conclusion ..... 181
B. Self-assembled monolayer of thiol based on the chain of oligo(ethylene glycol) and oligopeptide on gold ..... 182
I. Self-assembled monolayer preparation ..... 182
II. Kinetics study of the formation of the self-assembled monolayer of mPEG12SH on gold using atomic force microscopy ..... 183
III. Scanning tunnelling microscopy ..... 187
IV. Attenuated total reflection-Fourier transform infrared spectroscopy ..... 189
V. Conclusion ..... 190
C. Surface functionalization of the gold surface by binary self-assembled monolayer of the molecule on the surface ..... 191
I. Binary self-assembled monolayer preparation ..... 191
II. Contact angle measurement ..... 192
III. Scanning tunnelling microscopy ..... 193
IV. Electrostatic force microscopy ..... 195
V. Conclusion ..... 198
D. Conclusion ..... 199
**6. Conclusion and perspectives 200**

# Introduction

Push-pull chromophores provide an intramolecular charge separation between a Donor and an Acceptor group via a spacer (Fig. 1). Such an effect can be exploited in various fields such as nonlinear optics, solar cells[1,2], in the modification of the work function and the interface with electrodes, or the formation of a high dielectric permittivity layer[3,4] beneficial in micro-nanoelectronics, or in photovoltaics to hinder the recombination of photogenerated excitons. For this purpose, it is essential to orient all the dipoles in the same direction and to avoid head to tail arrangement. Self-assembled monolayers[5] of chromophores grafted on the surface is a very promising strategy making it possible for the chromophore to organize in the same orientation which is necessary to obtain controlled collective phenomena. Previous works on push-pull dealt with charged molecules which can hinder the organization by the effect of repulsion between charges.

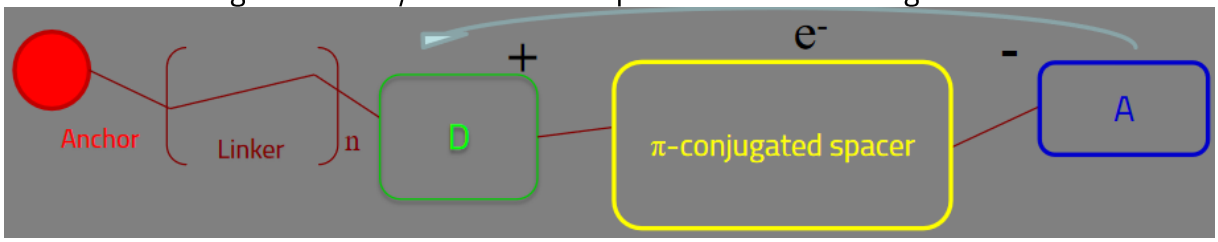


**Figure 1**: Structure of a push-pull chromophore with an anchor group for the grafting on a surface.

In this work, we propose to focus on the formation of ordered SAMs of original non-charged push-pull chromophores based on the expertise developed in the Nano group of IM2NP[1,6]. For this purpose, this PhD has been carried out in close collaboration with chemists from CINaM in Marseille to develop uncharged push-pull chromophores which ensure good organization of self-assembled monolayers and efficient charge separation. Once the organization of self-assembled monolayers has been mastered, the idea is to produce binary layers of complementary chromophores diluted in an inert thiol with a chain of oligo (ethylene glycol) mPEG12SH matrix for application to biosensors with selective detection. For this we worked on gold substrates with chromophores each presenting a potential of its own and which will serve to activate the deployment outside the inert matrix of an oligomer loaded with oligopeptide 4KC thus allowing the detection of target species within a biosensor[7] (Fig. 2).

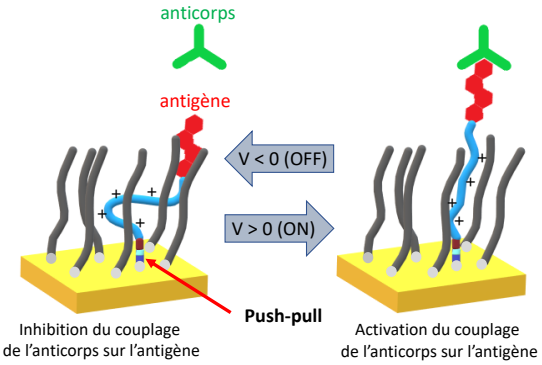


**Figure 2**: principle of detection of antibodies by the voltage applied to the surface.

The **first chapter** deals with bibliographic research on the subject. The first part is devoted to push-pull chromophores, its fundamental aspects. The second part addresses self-assembled monolayers on different substrates by various organosulfur molecules: the fundamental model of the self-assembled thiol monolayer on gold, the different organosulfur molecules. The last part is devoted to the different direct applications of self-assembled monolayers of push-pull chromophores, in particular solar cells (Grätzel, perovskites, ...) and nanodielectrics which take advantage of the orientation of dipoles in the organized layer on the surface.

The **second chapter** presents all the characterization methods used during the organic synthesis of push-pull chromophores, and to analyse the self-assembled monolayers of push-pull chromophores on the gold substrate: local probe microscopies for the self-assembled monolayer, optical spectroscopies for organic synthesis and self-assembled monolayer, mass spectroscopy for organic synthesis, contact angle measurement , and XPS, infrared, and Raman- SERS spectroscopy techniques for the self-assembled monolayer.

Regarding my experimental work, I first focused on the **chapter 3** on demonstrating the effect of the nature of the interfacial molecule between the substrate and the electro-active molecule on the electrical response of the latter. To do this, I worked on a model system by replacing the oligopeptide with a ferrocene-based molecule terminated by a carboxylic acid. The intermediate molecules chosen are cysteamine and aminothiophenol. The potential shifts of the ferrocene redox cycles as a function of using cysteamine or aminothiophenol as intermediate layers were analysed by cyclic voltammetry.

Then, to go on the study with appropriate push-pull chromophores, the synthesis of original non-charged push-pull compounds is addressed in **chapter 4**. The synthesis route is presented to obtain a chromophore comprising a thiol-based head allowing its grafting onto a gold substrate. All organic synthesis information, including all spectroscopic analyses of the synthesis products (Fourier transform infrared spectroscopy, nuclear magnetic resonance spectroscopy and mass spectroscopy with electro-spray ionization), are detailed.

At last, in the **chapter 5** I discuss the self-assembled monolayers of the synthesized push-pull chromophores, of mPEG12SH used as an inert matrix, and of 4KC charged

oligopeptide able to be unfolded under a potential. Finally, the possibility to prepare binary monolayers such as push-pull or 4KC isolated in PEG have been studied.

The last part of the manuscript deals with a **general conclusion and perspectives** of this work.

# 1. Bibliography

## A. Push-pull chromophores

### I. Fundamental aspects

The push-pull chromophore is a type of advanced functional material[8] and the first application of this kind of advanced functional material was the organic second-order nonlinear optical materials[9]. The electron-donating group, the electron-withdrawing group, and the π-conjugated spacer in between are key components of the push-pull chromophore. Organic π-systems are widely investigated in the domain of organic chemistry and material chemistry in the last four or five decades. Widespread applications were found across various branches of modern research in the chemistry, materials and physics. They are used as active substances in organic electronics and organic optoelectronics[10–12]. Compared to widely explored inorganic analogues, organic push-pull chromophore is used on the development in the fields of dye-sensitizing solar cells (DSSC)[13], organic photovoltaic cells (OPVC)[14], organic bulk-heterojunction solar cells (BHJ)[15], organic light-emitting diodes (OLED)[16] and organic field-effect transistors (OFET)[17].

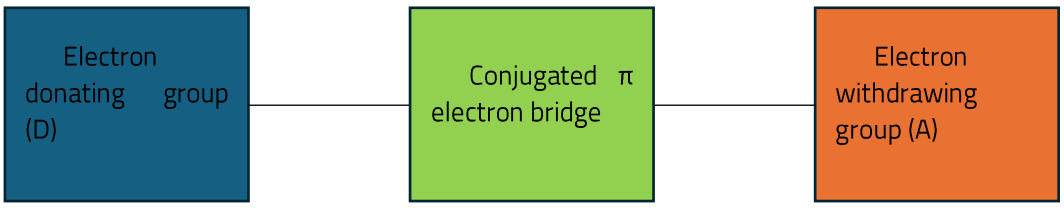


**Figure 1**: the structure of the push-pull chromophore

Organic push-pull chromophore constituted by an electron donating group (D), an electron withdrawing group (A) and conjugated π-systems in between represent a subclass of these molecules. The structure of the push-pull chromophore is presented in figure 1. In the optoelectronics, these two molecular orbitals are often the HOMO (highest occupied molecular orbital) and LUMO (lowest unoccupied molecular orbital). Due to the interaction between the electron donating group (D) and the electron withdrawing group (A), two new molecular orbitals (MO) are formed with smaller energy gap in the electronic structure. The absorption of photon is in the range of ultraviolet-visible light and therefore push–pull molecules are generally with significance of colour. They are referred to also as charge-transfer chromophores because the absorption is caused by internal charge transfer (ICT)[18]. The electron-donating group shows a partial negative charge due to the high electronic density and the electron-withdrawing group shows a partial positive charge due to low electronic density. This makes the push-pull chromophore a ferroelectric characteristic, which means a permanent electrical dipole. According to the mesomere structure in organic chemistry for a molecule, a dipolar structure in the reverse direction can be drawn. The electron transfer (internal charge transfer) direction is from the electron-donating group to the electron-withdrawing group via the π-conjugated spacer or the reverse direction

depending on the electrical potential. This ICT is also the mechanism for the reversion of the polarity of the push–pull chromophore.

The result of UV-vis spectrophotometry in figure 2 takes the p-nitroaniline (one of the most basic push-pull chromophore) as an example. The UV-vis spectroscopy can be used to see the optical properties of π-conjugated molecules. The UV/Vis absorption spectra were recorded for aniline (only D), nitrobenzene (only A), 3-nitroaniline and 4-nitroaniline. Only absorption in the UV region is observed for the aniline and nitrobenzene, whereas 4-nitroaniline showed bathochromically shifted and intense absorption maxima (internal charge transfer). However, 3-nitroaniline demonstrated a decreased peak because of the violation of the octet rule together with a non-conjugating structure of the amine functional group and the nitro functional group.

The internal charge transfer and optical properties such as absorption can be tuned by: 1. different electron donating group and different electron withdrawing group, (ii) efficient interaction between the electron-donating group and the electron-withdrawing group, (iii) composition, spatial arrangement and the length of the π-conjugated spacer, (iv) diminution of the bond-length alternation (BLA) for the π-conjugated spacer (v) planarization of the entire molecule[19]. By plotting the electronic structure of the molecule, the electronic density of the HOMO is on the position of the electron-donating group , the electronic density of the LUMO is on the position of the electron-withdrawing group and the interaction of π-electrons in between contributes the less intensive redshift of the absorption peak.

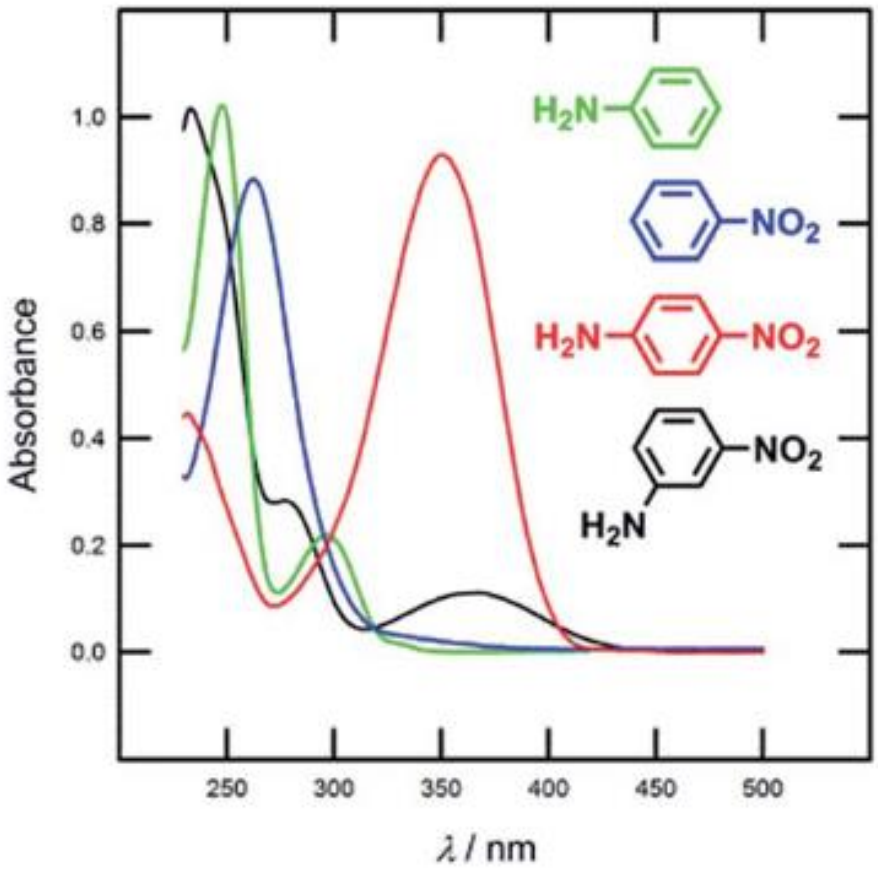


**Figure 2**: UV/Vis spectra for nitroaniline[8] and their derivatives.

In the field of push-pull chromophore, a group that has an electron-donating ability in the conjugated system is called an electron donor. The electron-donating ability is induced by electronegativity of the atom and/or by the mesomere structure. Aromatic and heterocyclic structures that are rich in electrons are usually used as electron donors. Normally, these structures are modified by one heteroatom with a lone pair of electrons, e.g., N, S[20], or O. The electron-donating ability increases in the following order: Br < $OC_6H_5$ < $SCH_3$ < OH < $OCH_3$ < $N(CH_3)_2$[8]. The electron donor donates an electron or charge in the form of π-π* charge transfer, and the heteroatom can enhance the π-π* charge movement in the molecule. The electron donors are mainly conducted to improve the electron-donating ability of the donor. As the strength of the electron donating group increases, the electronic density at the position of the electron-donating strength is larger.

Electron donors can be roughly divided into the following categories: aniline based electron donor, heterocyclic donor, and organometallic donor. They are summarized in figure 3.

The synthesis method of an aniline based electron donor (**1**-**9**) is simple. A strong electron-donating ability and good thermal stability are the reasons that it is widely used. An auxiliary donor is an electron-rich group that is introduced into the conjugated structure near the donor end; it can increase the electron cloud density at the donor location and enhance the electron-donating ability of the donor.

Compared with a benzene ring, the delocalization energies of heterocyclic donors such as pyrrole, thiophene, and furan in the heterocyclic structure are lower[21–24]. Nitrogen atoms are introduced into the heterocycle, and the lone pair of electrons can be delocalized more effectively, and the electron cloud density of the electron donor larger. Robin-le Guen and Franco et al. have reported a novel pro-aromatic electron donor based on pyranylidene (**10**). Such kinds of donors showed special electron-donating abilities and chemical stabilities[25–30]. In addition, electron donors based on tetrahydroquinolinyl and julolidinyl groups were prepared[26,31]. Compared with the traditional 4-(dialkylamino)phenyl donors or 4-diarylaminophenyl donors, the ring-fused aminophenyl structures in the tetrahydroquinolinyl and julolidinyl donors.

The structure of the ferrocene is an iron atom which is capped by two cyclopentadiene ligand in the middle, forming an electron donor. Free electrons on the iron atom enhanced the electron-donating ability and stability of cyclopentadiene. It was the first type of organic-inorganic hybrid donor. Some push-pull chromophores are based on ferrocene (**11**-**13**). And some other chromophores with metal complex structures were also reported recently[32]. In terms of the electronic structure, the most intensive electronic transition is often not the HOMO-LUMO transition. The HOMO in the organometallic compound often contains the d character after the complexation according to the ligand field theory. The most intensive transition is usually the π-π* transition, which is less relevant to the central metal ion.

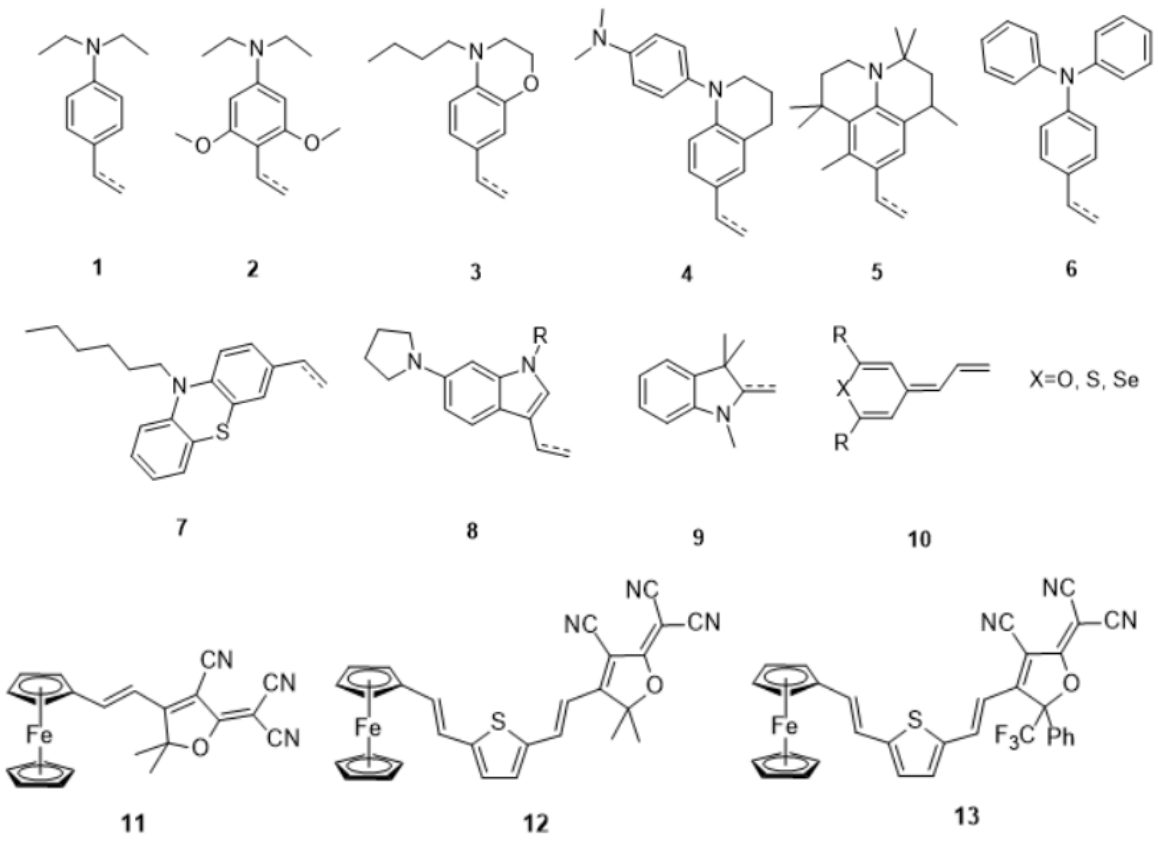


**Figure 3**: (top) Structure of electron donors and (bottom) push-pull chromophore based on ferrocene electron donating group[9]

The electron acceptor, as an electron-transfer terminal group that is induced in the chromophore conjugation system, is generally a group that has an electron-withdrawing ability. They are summarized in figure 1.4. The early electron acceptors generally included cyano groups (-CN)[33], nitro groups (-$NO_2$), and cyanoethylene[34]. The electron withdrawing groups can be divided into several kinds: malonic acid derivatives (**14**-**17**), indane-1,3-dione derivatives (**18**-**21**), cationic acceptors (**22**), and heterocyclic acceptors (**23**) and proaromatic acceptors (**24**-**27**). Several classical electron-withdrawing groups, including SDS, TCI, BBA, TCF, and TCP. Among them, the TCF acceptor and TCP[35] acceptor are used in most chromophores. The electron-withdrawing ability is stronger than those of the TCF and TCP acceptors. In addition, they also exhibited good chemical and physical stabilities due to their pentacyclic aromatic structure. Different substituents could be introduced to the TCF acceptor to improve the solubility and electron-withdrawing ability of the chromophore. An electron acceptor with excellent properties was obtained by modifying a methyl group to $-CF_3$.

The conjugated π electron bridge is an important part of the chromophore that connects the electron donor and acceptor[36–39]. Normally, as the conjugated electron bridge becomes longer, the first hyperpolarizability of the chromophore becomes larger and the maxima of the absorption in the visible region becomes larger. The relationship between the structure of the common conjugated π electron bridge in Figure 5 (**28**-**33**)[40,41].

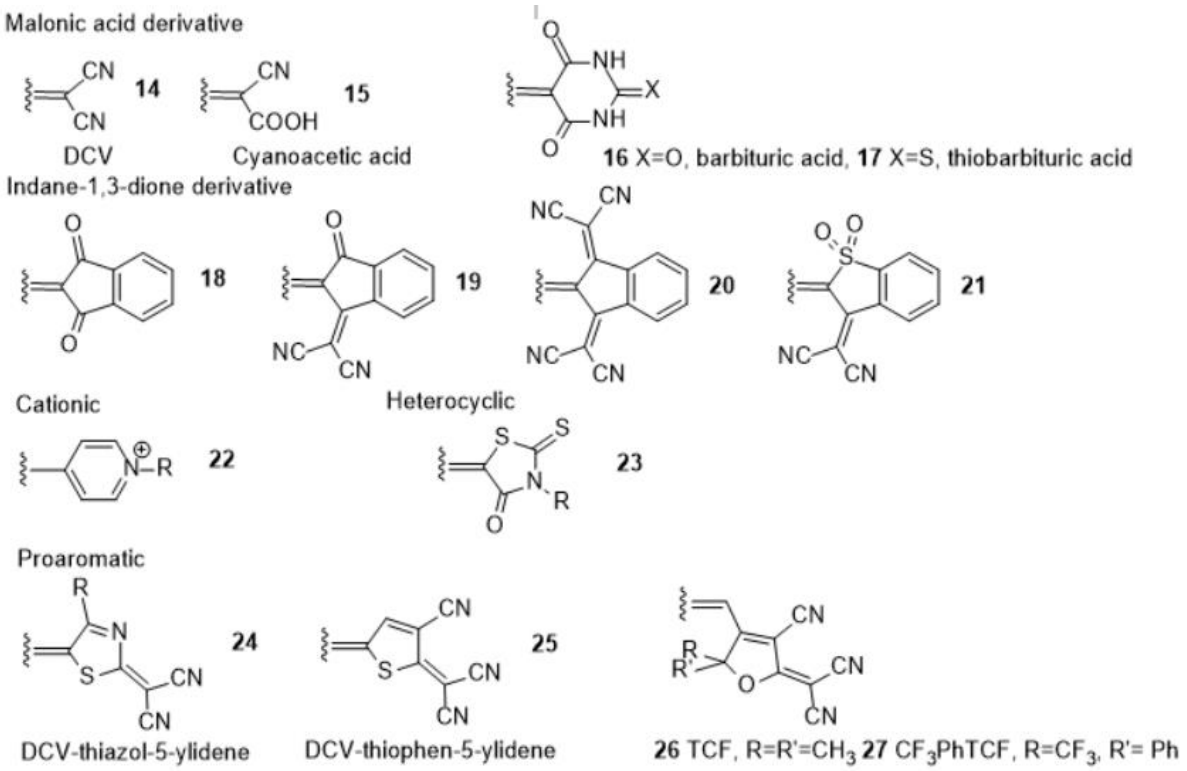


**Figure 4**: Electron withdrawing moieties applied as acceptors in push-pull chromophore[8]

Due to the advantages in 3d not fully occupied orbital of the sulphur, thiophene is widely used as a π electron bridge. A variety of different steric groups, such as rigid aromatic groups or flexible alkoxy chain groups, were introduced to the 3,4 positions of the thiophene ring. Moreover, the planarity of the push-pull chromophore is improved for a better electron transport ability[42–44]. There are many kinds of electron bridges. In addition to the conventional electron bridges mentioned above, polythiophene compounds are also used as electron bridges. However, the maximal saturation value is approximately 20 double bonds since the absorption wavelength of the chromophore will lead to absorption with too high wavelengths (1310 or 1550 nm).

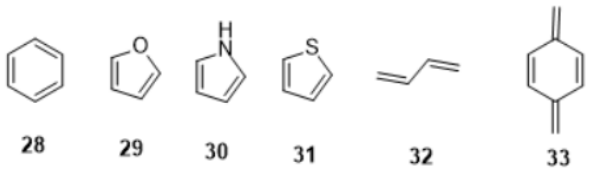


**Figure 5**: Common conjugated π-electron bridge structure [40,45]

The effect of the different π-conjugated spacers can be clearly shown in the result of the UV-visible spectrophotometry. The figure 6 shows the result of the UV-visible spectrophotometry of the push-pull chromophore with different π-conjugated spacers using N,N-dimethylamino electron-donating group and dicyanoimidazole electron-withdrawing group. Moreover, additional olefinic/acetylenic group induced (partial) planarization of the entire π-system. It is the case in styryl, stilbenyl and

phenylethynylphenyl. The biggest changes are observed concerning the HOMO energy levels. π-system extension lowered the HOMO–LUMO gap and further insertion of an olefinic unit caused a further decrease in the gap by additional 0.35 eV. The most efficient internal charge transfer has been achieved with phenylethynylphenyl. Keeping the same acceptor and donor, all changes represented in the UV-vis spectra can be interpreted by the change of the π-linker. The position of the charge transfer bands depends on the composition, length, and spatial arrangement of the π-system.

The LUMO levels can be lowered by the replacement of 1,4-phenylene group by 2,5-thienylene group. The result shows that the bandgap decreases from 1.51 to 1.34 eV if one the two 1,4-phenylene groups is replaced by a 2,5-thienylene group with a redshift by 52 nm for the maximum of the absorption. However, the HOMO–LUMO gap is not well influenced after the second replacement by 2,5-thienylene group with a smaller 24 nm redshift. With two thiophene moieties, chromophore 21c showed the highest vertically excited state and highest ground state of dipole moments and the most redshifted and intense charge transfer absorption peak at 525 nm.

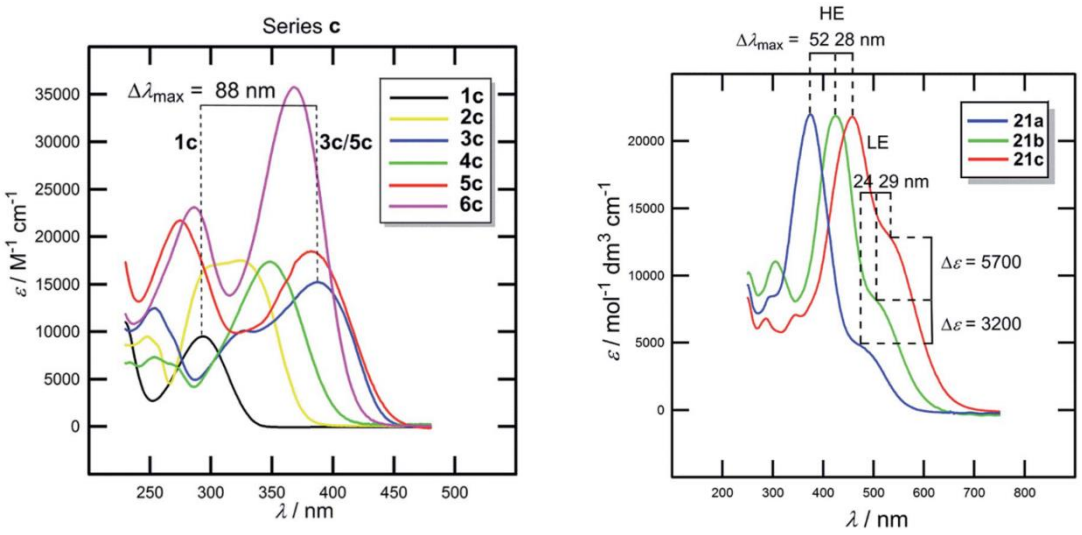


**Figure 6**: (left) UV/Vis absorption spectra of N,N-dimethylamino and dicyanoimidazole based push-pull chromophores with different additional π-conjugated bridges: 1,4-phenylene (2c), styryl (3c), biphenyl (4c), stilbenyl (5c) and phenylethynylphenyl (6c), (right) UV/Vis absorption spectra of N,N-dimethylamino and dicyanoimidazole based push-pull chromophores with different additional π-conjugated bridges: stilbenyl (21a), phenylethenylthienylene (21b) and thienylethenylthienylene (21c).

## II. Push-pull chromophore elaboration

Malytskyi et al. made a review of the molecule structure-photophysical property of the push-pull chromophores for the application of small molecule organic solar cells[1]. D-π-A, D-π-A-π-D and D-π-A-π-D-π-A-π-D structures are more interesting.

In this paragraph, the electron-donating group and electron-withdrawing group is not as simple as in the previous section. Push-pull chromophore based on conjugated triarylamine with di- or tricyanovinyl electron-withdrawing groups (**34** and **35** in figure 7) have been largely tested[46,47]. As predicted, the change of the electron-withdrawing group from di- to tricyanovinyl (DCV, TCV) leads to a pronounced redshift, due to higher electron withdrawing strength of TCV. The change is also accompanied by an increased molar extinction coefficient. Another improvement of the photophysical properties of the push-pull chromophore has been done with the modification of the donor unit with carbazole, which paves an appealing way to tune and improve optical properties, and the fused benzothiophene rather than 2-thienylbenzene as spacer[48]. The use of the second benzothiadiazole acceptor along the π-conjugated spacer showed further findings (**36** and **37** in figure 7). The combination of two different electron-withdrawing groups offers additional electron-withdrawing strength with the π configuration[49–51]. These D-π-A(benzothiadiazole)-π-A structures exhibit both smaller bandgap and lowered HOMO levels.

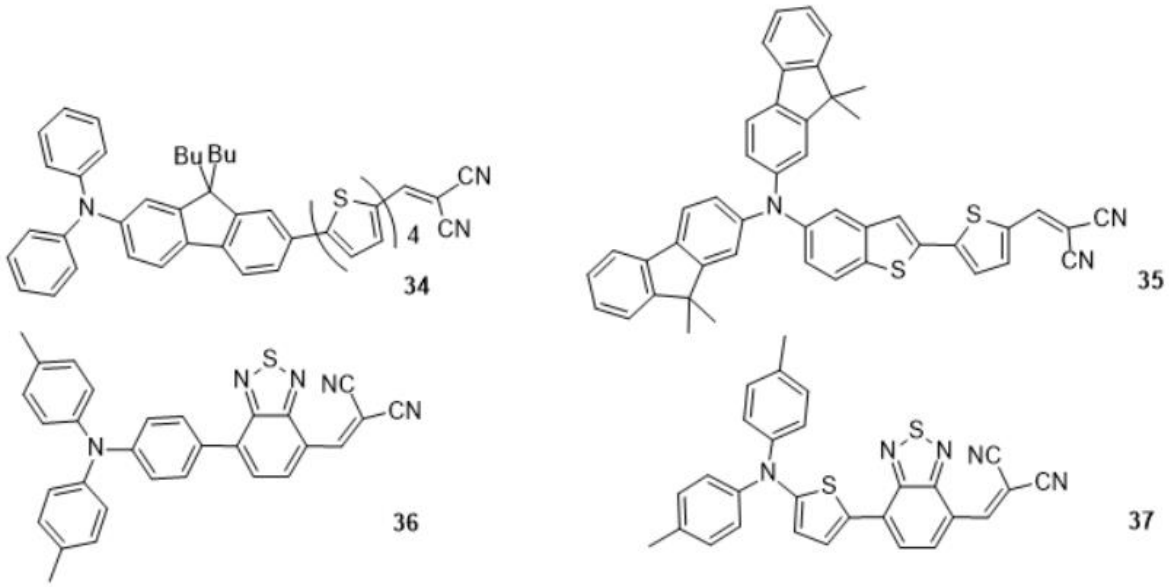


**Figure 7**: (**34**) the triphenylamine based push-pull chromophore with tetrathiophene spacer and the dicyanovinyl electron-withdrawing group; (**35**) push-pull chromophore with benzothiophene spacer; (**36**) triphenylamine-based-benzothiadiazole D-π-A-π-A push-pull chromophore; (**37**) thienyldiphenylamine-based-benzothiadiazole D-π-A-π-A push-pull chromophore.

D-π-A-π-D is an improvement of the design of the structure of the push-pull chromophore, especially interesting for the application for the bulk-junction organic solar cells when the electron-withdrawing group is dicyanovinyl. The mesomere ensures the simultaneous electron transfer from the electron-donating group to the electron-withdrawing group. In fact, one of the key processes for the organic solar cell is the formation of the exciton, which is a pair of an electron and a hole. In the case of the push-pull chromophore, the zwitterionic molecular structure upon the electron transfer process can be assimilated as an exciton since an electron jumps from the HOMO to the LUMO. Thus, D-π-A-π-D enables the formation of two excitons on the same molecule.

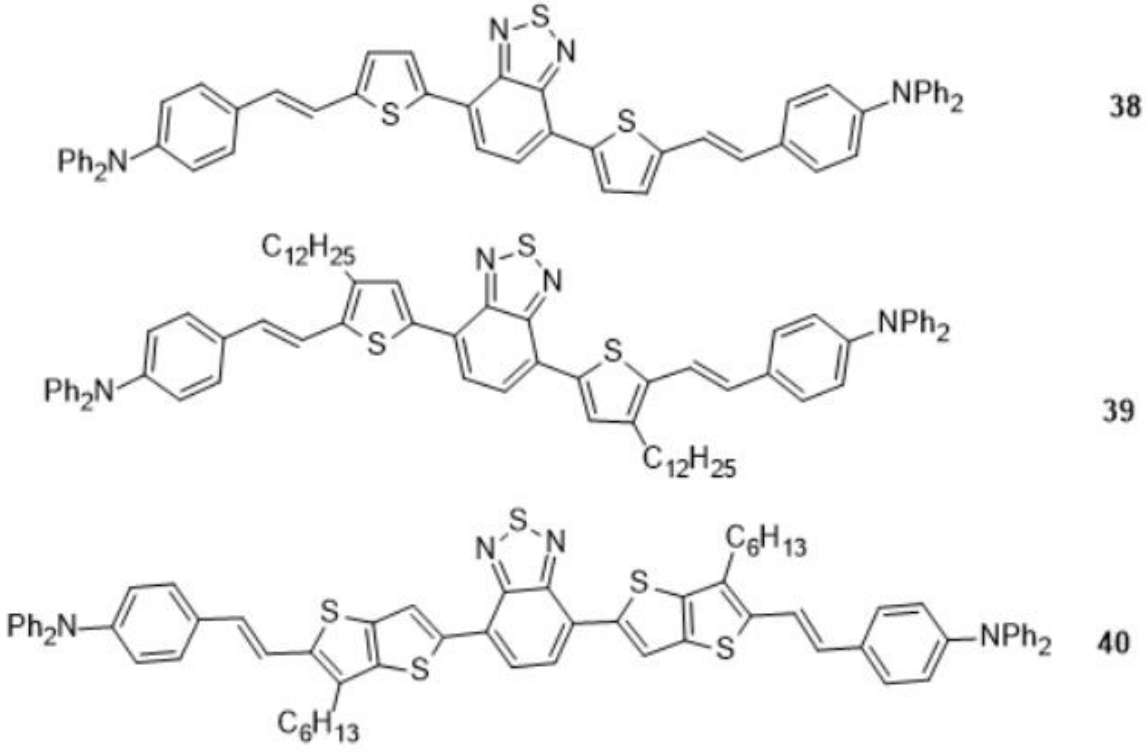


**Figure 8**: (**38**) the D-π-A-π-D push-pull chromophore with benzo [1,2,5]thiadiazole core; (**39**) the D-π-A-π-D push-pull chromophore with benzo [1,2,5]thiadiazole core decorated by a long alkyl chain; (**40**) the D-π-A-π-D push-pull chromophore with benzo [1,2,5]thiadiazole core and thieno[3,2-b]thiophene spacer decorated by a long alkyl chain

The work of Li[52] (**38** in figure 8) used the benzo[1,2,5]thiadiazole moiety as the central electron-withdrawing group (electron-withdrawing group) to create the push-pull chromophore. The push-pull chromophore is decorated by triphenylamine donors and connected using thiophenic linkers.

Further studies were done on compounds modified by a long alkyl chain along the π-conjugated backbone with the aim to have good solubility (**39** in figure 8). The compound is crystalline, and this will certainly enhance the performances of the devices. Due to its extended π-conjugated system, the result of UV-vis exhibits a centre of absorption at 456 nm in the visible region.

Li and coll. have changed the structure chromophore to increase its efficiency in bulk heterojunction solar cells[52]. The morphology is improved by the addition of hexyl side chains. The extension using the thieno[3,2-b]thiophene (**40** in figure 8) rather than thiophene as the π-conjugated spacer permits the broadening of the absorption spectra significantly since the molecular structure of the π-conjugated linker plays an important role to improve the performance. Moreover, Li et al. used a (dicyanomethylene)-pyran unit in chromophores by replacing the benzothiadiazole core.

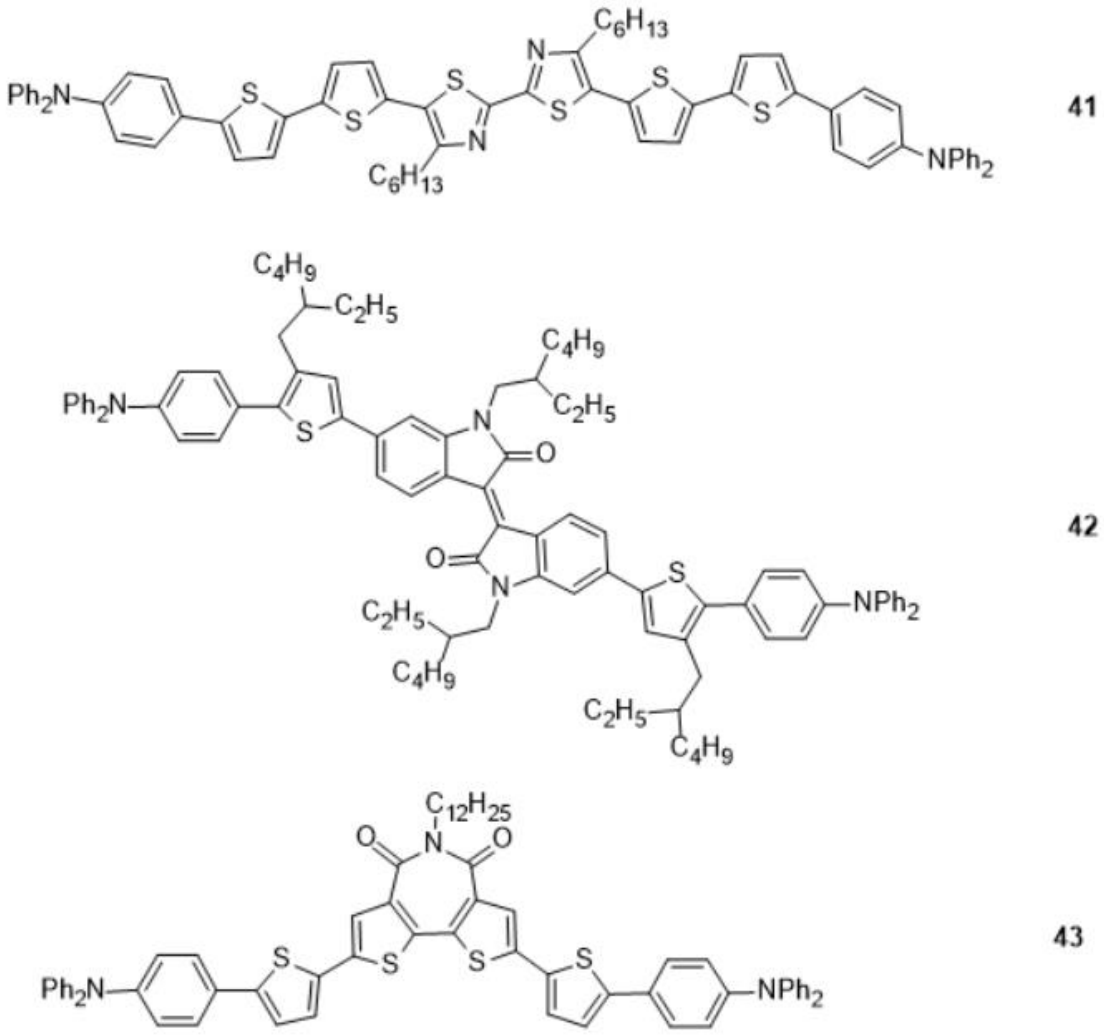


**Figure 9**: (**41**) the D-π-A-π-D push-pull chromophore with bisthiazole core; (**42**) the D-π-A-π-D push-pull chromophore based on triphenylamine and isoindigo; (**43**) the D-π-A-π-D push-pull chromophore with fused bithiophene imide as the electron-withdrawing group

Bisthiazole was adopted as the core as well as the electron-withdrawing group to synthesize push-pull chromophore which absorbs photons with lower energy[53] (**41** in figure 9). With longer π-conjugated spacer, the arrangement in the condensed state of push-pull chromophore becomes better. With the same goal to create push-pull chromophore which can absorb red light, isoindigo and triphenylamine were adopted as the electron-

withdrawing group and electron-donating group (**42** in figure 9) by Yang and coll[54,55] to fabricate dye-sensitized solar cells.

In another article, Suh et al. reported the synthesis of push-pull chromophore by designating the electron withdrawing unit using bithiophene imide (BTI) (**43** in figure 9)[56]. Apart from the strong electron withdrawing ability, the BTI based push-pull chromophore has good solubility in the organic solvents for the processing and close π–π stacking in the condensed state can be ensured by its planar architecture.

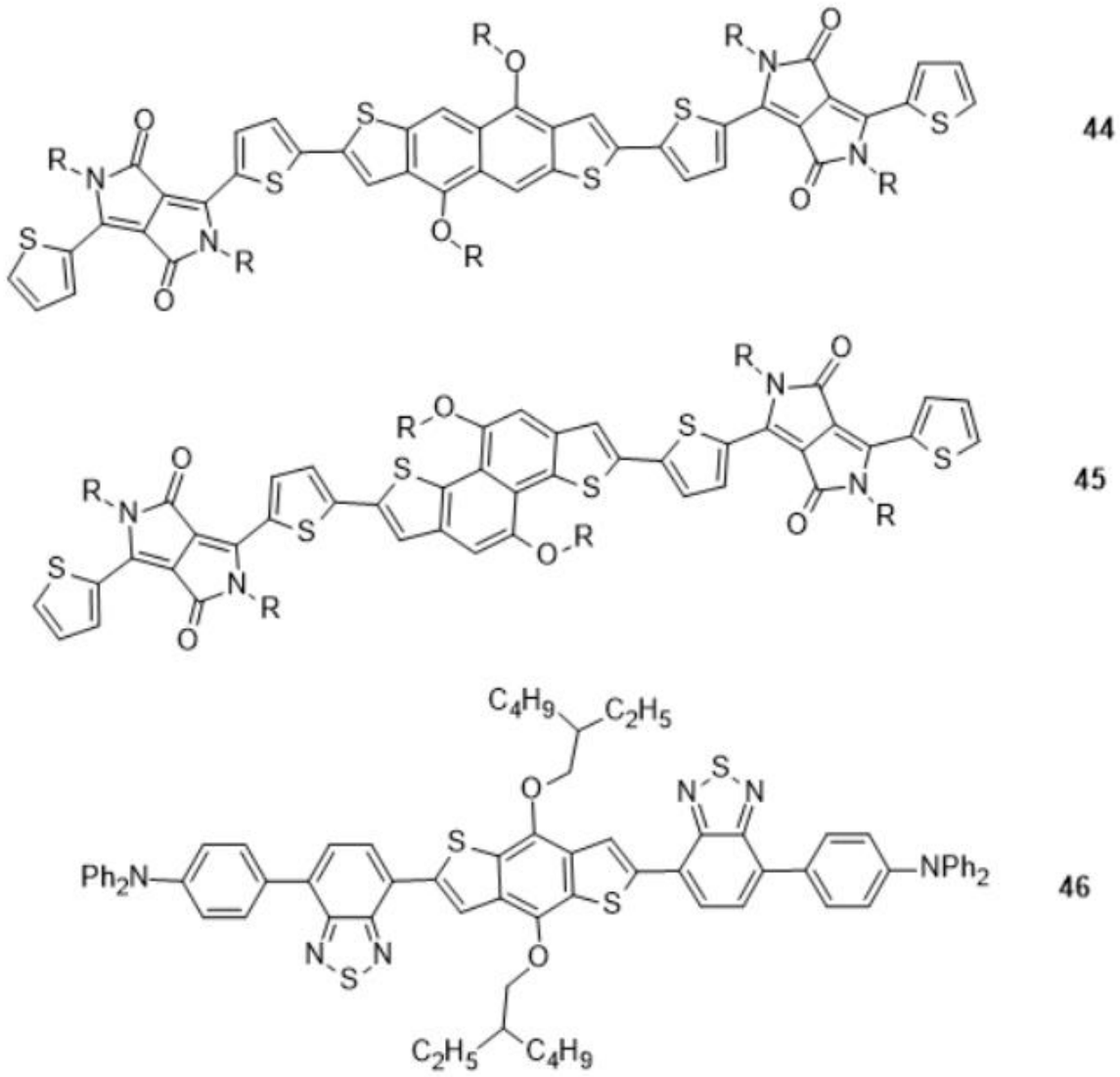


**Figure 10**: (from top to bottom) the D-π-A-π-D-π-A-π-D push-pull chromophore with linear naphthodithiophene core (R=2-ethylhexyl); the D-π-A-π-D-π-A-π-D push-pull chromophore with zig-zag naphthodithiophene core (R=2-ethylhexyl); the D-π-A-π-D-π-A-π-D push-pull chromophore with benzo[1,2-b:4,5-b']dithiophene(BDT) core

For the creation of D-π-A-π-D-π-A-π-D push-pull chromophores for the bulk-heterojunction solar cells, used naphthodithiophene as the central electron-donating group (**44** and **45** in figure 10) [57,58]. Lee et al. have taken BDT (benzo[1,2-b:4,5-b']dithiophene) as the core electron-donating unit (**46** in figure 10) for the same purpose as Marks et al.

## III. Typical reactions to synthesize push-pull chromophore

Here are some chemical reactions to form linear push-pull chromophore. An aldol condensation is a reaction by using α-carbon next to the carbonyl or other electron-withdrawing groups. These hydrogen atoms are much more acidic than other hydrogen atoms on the carbon chains. The most acidic proton is on the α-carbon between two carbonyl or other electron-withdrawing groups. The base takes a proton from α-carbon next to the carbonyl or other electron-withdrawing groups and the carbanion is stabilized by the mesomere structure (aldol condensation). Then this carbanion attacks the aldehyde group. After becoming more leaving group for the hydroxyl in the intermediate structure, a molecule of water as the byproduct of the reaction is formed along the elimination process according to the E1 mechanism.

Gadenne et al.[59] synthesized push–pull chromophores for a joint SERS/DFT study to probe the order of the structure of deposited on the substrate (figure 1.11). In this article, the electron-donating group is heterocyclic compound based on bithiophene. Due to poor content for the molecule grafted on the surface, the surface-enhanced Raman spectroscopy using nanostructured surface can be used to enhance the signal in the spectra. The result shows that the configuration of the push-pull chromophore molecule can be either flat on the surface or perpendicular to the surface by using different solvents after the interpretation using density functional theory analysis. The push-pull chromophores are made via aldol condensation reaction using commercially available 1H-indene-1,3-(2H)-dione (**48**) and 5′-bromo-5-formyl-2,2′-bithiophene (**47**) or 5′′-bromo-5-formyl-2,2′:5′,2′-terthiophene (**50**) respectively.

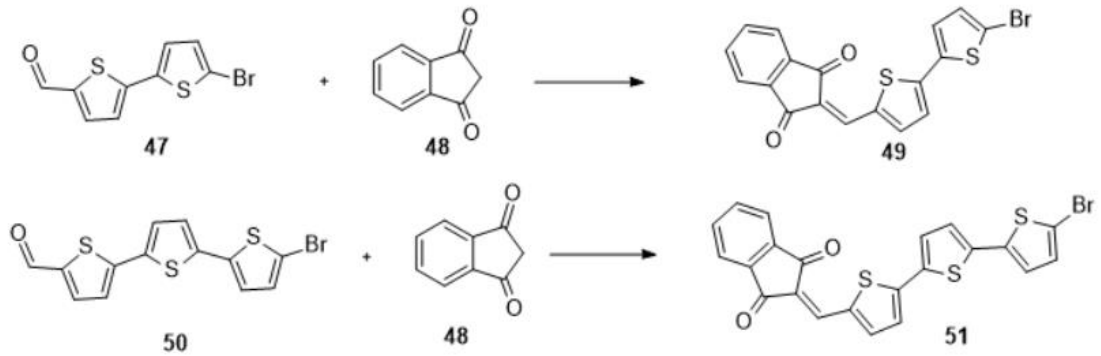


**Figure 11**: the reaction to synthesize the push-pull chromophore using 1H-indene-1,3-(2H)-dione (**48**) and 5′-bromo-5-formyl-2,2′-bithiophene (**47**) or 5′′-bromo-5-formyl-2,2′:5′,2′-terthiophene (**50**)[59]

The formation of alkene double bond can be done by aldolization then a [2+2] cycloaddition reaction. An example is in the article of Marco et al. (figure 1.12) where they created organic sensitizers whose electron-donating group is proaromatic pyranylidene (**53**) and a series of thienothiophene-based molecules as the π-conjugated spacer for the application of dye-sensitized solar cells. The enolizable proton is on the phosphoryl proton and a much stronger base such as n-butyllithium or potassium tert-butoxide are required to start the reaction. As the carbanion attacks the aldehyde group, the reaction undergoes

a [2+2] cycloaddition from the hydroxylate to the electrophilic centre of phosphoryl group and the byproduct of this reaction is not a water molecule but a diphenylphosphinate.

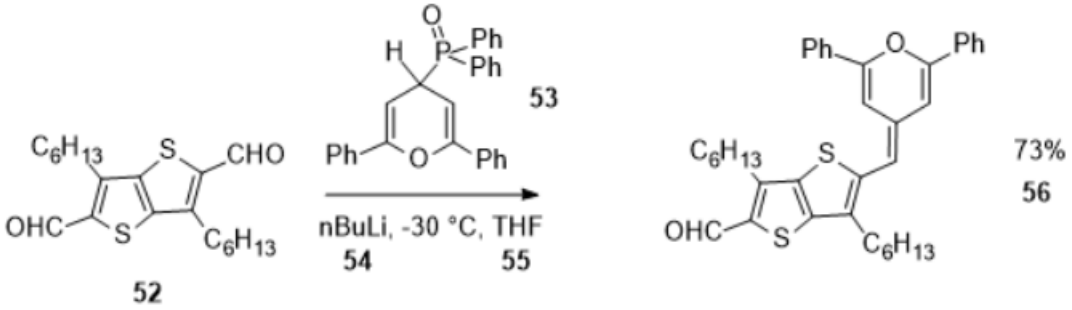


**Figure 12**: the reaction to combine the pyranylidene electron-donating group (**53**) and thienothiophene-based molecules π-conjugated spacer (**52**) for the push-pull chromophore (**56**)[60].

The Knoevenagel reaction can be considered as the upgraded version of aldol condensation reaction. In aldol condensation reaction, the enolizable proton of $\alpha$-carbon next to the carbonyl of the substrate is either absorbed by a strong base to form the enolate or by a water molecule after the activation of the carbonyl by the proton. In the case of the basic enolization, the kinetic enolate is formed preferentially, however, the reaction condition is sometimes harsh such as the use of sodium hydride. In the case of the acidic enolization, the thermodynamic enol is formed preferentially, but the reaction speed is much slower, and some functional groups is not compatible with such acidic conditions such as the acetal protection of aldehyde or diol. The use of the piperidine in the Knoevenagel reaction activates the carbonyl via the iminium intermediate to form the electrophile for the aldol condensation reaction gives a much milder condition under which the anhydrous solvent and the inert gas environment is no longer in need.

Cyanoacrylic acids are one of the most adopted malononitrile derivative electron-withdrawing group, it is more than electron-withdrawing because the carboxylic group can be considered as an anchoring group. Unny et al. (figure 13) have designed and synthesized a new sensitizer with an architecture of D-π-D′-π–A (**61**) containing pyrene and carbazole as donor moieties and cyano-acrylic acid as the acceptor bridged by a double bond spacer. The photophysical property of this sensitizer is checked by measuring the power conversion efficiency.

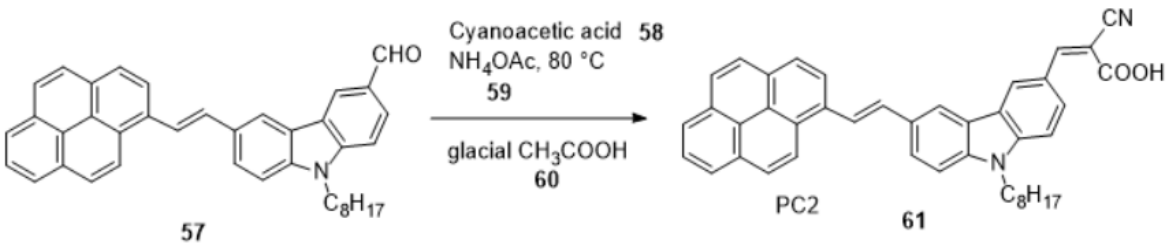


**Figure 13**: synthetic route of pyrene–carbazole dye PC2(**61**)[61]

Wittig reaction is a very famous reaction to create novel carbon-carbon double bond in the structure of the molecule. An example (figure 14) to use the Wittig reaction to design the push-pull chromophore is in the article of Paul. et al. They created an innovative

application for the push-pull chromophore. A stilbene based push–pull chromophore is used as photoremovable protecting group. Compared to conventional protecting group, the deprotection reaction occur after illumination by visible light. Then, alcohols and carboxylic acids will be released via the cyclization and aromatization. The whole releasing reaction can be evidenced in real time due to fluorescence phenomenon in polar medium. This push–pull stilbene can be tested for in vitro drug delivery.

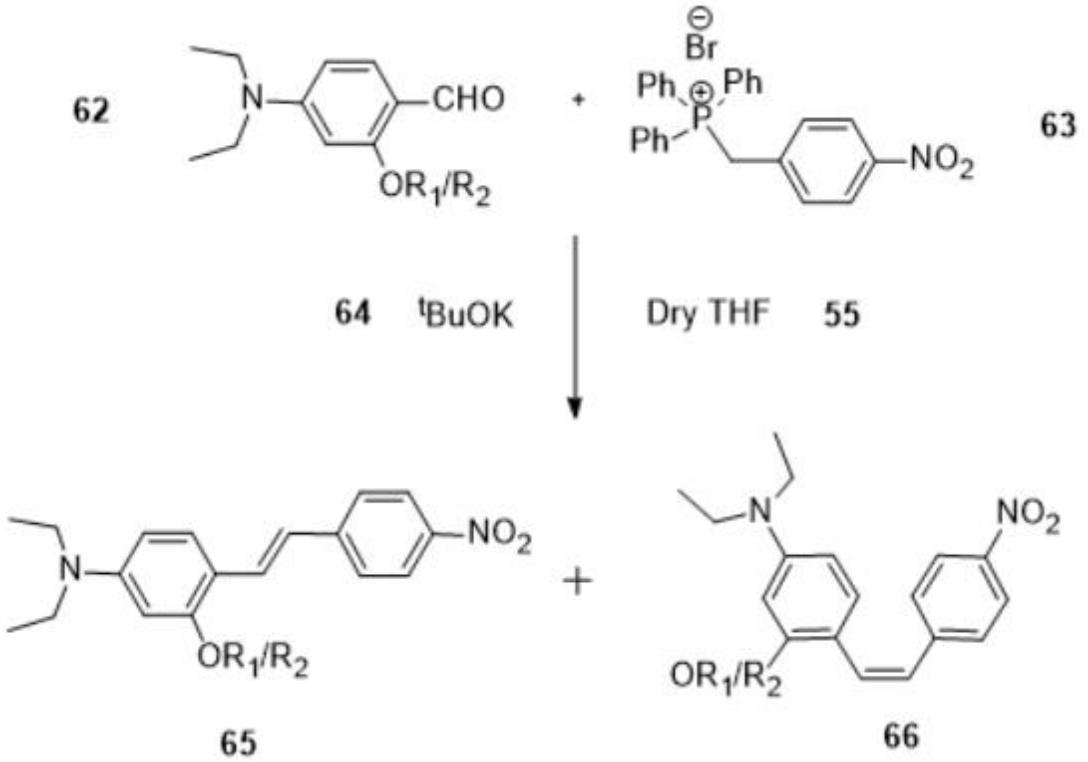


**Figure 14**: Wittig reaction for the synthesis of push-pull chromophore for the drug delivery using photochemical reaction[62].

Horner-Wadsworth-Emmons reaction is another chemical reaction to form the carbon-carbon double bond, and it is like the Wittig reaction. D. R. Robello (figure 15) created polymers bearing non-linear optics-active dyes on side chains. This kind of polymer has been successfully synthesized by free radical polymerization process. Much greater concentrations of chromophore can be achieved in these polymers compared to systems in which non-linear optics-active guest molecules are dispersed in host polymers. During the synthetic procedure of the push-pull chromophore monomer (**74**), the electron-donating group and the electron-withdrawing group are connected by Horner-Wadsworth-Emmons reaction. The reaction is launched by enolization using a strong enough base and the carbanion attacks the carbonyl of the aldehyde. The reaction is finished by the [2+2]cycloaddition and the byproduct is phosphonate molecule. The advantage of this reaction compared to Wittig reaction is that the byproduct is more soluble in water and E-configuration of the double bond is more favoured.

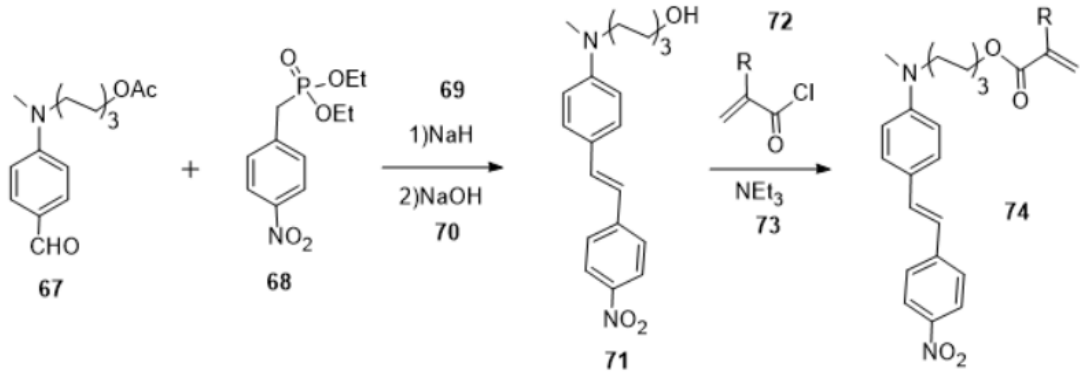


**Figure 15**: Horner-Wadsworth-Emmons reaction for the synthesis of D-π-A structure of push-pull chromophore for the application of non-linear optics-active polymer[91]

It was a big obstacle to create additional unsaturated bonds in the molecular structure. Organic chemists finally found a way to make a carbon-carbon single bond to link two π-conjugated structures. Here we offered three examples: Heck reaction, Sonogashira reaction and Suzuki-Miyauna reaction.

Heck reaction is a palladium (0) catalysed cross coupling reaction between the H-terminal alkene and aryl halide to form an alkene bond in E-configuration. In the article, Heck found that the triphenylphosphine is a good ligand for the reaction. According to the reaction mechanism, as the palladium (II) precatalyst is activated, the aryl halide will react with palladium (0) via oxidative addition, then the alkene will be added to the palladium(II) centre via π-coordination. The next step is the migration insertion from the palladium(II) centre to the alkene, followed by the β-elimination to form the E-alkene. The final product will leave the palladium(II) centre via dissociation[64].

Sonogashira reaction is a palladium(0) catalysed cross coupling reaction with a copper(I) cocatalyst by which the aryl halide will relate to a H-terminal alkyne with a global view. According to the reaction mechanism, the H-terminal alkyne will be substituted by copper(I) and the aryl halide will be added on the palladium (II) ion by oxidative addition after the activation of palladium (II) pre-catalyst. The Sonogashira reaction is finished after the Pd-Cu transmetallation and the reductive elimination to recover the palladium (0) catalyst.

Götzinger et al. (figure 16) have established a straightforward general synthesis of 3-aryl propionic esters in good yields with excellent consumption of this substrate. The optimized conditions were then employed for the synthesis of D-π-A structure of the push-pull chromophore with an ethylnyl bond as the π-conjugated spacer (**81**). The result shows interesting electronic properties such as large Stokes shifts. The experimentally obtained results were corroborated and rationalized by calculations on the DFT and TD-DFT level of theory. This is helpful for the application of the functionalized phenothiazines for obtaining novel luminescent electrophores.

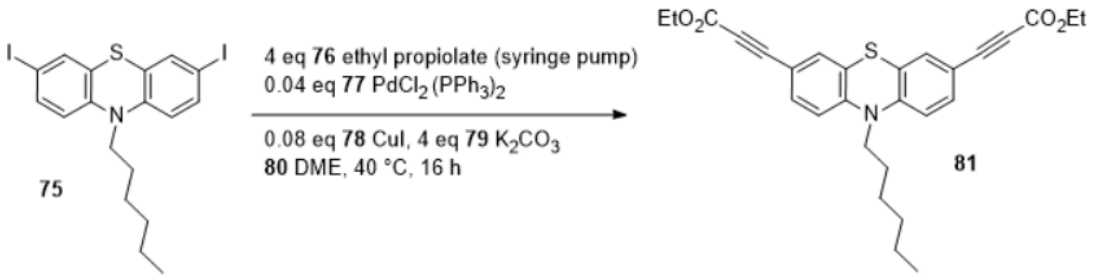


**Figure 16**: synthetic route of diethyl-3,3'-(10-hexyl-10H-phenothiazin-3,7-diyl)dipropiolate[65]

Justin Thomas et al. (figure 17) designed and synthesized a new series of compounds that contain electron-deficient quinoxaline, electron-rich triarylamine segments, and fluorophores such as pyrene, carbazole, and fluorene. Combined with the high glass transition temperature, thermal stability, and good fluorescence properties, these molecules are potential candidates for electronic devices.

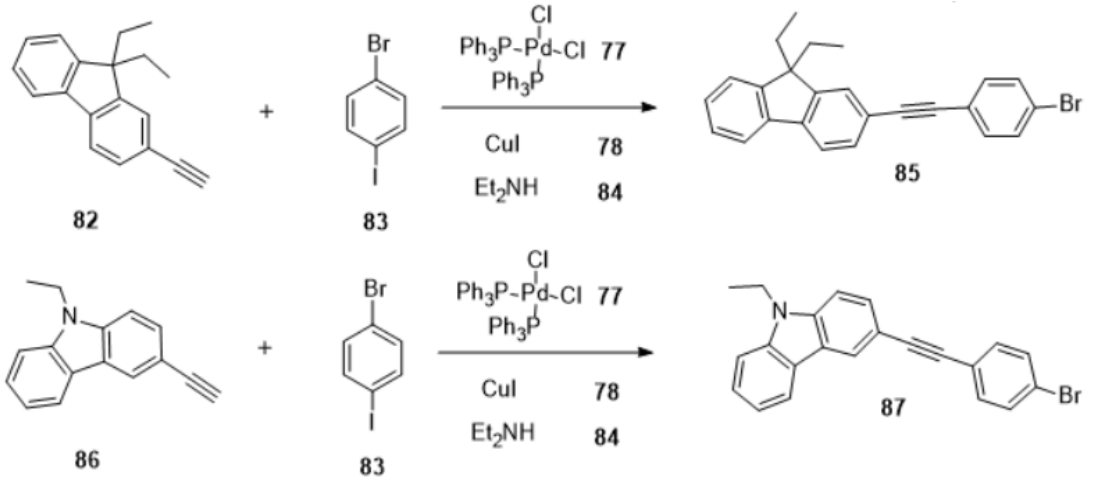


**Figure 17**: synthetic route of efficient electroluminescent materials via Sonogashira cross-coupling reaction[66]

Another example is in the article of Shinotsuka et al.[67] They synthesized novel environment-sensitive fluorophores (figure 1.18) using a unique fluorogenic core quinolyl-pyrrole (QP, 2-(1H-pyrrol-2-yl)quinoline). QP was obtained from isatins and 2-acetylpyrrole by Pfitzinger quinoline synthesis.

The quinoline and pyrrole rings related to a N,N-dimethylaniline group using the Sonogashira–Hagiwara cross coupling at the quinoline side of the QP. This resulted in a significant redshift in the fluorescence colour from blue to red. These dyes may be utilized for the studies on the activities of chloroplasts or neurons.

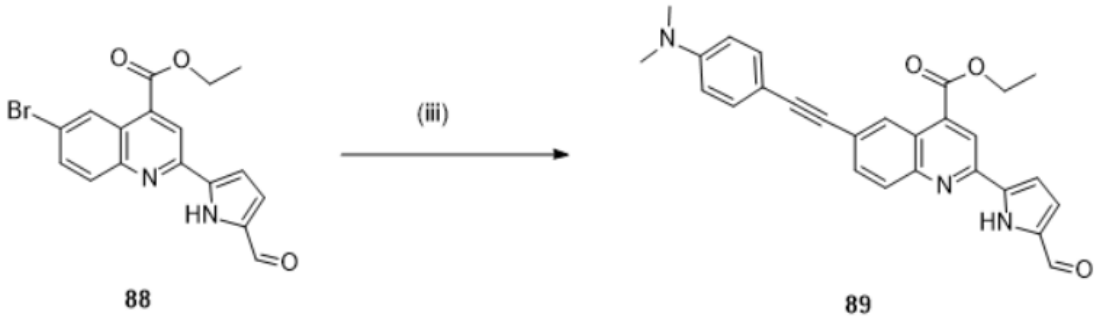


**Figure 18**: Sonogashira–Hagiwara cross coupling to introduce a dimethylaminophenylethynyl moiety at the quinoline side of the fluorogenic core quinolyl-pyrrole[67].

Suzuki-Miyaura reaction is a palladium (0) catalysed cross coupling reaction between an aryl halide and a boronic ester or a boronic acid. The boronic ester can be made by using strong nucleophile to attack strong electrophilic boron centre or by a cross coupling reaction between the alkoxydiboron and aryl halide. The interesting point of the Suzuki-Miyaura reaction is to link two aromatic molecules via a simple carbon-carbon bond. According to the reaction mechanism, as the palladium (II) precatalyst is activated, the aryl halide will be added to the palladium (0) via oxidative addition. Then a strong base reacts with the palladium(II) complex by an acid-base reaction and another acid-base reaction between the boronic ester and the strong base. Then the Pd-B transmetallation undergoes and the final product is released via a reductive elimination.

L.Han et al. (figure 19) synthesized a series of novel coumarin-type push-pull chromophore with cyanoacetic acid or rhodanine acetic acid acceptor, π-conjugated bridges and coumarin donor. The photovoltaic performance of these dyes and light-harvesting capabilities were investigated systematically. The molecule with phenylthiophene bridge and cyanoacetic acid acceptor shows the highest photoelectricity conversion efficiency. They used Suzuki-Miyaura cross coupling to add the π-conjugated spacer to the aryl halide of couramin electron-doner.

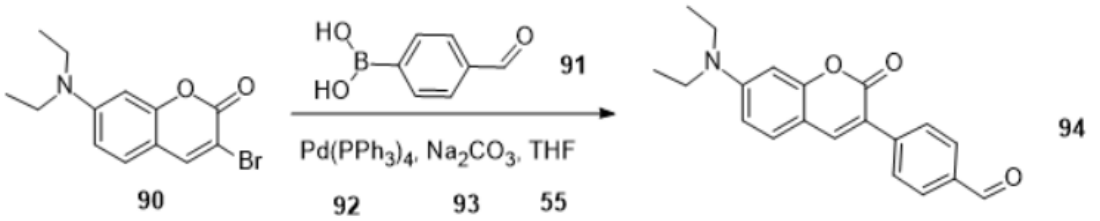


**Figure 19**: Suzuki-Miyaura cross coupling reaction to add the π-conjugated spacer to the aryl halide of couramin electron-doner[68].

Another example is in the Kumar et al. (figure 20) where they made radical and light initiated self-assembly of strongly dipolarbis-acetamido-functionalized triarylamines push–pull chromophores using hydrogen bonds. This self-assembled nanostructure enhances the performance of organic solar cells. The Suzuki-Miyaura reaction is used to link the triarylamine electron-donor and the bithiophene π-conjugated spacer.

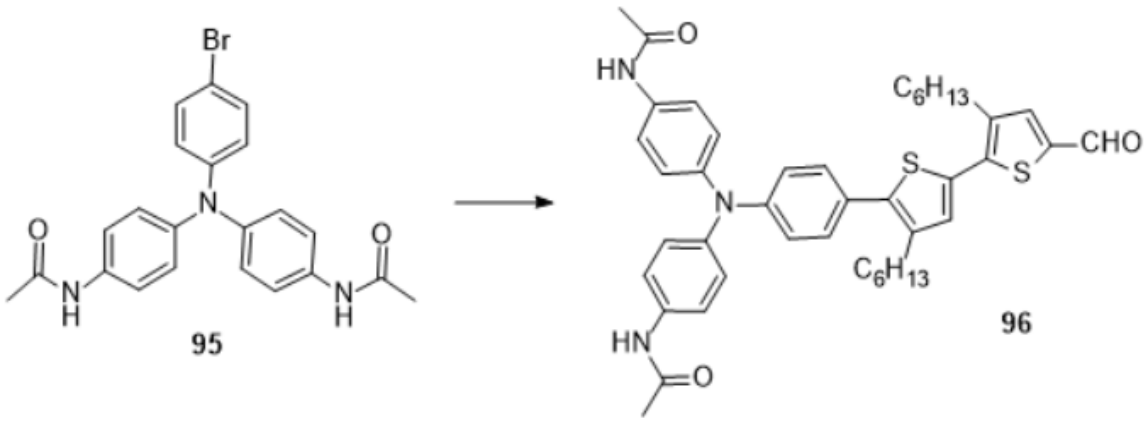


**Figure 20**: Suzuki-Miyaura cross coupling reaction to link the triarylamine electron-donor and the bithiophene π-conjugated spacer. Reaction condition:3,4′-dihexyl-5′-(4,4,5,5-tetramethyl-1,3,2-dioxaborolan-2-yl)-2,2′-bithiophene-5-carbaldehyde, $Pd(PPh_3)_4$, $Cs_2CO_3$, toluene, reflux, 16 h[69]

# B. Surface functionalization by molecular self-assembled monolayer

## I. Surface functionalization of the substrate by self-assembled molecules

The formation of self-assembled monolayers on surfaces is an example of the universal phenomena of self-assembly. It is a bottom-up approach to synthesize a material in the domain of material chemistry. Self-assembly results in supramolecular hierarchical organizations of basic units that creates very sophisticated systems in nature. SAMs help increasing fundamental comprehension of structure-property relationships, self-organization, and interfacial phenomena. For the domain of statistical physics in two dimensions and physical chemistry, SAMs are good model systems for studies.

The design flexibility both at the individual molecular and at the material levels makes it enable the investigation of specific interactions at interfaces, and of the effect of increasing stability of two-dimensional assemblies and molecular complexity on the structure using SAMs. The fabrication and manipulations of molecular assemblies, biomineralization, molecular recognition, hierarchical structure and function, and computational chemistry to interpret structure-function relationships have become central themes in modern chemistry.

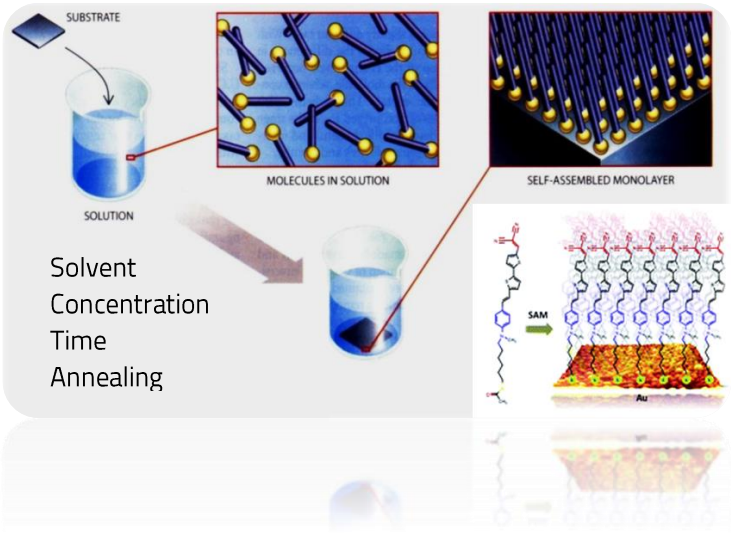


**Figure 21**: The schema to prepare a self-assembled monolayer on the surface and the key parameters

In practical, the surface functionalization is prepared by immersing the substrate in a solution and the self-assembled monolayer on the substrate is finished with cleaning. In the microscopic view, there are four main steps for the creation of self-assembled monolayer. The first step is the physical adsorption of the molecule on the surface after the mass transfer of the molecule from the solution onto the surface. The second step is the chemical adsorption after the reaction between the grafting unit of the molecule and the atom on the surface. The third step is the covering of the substrate surface (physical

adsorption can also cover the whole surface). The fourth step is the rearrangement of the supramolecular structure on the surface. The whole process is exothermal. The negative enthalpy comes from the reaction between the grafting unit and the atom on the surface and the rearrangement of the supramolecular structure by intermolecular forces.

There are three main systems for the surface functionalization: silicon oxide-silane, silicium-alkene/alkyne and gold-thiol. A brief introduction will be done for three systems to give the similarities and differences. Some examples will be given for silicium oxide-silane and silicium-alkene/alkyne system. The next section will be dedicated to the gold-thiol system.

The surface of silicon oxide is full of hydroxyl group, and they are called silanol together with the central silicon atom. The silicon substrate is covered by a layer of silicon oxide. The silane is often alkanetrichlorosilane, alkanetrimethoxysilane or alkanetriethoxysilane. The reaction responsible for the chemical adsorption is like the nucleophilic substitution for trichlorosilane. The reaction is called sol-gel method. The first step of the sol-gel method is the hydrolysis of the trialkoxysilane to render silanol. The second step is the condensation. The whole process is as same as a polymerization with water molecule as the initiator. The process of self-assembled monolayer created by silicon oxide-silane system has an additional step of cross-linking during the covering of the surface thanks to the triply substituted silane structure.

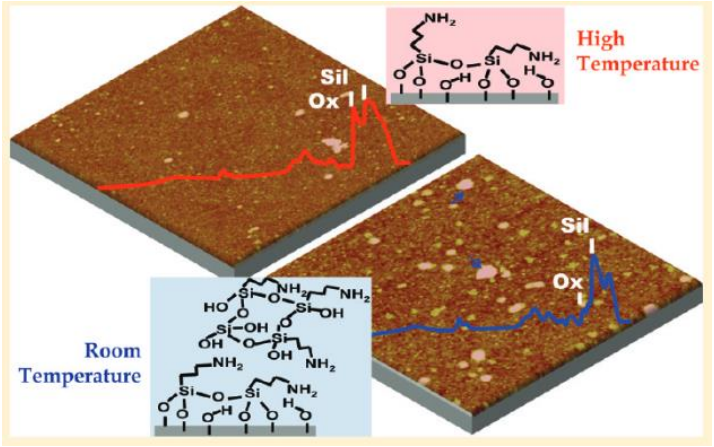


**Figure 22**: The schema to show the influence of the temperature on the structure of the (3-aminopropyl)triethoxysilane layer on silicon oxide on silicon substrate[70].

The first example of silicon oxide-silane system is the work of Aissaoui et al.[70] where the mechanism of the adsorption of (3-aminopropyl)triethoxysilane (APTES) on silicon oxide surfaces (figure 22). The experimental parameters such as concentration, temperature and time are changed to see the influence on the quality of the APTES layer. Highly sensitive grazing angle attenuated total reflection (GA-ATR) infrared spectroscopy was adopted to probe the structural information on the layer of APTES. The topography of this layer was investigated by atomic force microscopy in aqueous medium. The mechanism of silane grafting is deduced after the combination of the result of infrared spectrum, contact angle measurement and atomic force microscopy in aqueous medium.

The result shows that the temperature is very crucial for the APTES layer on the substrate. The adsorption of proteins on the APTES layer was achieved and monitored using ex situ GA-ATR analyses and in situ quartz crystal microbalance with dissipation monitoring.

In the article of Tanaka et al.[71], trialkoxysilanes bearing a ferrocene moiety were grafted on silicon oxide on silicon wafer for analysis by electrochemical methods (figure 23). Silicon wafer was immersed in trialkoxysilane solution for surface functionalization without oxidation treatment. After the attempt with various temperature, molecular structure, solvent, and concentration, the cyclic voltammetry is used to determine surface density of the immobilized ferrocene–silane on silicon surface and the blocking effect to obtain insight into density leading to the close-packed layer in the cyclic voltammogram. The formation of a close-packed layer to show significant blocking effect was observed.

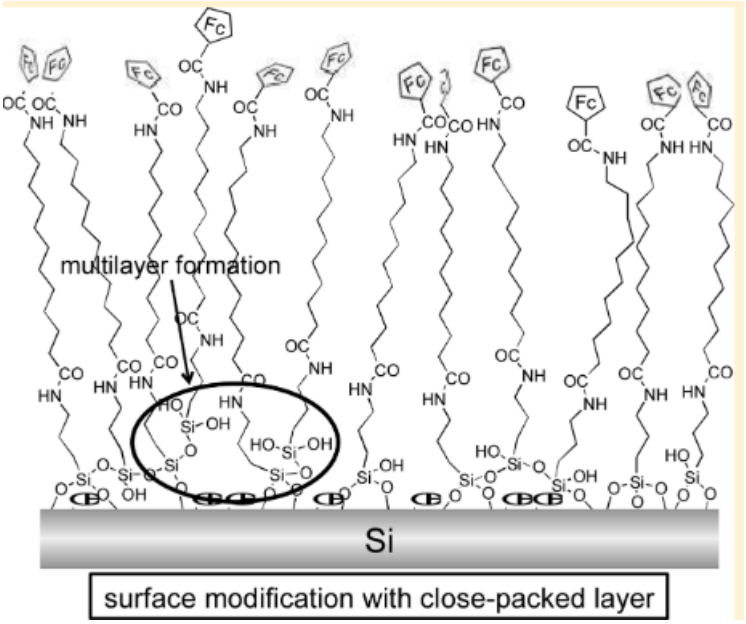


**Figure 23**: The schema to show the surface functionalization with close-packed layer of ferrocene-based trialkoxysilane on silicon oxide on silicon substrate[71].

Although a close-packed layer is formed, the surface of silicon oxide modified with trialkoxysilane is a partial multilayer rather than monolayer. This is a drawback of the silicon oxide-silane system.

Arndt et al.[72] created photoresponsive coatings. Upon illumination, the wettability of the photoresponsive coatings strikingly change. They present arylazopyrazoles (AAPs)-based photoswitchable self-assembled monolayers. The AAP photoswitch is terminated with triethoxysilanes for an easy, one-step functionalization of silicon oxide and glass surfaces (figure 24). The self-assembled monolayers are examined by X-ray photoelectron spectroscopy (XPS), UV/vis spectroscopy, contact angle goniometry, and time-of-flight secondary ion mass spectrometry.The excellent photoswitch ability of the self-assembled monolayer of the AAPs is confirmed upon alternating irradiation with green (520 nm) and UV (365 nm) light.

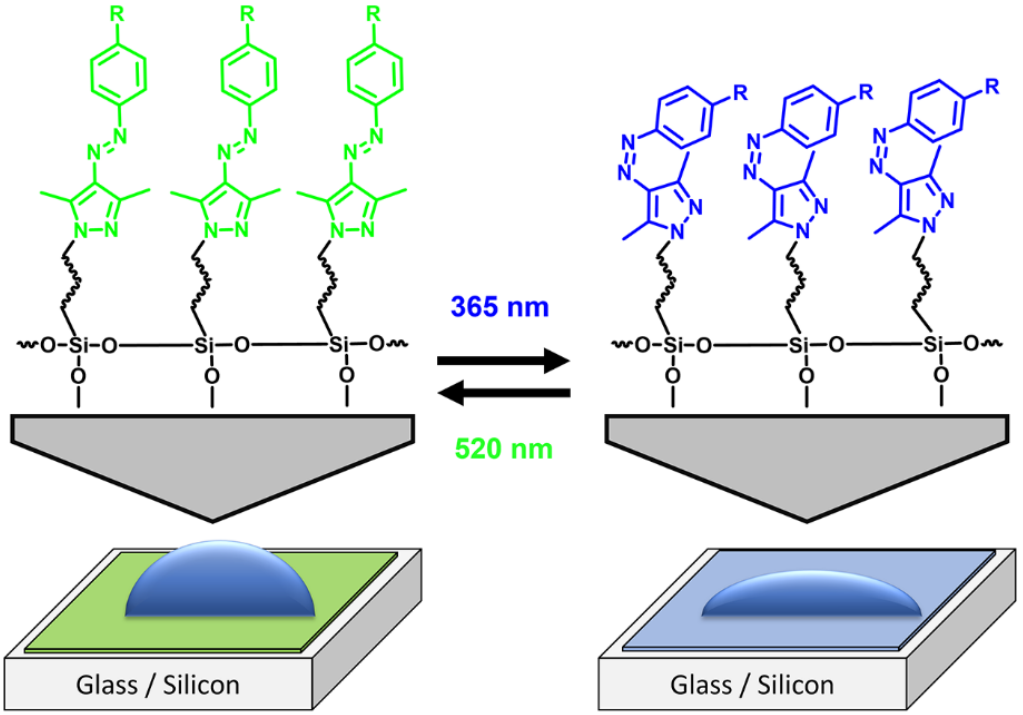


**Figure 24**: The change in configuration of the AAP photoswitchable headgroup upon alternating irradiation with UV (365 nm) and green (520 nm) light results in a reversible change in wettability[72].

The next system to introduce is silicon-alkene/alkyne. The layer of silicon oxide on silicon substrate can be removed in hydrofluoric acid (HF) to give a hydrogen-terminated silicon surface. Moreover, the roughness of the substrate will be enhanced. The hydrogen-terminated surfaces undergo hydrosilylation with alkene or alkyne to form a stable monolayer on the surface. The hydrosilylation reaction can be initiated with UV light at room temperature or with heat (typical reaction temperature 120-200 °C), under moisture-free and oxygen-free condition[73]. There is no problem with the cross-linking process in silicon-alkene/alkyne system.

The first example of silicon-alkene/alkyne system is in the article of Langner et al.[74] where they reported the immobilization of indene ligands onto two types of hydrogen-terminated surfaces, oxide-free Si and oxidized Si. The quality of the surface functionalization has been investigated by infrared absorption spectroscopy. They found also that the UV irradiation on oxide-free surfaces promotes a cleaner and more efficient reaction without substrate oxidation. The UV-induced immobilization is mediated according to them solely by the excitation of electron-hole pairs (excitons) in the substrate rather than the result of direct Si-H bond breaking. Liu et al.[75] reported also this Si surface functionalization via hydrosilylation at room temperature for 24–40 h to give modified surfaces with a coverage of 31–56% by XPS analysis. The molecules used are alkynes such as propiolate esters, propiolic acid, but-3-yne-2-one, propiolonitrile and phenylacetylene at room temperature. However, they deduced a radical propagation process initiated by trace dioxygen molecules to illustrate the formation of surface functionalization (figure 25).

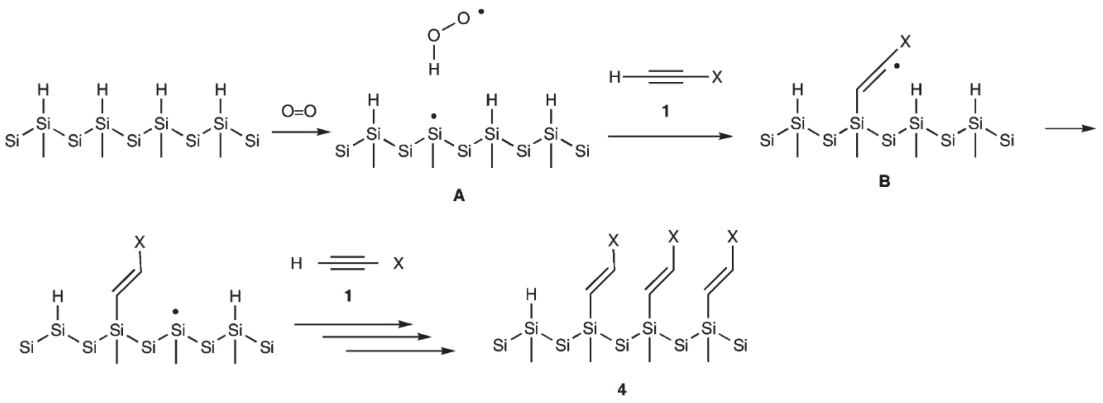

**Figure 25**: The schema of radical propagation process initiated by trace dioxygen molecules to illustrate the surface functionalization of H-terminated silicon substrate by alkyne molecule[75].

Zhong et al.[76] reported efficient chemical functionalization of hydrogen-terminated Si(111) with simple and bifunctional 1-alkenes was achieved utilizing just a simple ultrasonic bath via novel sonochemical activated hydrosilylation (figure 26). It is an extremely mild method that allows the specific attachment of unprotected bifunctional alkenes with even a heat/UV-sensitive alkene, bearing an activated leaving group (N-succinimidyl undecylenate), without suffering any degradation.

The gold-thiol system will be introduced in the next section.

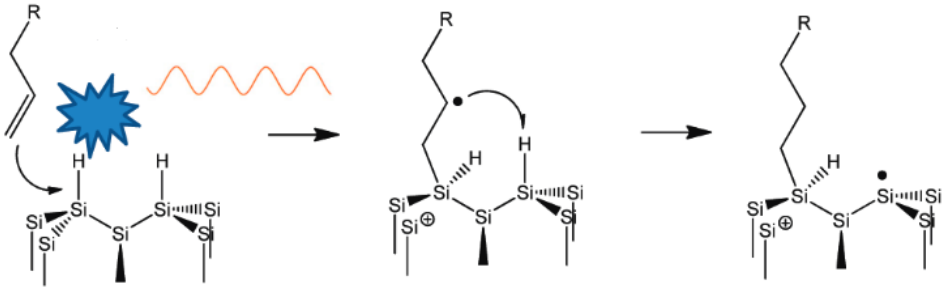

**Figure 26**: the schema to show the mechanism of sonochemical activation of H-terminated Si(111) surface for hydrosilylation reaction with terminal alkene followed by radical propagation on the silicon surface[76].

## II. Surface functionalization of gold by self-assembled molecules with thiol functional group

The study of kinetics using alkanethiol adsorption onto the surface of Au(111) have demonstrated that two different adsorption kinetics can be observed at relatively dilute solutions ($10^{-3}$ M). In the first a few minutes, it is a very rapid step, and the contact angles are almost the limiting values, and the thickness is about 80-90% of its saturated value by the end. Then a slow step takes several hours, and the thickness and contact angles reach their final values[77]. The initial steps described well by diffusion-controlled Langmuir adsorptions, and it strongly depend on thiol concentration. It required over 100 min at 1 μM concentration for the first step but over after 1 min at 1 mM solution[77]. The second step can be designated as a process of surface crystallization. The alkyl chains grafted on the surface arrange themselves from the disordered state to unit cells, forming a crystal in two-dimension. Consequently, the kinetics of the first step is controlled by the reaction between the surface-head group and the metal ion on the surface. Besides, the activation energy may depend on the electron density of the adsorbing sulphur. The chain disorder (e.g., gauche defects), the surface mobility of chains and the different components of chain-chain interaction (VDW, dipole-dipole, etc.) are key components for the second step. It was also found that the kinetics is faster for longer alkyl chains, probably due to the increased hydrophobic interactions[77].

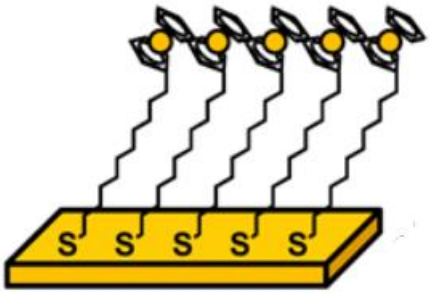


**Figure 27**: the schema of the self-assembled monolayer of ferrocene-terminated alkanethiol on gold[78]

In the case of alkanethiol, the reaction may be described formally as an oxidative addition of the S-H bond to the gold surface, followed by the homolytic break to make thiyl radicals (RS·) with the emission of dihydrogen[79–82]. The self-assembled monolayers of alkanethiolates on Au(111) surfaces show that the symmetry of sulphur atoms is hexagonal with an S-S spacing of 4.97 Å, and calculated area per molecule of 21.4 $Å^2$ after electron diffraction studies[83,84]. The structure formed by dodecanethiol on Au(111) is commensurate with the underlying gold lattice and is a simple $\sqrt{3}x\sqrt{3}$ R30° overlayer after atomic force microscopy (AFM)[85] studies.

Two binding modes at the Au(111) hollow site were found for alkanethiolates, one with a sp hybridization of sulphur and a bond angle of 180° and the other with a $sp^3$ hybridization and a bond angle of 104°. The latter is more stable by 0.41 kcal/mol[86]. Many studies have suggested that this angle in monolayers on Au(111) surfaces must be tetrahedral, which corresponds to a $sp^3$ hybridization[87]. Modelling of terphenylthiolate

($C_6H_5C_6H_4$-$C_6H_4$-S-) monolayers on Au(111) suggest a tilt angle of 6° from the surface normal[88] because of the sp hybridization of the sulphur. X-ray data show narrowing of the diffraction peak when monolayers of alkanethiolates on Au(111) were annealed[89]. Thus, the heating and cooling can enlarge the domain size on the self-assembled monolayer.

They found that the roughness of the substrate is an essential parameter. It is concluded that a rougher substrate surface leads to stronger variations in the conductive properties. The use of rough substrate should be avoided because the article shows that the lateral variation of the conductive properties of molecular SAMs is governed by the choice of the substrate. To achieve comparable, well-measurable currents and conductive properties, flat substrates are favourable.

During the preparation of the self-assembled monolayer, there are several parameters that influence the quality of the final self-assembled monolayer.

The type of the solvent used for the preparation of the self-assembled monolayer formation is crucial for the quality. In the case of the mixed self-assembled monolayer, the choice of the solvent can favour the adsorption of a molecule rather than the other molecule. It is showed that during the grafting of two thiols which have different polarity, the use of a non-polar and non protic solvent such as hexadecane brings the formation of a self-assembled monolayer which is mainly constituted by polar molecules. In a polar solvent, the adsorption of a polar molecule is less favoured than a less polar molecule.

Dai et al.[90] conducted another fundamental research for the best solvent for the elaboration of the self-assembled monolayer using electroanalytical methods such as cyclic voltammetry and electrochemical impedance spectroscopy (figure 28). By looking at the blocking ability of the electrochemical reaction of the probe and the value of the impedance, the best solvents are ethanol or ethanol-water solution.

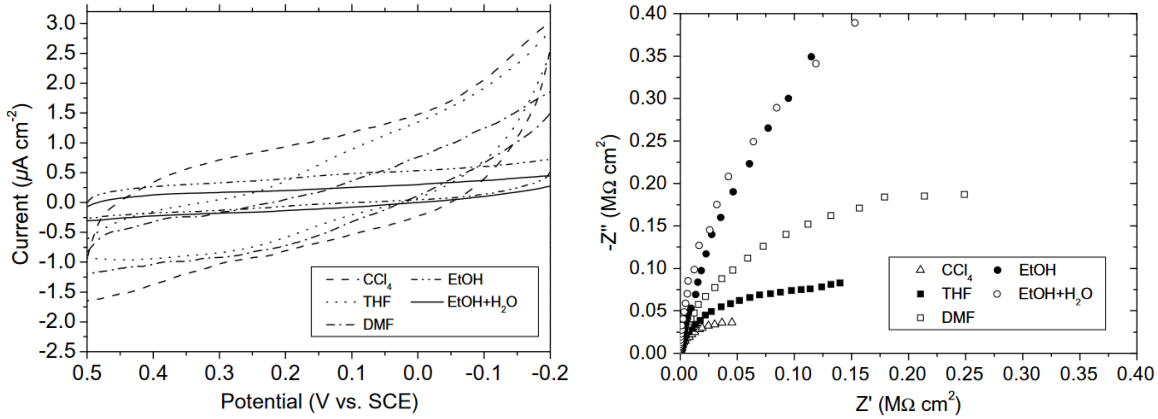


**Figure 28**: (left) Cyclic voltammograms of $C_{12}$SH-SAMs formed from different solvents in 0.1 M $Na_2SO_4$ containing 2 mM $K_3Fe(CN)_6$ at 0.1 V/s. (right) Impedance (Nyquist) plot of $C_{12}$SH-SAMs formed from different solvents in 0.1 M $Na_2SO_4$ containing 2 mM $K_3Fe(CN)_6$–2 mM $K_4Fe(CN)_6$.

Delamarche et al.[91] conducted fundamental research about the structural changes as function of annealing time in air and temperature in monolayers of dodecanethiol self-assembled on gold (figure 29). The results were studied by X-ray photoelectron spectroscopy, contact angle microscopy and high gap impedance scanning tunnelling microscopy. Here are some conclusions for this study. The formation of the self-assembled

monolayer of dodecanethiol is a domain-like growth which differs with different sulphur lattice positions and different chain tilt azimuths upon different preparation process. At 50 °C, the chain tilt azimuth mismatches disappear and lead to a larger domain size compared to room temperature. At 100 °C the top layer of the gold becomes mobile and the depressions fuse with terrace edges. In addition, the sulphur domain boundaries also become mobile and arrange into a new striped pattern which is most prominent after 10 h of annealing. The shape of the depressed lines allows the relative lack of thiol molecules and the direction of the chain tilt to be determined.

For longer annealing times the line spacing of the striped pattern decreases. This probably reflects the increasing relative deficiency of thiol molecules as the annealing time is increased. At higher temperatures, the order in the film collapses much earlier since multiple desorption can occur. At even higher temperatures (130 °C) the SAM is removed totally, leaving behind an uncovered gold surface. Studies on SAM annealing and decomposition provided further insights into the mechanisms that govern the structure of organic monolayers in different crystalline and liquid-like phases.

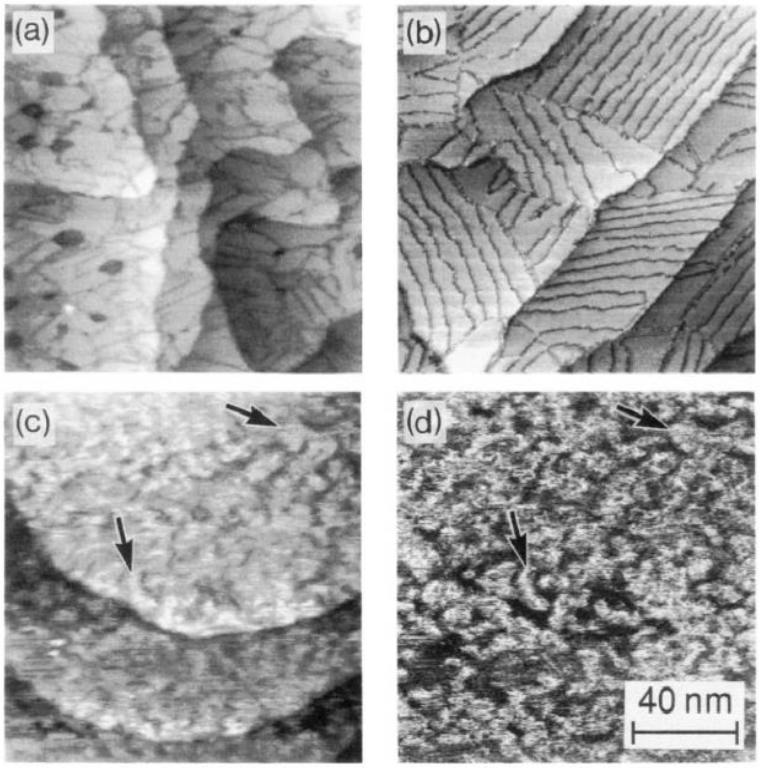


**Figure 29**: STM images (lateral dimension is 140 nm) recorded at tunnelling resistances of 140 GΩ on samples exposed for 10 h to different annealing temperatures of (a) 85 °C, (b) 100 °C, (c, d) 115 °C. (c) Topography (obtained in constant current mode); (d) the response of the tunnelling current due to gap modulation (dI/dz) recorded simultaneously with (c).

The concentration is also an important parameter. In terms of the kinetics, the concentration of the molecule in the solution has a direct impact on the growth of the monolayer. The higher the concentration, the shorter for the self-assembled monolayer attains the thermodynamic equilibrium[92]. It is very special for gold-thiol system. In terms of the thermodynamics, there are several models to describe the surface coverage (θ) in the

function of the concentration (C). The most common one is Langmuir isotherm where there is a rapid increase of surface coverage when the concentration is small, and a plateau of surface coverage will appear when the concentration is much higher. Since the adsorption process is in dynamic equilibrium, the chemical reaction can be written as a reaction between the surface site (S) and the adsorbent (A) to form adsorbed molecule ($A_S$) with an equilibrium contant ($K_L$) expressed by the concentration of the species in square brackets. Taking the first order rate equation ($k_a$ for the adsorption rate and $k_d$ for the desorption rate), the surface coverage at equilibrium ($\Theta_e$) when the concentration of the adsorbent in the solution ($C_e$) can be determined by assuming the adsorption rate $r_a$ is equal to the desorption rate $r_d$ [93]:

$$A + S \leftrightarrow A_S$$

$$K_L = \frac{[A_S]}{[A][S]}$$

$$r_a = k_a C(1 - \theta)$$

$$r_d = k_d \theta$$

$$\theta_e = \frac{K_L C_e}{1 + K_L C_e} \; if \; r_a = \; r_d$$

In the next section, other organosulphur based molecules for the adsorption on gold will be presented, especially disulfide.

# III. Surface functionalization of gold by self-assembled multidentate organosulphur molecules

Multidentate ligands can be taken to produce new classes of molecule-metal complexes where the central metal ion is wrapped by multiple bonds due to the ligand and give rise to distinct reactivity, unique geometry, and improved stability by calculating the complexation coefficient β[94,95]. It is well known among inorganic chemists. The reason to explain this can be more negative value for the reaction enthalpy in the view of thermochemistry or higher β for multidentate ligands[94,95]. For the point of view of surface science, the only difference is that the surface is no longer a single ion/atom, but a plane constituted by ions/atoms. Therefore, more stable self-assembled monolayer can be prepared using multidentate adsorbent since one molecule can be attached to the surface by more atoms. Nanoscale film can be created after the spontaneous chemisorption of alkanethiol molecules as mentioned in the previous chapter and the physical and the physiochemical properties of the surface can be modified.[5,96]. Applications are in the fields such as controlled adhesion[97], lubrication[98], corrosion prevention[99], biosensing[100], and electrode modification[101]. In the framework of the PhD, there are two additional parts for the push-pull chromophore to enable the possibility to form self-assembled monolayer on the gold surface: an additional linker and a sulphur-based grafting unit.

The first kind of sulphur-based adsorbate is alkanethiol (RSH). Dialkyl disulfides (RSSR) and dialkyl sulphides (RSR) are also popular. Because of the insufficient stability caused by displacement and desorption of the molecule from the surface in solution, SAMs prepared using these three kinds have found limited applicability. Chinwangso et al.[102] wrote an article to mitigate this problem. The utility of SAMs derived from multidentate adsorbates in emerging nanoscale materials and technologies can be foreseen.

Multidentate adsorbate is an attractive strategy to create stable and well-defined organic monolayers centres on the use of multiple contacting points. The structures are designed to possess, for example, two (bidentate) or three (tridentate) active headgroups that can interact with the substrate surface. Two or more chemically distinct terminal components can be incorporated into the same adsorbate, which allows the generation of homogeneously mixed multicomponent surfaces, stabilized by the presence of more than one surface bond. Accordingly, these structures can be linked to the substrate in a manner like metal ligand complexes, providing added stability to both the individual adsorbate and the SAM.

Multidentate adsorbates have been developed to generate films that overcome these limitations. The work of Nuzzo and Allara in 1983 (**97** in figure 30) used a series of disulfides with symmetrical ramification derived from 4, 5-dihydroxy-1,2-dithiane (DTT-H) to form self-assembled monolayers[103]. Given that these studies focused on the spontaneous adsorption of organic disulfides on gold, the advantages of the chelating character were not considered. In 1997, Cahen and co-workers (**98** in figure 30) used a similar DTT-H-based structure to create multifunctional molecular assemblies on gold substrates[104]. The authors generated homogeneously mixed monolayers by grafting two

different functional groups on a single adsorbate. Since the two substituents were both covalently bound to the six-membered ring, no phase separation could occur during SAM formation as the S-S bond cleaved to form two thiolate bonds on the surface.

Bidentate adsorbate was introduced by Kim and co-workers who reported the self-assembly of 1,2-benzenedithiol on gold and silver surfaces (**99** in figure 30)[105]. They showed that the desorption rate of the film derived is 200 times slower than that of the octadodecanethiol film. It is suggesting that the monolayer formed from the dithiol is more stable than the normal alkanethiol film. In a subsequent paper, o-xylene-R,R′-dithiol was used to form a close-packed, highly ordered monolayer on gold[106]. The intervening methylene units at the sulphur headgroups provided added flexibility to the structure and possibly put the two sulphurs in ideal positions to coordinate to the gold substrate.

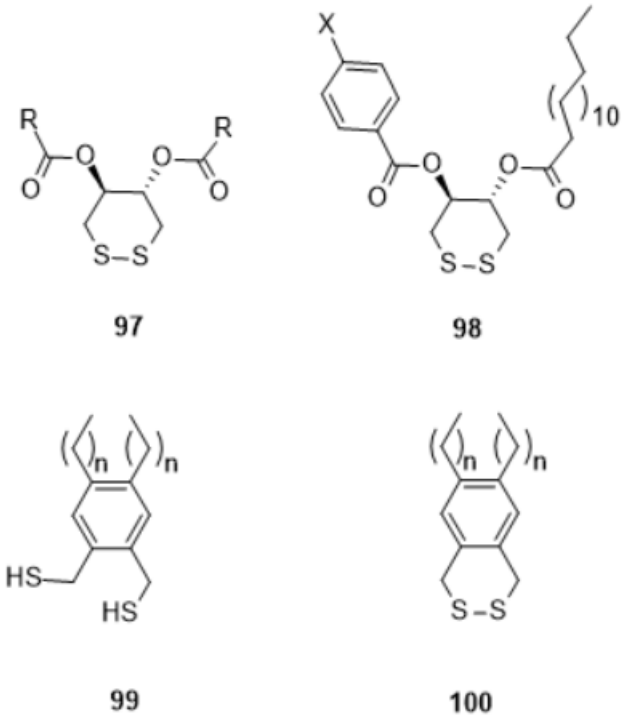


**Figure 30**: (**97**) Disulfides with symmetrical ramification in the work of Nuzzo and Allara[103]; (**98**) Disulfides with asymmetrical ramification in the work of Cahen[104]; (**99**) 1,2,4,5-tetrasubstituted benzene based dithiols for the surface functionalization[107]; (**100**) 1,2,4,5-tetrasubstituted benzene based disulfide for the surface functionalization[108]

A kinetic study showed that the formation of thin films with o-xylene-R,R′-dithiol was 10 times faster than that of the octadodecanethiol film. However, Tao et al. noted in a study involving aromatic monothiols that the insertion of one methylene unit between the aryl and the thiol group improved intermolecular interactions; a bond angle preference for the sulphur atom of benzyl mercaptan ($sp^3$) as compared to that of thiophenol (sp) was also observed[109]. Thus, the different behaviour between 1,2-benzenedithiol and o-xylene-R,R′-dithiol can be attributed to the extra methylene unit, which diminishes steric interference of the headgroups and offers flexibility in binding to gold surfaces. Additionally, thermodynamic studies[106,110] found the adsorption free energies ($\Delta G_{ads}°$ ) of o-xylene-R,R′-

dithiol and octadodecanethiol on gold surfaces to be -28.9 and -23.0 kJ/mol, respectively. By looking at the value of the adsorption free energy, it is for sure bidentate adsorption is more stable in the aspect of thermodynamics.

Two alkyl chains were incorporated into the structure of o-xylene-R,R'-dithiol to provide 1,2,4,5-tetrasubstituted benzenes. The SAMs derived from these dithiols were densely packed and highly ordered. Thermal desorption studies of these SAMs in solution showed that the monolayers were more robust than analogous normal alkanethiolate and aromatic monothiolate SAMs[111]. The authors also investigated SAMs using the corresponding aromatic disulfides[108] (**100** in figure 30) rather than the dithiol and found that disordered or incomplete monolayers were formed.

Another method for enhancing SAM stability is to use different organosulfur functional group. Lee and co-workers[112] reported SAMs generated from aliphatic dithiocarboxylic acids (**101** in figure 31). Despite the potential effect to enhance the stability of these bidentate ligands, stability tests of SAMs derived from aliphatic dithiocarboxylic acids under argon, in air, and under oxygen atmospheres showed that they were less stable than the corresponding alkanethiolate SAMs[113]. The authors noted the fragile nature of the dithiocarboxylic acid itself, which undergoes facile decomposition upon exposure to mild reagents and conditions[114].

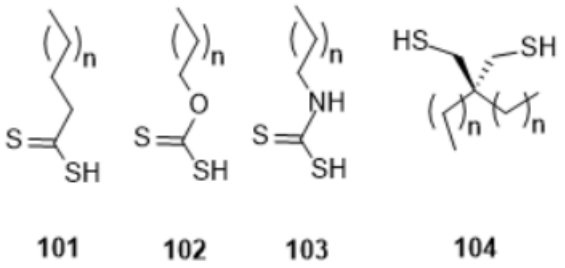


**101** **102** **103** **104**

**Figure 31**: (**101**) aliphatic dithiocarboxylic acid, (**102**) aliphatic xanthic acid, (**103**) aliphatic dithiocarbamic acids and (**104**) spiroalkanedithiols

Similar bidentate structures including xanthic acids (**102** in figure 31) and dithiocarbamic acids (**103** in figure 31) have also been used to form monolayers on gold. Moore compared SAMs derived from xanthic acids with those derived from corresponding versions of aliphatic dithiocarboxylic acids and alkanethiols, finding that the former SAM was more disordered and lower in effective packing chain density relative to the latter two films.A novel "spiroalkanedithiols" adsorbates ($[CH_3(CH_2)_{n-3}]_2C[CH_2SH]_2$) (**104** in figure 31) was designed by Shon and Lee[115]. This adsorbent is constructed with a central branch point carbon, and two alkyl chains and two methylenethiol headgroups are at this carbon.

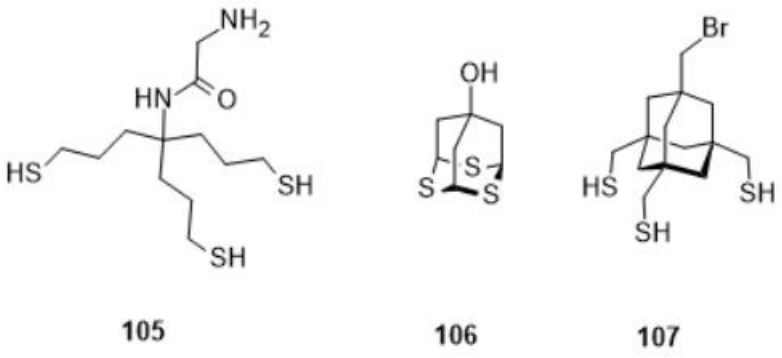


105 106 107

**Figure 32**: (from left to right) An aminotrithiol, sulphur containing adamantane derivatives, and bromine-terminated adamantane based trithiol.

Tridentate structures have three active headgroups on a single adsorbate can be attached to the solid surface. They have been utilized to engineer monolayer assemblies. The first example of tridentate adsorbent is an aminotrithiol created by Whitesell and Chang (**105** in figure 32)[116]. The tridentate adsorbent on gold is more stable than the alkanethiol on gold because the tridentate molecule will not be substituted after the immersion in the solution containing alkanethiol[117]. Whitesell and co-workers discovered with sulphides (**106** in figure 32) and the molecule bounds to gold via all sulphur atoms[118]. Kitagawa et al. found a similar result by making bromine-terminated adamantane derivatives adsorbate[119]. Additionally, SAMs formed from this molecule showed an ordered hexagonal two-dimensional arrangement for the adsorbed molecules on the Au(111) substrate. The distance between two sulphur atoms on the surface was 5.0 Å (**107** in figure 32)[120].

An extended study by Katano et al. (figure 1.33) also confirmed the three-point contacts of bromine-terminated adamantane based trithiol on Au(111) surfaces and the highly ordered SAMs that were formed[121]. The unit cell is shown by a hexagon. All molecules are drawn in the same orientation to minimize unfavourable intramolecular interactions. Sulphur atoms are assumed to be located on the near-top sites in figure 1.33. In the study, they made STM measurements under ultrahigh vacuum (UHV) (figure 34) conditions to establish a plausible model for the adsorption structure of bromo adamantane trithiol on the Au(111) surface. The growth of bromo adamantane trithiol SAMs to be characterized by a formation of localized hexagonal units consisting of bromo adamantane trithiol trimer subunits. In terms of the crystallography, the unit cell can be identified on the surface. Of further interest is the fact that these SAMs exhibit a chirality inherited from their hierarchical subunits. We note that the chirality of these subunits shifts from racemic to enantiomorphic phases when SAMs layers develop two-dimensionally. It is very interesting because the self-assembled monolayer can be considered as a kind of soft matter where two states are mainly concerned: the disordered liquid phase and the ordered solid phase. In most cases, the self-assembled monolayer is in liquid phase at room temperature. Of course, it can be crystallized into solid phase when the temperature is below a critical temperature. The disorder is caused by the thermal translation ($k_BT$). In statistical physics,

the variance of a variable X which follows the Maxwell-Boltzmann distribution can be written as (μ is the chemical potential):

$$\langle X^2 \rangle = \frac{{k_B}^2 T^2}{\mu}$$

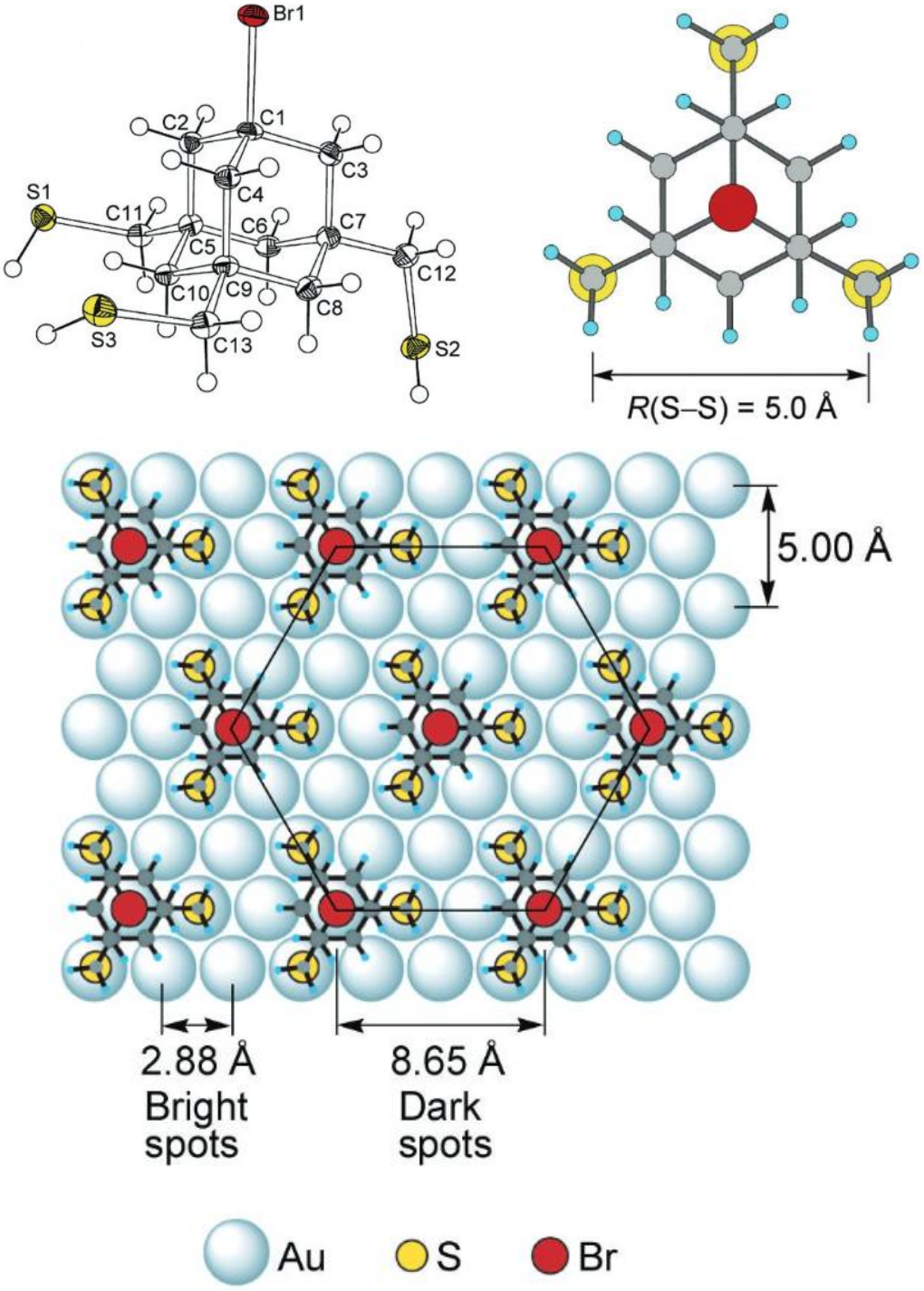


**Figure 33**: (Top left) ORTEP drawing of bromo adamantane trithiol as determined by single-crystal X-ray diffraction analysis at 100 K; (top right) Top view of bromo adamantane trithiol. Thiol hydrogens have been omitted. (bottom) Top view of a possible arrangement of bromo adamantane trithiol for the SAM on Au(111). sites[119].

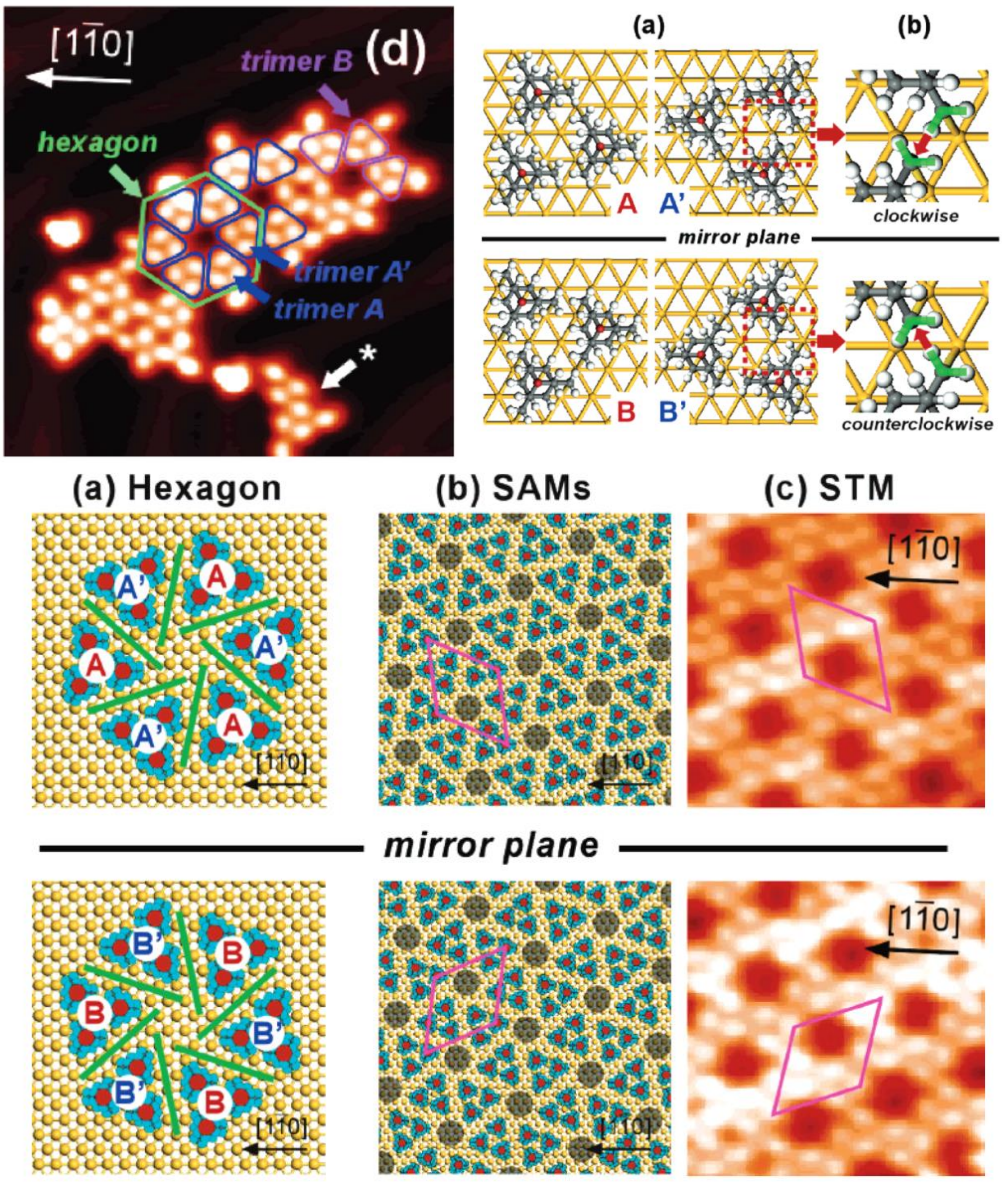


**Figure 34**: (Top left) STM image of a ribbon-shaped bromo adamantane trithiol island ($V_s$=-0.5 V, $I_t$=0.5 nA) with the indication of the trimer and hexagon units; (top right) (a) Schematic adsorption models of bromo adamantane trithiol trimers. B (B') is the enantiomer of A (A'), whose mirror plane is aligned parallel to the [1$\bar{1}$0] direction. 180°-rotated configuration of A (B) is presented as A' (B'). (b) Expanded model of (a). The chirality for the assembled layers is caused by meshing of methylene between adjacent molecules. The methylene is associated with formation of the chiral configuration.
(bottom) Schematic self-assembly models of (a) hexagon and (b) SAMs of bromo adamantane trithiol on Au(111). The chiral components of the trimers are indicated as A, A', B, and B'. The hierarchical assembly is passed from trimer to hexagon and then to SAMs. Each enantiomeric hexagon is composed of the same chiral trimers as shown in (a). The unit cell of the SAMs are indicated in (b). (c) Corresponding STM images of monolayer SAMs ($V_s$=-0.8 V, $I_t$=0.3 nA)[121].

This kind of molecular crystalline structure is inspired by the idea of molecular crystal. This kind of can be also seen with following molecules in the reference: naphthalene, anthracene, diphenyl system, pyrene, n-alkane, ferrocene, proteins (hydrogen

bonds in α-helix and β sheets) and DNA (hydrogen bonds between the adenine and thymine and between the cytosine and guanine)[122].

Unlike the surface of the substrate, Mattoussi and co-workers grafted their molecules on the gold nanoparticles and semiconductor quantum dots (QDs) to test the stability of functionalized with bidentate (i.e., thioctic acid, TA, and dihydrolipoic acid, DHLA)[123,124] and tetradentate (i.e., bis(TA) and bis(DHLA) (**108** in figure 35))[125] poly(ethylene glycol) ligands. As surfactants for colloidal systems, the colloidal stability under harsh conditions is ensured (e.g., extreme pH, thiol-rich environments, high salt concentrations, and the presence of metal etchants).

Some adsorbates have even more grafting unit on a single molecule. Researchers investigated SAMs derived from multidentate cyclodextrin-based(**109** in figure 35)[126,127] and resorcinarene-based[128,129] thiols and sulphides. However, electrochemical probes and IR spectroscopy show that the SAM created by these molecules contain a lot of defects whereas the stability is super.

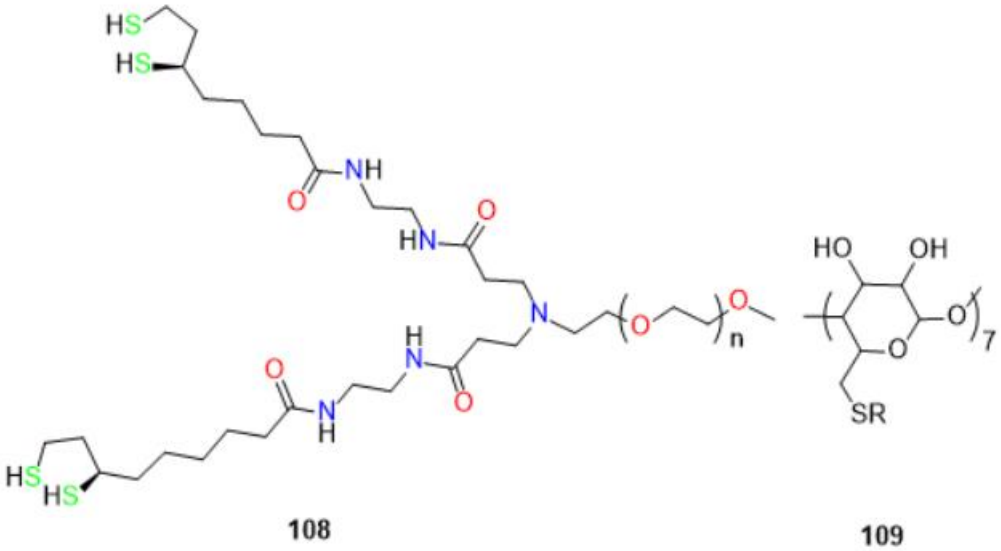


**Figure 35**: Structures of multidentate bis(DHLA)-PEG-$OCH_3$ (**108**) and cyclodextrin-based (**109**) adsorbates (where R = H or alkyl)[102].

# C. Potential applications using self-assembled monolayer of push-pull chromophore

## I. Solar cell

The first application of the push-pull chromophore is the solar cell. The renewable solar energy is considered as one of the most important bases for sustainable development. In general, a solar cell is made by a single p-n junction without the external bias, but it can be linked by a load resistance. Push-pull chromophore is considered as the organic semiconductor material by assimilating the HOMO (highest occupied molecular orbital) as the edge of the valence band and the LUMO (lowest unoccupied molecular orbital) as the edge of the conduction band.

One of the most important applications in various types of the solar cell is dye-sensitized solar cell, as the electron-hole pair is created, the electron will be injected into the conduction band of the photoanode, and the hole will be transferred to the photocathode via the electrochemical shuttle. The push-pull chromophore can serve the dye in the dye-sensitized solar cell. In the form of the self-assembled monolayer of the push-pull chromophore, the self-assembled stuff can form crystal orbitals to mimic the perovskite solar cell. Indeed, the perovskite is just a crystallographic structure and many perovskites solar cell has organic components.

In the structure of the dye-sensitized solar cell (figure 36), there are several processes that contribute to the generation of photocurrent and the collection of solar energy. Each component in the structure and its electronic structure is important. The main process includes the absorption of the photon, the electron injection from the excited dye molecule to the conduction band of the titanium oxide, the dye regeneration via the electrochemical process and the hole transport process by the electrochemical reaction at the photocathode. However, there are some parasite processes including the spontaneous electron-hole recombination after the electron injection process and the leakage for the contact of triiodide ion and the electron at the photoanode. To increase the photocurrent, meso-porous nanoparticles of the titanium oxide is used because this kind of nanostructured particles tremendously increase the loading amount of the dye at the surface without breaking the electronic structure of the titanium oxide, which is crucial for the solar energy generation.

After photoexcitation of the dye, the generated exciton must then dissociate efficiently (charge separation process[130]) to let the hole react with the electrochemical shuttle and to inject an electron into the $TiO_2$ conduction band. The charge separation energy which is strongly related and proportional to the exciton binding energy must be overcome for such a process. This energy depends strongly on both the geometry of the dye and the electronic structure.

The first crucial factor that governs the electron-injection efficiency, and hence the $J_{SC}$ of the cell is the binding energy and the relaxation dynamics of the exciton[131]. The second key parameter is the difference between the LUMO level of the dye and the conduction

band of the semiconductor. This parameter is called the driving force for electron injection ($\Delta G_{inj}$). To make the electron injection process thermodynamically possible (i.e., $\Delta G_{inj} < 0$), the LUMO level of the dye must lie above the $TiO_2$ conduction band, and the resulting overpotential satisfies a minimum value to make it efficient. The best performing dyes are usually able to reach a quantum yield of electron injection efficiency ($\varphi_{inj}$) close to unity.

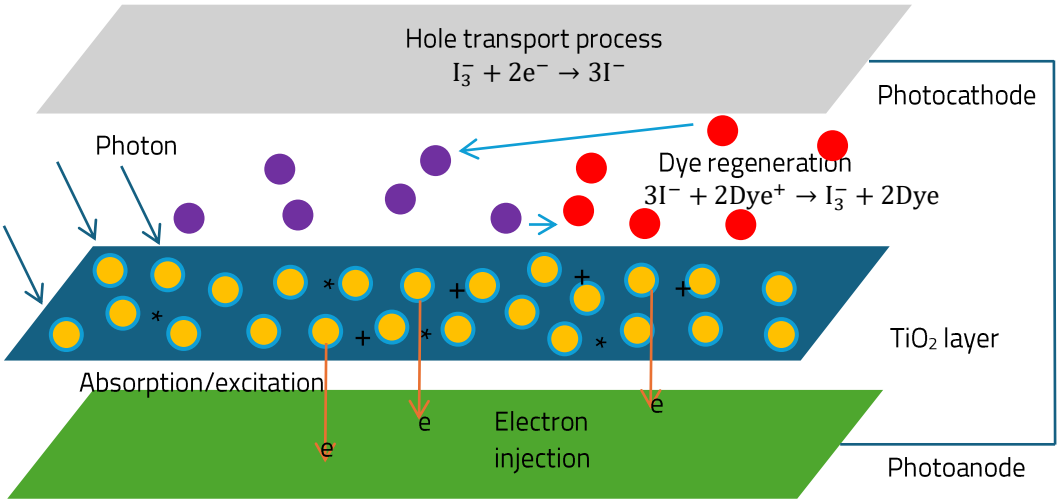


**Figure 36**: the photocurrent generation process inside a dye-sensitized solar cell.

Also, improvement of the $V_{OC}$ (open-circuit voltage) can be made by the recent efforts devoting to develop other new shuttles with higher redox potential and/or lower overpotential needed for efficient dye-regeneration[132–135] to reach greater $V_{OC}$ in DSSCs, such as one-electron outer sphere redox couples including ferrocene derivatives[136,137], copper[138], or cobalt[139,140] complexes. Other hole transporting material has been discussed in the next generation of solar cells such as graphene[141,142], transparent PEDOT:PSS[141] (poly(3,4-ethylenedioxythiophene)-poly(styrene sulfonate)), P3HT[142–144] (poly(3-hexylthiophene-2,5-diyl) and spiro-OMeTAD[144,145] (2,2′,7,7′-Tetrakis(N,N-di(4-methoxyphenyl)amino)-9-9′-spirobifluorene).

Imagine that we have a structure here with only four components: the substrate layer as the photoanode, the layer of the push-pull chromophore as the active layer, the transparent layer of photocathode and a load resistance. This compact structure will serve as a solar cell of 2D organic solid-state solar cell. The problem for this is that the electronic structure in the part of the push-pull chromophore will change. The electronic structure of the push-pull chromophore will alter if the molecules are not well solvated. There are two kinds of the electronic structure change caused by aggregation: the H-aggregation and the J-aggregation. The H-aggregation will increase the energy for the absorption of the light and the J-aggregation will decrease the energy for the absorption. If the self-assembled monolayer of the push-pull chromophore is crystalline, we even can infer the electronic structure of this active layer using tight-binding model in the domain of solid-state physics. The theory of the crystal orbital tells us that the if the structure of the matter is periodic (crystalline), the eigenvalue (energy level) and the eigenstate (wavefunction) of the time-independent Schrödinger equation is also periodic (Bloch's theorem). The electronic

structure will no longer be discrete, and bands are formed. The HOMO will become the valence band and the LUMO will become the conduction band if the molecule is considered the basic unit to construct crystal orbitals are molecules. In this case, it is the same case for the inorganic solar cells. One of the differences in terms of the absorption process between the conventional solar cell and organic solar cell is that an electron and a hole are created in the inorganic solar cell after the absorption of a photon while an exciton is created (a pair of an electron and a hole) in the organic solar cell after the absorption of a photon. Assume that the electronic structure of the photoanode and photocathode are well located to ensure the efficient separation of the electron and hole in an exciton and the efficiencies of the injection of the electron and hole are ensured. If the exciton generation rate is faster than the rate of the recombination, the photocurrent will be generated and collected by the load resistance.

Beside DSSCs, push–pull chromophores are adopted within perovskite solar cells as an interfacial layer to enhance the performance. The lack of stability impedes the commercial application of perovskite solar cells to replace the silicon-based solar cells. Push–pull chromophores have used to extend the lifetime of the perovskite solar cells. Liu and co-workers have designed an acceptor–donor–acceptor chromophore as an interfacial organic layer[146]. The push–pull chromophore has a structure of dithienyl diketopyrrolopyrrole (DPP-2T) with two ammonium cations attached to both sides of the DPP unit, thus allowing electrostatic interaction with inorganic $[PbI_6]^{4-}$ sheets within the perovskite cell. DPP-2T push–pull chromophores improved the performance of the cell with a PCE as high as 18.6%.

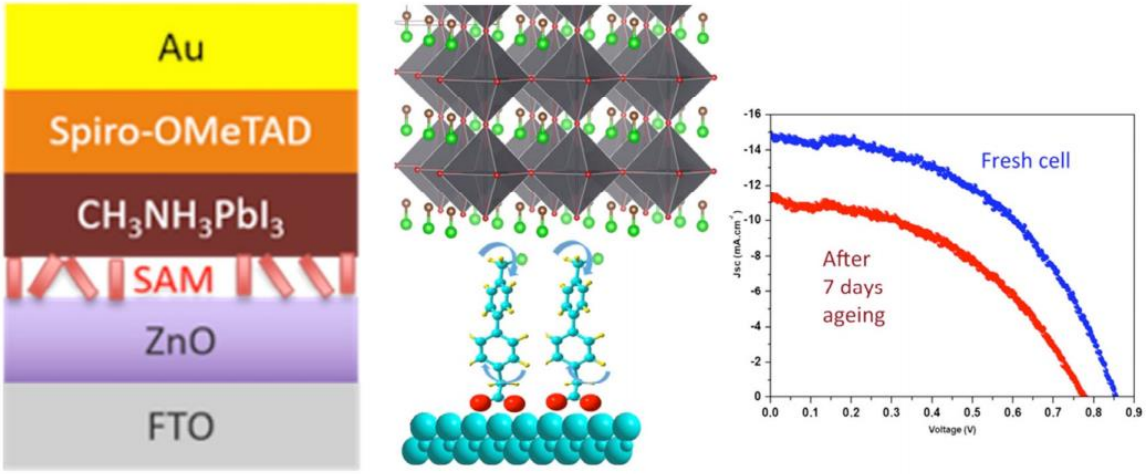


**Figure 37**: Interfacial SAM between the ZnO electron transport layer and perovskite (left) and their effect on the solar cell stability (right)[147].

Another key issue for perovskite solar cell is the surface passivation, which is also beneficial to enhance the performance and stability. Some studies have also shown the successful use of push–pull SAMs. Biphenyl-based SAMs have been successfully used as an interfacial layer between the ZnO electron transport layer and $CH_3NH_3PbI_3$ perovskite layer[147], as shown in Figure 37.

Alagumali and co-workers[148] used push–pull D–π–A organic small molecules to passivate the $Pb^{2+}$ defects. Besides, the electronic band structure is aligned and hydrophobicity of the surface increased, which results in the improvement in the solar cell stability by hindering the moisture effect (Figure 38).

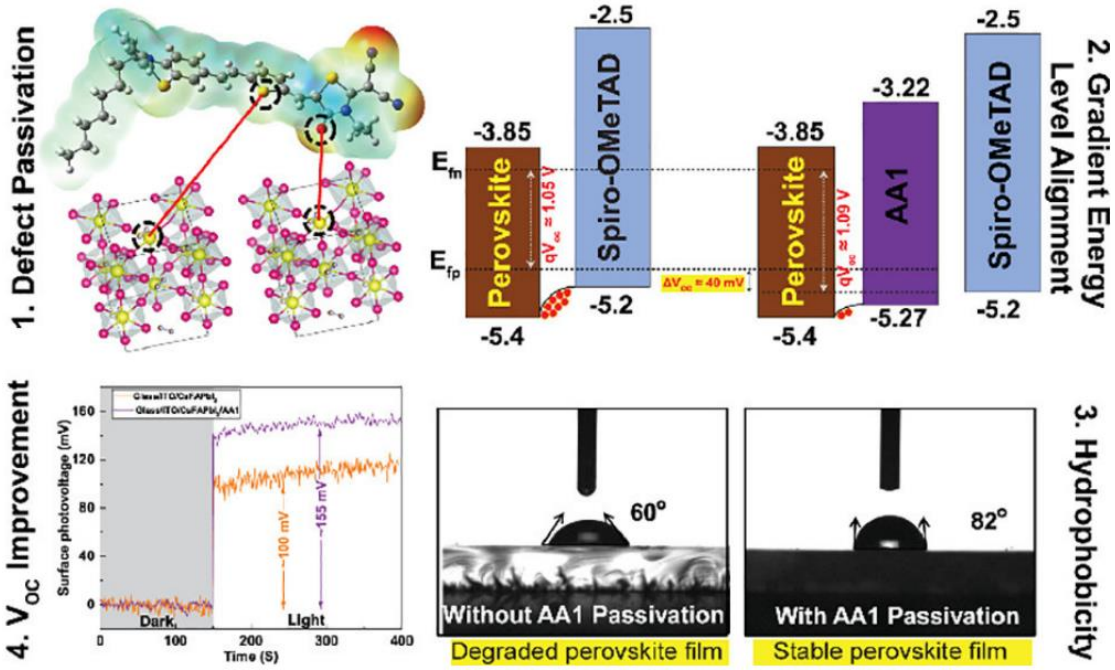


**Figure 38**: Scheme of the push–pull incorporation within perovskite materials, induced band alignment, and evidence of the increase in open circuit voltage and hydrophobicity[148].

Liu et al[149]. tackle the passivation issue by using 3D polydendate-complexing agents. The 3D complexing agents are phytic acid (PA) and phytate dipotassium (PAD). The six branches of the PA material undergo multiple chemical complexations, which result in defect passivation.

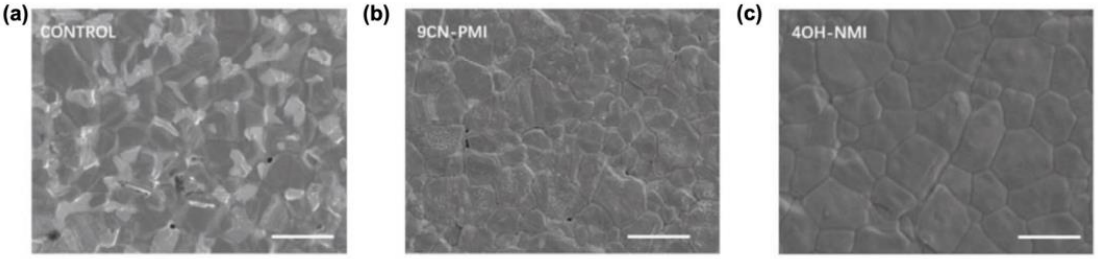


**Figure 39**: Scanning electron microscopy (SEM) images: (**a**) control film; (**b**) 9CN-PMI-modified film and (**c**) 4OH-NMI-modified film. The scale is 2 μm[150].

Another example of passivation is presented in the article by Zhang et al.[150], where they used polyaromatic molecules based on naphthalene-1,8-dicarboximide (NMI) and perylene-3,4-dicarboximide (PMI) with different molecular dipoles.

It is shown that such push–pull chromophores provide the passivation of defects (Figure 39) and, notably, NMI enables energy band alignment. Particularly, NMI passivation leads to the reduction in grain boundaries and defect density by about three times, which allows for a reduction in the non-radiative recombination rate and for an increase in the carrier lifetime, thus resulting in an increase of nearly 24% of the perovskite solar cell efficiency (PCE). Moreover, NMI-modified perovskite cells exhibit noticeably higher stability upon exposure to $N_2$ as well as oxygen and humidity (Figure 40).

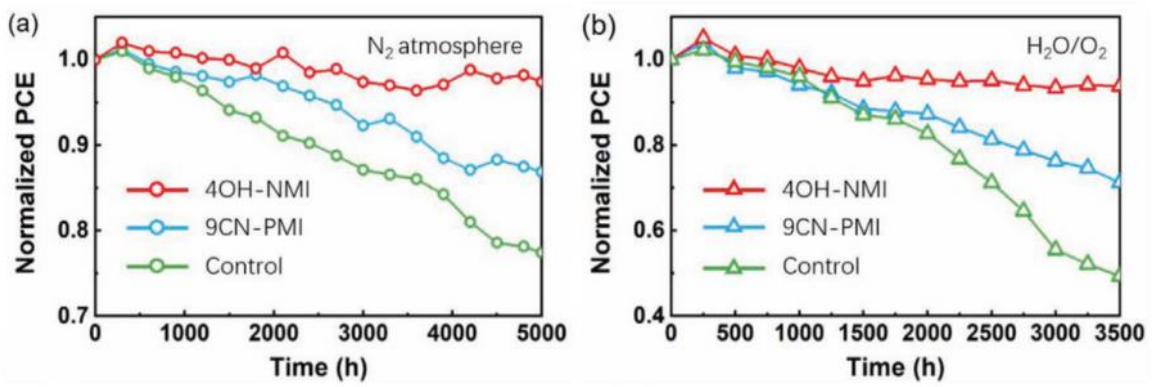


**Figure 40**: Stability test of 4OH-MNI-modified (red), 9CN-PMI-modified (blue) and control (green) perovskite solar cells upon exposure (a) to $N_2$ atmosphere (b) oxygen, and 20–30% relative humidity[150].

# II. Nanodielectric material based on ferroelectric push-pull chromophore

The self-assembled monolayer can be used for the construction of the surface electrical dipole. With the additional push-pull chromophore on the surface, the electrical permittivity ($\varepsilon$) will be increased for the surface. The electrical permittivity ($\varepsilon$) can be expressed by relating the electrical susceptibility ($\chi$) and the vacuum permittivity ($\varepsilon_0$) by the following equation:

$$\varepsilon = \varepsilon_0(1 + \chi)$$

The following equation in the scalar form can relate the macroscopic polarization (P), electrical field (E) and electrical susceptibility ($\chi$):

$$P = \varepsilon_0 \chi E$$

In the case of the three-dimensional system like n layer of self-assembled monolayer with a certain aera (A), the surface dipole density ($\sigma$) can be used to determine the electrical permittivity. Supposing that the electrical dipole of the push-pull chromophore is p=qd, and assuming that the tilt angle of the molecular dipole with the normal of the surface is $\theta$, macroscopic polarization can be expressed as:

$$P = \frac{dp}{dV} = \frac{n\sigma Aqd}{nAdcos\theta} = \frac{\sigma q}{cos\theta}$$

Then the electrical permittivity of the self-assembled monolayer ($\varepsilon_{SAM}$) is:

$$\varepsilon_{SAM} = \varepsilon_0 + \frac{\sigma q}{Ecos\theta}$$

According to this formula, the electrical permittivity of the self-assembled monolayer ($\varepsilon_{SAM}$) depends on three parameters: the charge q in the electrical dipole moment of the push-pull chromophore, the tilt angle of the molecule to the normal of the surface $\theta$ and the surface density of the dipole on the surface $\sigma$. The parameters to influence the electrical strength of the push-pull chromophore is summarized in the section dedicated to the push-pull chromophore. The linker and the anchoring group also participated in the contribution of the electrical dipole moment. The surface density of the push-pull chromophore on the surface is related to the structure of the push-pull chromophore and the reaction on the surface. The tilt angle depends on the growth mode, but high surface density can decrease the tilt angle towards the normal of the surface due to the transition from laying down phase to standing up phase.

There are several examples to use self-assembled monolayer on the surface.

In the work of Yoon et al. (figure 41), self-limiting chemisorptive deposition was used to prepare nanodielectric material. The structure can be described as the combination of three layers: the first layer is the self-assembled head and tail trichlorosilane functionalized alkane chains which can be grafted on a silicon oxide surface by nucleophilic substitution from hydroxy group to electrophilic silicon atom. The second layer is highly self-assembled layer by ferroelectric ''push– pull'' chromophore stilbazolium molecule. The third layer is octachlorotrisiloxane capping layers (Cap) to enhance multilayer structural robustness.

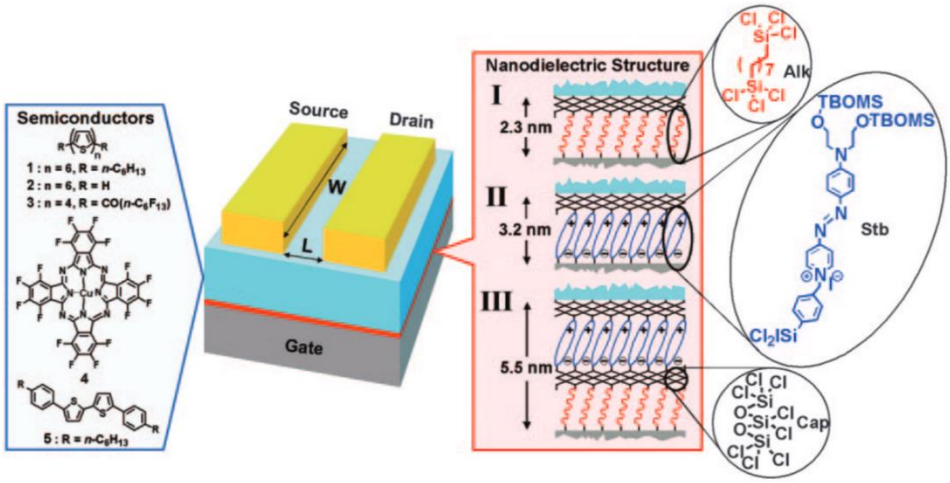


**Figure 41**: Schematic representation of the components of an OTFT showing the molecular structures of various organic semiconductors (Left) and self-assembled nanodielectrics I–III (Right). Highly n-type doped Si (100) wafers with a 1.5-nm native oxide or smooth ITO (a transparent conductor) were used as substrategate electrodes. Nanodielectric layers then were sequentially deposited from solutions of silane precursors Alk, Stb, or Cap. The OTFT device was completed by vacuum-deposition of 50-nm-thick layers of p- or n-type organic semiconductors 1–4 or solution-deposition of semiconductor 5, followed by source-drain gold electrode (100 nm) vacuum deposition[151].

A novel nanodielectric material (figure 42) has been created based on the combination of alternating nanostructured thin hafnium oxide $HfO_2$ film and the self-assembled layer of 4-[[4-[bis(2-hydroxyethyl)amino]phenyl]diazenyl]-1-[4-(diethoxyphosphoryl) benzyl]pyridinium bromide) (PAE)[152].

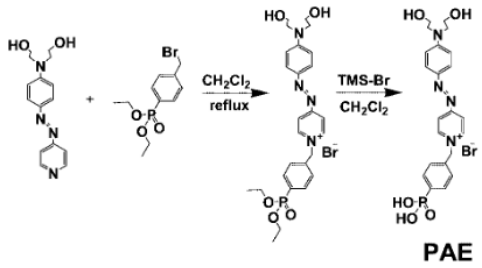


**Figure 42**: Synthesis of Polarizable Phosphonic Acid-Based p-SAND π-Electron Building Block

The multilayered nanodielectric material has been prepared by repeating the preparation the nanolayer of the $HfO_2$ and the self-assembled monolayer of PAE (figure 43). The nanolayer of the $HfO_2$ is prepared by the baking after the spin-coating of the $HfCl_4$ solution. Then the $HfO_2$ nanolayer will be immersed in the 3 mM PAE solution using methanol. Then samples are rinsed with methanol and blown dry with filtered $N_2$ after 60 min immersion at 60 °C. The third layer is prepared by repeating the procedure of $HfO_2$ nanolayer.

AFM was used after the successive preparation of Hf-SAND-n variants ranging from one to four bilayers (Hf-SAND 1~4) to examine the surface roughness, contiguity and conformality (figure 44). The images are in fact the outmost $HfO_2$ nanolayer and they are featureless. These films RMS roughness increases from 1.3 Å for a single layer to 1.7 Å for

the four-layer variant[153]. The smooth surfaces are key parameters for the fabrication of back-gated transistor devices TFT[154].

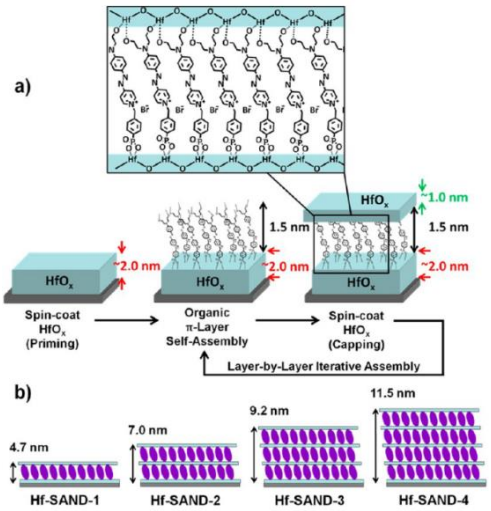


**Figure 43**: (a) Solution-based Hf-SAND self-assembly procedure employed in this study. (b) Schematic of the various Hf-SAND multilayers produced including the corresponding X-ray reflectivity derived thicknesses (Hf-SAND-1, -4) and estimated thicknesses (Hf-SAND-2, -3).

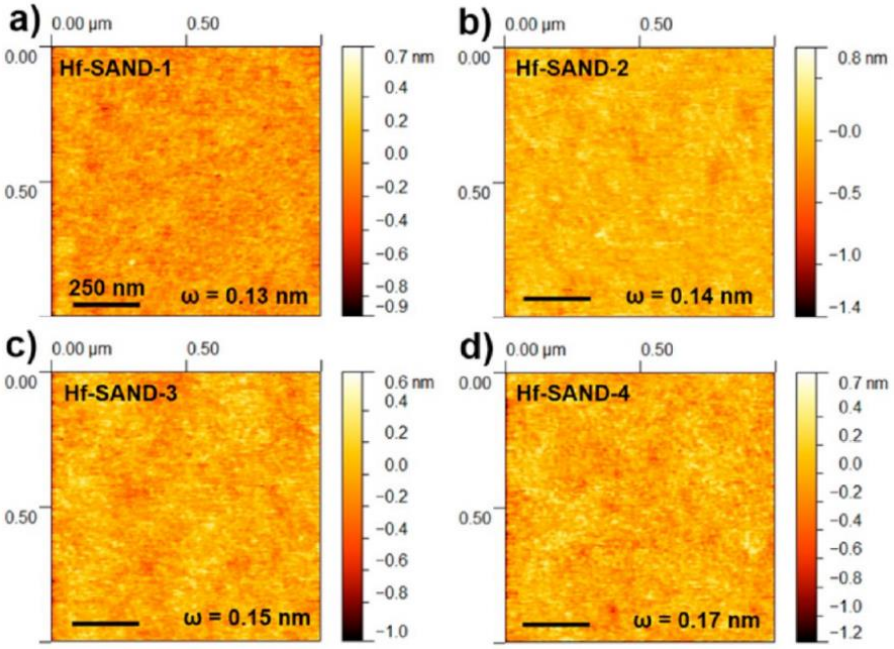


**Figure 44**: AFM images of monolayer (a) Hf-SAND-1, (b) Hf-SAND-2, (c) Hf-SAND-3, and (d) Hf-SAND-4 systems, and ω indicates the RMS roughness.

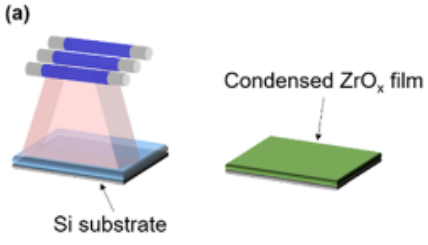


**Figure 45**: Schematic representation of $ZrO_2$ film fabrication by UV irradiation.

Conventional annealing requires high temperature and limits SAND application especially with many biocompatible polymer substrates for SAND fabrication. In the contribution for the development of biointegrated electronics, Huang et al[155] created SANDs based on alternating zirconium oxide nanolayer using UV radiation processing (figure 45). The XPS spectra concluded that the reaction to form oxide from the precursor by UV irradiation is more appealing than conventional thermal annealing because the quality of the zirconium oxide thin film is better using UV radiation. Besides, $ZrO_2$ layer can protect organic PEA layer against UV damage.

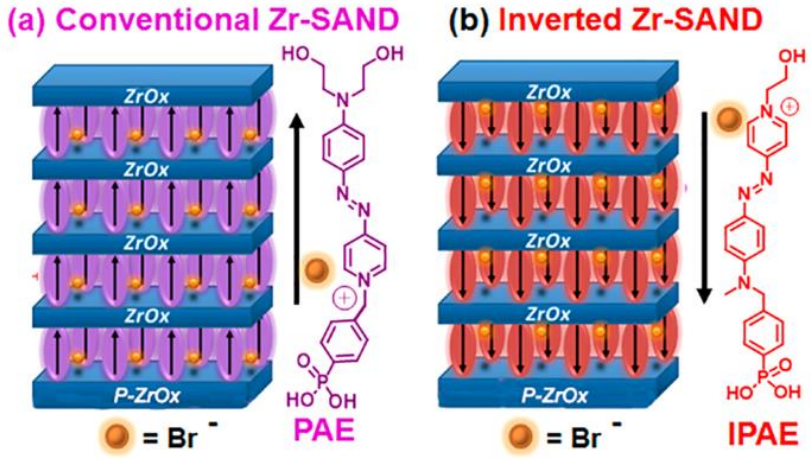


**Figure 46**: Dielectric stacks comprising four-chromophore/$ZrO_2$ layers on top of the $ZrO_2$ (p-$ZrO_2$) primer film. (a) Conventional Zr-SAND with a phosphonate π-electron (PAE) unit. (b) Inverted IZr-SAND with an inverted PAE (IPAE) π-unit.

An "inverted" PAE unit, named IPAE with a reversed electrical dipole is used to create a structurally inverted SAND[156] (figure 46). The PAE and IPAE have the same grafting unit to connect $ZrO_2$ nanolayer. The minor difference is two hydroxylethyl fragments in the latter versus one in the former structure. More importantly, PAE and IPAE follow the same adsorption kinetics because they have same grafting unit.

The absorption spectra were recorded for PAE and IPAE in methanol. Optical absorption spectra were done for IPAE and PAE optical spectra in methanol solution. The latter features a blueshift of 20 nm in $\lambda_{max}$ and half the molar extinction coefficient $\varepsilon$ of PAE. This result likely revelated the minor influence caused by the molecular structure. The phosphonic acid is electron-withdrawing and aliphatic alcohol is electron-donating. Thus, the push-pull characteristic is more significant with the case if the phosphoric acid relates to pyridinium, and aliphatic alcohol relates to aromatic amine (the case of PAE). And for IPAE, the blueshift is due to diminished intrinsic electric dipole strength inside the molecule.

# III. Biosensors

Within the framework of the PhD, we would like to investigate the possibility to apply push-pull chromophores in the domain of biosensors after review of its application as the active layer for the organic solar cell, passivation and charge-transfer layer in the perovskite solar cell, active layer of dielectric material for the capacitor and for the gate electrode for transistor.

The biospecific adsorption of proteins at interfaces that present appropriate functional group is important for biosensors[157], and biocompatible surfaces[158]. The goal is to find a versatile but precisely defined, synthetically feasible and flexible system to investigate biomolecular recognition at surfaces. One of the systems is to use self-assembled monolayer examined by surface plasmon resonance (SPR) spectroscopy. The work of Mrksich et al. (figure 47) is based on self-assembled monolayer using a model system with immobilized benzenesulfonamide groups on the surface. This group interacts with bovine carbonic anhydrase for the detection.

Compared to the surfaces based on traditional material, SAM has advantages. The first advantage is that the density of the functional group to enable physical and chemical biomolecular recognition is controllable. The second advantage is that the SAM can be tailored to avoid non-specific adsorption of the protein. The third advantage is that the biomolecular interaction can be changed by choosing different linker and molecular identity of the surface. Finally, SPR is not the only analytical technique for measuring protein adsorption for SAM. There remain many techniques compatible with SAM.

Several Mixed SAMs were tested with different mole fractions of an ethylene glycol chain thiol terminated in a benzenesulfonamide group. The tri(ethylene glycol)-terminated alkanethiol was used as the matrix to these SAMs.

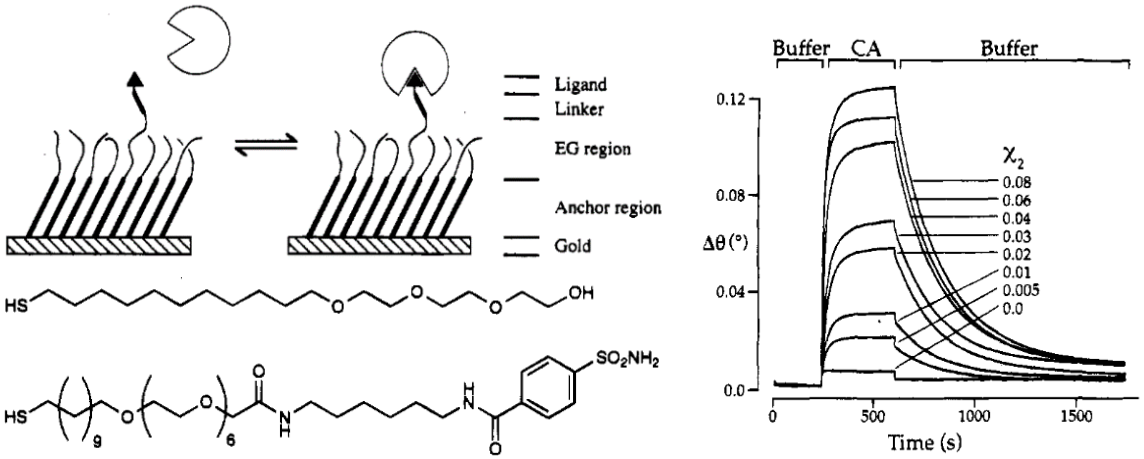


**Figure 47**: (left):(top) cartoon showing reversible adsorption of CA to mixed SAMs presenting ligands, (middle) the molecular structure of the thiol without benzenesulfonamide group and (bottom) the molecular structure of the thiol with benzenesulfonamide group; (right) real-time SPR response curves for binding of CA to mixed SAMs having different values of benzenesulfonamide group on the surface. The change in resonance angle is plotted against time; the curves were adjusted vertically to facilitate comparison of the data.[159]

Graphene has gained great attention for the scientists. It is considered as an alternative material for biosensing because not only it has outstanding electrical, physical and optical properties, but also it is a two-dimensional material. Huang et al.'s study[160] shows that graphene is a candidate for the development of potential real-time nanoelectronic biosensors (figure 48 and figure 49). For this purpose, a field-effect transistor was produced based on the large-sized graphene transistor by chemical vapor deposition. Two enzymes were tested: the glucose oxidase and glutamic dehydrogenase. They are catalysts for the oxidation reaction of glucose and dehydrogenation of glutamate. Since they are both redox reactions, Faradic current will be generated. These two enzymes were immobilized on the surface via strong by π–π interaction with a pyrene group attached to the 1-pyrenebutanoic acid succinimidyl ester as the linker. Glucose or glutamate molecules were detected by the current change of the graphene transistor.

GOD (glucose oxidase) catalyses the oxidation of glucose in the following reaction: β-D-glucose + $O_2$ +$H_2O$ → D-glucono-1,5-lactone + $H_2O_2$. The current value increases as the glucose is injected in the solution and saturates from 10 mM. At 0.1 M, the value of the current increases 0.76% but 0.07 % in the control experiment. The control experiment indicates that the graphene based nanoelectronic biosensor can specifically detect glucose.

GluD (glutamate oxidase) oxidizes glutamate in the following reaction: L-glutamate + β-NAD + $H_2O$ → α-ketoglutarate + β-NADH + $NH_4^+$. To facilitate the oxidation reaction, 5 mM β-NAD (Sigma-Aldrich) was added to the recording chamber before addition of glutamate. The current increases in two linear regimes before the saturation. From 5 to 50 μM and from 50 μM to 1.2 mM, respectively. When the concentration of glutamate is 5 mM, the current increases 0.35±0.08% (3 devices), much higher than the noise level. The control experiment shows that the sensor is specific to the glutamate because other molecules will not create any currents caused by redox reactions.

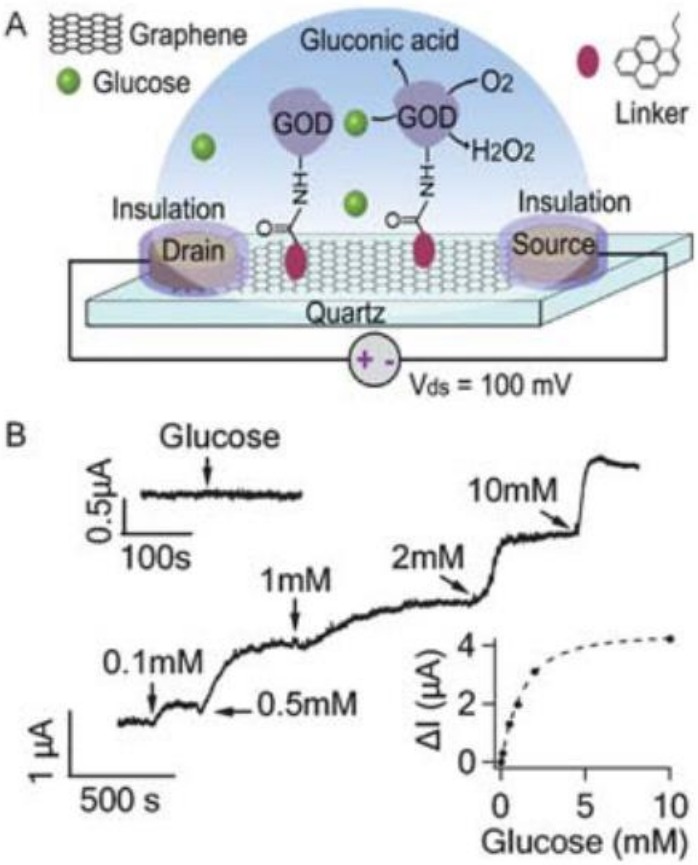


**Figure 48** : (A) Schematic illustration of glucose oxidase functionalized graphene field effect transistor. (B) Current responses to the addition of glucose to various concentrations. The upper inset shows that GOD free graphene FET is not responsive to 10 mM glucose. The lower inset shows the response curve of the graphene FET to glucose fitted by a function[160].

The interfaces which is responsive to certain stimuli is a trend of development for the biomedical and biotechnological applications because the biomolecular interactions can be modulated. However, no attempts have been made yet to control antibody–antigen binding in an on-demand mode. In the work of Santos Gomes et al.,[7] (from figure 51 to figure 54), a surface is functionalized by the oligopeptide which allows for the conformational changes decorated with a distal progesterone antigen in the matrix of the thiol with a chain based on oligo(ethylene glycol) for the application of biosensor. The progesterone antigen-antibody interaction can be activated (ON state) or inhibited (OFF state) with different voltage.

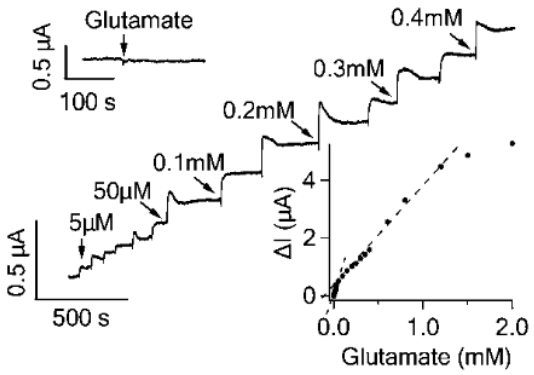


**Figure 49**: Current responses of GluD functionalized graphene FET to the addition of glutamate to various concentrations. The upper inset shows that GluD free graphene FET is not responsive to 1 mM glutamate. The lower inset shows the response curve of the graphene FET to glutamate with two fitting lines indicating the two linear response regions[160].

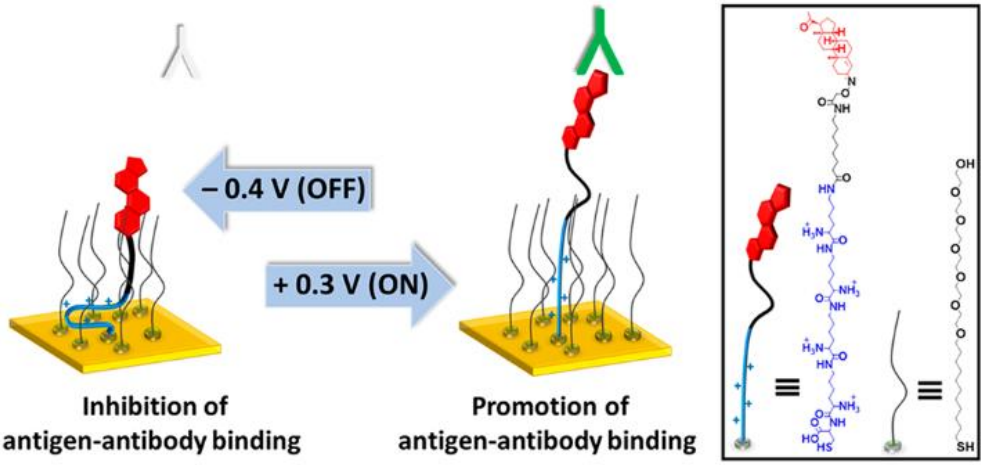


**Figure 50**: Schematic of the binary SAM for temporal control of antibody binding. The electrically responsive unit conceals the rigid progesterone unit under a negative potential (–0.4 V) (folded conformation), inhibiting antibody binding. Conversely, a positive potential (+0.3 V) promotes antigen activity and consequently allows high antibody binding capacity. (inset) Chemical structures and cartoons of the progesterone-C7-4KC oligopeptide (left) and oligo(ethylene glycol) thiol (C11EG6) (right) used for mixed SAM formation[7].

The stimuli-responsive surface is on a gold substrate by a binary SAM (Figure 50). The first part is an oligopeptide attached to the distal progesterone (progesterone-C7-4KC) and the second part is a hexaethylene glycol-terminated thiol (C11EG6). The oligopeptide contains (i) a terminal L-cysteine containing a thiol functional group for the grafting to the gold surface, (ii) four lysine residues linked by peptide bond using amine functional group at ε position (An alpha carbon is the carbon that is next to a functional group. The carbon that is next to the alpha carbon in the main carbon skeleton is beta carbon. So, the epsilon carbon is the fifth carbon in the main carbon skeleton by counting the alpha carbon as the first), (iii) an alkyl linker that separates the switching unit (lysine moieties) from the distal progesterone while also presenting the antigen above the surface for optimal antibody recognition, and (iv) the rigid progesterone antigen binding unit. The amino group at the ε

position is protonated and therefore a tetracation at physiological pH is formed. Therefore, it is responsible for the conformation change as the electrically responsive switching unit.

Then attention was turned to the ability to use the change of the conformation of the oligopeptide to switch progesterone antigen activity on-demand and the antibody binding capability for the attached antigen. Two different types of control SAMs were prepared and analysed to demonstrate that electrical potential control over antibody binding occurs due to conformational changes of the oligopeptide, which lead to the concealment or exposure of the progesterone antigen. The first control SAM constituted by a 5KC:C11EG6 mixed SAM prepared at a mole fraction in solution of 0.98 for C11EG6 in which no progesterone is present, serves as the reference. The sensorgrams were recorded for the 5KC:C11EG6 mixed SAM at different electrical potential conditions (OC, –0.4, and +0.3 V) (figure 51). The amount of antibody that adsorbed non-specifically to the 5KC:C11EG6 mixed SAM under OC, –0.4, and +0.3 V was very limited.

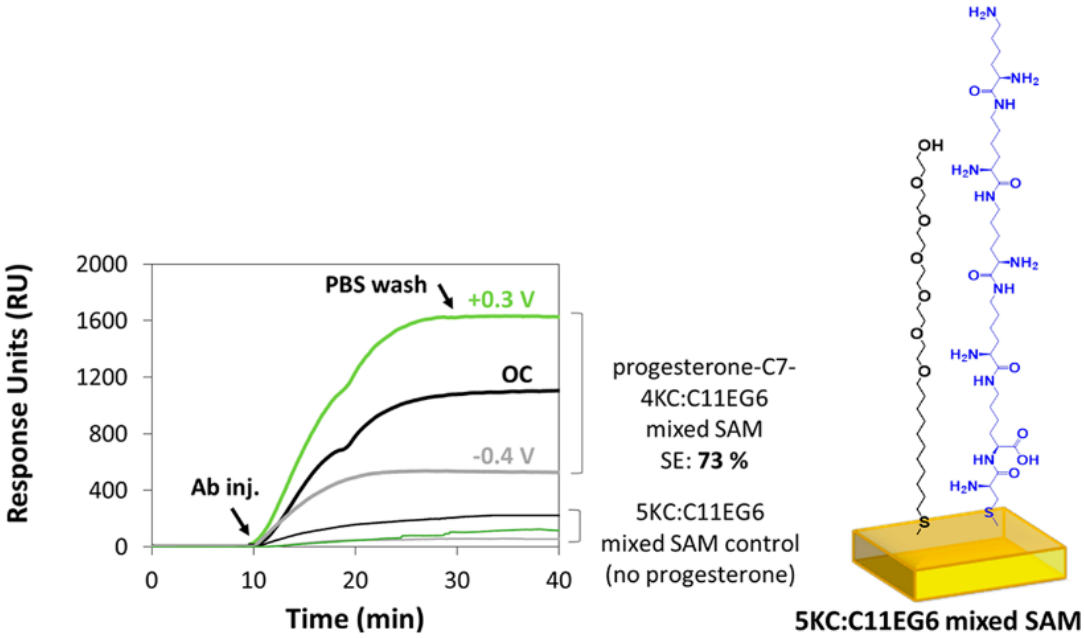


**Figure 51**: (left) SPR sensorgrams for the binding of anti-Pg mAb to the control 5KC:C11EG6 mixed SAM (no progesterone), in PBS, under OC (no applied potential), ON (+0.3 V), and OFF (–0.4 V) conditions; sensorgrams for the binding of anti-Pg mAb to the progesterone-C7-4KC:C11EG6 mixed SAM are also included, for comparison purposes. (right) Chemical structures of the components used for the formation of the 5KC:C11EG6 mixed SAM[7].

Another control mixed SAM was designed, prepared, and characterized to demonstrate that modulation of antibody binding was due to the conformational changes of the oligopeptide on the surface induced by an electrical potential. The control mixed SAM was prepared with a non-switchable progesterone thiol (progesterone-C11-SH) and a tri(ethylene glycol) thiol (EG3SH) (figure 52). The results demonstrate that the electrical potential has minimal direct effect on attracting or repelling the antibody to or from the surface.

The progesterone-C11-SH compound was synthesized by EDC/HOBt coupling of progesterone 3-(O-carboxymethyl)oxime and 11-amino-1-undecanethiol hydrochloride

and isolated after column chromatography purification. The recorded sensorgrams for the progesterone-C11SH:EG3SH mixed SAM at different electrical potential conditions (OC, –0.4, and +0.3 V). While the progesterone antibody binds to this surface, the effect when different electrical potential conditions is applied is limited, with a calculated switching efficiency of 18 ± 5%. The differences in binding observed for the different applied potentials might arise from a small effect that the OC, –0.4, and +0.3 V might have on attracting or repelling the antibody to or from the surface, thus, to a small extent, promoting or inhibiting antibody binding. However, the switching efficiency of 18 ± 5% for the control is significantly lower than that obtained for the switchable progesterone-C7-4KC:C11EG6 mixed SAM, which exhibits a switching efficiency of 73 ± 3%. This result is another indication that the switching is due mainly to the oligopeptide conformational changes. These control experiments provide valuable evidence that antibody binding is controlled by the exposure of the progesterone moiety, which in turn is controlled by the oligopeptide conformational changes induced by the application of an electrical potential.

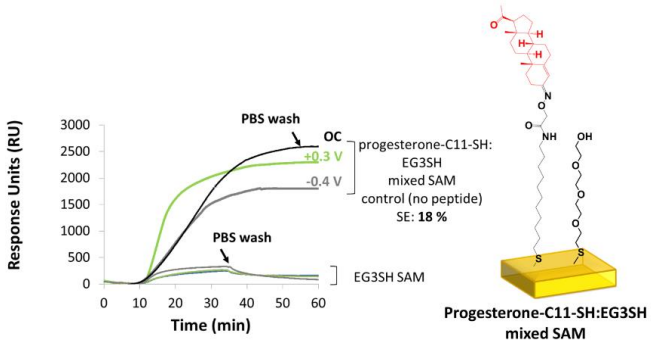


**Figure 52**: (left) SPR sensorgrams for the binding of anti-Pg mAb to the control progesterone-C11-SH:EG3SH mixed SAM (no peptide) and to the EG3SH SAM, in PBS, under OC, ON (+0.3 V) and OFF (–0.4 V) conditions. (right) Chemical structures of the components used for the formation of the progesterone-C11-SH:EG3SH mixed SAM[7].

At the end of the bibliographic research, it is the time to show the aim of the PhD thesis: the elaboration of the potential-modulated electroresponsive self-assembled monolayer to monitor the antigen-antibody interaction on demand. This requires firstly the elaboration of the push-pull chromophore, secondly the self-assembled monolayer of push-pull chromophore on the substrate. The third step is the incorporation of self-assembled monolayer of push-pull chromophore and the binary self-assembled monolayer reported in the article of Santos Gomes. The final step is to test under different potentials.

The principle is simple. The change of the conformation of the oligopeptide is caused by the electrostatic force. The applied potential gives the electric field between the anode and the cathode. At physiological pH, the chain of the oligopeptide is a polycation and the charge will be influenced under the electrostatic field. The addition of the push-pull chromophore will booster the strength of the electrostatic field since the push-pull chromophore is an electrical dipole under the electrostatic field. If the push-pull chromophore will form an electrical dipole with negative sign near the electrode and a positive sign far from the electrode, the deployment of the oligopeptide chain will be accelerated with a positive potential at the electrode because of a strengthened repulsion.

If the push-pull chromophore will form an electrical dipole with positive sign near the electrode and a negative sign far from the electrode, the retraction of the oligopeptide chain will be accelerated with a negative potential at the electrode because of a strengthened attraction. In another point of view, if the conformational change needs a fixed effective potential, the stronger the electrical dipole in the structure, the less the applied potential to start the conformation change of the oligomer chain (figure 53).

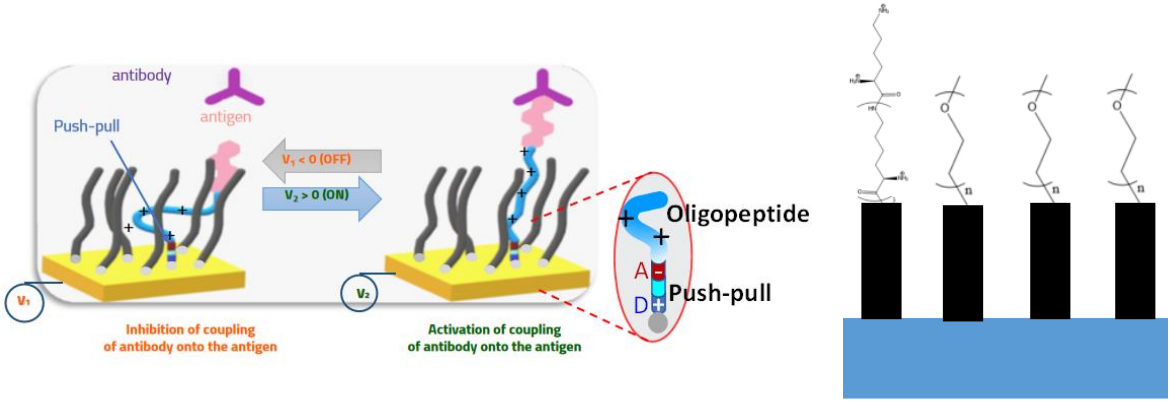


**Figure 53**: (left) The structure of the binary self-assembled monolayer which uses push-pull chromophore to link the substrate and the oligopeptide to do the potential modulation of the potential for the control of the conformation of the oligopeptide. (right) The structure of the self-assembled monolayer which uses self-assembled monolayer of push-pull chromophore to link the oligo(ethylene glycol) and the oligopeptide to do the potential modulation of the potential for the control of the conformation of the oligopeptide.

# 2. Characterization methods

The characterization methods are important because they are the tools that scientists can use to monitor the chemical reaction and analyse the properties of the materials and compounds. Here we present common characterization methods used during the PhD for the molecules and the molecular self-assembled monolayer on the surface.

## A. Electrospray ionisation mass spectroscopy (ESI-MS)

Mass spectroscopy is an analytical tool for chemical compounds in different physical state: solid, liquid, or gaseous. Mass spectroscopy can determine the molar mass of the compound, determine the structure of the compound by finding fragmentation evidence in the spectrum, study the fragmentation mechanism and make quantitative analyses such as the purity. The limit of detection is from nanogram to picogram. It is widely used in the biology to determine the molar mass of the protein, in the environmental science to study the pollutant impact, in the sport games to detect illegal drug use and in the airport to detect explosives and drugs for the security. The high sensitivity, high selectivity and rapidity make the mass spectroscopy attractive for its application.

The principle of the mass spectroscopy is to ionize the molecule and to analyse the fragments of the molecule. Thus, the molecules will be volatized in gaseous phase to have enough space among the molecules, and they will be then ionized using electrical field and finally they will be analysed by different detectors. The mass spectrometer is constituted by two parts: the ions source for the volatilization and ionization, and the analyser to determine m/z. The whole process is described in figure 1.

The ion source can volatilize and ionize separately or simultaneously according to different types. It can guide and displace the ions with very precise electrostatic field. There are numerous types of sources, and each uses a different principle of physics. The principle of physics which permits to volatilize and ionize for a kind of compounds is chosen by considering the characteristics of the molecule to analyse. The analyser can determine the ratio of mass/number of charges. A sufficient vacuum is required to have enough average free flying distance for the molecule to be analysed without any destruction and deviation. The ions formed in the ion source are directed (extraction and focalization) to the analyser by the electrical field which can be several volts or several tens of kilovolts. The speed of displacement of ions in the analyser is dependent of the intensity of the extraction field.

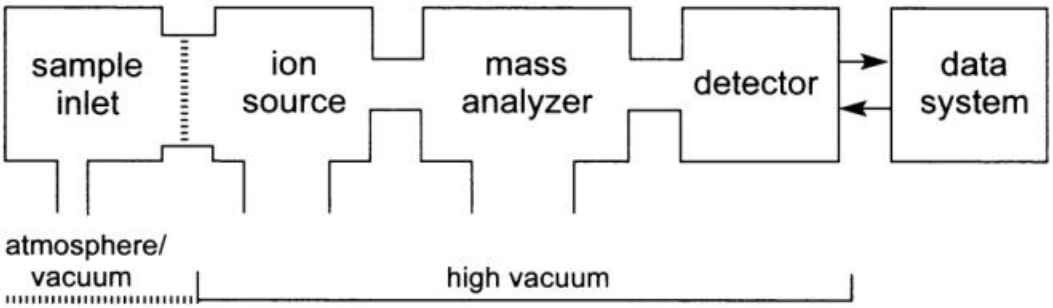


**Figure 1**: the structure of the mass spectrometer[161]

The whole mass spectrometer machine can de described by five parts in figure 1:

1. The port for the introduction of the sample.

2. The ionization chamber and the chamber to accelerate the ions. This is the main part for the ion source.

3. The analyser to separate the ions with different m/z.

4. The ion collector and the amplificatory of the signal. It can determine the relative abundance of each ion.

5. The recording system and the data processing system.

The ion sources can be divided into two categories: the hard ion source and the soft ion source. Numerous ionization methods are invented to ionize and volatilize bigger, more polar and more fragile molecules. The ionization method used here is a soft ionization method called electrospray. An ESI source of sufficiently advanced design for mass spectrometry was designed by the Fenn group in the mid-1980s (Figure 2). The dilute sample solution is forced by a syringe pump through a hypodermic needle at a rate of 5-20 μL/min. The needle is held at a potential of 3-4 kV relative to a surrounding cylindrical electrode. Then, the electro-sprayed aerosol expands into a countercurrent stream of dry nitrogen gas that serves as a heat supply for vaporization of the solvent. A small portion of the sprayed material enters the aperture of a short capillary (0.2 mm inner diameter, 60 mm length) that interfaces the atmospheric pressure spray to the first pumping stage (ca. 102 Pa). Most of the gas expanding from the desolating aerosol is pumped off by a rotary vane pump as it exits from the capillary. A minor portion passes through the orifice of a skimmer into the high vacuum behind (ca. $10^{-3}$-$10^{-4}$ Pa). At this stage, desolation of the ions is completed, while the ions are focused into a mass analyzer. Suitable potential applied to capillary, skimmer, and lenses behind provide an effective transfer of ions through the interface, whereas neutral gas is not affected.

The mass spectroscopy is good for the determination of the molecular mass of the molecule and the structure of the molecule, especially good for the atoms whose nuclear magnetic moment is zero. We have used this method to characterize

molecules for the synthesis of the push-pull chromophores. For the High-resolution mass spectroscopy was made with a Qstar Elite spectrometer (Applied Biosystems SCIEX) with ionization electrospray source (ESI) through the Spectropôle facility of Aix-Marseille University.

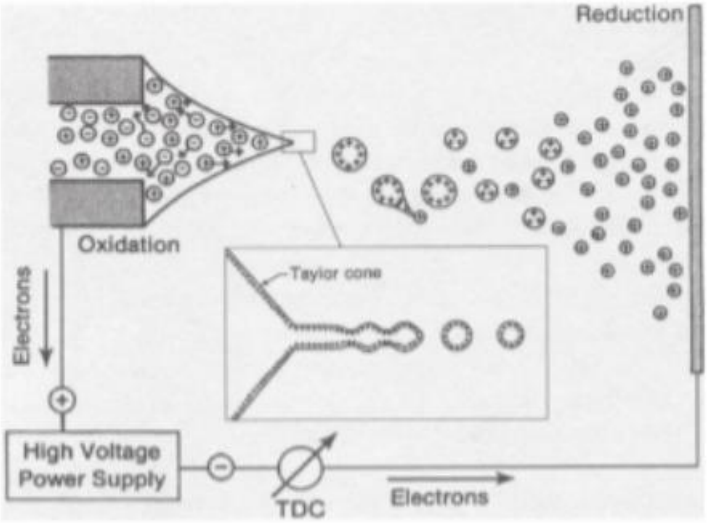


**Figure 2**: Schematic of Taylor cone formation, ejection of a jet, and its disintegration into a fine spray also including the electrochemical processes of ESI[161,162]

# B. Nuclear magnetic resonance spectroscopy (NMR)

In the framework of the spectroscopy for the chemistry, nuclear magnetic resonance spectroscopy (NMR) is the key tool to probe the molecular structure. In the framework of the quantum mechanics, the spin is a vector precessing in the complex Hilbert space in the time described by the wavefunction.

Each kind of nucleus and electron has its specific precessing frequency. This frequency is called the Larmor frequency or Larmor angular frequency (ω), which is defined by the following equation (q the charge value, m the mass and the B the intensity of the external magnetic field, the negative value showing the opposite rotating direction):

$$\omega = -\frac{q}{2m}B$$

The situation above is only valid for a single nucleus or the electron. Every NMR experiment is exercised on an ensemble made of the nucleus and the electron. The resonance frequency is sensitive to the local environment of the nucleus of the atom. Each atom possesses a nuclear magnetic moment even though the global magnetisation of the molecule is zero because of the thermal perturbation (figure 3).

An experiment of nuclear magnetic resonance spectroscopy must be done under a strong magnetic field. Let's take the example of the proton (two spin states) to illustrate it. Without the external magnetic field, the two spin states (spin-up and spin down) has the same energy states. The effect of the magnetic field caused a splitting of the energy level for two spin states and the direction of the magnetic moment turns to be parallel or anti-parallel to the direction of the external magnetic force. If the field is sufficiently high, the splitting of the energy level between the spin-up and spin-down will be so big that the probability to find an electron in the spin-up state is very small according to the Maxwell-Boltzmann distribution and all the nuclear magnetic moments will be parallel to the external magnetic field. This big field is called the static field (figure 3).

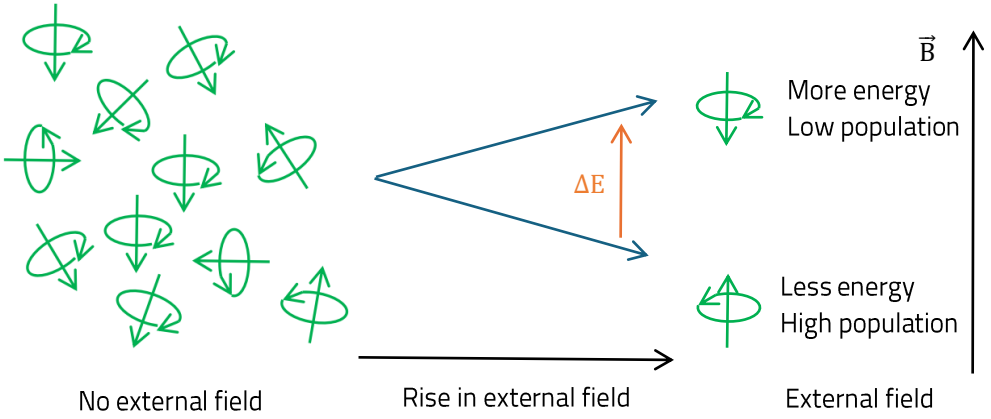


**Figure 3**: the energy splitting of an ensemble of hydrogen nuclear magnetic spins with the external magnetic field.

A perturbative magnetic field (a pulse with the energy equal to the energy level difference between two spin states) is required to launch the precession of the spin, which is very important. The precession of the nuclear magnetic moment can be described in the Bloch sphere. The nuclear magnetic moment at the fundamental state is a vector in the spherical complex space pointing the North pole. In the Bloch sphere, only the component along the z axe is counted to calculate the probability and to determine the spin state. The component projected on the XY plane will be also recorded. Taking a pulse of 90°, the nuclear magnetic moment will be pointing with a 90° angle with the z axis. The precession starts just after the pulse and the spin state will point the North pole after spiro movement. In the dynamic process, two times are important: the transverse relaxation time $T_1$ (relaxation time described in figure 4 of the component along the z- axis or spin-lattice relaxation time) and the longitudinal relaxation time $T_2$ (relaxation time of the component on the xy plane or spin-spin relaxation time).

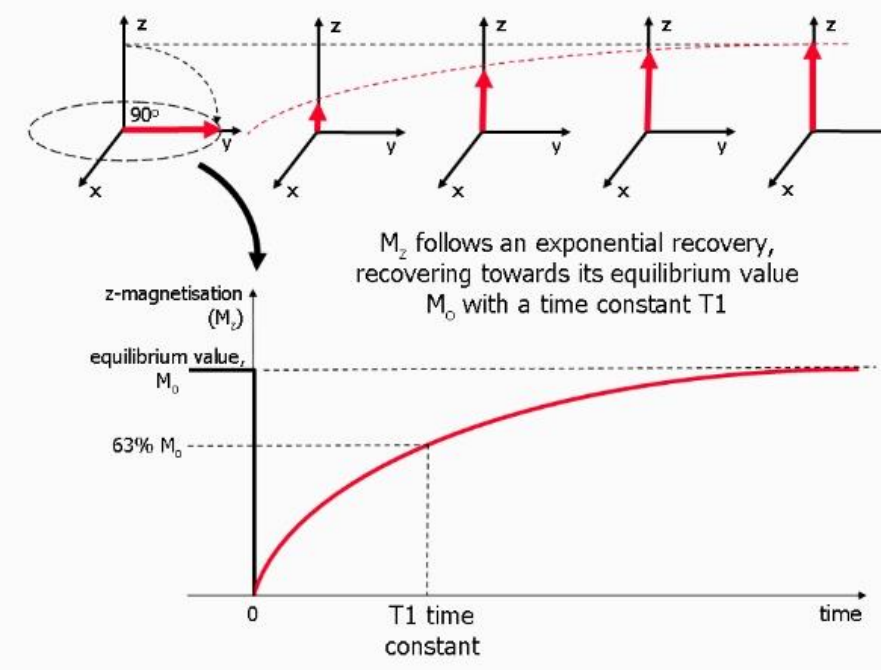


**Figure 4**: $T_1$ relaxation process. Diagram showing the process of $T_1$ relaxation after a 90° radiofrequency pulse is applied at equilibrium. The z-component of the net magnetisation, $M_z$ is reduced to zero, but then recovers gradually back to its equilibrium value if no further radiofrequency pulses are applied. The recovery of $M_z$ is an exponential process with a time constant $T_1$. This is the time at which the magnetization has recovered to 63% of its value at equilibrium[163].

Since the quantum superposition state will be destroyed after the measurement, so to measure these two relaxation times, a series of the pulse must be done to plot the variation of the two components and the relaxation time. Due to the inhomogeneity inside the matrix of the analysis, the dephasing of the spin occurs. This phenomenon can be smoothed by spin-echo sequence using inverse pulse. But in NMR experiment, the FID (Free Induction Decay) is taken and the

apparent longitudinal relaxation time $T_2^*$, where the dephasing of the spin cannot be neglected, is recorded, and used for the NMR spectrum.

The overall term for the observed loss of phase coherence (dephasing) is $T_2$* relaxation, which combines the effect of $T_2$ relaxation and additional de-phasing caused by local variations (inhomogeneities) in the applied magnetic field. $T_2$* relaxation is the result of spin-spin interactions and due to the random nature of molecular motion, this process is irreversible. $T_2$* relaxation accounts for the more rapid decay of the FID signal. Both $T_2$ and $T_2$* are exponential processes with times constants $T_2$ and $T_2$* respectively.

Now, the data are in the time space and the form of the data is in the form of damped harmonic oscillation. This is called the free induction decay. To obtain a NMR spectrum, the Fourier transform must be done and the spectrum will be presented using ppm as the unit because the frequency shift caused by the environmental change is very small.

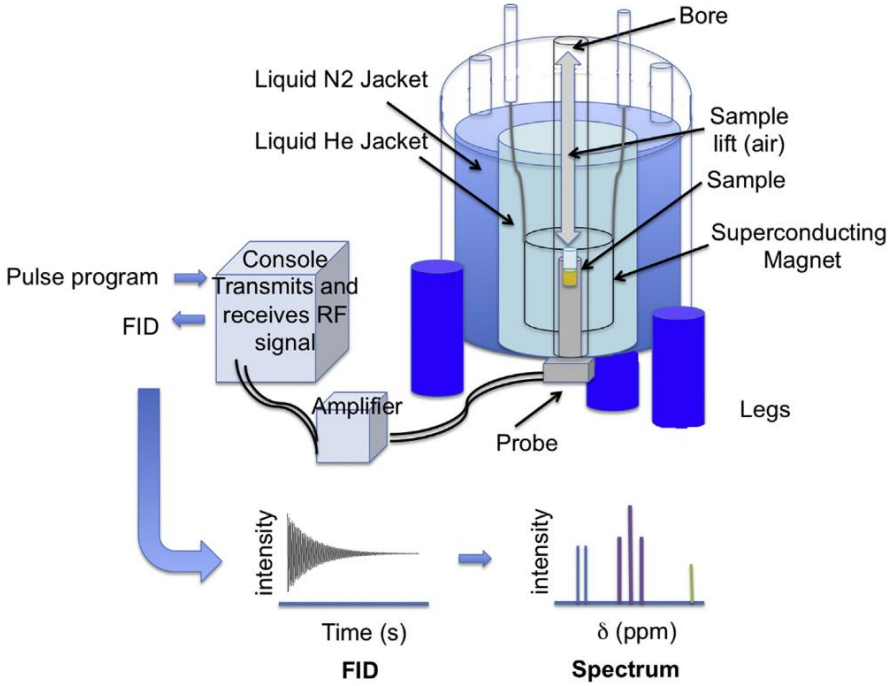


**Figure 5**: the structure of the NMR spectrometer[164].

During the PhD, the nuclear magnetic resonance spectroscopy is used to determine the structure of the molecule, especially good for atoms whose nuclear magnetic moment is not zero in the molecule. $^1$H and $^{13}$C NMR spectra were recorded on JEOL-400 at 400 MHz, and 101 MHz respectively. The starting pulse of NMR is 45° and the signal is recorded with a 5s delay to the starting pulse. The accumulation of the spectrum is at most 128 for the NMR spectroscopy except $^{13}$C (4096 accumulation).

# C. UV-visible spectroscopy (UV-vis)

In the framework of the spectroscopy for the chemistry, the UV-visible spectroscopy is the tool often adopted for the electronic transitions in the atom and the molecule. The energy levels are constructed by the solution of the time-independent Schrödinger equation and the construction based on the interaction of atomic orbitals. The energy levels are discrete for the molecule and the atom. The molecule absorbs the light with a certain wavelength to probe different energy levels. For a molecule which is composed by only s block and p block elements (carbon, hydrogen, nitrogen, oxygen, sulphur etc), there are five kinds of molecular orbitals: σ bonding molecular orbital, π bonding molecular orbital, n non-bonding molecular orbital, σ* anti-bonding molecular orbital and π* anti-bonding molecular orbital (figure 6). For organometallic molecule, the situation becomes more complex as the d orbitals of transition metals and f orbitals of rare earth orbitals intervene. For transition metals, the d orbitals can form chemical bonds, and their energy levels can be predicted by crystalline field theory or ligand field theory. For rare earth orbital, the 4f orbitals will not form any chemical bonds and they are more inert as their energy levels can only be slightly influenced by coordination and ligands. The vibrational states can also join in the fine energy levels according to the Franck-Condon overlap.

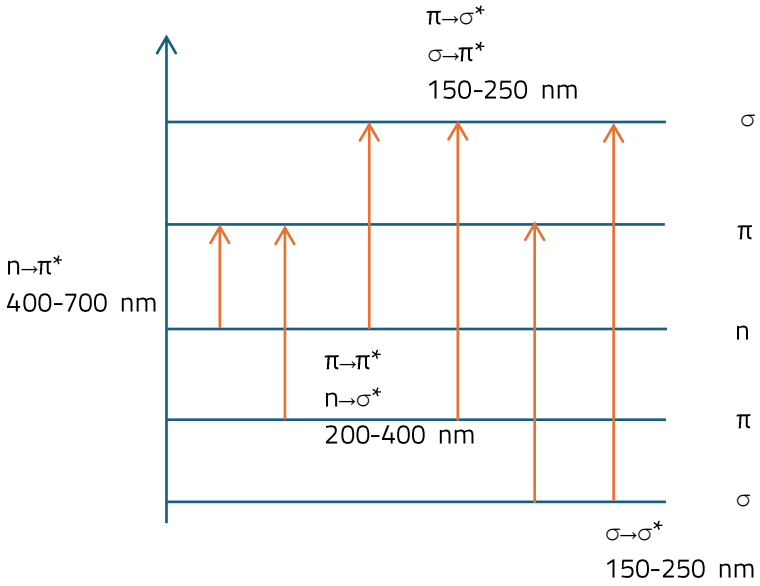


**Figure 6**: different kinds of molecular electronic transitions

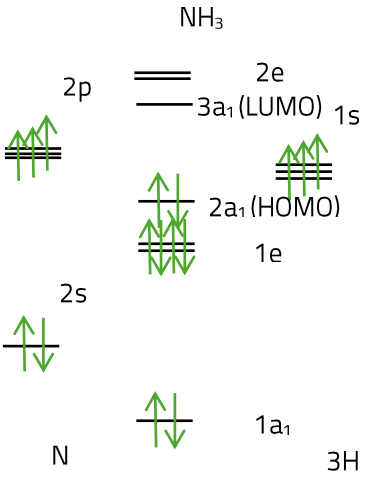


**Figure 7**: electronic structure of ammonia molecule

There are three principal processes for a photon: the absorption, the spontaneous emission, and the stimulated emission. In our approach, the absorption spectrum was recorded for our push-pull chromophores. As the energy levels are constructed by interaction of atomic orbitals and by time-independent Schrödinger equation, the filling situation of the electron is also important to determine the possible electronic transitions. The filling situation follows the Hund's rule in the atomic orbital in each atom. As the molecular orbitals are constructed by the interaction of atomic orbitals, the Hund's rule is expanded, and we can find the highest occupied molecular orbital (HOMO) and lowest unoccupied molecular orbital (LUMO) with or without the degeneracy. The HOMO-LUMO electronic transition is indeed the least energy-consuming electronic transition. An example is presented in figure 7 for the electronic structure of ammoniac molecule.

There are two modes for the UV-vis spectroscopy: transmission mode and reflection mode. In the transmission mode, the dye is often dissolved in a solvent in the quartz cuvette. The light source is from the halogen lamp for the visible region and deuterium lamp for UV region. The light source is not monochromatic, and a setup of light filter and monochromator is applied to get monochromatic light source. The incident light goes across the quartz cuvette and the detector receives the transmitted light. The Rayleigh diffusion occurs as the photon encounters photon-insensitive matter. Since a part of the light is absorbed, the diminution of the transmission will be converted to absorption. The mode of the reflection is often used when the sample is in the form of powder and self-assembled monolayer because the transmission is very small. The reflection mode can be either internal reflection or external reflection mode. For the UV-vis spectroscopy, the light source can be also a laser, which is highly monochromatic and coherent. A simplified presentation is given in the figure 8.

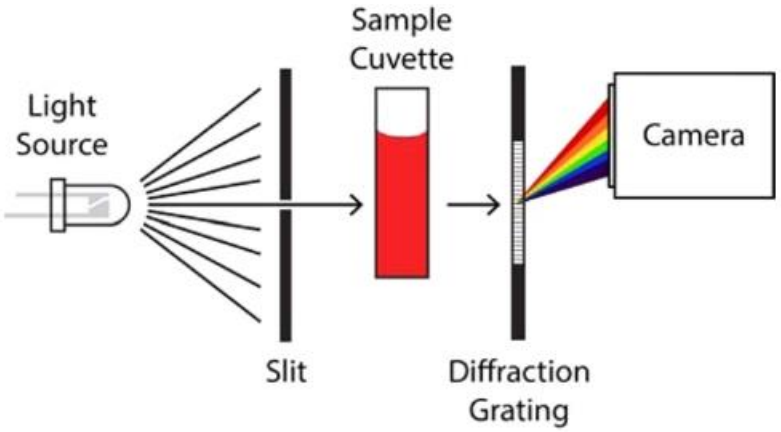


**Figure 8**: schema for the UV-visible spectrophotometer in transmission mode[165].

During the PhD, the UV-vis spectrophotometer is used to characterize the light absorption ability of the push-pull chromophore in the solution (the wavelength of the absorption maxima and the molar extinction coefficient). UV-visible absorption spectra were obtained on a Varian Cary 1E spectrophotometer. The Lamps are tungsten lamp, the wavelength range is from 330-900 nm.

# D. Attenuated Total Reflection-Fourier Transform Infrared spectroscopy (ATR-FTIR)

Infrared spectroscopy is used to probe the asymmetrical molecular vibration where the electrical dipole changes. In analytical chemistry, the infrared spectrum can help the scientists diagnosing the chemical functional group in the structure of the molecule. The vibrational characteristics of the chemical bond can be deduced. Taking the example of the vibration between two atoms, this process can be assimilated as two mass points linked by a spring. In this model, important parameters are the mass of the atoms, the distance of two atoms and the energy of the chemical bond. In classical mechanics, we have:

$$\nu = \frac{1}{2\pi}\sqrt{\frac{k}{\mu}} \quad \text{and} \quad \mu = \frac{m_A m_B}{m_A + m_B}$$

where $\nu$ is the vibration frequency, k is the spring constant for the chemical bond, $\mu$ is the effective mass and $m_A$ and $m_B$ for the masses of the two atoms.

The vibrational energy levels are discrete, and the principle of the infrared spectrum is based on the absorption of the infrared light, it is appropriate to take quantum aspect into consideration. Then we have according to the Schrödinger equation:

$$E_v = h\nu(n + 1/2)$$

where $\nu$ is the vibration frequency in the classical mechanics and n the discrete integer energy level.

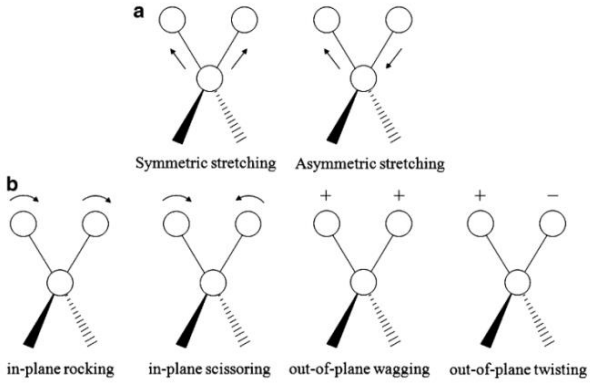


**Figure 9**: different kinds of molecular movements[166]

For a molecule, all the axial translations between atoms, angular translation among three atoms, torsion among four atoms etc form a set of discrete energy levels. Different molecular movements are summarized in the figure 9. Photons with the energy equals to the transition can be absorbed for each vibration mode.

To create a spectrum, two spectra must be done in succession. The first is the spectrum of the reference. The reference is often the air. The air contains

nitrogen gas, oxygen gas, carbon dioxide etc and they can make the perturbation of the spectrum of the product.

The second spectrum is the spectrum recorded for the sample. Fourier Transform will be used to obtain the final spectrum. The data recorded in the frequency domain will be divided in the time domain then recovered by inverse Fourier Transform using the reference spectrum of air. A FTIR spectrum is often recorded from 4000 $cm^{-1}$ to 400 $cm^{-1}$. In the analytical chemistry, the peak higher than 1400 $cm^{-1}$ are the characteristic to distinguish different functional groups. The peaks located lower than 1400 $cm^{-1}$ are difficult to interpret. Here are some examples:

| Chemical bond | Wavenumber ($cm^{-1}$) | Chemical bond | Wavenumber ($cm^{-1}$) |
|---|---|---|---|
| C=O | 1650-1750 | C=C | 1550-1650 |
| C-C alkyne | 2100-2300 | C-N nitrile | 2200-2400 |
| O-H carboxylic acid | 2500-3200 | C-H alkane | 2800-3000 |

In terms of the instrumentation, the ATR-FTIR is based on the interferometer which guides the laser into the ATR crystal on which the sample is placed. The light source is an infrared laser which has a thin sharp spectral distribution.

The interferometer (figure 10) used here is Michelson interferometer. It is constituted by two mirrors and a beamsplitter. IR radiation is passed from the source onto a beam splitter and separated into two beams. One is reflected by a stationary mirror while the other is reflected by a mirror moving with constant velocity. After recombination of the beams, they are brought into contact with the sample (by transmission in the depicted case) and then recorded by the detector. The beamsplitter is often cubic to ensure the same optical path. The beamsplitter is half-reflective or half-transmitted which means that it can let half the photons to pass through and the other half reflected. In the way, the light beam is divided into two different beams with almost same intensity. Two beams are reflected by two mirrors and encounter again at the beamsplitter. The two light beams will be collected for the sampling, i.e. the light beam which is transmitted for the first time and reflected at the second time, and the light beam which is reflected for the first time and transmitted for the second time. The name interferometer is called because the position of the two mirrors can be changed so that the two beams are in phase to cause constructive interference. This can be explained by the following equations in electromagnetism:

$$First\ beam: E_1 = E_0 e^{i(\vec{k}\cdot\vec{r}-\omega t)}$$
$$Second\ beam: E_2 = E_0 e^{i(\vec{k}\cdot\vec{r}-\omega t+\varphi)}$$
$$Together: E = E_0 e^{i(\vec{k}\cdot\vec{r}-\omega t)}(1+e^{i\varphi})$$
$$Constructive\ interference: if\ \varphi = 2n\pi\ (n\ integer)$$

The ATR crystal (figure 10) is used which is more appealing for the component near the surface due to the creation of the evanescent wave. The IR beam enters the crystal and is reflected at the crystal boundaries in contact with the sample. An evanescent wave penetrates the sample for a few mm and is attenuated by the IR radiation that is absorbed by the sample. After one or more reflections (in this case four) in the crystal the IR beam is guided back to the detector of the instrument. This can be explained by the following equations by assuming an incident electromagnetic wave totally reflected by y=0 plane.

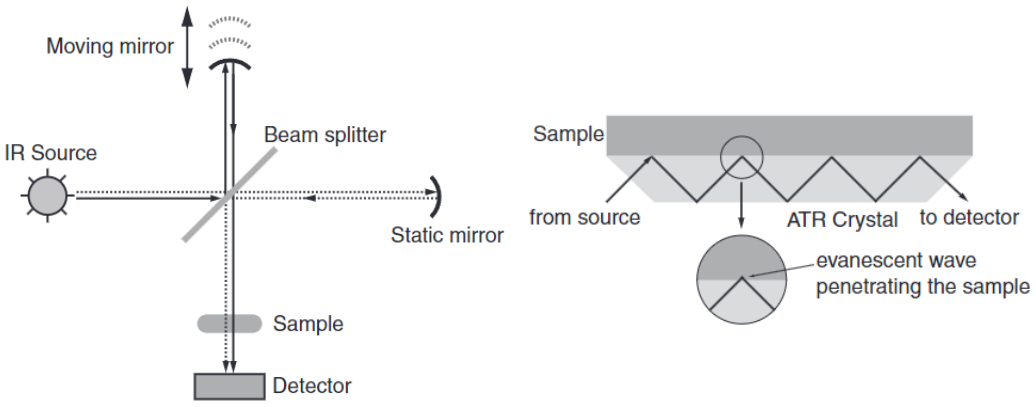


**Figure 10**: (left) Interferometer used in FTIR spectrometers. (right) Schematic representation of an ATR crystal with four reflections.[167]

The detector is a deuterated triglycine sulphate-based detector. The setup is an Agilent Cary 630 FTIR spectrometer. The spectra are recorded from 4000 $cm^{-1}$ to 600 $cm^{-1}$ with a resolution of 2 $cm^{-1}$ and 64 accumulations.

ATR-FTIR helps diagnosing the chemical functional group in the structure of the molecular self-assembled monolayer. The vibrational characteristics of the chemical bond can be deduced. Benefiting from the multiple reflections, the intensity to probe the thin monolayer can be ensured. Moreover, the ATR-FTIR can be used to determine the orientation of the molecule in the self-assembled monolayer. The electromagnetic wave is evanescent at the interface between the sample and the ATR crystal. It means that the intensity of the infrared light decreases exponentially perpendicular to the surface. The chemical bonds near the ATR crystal surface absorb more and a more intensive signal for the absorption can be seen in the spectrum.

For the self-assembled monolayers, the substrates used were prepared by Joule evaporation of ~100 nm of gold on top of an GaAs wafer surface preliminary coated by a few nanometer thick Cr layer. The ATR-FTIR spectrum is recorded with Brucker Invenio in the range from 4000 $cm^{-1}$ to 600 $cm^{-1}$ with a mercury cadmium telluride detector and the ATR crystal is made by diamond. The number of accumulations is 32 and the resolution of the spectrum is 4 $cm^{-1}$.

The signal can be enhanced thanks to the multiple total reflection if the optical path is carefully designed. Another advancement could be the use of liquid nitrogen to cool the detector in the instrument. This is used to decrease the homogenous linewidth which is the linewidth caused by a single photon transition due to the Heisenberg uncertainty principle and increases enormously with temperature. This is advantageous to probe electronic more precisely. In the spectroscopy, there are electronic structures in three scales: electronic, vibrational and rotational electronic structures. When liquid nitrogen cooled the detector, the spectrum in the ATR-FTIR can reveal the rotational electronic structure. For this purpose, mercury cadmium telluride (MCT) detector is used instead of deuterated triglycine sulphate-based photodetector.

In our case, we used a Bruker Invenio with a MCT detector and a diamond ATR crystal. We performed 32 scans with a resolution of 4 $cm^{-1}$. The SAMs were prepared on a gold coated glass or GaAs samples after the cut by a diamond pen.

# E. Surface-enhanced Raman spectroscopy (SERS)

As a vibrational spectroscopy method, Raman spectroscopy is a method to probe the symmetrical molecular vibration during which the polarizability changes. The Raman spectroscopy is often a complementary method for the infrared spectroscopy because all the vibration modes are only infrared active, only Raman active or both Raman and infrared active.

The origin of the Raman spectroscopy is the diffusion of the photons. When a photon comes, it can be scattered (transmitted or reflected) or absorbed or emitted. If the incident photon has the energy much larger than vibrational energy states, then the scattering phenomenon is more significant. For the part of the scattering, there are two cases in terms of the energy change of the photon: Raileigh scattering where no energy change or Raman scattering where the energy changes. In the spectroscopy, the scattering is a process with two photons. For a phonon (the quantization of the molecular vibration) at a known vibrational state, when a photon arrives for the scattering, this phonon will be excited to a virtual energy level, then returns to the initial energy level. This process is described for the Raileigh scattering and Raman scattering if the phonon returns to a higher excited energy state (figure 11). Compared to the intensity of the Raileigh scattering, the intensity of Raman scattering is around one thousand time smaller. The intensity of Raileigh scattering, and Raman scattering depend on the frequency of the incident laser beam. The portion of Raileigh scattering is higher if the incident laser beam has a higher energy. For the Raman scattering, there are Stocks peaks and anti-Stocks peak. The Stokes peaks are caused by the scattered photons who lose energy. The incident photon gave the molecule the energy equal to the transition from the fundamental vibrational energy state to the first excited vibrational energy state. The anti-Stokes peaks are caused by the scattered photons who gain energy. The incident photon acquires the energy from the excited molecules equal to the

transition from the first excited vibrational energy state to the fundamental vibrational energy state.

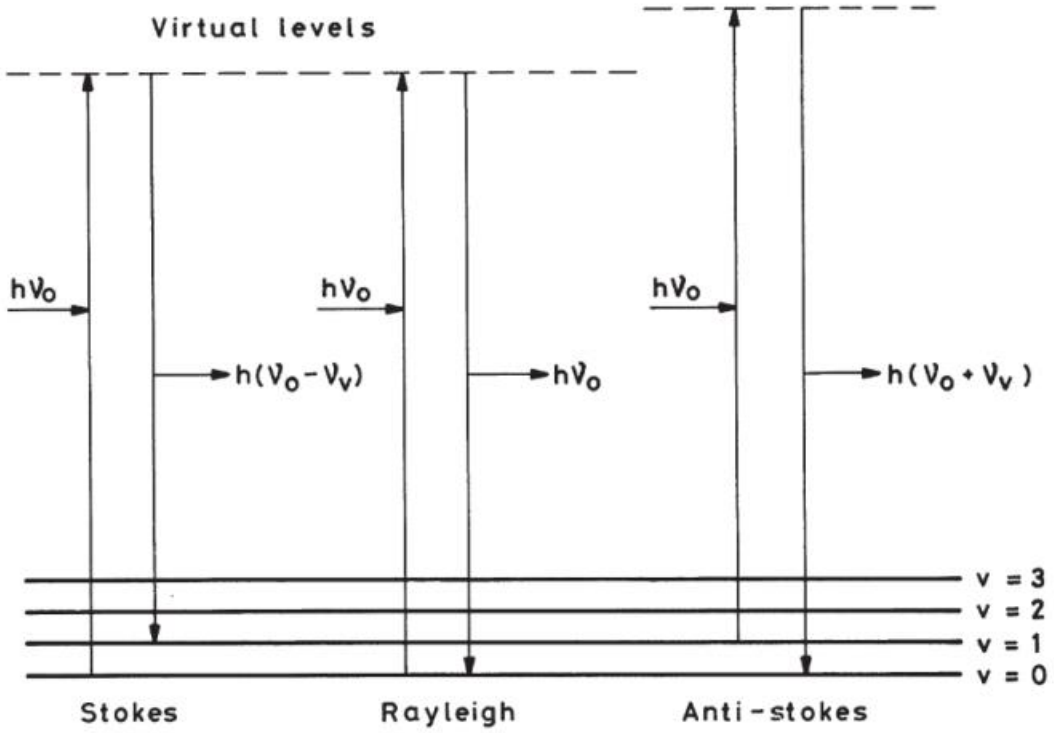


**Figure 11**: Idealised model of Rayleigh scattering and Stokes and anti-Stokes Raman scattering[168]

For the detection of the molecule where the quantity of the matter and/or the concentration is so small, such as the self-assembled monolayer, the ordinary Raman spectroscopy doesn't give a strong signal, a new method called Surface-enhanced Raman spectroscopy (SERS) can solve this problem thanks to the LSPR effect (localized surface plasmon resonance) of the noble metal based nanoparticles or the nanostructured substrate under the stimulation such as incident laser. The LSPR phenomenon is created in the following way (figure 12): the noble metal based nanoparticle, or the substrate is a dielectric material (neutral without stimulation). Under a static electrical field at one side, mobile electrons in the material will accumulate in the anti-parallel part of the nanoparticle referenced by the direction of the static electrical field. In this case, an electrical dipole is formed inside. The photon is the quantization of an electromagnetic wave which oscillates in the space with the time. Since the noble metals are very gold electrical conductor, electrons inside will also oscillate with the electromagnetic wave. However, the size of the nanoparticles must be higher than 15nm to ensure the good LSPR effect. The electron conductivity inside the nanoparticles will be lower and the dielectric constant of the nanoparticle will change. Also, the electronic structure of the gold will be discrete due to the confinement and the LSPR effect disappears.

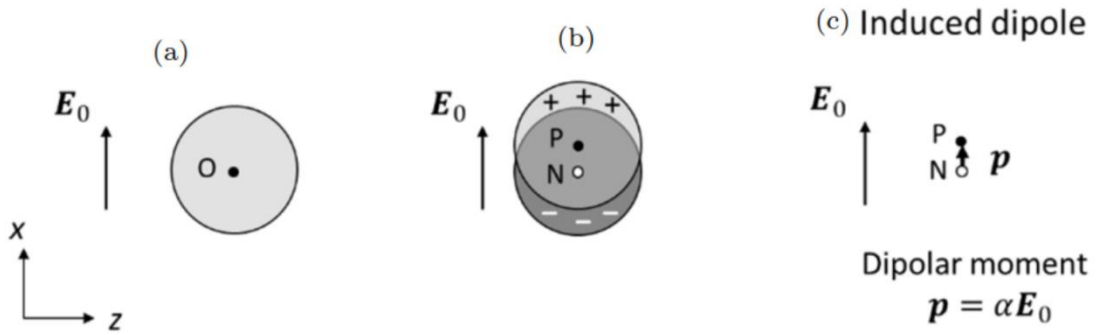


**Figure 12**: the internal dipole formation of the gold nanoparticles under the external electrical field: a) the electron distribution just before the effect of electrical field; b) the electron distribution just after the effect of electrical field; c) the modelling of the induced electrical dipole[169]

The interesting point of the LSPR effect for the SERS is that under the stimulation, a strong evanescent local electrostatic field is created to increase the sensibility. For the nanostructured substrate, the phenomenon of SPP (surface plasmon polariton) appears also for the enhancement of the electrical field. Normally the molecule is adsorbed on the surface of the nanoparticles after the spin-coating.

For all the results, the experiment is taken in the external reflection mode. The SERS is used to see whether the push-pull chromophore is adsorbed on the surface after the enhancing of the signal on the surface. A special nanostructured gold substrate with LSPR effect was used to prepare the sample for SERS spectra. The SERS active surfaces were obtained by thermal evaporation, under ultrahigh vacuum conditions ($2 \cdot 10^{-6}$ mbar) as a gold thin film with thickness around 7 nm on a glass substrate[59]. Those nanostructured substrates are made of gold island films and have a low electrical conductivity. High resolution Raman spectra were recorded on a Horiba Jobin-Yvon HR800 LabRam, using a power of 0.005 mW with an acquisition time of 5 s, and with the wavelength of helium-neon laser $\lambda$= 632 nm.

# F. X-ray photoelectron spectroscopy (XPS)

X-ray photoelectron spectroscopy is a spectroscopy method based on the photo-electric effect where an electron is ejected from the sample after the absorption of the photon. It is widely used for the analysis of the superficial layers with a thickness about 5 nm for the solid. X-ray photoelectron spectroscopy can probe the valence electrons for the electronic structure of the molecule, and it can also probe the core electrons for the chemical composition of the material. The source for the X-ray photoelectron spectroscopy is either monochromatic UV light (below 10 eV and in this case also called UPS for the abbreviation of ultraviolet photoelectron spectroscopy) or monochromatic X-ray light (100-1000 eV). The analysis of the X-ray photoelectron spectroscopy is based on the kinetic energy value of the ejected electron after the photoelectric effect. The invention of X-ray photoelectron spectroscopy has been awarded by Nobel Prize in 1981.

The photoelectric effect was first observed by Hertz experiment in 1887 to prove the propagation of electromagnetic wave and theorized by Einstein in 1905. This phenomenon was awarded by Nobel prize in 1921. The whole process can be summarized in the following equation:

$$E_k = h\nu + \Phi + E_b$$

In this equation, the $E_k$ is the kinetic energy of the ejected electron after the photoelectric effect, $h\nu$ is the energy of the incident photon, $\Phi$ is the work function to represent the necessary energy to remove one electron from the sample and the $E_b$ is the binding energy which represents the energy gap from the core electron to the work function. For the analysis for the chemical composition, the data of the kinetic energy will be transformed to the data of binding energy with the respect to the equation above. Finally, the data will compare with the table for the core electron energy levels which is shown above for example.

Since each element has its distinct peak in the XPS (figure 16), this method is used to determine the chemical composition of the material or to follow the chemical reaction on the surface and the adsorption process on the surface. Also, there is a phenomenon of the chemical shift in the XPS peak, which is the basic to distinguish the element with different oxidation state or the same element in the different functional group. Also, sometimes two peaks can be seen rather than a simple signal. This is due to the spin-orbit coupling effect in which the orbital momentum of the electron strongly interacts with its spin momentum. This gives two peaks:

$$\vec{j} = \vec{l} + \vec{s}$$

For example, the spin-orbit coupling will cause two peaks for 4f gold electrons and there are $4f_{7/2}$ and $4f_{5/2}$ two peaks.

In fact, there is a special problem for the self-assembled monolayer on the surface: the XPS signal from the substrate. In fact, even if the XPS is a method for surface science, its range is larger than the thickness of the self-assembled monolayer. Thus, a non-negligible part of the XPS signal from the substrate can be seen. To reduce the content of the substrate and increase the content of the self-assembled monolayer, grazing incidence X-ray photoelectron spectroscopy (GIXPS) can be adopted since the incident photons can more diffuse in the layer of self-assembled monolayer. The substrates used were prepared by Joule evaporation of ~100 nm of gold on top of an GaAs wafer surface preliminary coated by a few nanometer thick Cr layer.

For the push-pull SAM analyses, X-ray photoelectron spectroscopy (XPS) measurements were performed in a SPECS ProvenXPS system equipped with a PHOIBOS 150 2D-CMOS hemispherical analyser and a monochromated X-ray source FOCUS 500. The Al Kα X-ray source (1486.6 eV) running at 400 W is separated from the analyser by an angle of 55°. A medium magnification mode and constant pass energy of the analyser equal to 20 eV were used for analysis. Photoelectron data were recorded at a take-off angle of 90° (normal detection). The survey spectrum and the high-resolution spectra were recorded with an energy step of 0.5 eV over 1400 eV and 0.1 eV, respectively. A flood gun was used for surface charge compensation. The electron binding energies ($E_b$) were calibrated to maximum of the valence band. Binding energies, line widths and areas of the different XPS peaks were obtained by a weighted least-squares fitting of a Gaussian model curve to the experimental data using the Origin.

Ferrocene-derivative-based SAMs were characterized using an Omicron brand EA 125 model with a DAR 400 X source. The following utilizes the Mg Kα anode (E = 1253.6 eV) and a hemispheric analyser working at constant energy of 20 eV for the acquisition of high-resolution spectra. A high-resolution measurement was made and after the acquisition, the exploitation of the experimental data was carried out by the XPSPEAK41 software and Origin.

# G. Cyclic Voltammetry

The cyclic voltammetry is the object for the experimental determination for the relationship between the current and the potential of the electrode and this relationship will be represented by the cyclic voltammetry plot. The knowledge of the fundamental characteristics of an electrochemical reaction is done by the measurement of the variation of the current in the function of applied potential in the electrochemistry cell. To apply the potential on the electrode and to produce electrochemical reaction, the experiment must be done in an electrochemical cell where three electrodes are connected to potentiostat. These three electrodes are the reference electrode, the working electrode, and the counter electrode (figure 13). During the thesis, the electrodes functionalized by molecules are working electrodes. Sometimes, the thermometer is applied to control the temperature and inert gas are introduced to purge undesired electroactive gas in the solution.

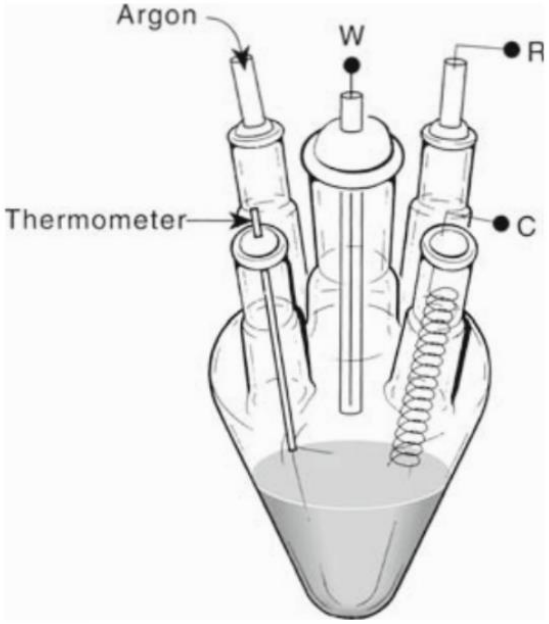


**Figure 13**: Cell for cyclic voltametric experiments with three-electrode configuration[170]

From practical point of view, the cyclic voltammetry (scanning for a round trip of the potential: in the anodic direction followed by the inversion or vice versa) is characterized using immobile solution and fixed indicative electrodes (no convection, not hydrodynamic condition). So, these methods have great interesting point to elucidate the charge transfer mechanism and the reaction mechanism. The form of the excitation signal in the cyclic voltammetry is in general an isosceles triangle and in this case the response of the signal (I=f(E) plot) is represented as a peak in the cyclic voltammetry graph (figure 14).

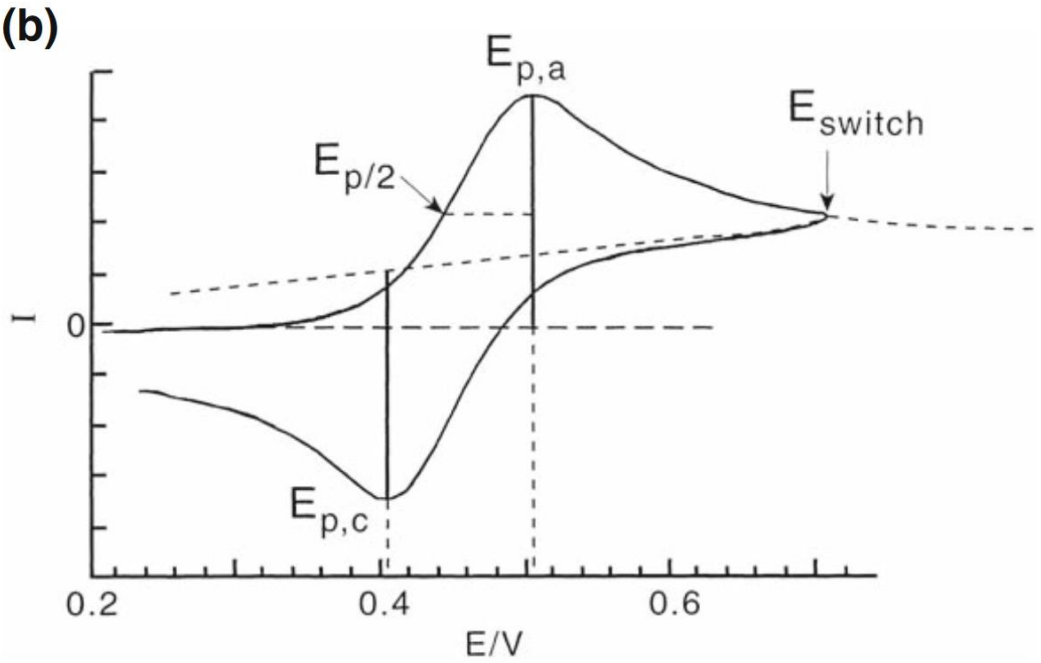


**Figure 14**: A typical cyclic voltammetry curve $E_{p,a}$ and $I_{p,a}$ for oxidation potential and anodic current, $E_{p,c}$ and $I_{p,c}$ for reduction potential and cathodic current and $E_{p/2}$ for midpoint potential[170]

During the initial course of a cyclic voltametric experiment, the diffusion layer also moves into the solution phase. The liquid phase in an electrochemical experiment typically consists of a solvent containing the dissolved material to be studied and a supporting electrolyte salt to achieve the required conductivity and hence minimize the potential drop. With sufficient supporting electrolyte, the electrical double layer at the working electrode occupies about 1 nm from the electrode surface (Figure 15). This layer has been shown to consist of a compact or 'inner Helmholtz' layer and the diffuse (not diffusion layer) or 'Gouy–Chapman' layer. The extent to which the diffuse layer extends into the solution phase depends on the concentration of the electrolyte and the double layer may in some cases affect the kinetics of electrochemical processes. Thus, experiments with low concentrations or no added supporting electrolyte can be desirable but, since the double layer becomes more diffuse, they require careful data analysis and the error during the experiment is an obstacle[171].

Under most experimental conditions, the size of the diffusion layer (see above) is several orders of magnitude larger than that of the diffuse layer. Initiated by a change in the electrode potential, a perturbation of concentration begins from the electrode surface into the solution phase and a time is required for diffusion layer to be established. With a very slow scan rate cyclic voltammetry, an upper limit of the scan rate where standard theory prevails is given by the condition that the diffusion layer becomes comparable in size to the diffuse layer. In the other extreme, at very high scan rates, natural convection is known to affect the shape of experimental cyclic voltammograms. The higher the scanning rate, the fewer electroactive compounds can shock the electrode for the electrochemical reactions.

In principle, the scanning speed of the potential, the scanning speed is from 1mV/s to thousands of mV/s.

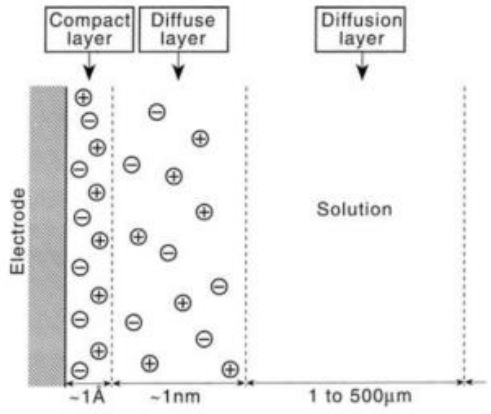


**Figure 15**: schematic representation of the composition of the solution phase in the vicinity of the electrode surface (not to scale)[170].

The principle of the cyclic voltammetry is based on the fact a return scanning will be made as soon as the go scanning is finished. For each redox couple, the electrochemical reaction can be written as Ox + n $e^-$ → Red. There are two aspects for each redox couple. The first is the thermodynamical aspects and each redox couple is attributed to a normal standard potential to show the potential where two species at both sides have same amount. The other aspect is the kinetic aspect and in the pure diffusion regime, each redox couple can be considered as rapid (reversible) system, quasi-rapid (quasi-reversible) system or slow (irreversible) system. During PhD, the only studied system is the reversible system.

An electrochemically reversible system has following characteristics:

-The anodic and the cathodic pics are separated by 58/n mV at 25 °C and they are same in the absolute value if there are no absorption phenomenon and no redox reactions. 58/n mV can be shown according to the Nerst equation for a redox reaction (Ox for oxidizing agent, n for the number of the electrons involved in the electrochemical reaction, E for the potential, R for the ideal gas constant, T for the temperature, F for the Faraday constant and Red for reducing agent):

$$Ox + ne^- = Red$$

$$E = E^0_{Ox/red} + \frac{RT}{nF} ln10 log \frac{[Red]}{[Ox]} = E^0_{Ox/red} + \frac{58\,mV}{n} log \frac{[Red]}{[Ox]}$$

-The intensity of the peak is proportional to the square root of scanning speed (Randles-Sevcik law):

$$i_p = (2.69 * 10^5) n^{3/2} S D^{1/2} C \nu^{1/2}$$

where the current in Ampere, S (area of the electrode) in $cm^2$, D (diffusion coefficient) in $cm^2/s$, C (concentration) in $mol/m^3$ and $\nu$(scanning rate) in V/s.

-The position of the peaks is independent to the scanning speed and the normal standard potential value can be determined by the following relation:

$$\mathrm{E°} = (\mathrm{E_{pa}} + \mathrm{E_{pc}})/2$$

During the PhD, the cyclic voltammetry is used to measure the redox potential of a solution of 3-ferrocenoylpropionic acid. A 0.1 M $nBu_4NPF_6$ in anhydrous acetonitrile solution was prepared as the electrolyte solution and degassed by $N_2$. The electrode potential was controlled by a potentiostat (Princeton Instrument). Ag/AgCl was used as the reference electrodes and the rond metallic rotating disk for working electrode. Pt wire was used as the counter electrode. For Dropsens, a cable system is used to connect the working electrode, the reference electrode and the counter electrode simultaneously and the area is about 0.14 $cm^2$.

In the PhD work, the molecule is strongly adsorbed by chemical bonds to the surface of the substrate to form the self-assembled monolayer and the theory above doesn't cover this situation even for the reversible systems. Reversible cyclic voltammograms are not always governed by diffusion-controlled processes. For example, the cases of a redox reagent adsorbed onto an electrode surface or confined to a thin layer of solution adjacent to the electrode surface are also of considerable importance. For redox processes for adsorbed molecules at the electrode surface, the peak current becomes linear with respect to the scan rate:

$$I_p = \frac{n^2 F^2}{4RT} \nu A \Gamma_0$$

where the $I_p$ for the peak value in the cyclic voltagram, n the number of the electrons involved in the redox process, F the Faraday constant, R the molar gas constant, T the temperature, $\nu$ the scanning rate, A the surface aera and the $\Gamma_0$ for the surface coverage.

The full width at half maximum (FWHM) of the voltametric peak (for the adsorption) can be determined as $\Delta E_{hh}$ =3.53 RT / (nF) = 90.6mV for a one-electron process at 25°C[332]. For the case of strongly adsorbed systems, any deviation from individual redox centres on the electrode surface manifests itself as a change of $\Delta E_{hh}$. Of course, departure from reversibility also leads to changes in wave shape as a function of scan rate, as same as the situation in the redox process in the solution[333].

Here are the experimental details: a 0.1 M $nBu_4NPF_6$ in anhydrous acetonitrile solution was prepared as the electrolyte solution and degassed by $N_2$. The electrode potential was controlled by a potentiostat (Princeton Instrument). Ag/AgCl was used as the reference electrodes and the surface functionalization on gold for working electrode. Pt wire was used as the counter electrode. For the substrates we used QCM gold plates on quartz purchased from OpenQCM, and Dropsens 220AT. The geometric area of the working electrode was about 0.25 $cm^2$. For Dropsens, a cable system is used to connect the working electrode, the reference electrode and the counter electrode simultaneously and the area is about 0.14 $cm^2$.

# H. Contact angle measurement

The interface phenomenon is common in daily life. The molecules inside a condensed phase are more stable than those on the interface. In fact, if we take the case of liquid-vapor interface (also for other kinds of interface), the molecules inside the solution are totally solvated whereas partially solvated at liquid-vapor interface. The molecules which are partially solvated are less stable in terms of the energy than the molecules inside a solution. A repelling force is preventing all the increase of the surface of a system to stabilize the system in minimizing the interfacial surface. The repelling force is thus interfacial tension. The figure 16 collected some interfacial tension values of the liquid drop and the figure 17 collected some water contact angle value on various self-assembled monolayers. When a new surface is formed, the process will occur in two steps: the formation of a new surface and the rearrangement of atoms at the surface to attain the new equilibrium position. These two processes cannot be separated for a liquid surface because of the high mobility of the molecule in the liquid which permits to attain quasi-instantly new equilibrium position. This high mobility doesn't exist in a solid and the relaxation can be long or even no relaxation. Consequently, the formation of the surface is associated with an energy which is different to the surface energy.

| Substance | $\gamma$ at 20°C (mJ $m^{-2}$) |
|---|---|
| *n*-Hexane | 18.4 |
| Ethyl ether | 17.0 |
| *n*-Octane | 21.8 |
| Carbon tetrachloride | 26.9 |
| *m*-Xylene | 28.9 |
| Toluene | 28.5 |
| Benzene | 29.0 |
| Chloroform | 28.5 |
| 1,2-Dichloroethane | 32.2 |
| Carbon disulfide | 32.3 |
| Water | 72.8 |
| Mercury | 484 |

**Figure 16**: Examples of values of interfacial tensions of several kinds of liquids[172].

This PhD work has a big part on the adsorption of the solute in the solution. There are two species in the solution, the solute, and the solvent. The notion of superficial excess of a specie i is defined as $\Gamma_i = -n_i/A$ in mol/cm$^2$. It represents the matter quantity of i on the surface in excess compared to the i in the solution. On the surface, the ratio $n_2/n_1$ (number of moles of the solute and the number of moles of the solvent) is different from the value $n_{20}/n_{10}$ which is the ratio of the number of moles of the solute and the number of moles of the solvent in the solution. If $n_2/n_1 > n_{20}/n_{10}$, the adsorption $\Gamma$ is positive (accumulation of solute on the surface in the liquid phase).

| RSH | $\theta_a$ [a,b] $H_2O$ | HD | RSH | $\theta_a$ [a,b] $H_2O$ | HD |
|---|---|---|---|---|---|
| $HS(CH_2)_2(CF_2)_5CF_3$ | 118 | 71 | $HS(CH_2)_{11}OCH_3$ | 74 | 35 |
| $HS(CH_2)_{21}CH_3$ | 112 | 47 | $HS(CH_2)_{12}SCOCH_3$ | 70 | 0 |
| $HS(CH_2)_{17}CH{=}CH_2$ | 107 | 39 | $HS(CH_2)_{10}CO_2CH_3$ | 67 | 28 |
| $HS(CH_2)_{11}OSi(CH_3)_2$-$(C(CH_3)_3)$ | 104 | 30 | $HS(CH_2)_8CN$ | 64 | 0 |
| | | | $HS(CH_2)_{11}OH$ | 0 | 0 |
| $HS(CH_2)_{11}Br$ | 83 | 0 | $HS(CH_2)_{15}CO_2H$ | 0 | 0 |
| $HS(CH_2)_{11}Cl$ | 83 | 0 | | | |

[a] Measured by method A. [b] "0" is used to represent drops with irregular drop shapes and contact angles <10°

**Figure 17**: Examples of advancing contact angle values of water and hexadecane on various self-assembled monolayers[77].

The surface tension of the liquid is an interesting parameter to study the property of the liquid on the solid surface. Another important parameter to study the solid/liquid interface is the contact angle which gives the information about the wetting property of the liquid on the solid (figure 18). This information is particularly interesting for automobile, cosmetics, and energy industry.

The contact angle can be deduced by the Young equation:

$$\gamma_{SG} = \gamma_{SL} + \gamma_{LG}\cos\theta$$

$$\cos\theta = \frac{\gamma_{SG} - \gamma_{SL}}{\gamma_{LG}}$$

The liquids are divided into several categories according to the value of the contact angle $\theta$ :

-If $\theta = 0$, the surface is extremely hydrophilic.

-If $0 < \theta < 90°$, the surface is hydrophilic.

-If $\theta > 90°$, the surface is hydrophobic.

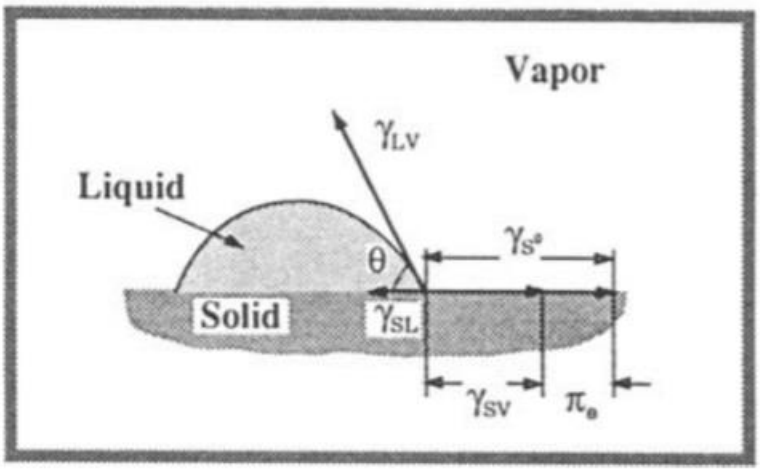


**Figure 18**: Components of interfacial tension needed to derive Young's equation[172].

The Cassie's law (figure 19) is used to determine the surface fraction of different kinds of components on the surface for a binary self-assembled monolayer using the water contact value of pure self-assembled monolayer ($x_1+x_2=1$):

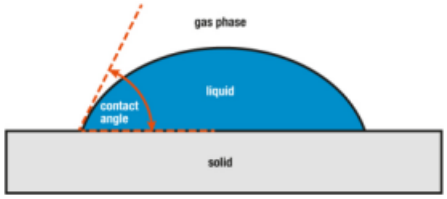


$$\cos\theta = x_1 \cos\theta_1 + x_2 \cos\theta_2$$

Cassie's law

**Figure 19**: the principle of the Cassie's law

The water contact angle values are measured to verify if the surface functionalization works. It can also be used to determine the terminal group of the molecule on the surface. The molar fraction on the surface for different components can be deduced using the Cassie's law. All the contact angle measurements were done using Krüss DSA 10 Mk2 Drop Shape Analysis System with circle fitting method. The substrates used were prepared by Joule evaporation of ~100 nm of gold on top of an GaAs wafer surface preliminary coated by a few nanometer thick Cr layer.

# I. Scanning probe microscopy (SPM)

Scanning probe microscopy is a versatile instrument in the domain of surface science, nanoscience, nanotechnology and biology (Figure 20). With different scanning probe, microscopy can determine in a two dimensional image the three dimensional information of topography, morphology etc. Also, with appropriate preparation, spectroscopy can also be made at the nanoscale, which is the key tools to probe localized properties. The original idea to use the scanning probe microscopy is to see the atomic and molecular structure which can't be seen directly by optical instrument due to the diffraction limit of visible light. Unlike the electronic microscope which uses the matter wave of electron to replace the visible light, scanning probe microscopy uses the probe to see the structure in a different way rather than optical way. The piezoelectric controller allows the tip to scan the sample line by line in the (x,y) plane to give the surface structure information in the form of z=f(x,y). A value called setpoint is fixed to maintain the sufficient distance between the tip and the substrate without collision. The interaction signal is recorded and compared to the fixed setpoint. If the values are different, the feedback loop will operate on the tip-sample distance to bring the measured signal value to the setpoint. In fact, the information of the image of the scanning probe microscope is the convolution product of the information of the nanostructure and the probe.

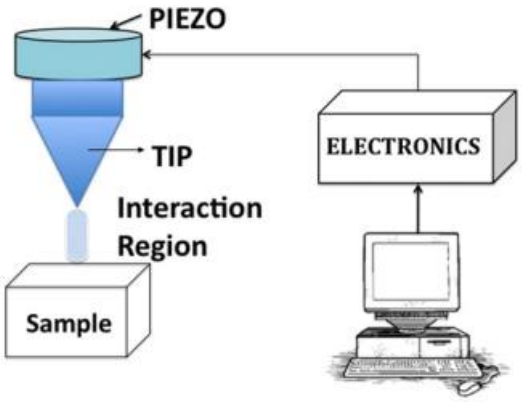


**Figure 20**: the simplified structure of the scanning probe microscopy[173]

# I. Scanning tunneling microscopy (STM)

Scanning tunnelling microscopy (STM) uses the current of tunnelling effect to probe the topography of the surface (figure 21). The substrate must be as flat as possible to have a good quality of the image. Au(111)/mica substrates purchased from Phasis (Swiss) were used. The principle of the tunnelling effect is that the air is the barrier for an electron because it is insulating. If an electron possesses the particle property, this electron cannot pass. However, an electron also possesses the wave property which helps the electron to pass. According to atom theory, if the probability of the existence of the electron is not zero behind the barrier, the electron can go through. The tunnelling current after the tunnelling decreases exponentially if the distance of the barrier increases (figure 21).

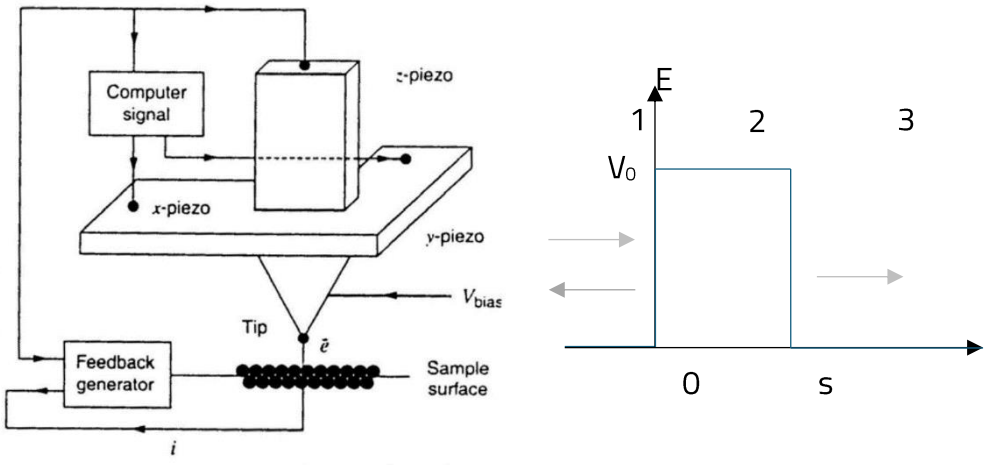


**Figure 21**: (Left) Schema of scanning tunnelling microscope (Right) Modelling of 1D tunnelling effect situation[174].

According to the time-independent Schrödinger equation, we have (figure 21):

$$-\frac{\hbar^2}{2m}\frac{d^2\Psi}{dx^2} + (V_0 - E)\Psi = 0 \ (V_0 > E \text{ in region 2 otherwise } V_0 = 0)$$

If we have a unit amplitude plane wave travelling to the right, we have in different regions (region 1 for incident and reflected wave due to wave particle duality, region 2 for tunnelling barrier and region 3 for transmitted wave):

$$\Psi_1 = e^{ikx} + Re^{-ikx} \ \left(k^2 = \frac{2mE}{\hbar^2}\right)$$

$$\Psi_2 = Ae^{Kx} + Be^{-Kx} \ \left(K^2 = \frac{2m(V_0 - E)}{\hbar^2}\right)$$

$$\Psi_3 = Te^{ikx} \ \left(k^2 = \frac{2mE}{\hbar^2}\right)$$

In the equations above, the term with R is the reflected wavefunction, the term with T is the transmitted wavefunction, then we have the transmission probability $|T^2|$ and the tunnelling current density j:

$$|T^2| = \frac{4\mathrm{k}^2\mathrm{K}^2}{4\mathrm{k}^2\mathrm{K}^2 + (\mathrm{k}^2 + \mathrm{K}^2)^2 \sinh^2(\mathrm{Ks})} \approx \frac{16\mathrm{k}^2\mathrm{K}^2}{(\mathrm{k}^2 + \mathrm{K}^2)^2} \exp(-2\mathrm{Ks})$$

$$j = \frac{-\mathrm{i}\hbar}{2\mathrm{m}}\left(\Psi^* \frac{\partial \Psi}{\partial \mathrm{x}} - \Psi \frac{\partial \Psi^*}{\partial x}\right) = \frac{k\hbar}{m}|\mathrm{T}^2|$$

The STM has a lateral molecular resolution because the real tip in the STM is only several atoms at the edge even the true shape of the tip can be much larger. The tip preparation method is the chemical etching or the mechanical cutting of the metal wire. The quality of the edge is important for the quality of the image and the tip shape can be considered as a triangle (figure 22). Since the molecule has comparable dimension as the radius of the tip, convolution can have a great effect on the shape of the image for the molecular adsorption on the surface.

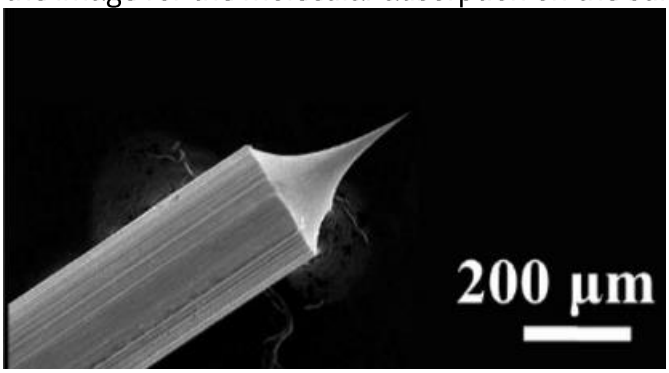


**Figure 22**: the shape of scanning tunnelling microscope tip after the preparation using chemical etching[175]

The scanning tunnelling microscope is used to check whether the molecule is adsorbed on the surface and the scanning tunnelling spectroscopy is adopted to determine the electrical properties at nanoscale. STM measurements were performed at ambient conditions using a Bruker Multimode 8 equipped with a Nanoscope V electronics. For STM experiments voltage was applied to the substrate with respect to the grounded Pt/Ir cut tips. The tip is made from Pt/Ir alloy wire cut by hands. The images were recorded in constant current mode, with voltage within 1V and current between 1 and 10 pA. Without special notice, the integral gain is 0.2 and the proportional gain is 0.2 for STM.

## II. Atomic force microscopy (AFM)

Atomic force microscopy (AFM) is based on the interaction between two atoms. The most common way to describe this interaction is the Lennard-Jones potential. This potential is comprised by two parts: the repulsive part whose potential is proportional to the $1/r^{12}$ and the attractive part whose potential is proportional to the $1/r^6$. The origin of the repulsion is the nucleus-nucleus interaction and electron-electron interaction, and the origin of the attraction is the interaction of nucleus and electron. This potential goes to plus infinity if the distance between two atoms goes to zero and it has a minimal value at the equilibrium position of two atoms and the potential returns to zero if the distance between two atoms is plus infinity. When the repulsive force takes the main role, the AFM is in the contact mode. The intermittent contact mode or tapping mode is in between where the attractive force and the repulsive force both play a role. The tapping mode is also called amplitude modulation AFM because the tip and the cantilever will vibrate by an electrical force with a certain amplitude. This is a mode of AFM in intermittent mode. The topography will be probed based on the diminution of the forced vibration amplitude of the cantilever. Compared to the scanning tunnelling microscope, the atomic force microscope can work for the samples which are not conductive. The shape of the AFM tip is often a gaussian shape. A scheme describing AFM is presented in figure 23.

To further understand the motion of the tip, several authors have considered the cantilever-tip ensemble as a point-mass spring, then the tip motion could be approximately described by a non-linear, second-order differential equation:

$$\mathrm{m}\ddot{z} + kz + \frac{m\omega_0}{Q}\dot{z} = F_{ts} + F_0 cos(\omega t)$$

where $F_0$ and $\omega$ and the amplitude and the frequency of the driving force, respectively. Q, $\omega_0$ and k are the quality factor, the angular resonance frequency and force constant of the free cantilever, respectively. $F_{ts}$ includes the tip-surface interaction force.

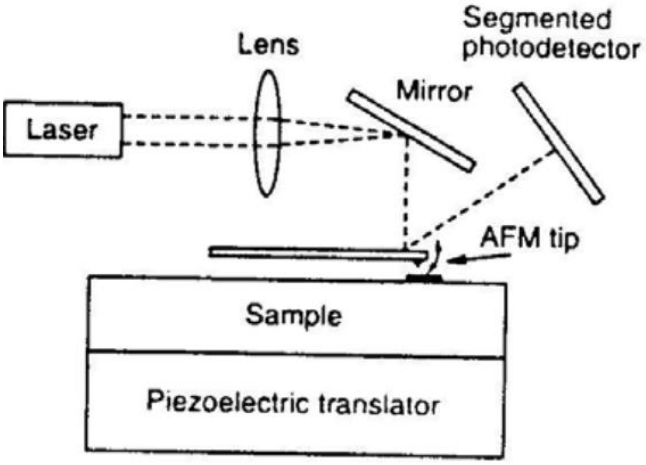


**Figure 23**: the schema of atomic force microscope[174].

As we can see from the equation, the equation is a damped harmonic oscillator without the tip-surface interaction. The composition of the $F_{ts}$ is very sophisticated and for now, it is believed that the dominant forces are Van der Waals interactions, short range repulsive interactions and adhesion and capillary forces. For the Van der Waals interactions, there are several models.

The harmonic oscillator approximation helps us to understand the functioning of the tapping mode AFM. If the tip is excited at the natural frequency, the approaching of the tip towards the surface will modify the resonance frequency which in turns implies a modification of the oscillation amplitude. If the attractive force is dominant, the resonance frequency will shift towards a smaller value and towards a bigger value for the resonance frequency when the repulsive force is dominant. Moreover, the new oscillation amplitude will be smaller than the amplitude in free oscillation in most cases. An example is presented in figure 24.

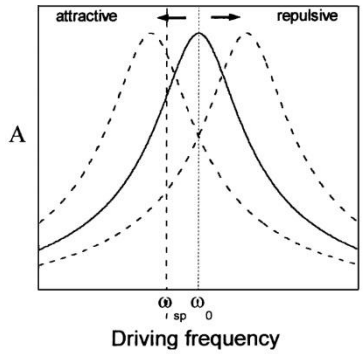


**Figure 24**: Resonance for a single harmonic oscillator (solid line) and under the influence of attractive and repulsive forces (dashed line)[176].

The atomic force microscope is used to check whether the molecules are adsorbed on the surface. AFM measurements were performed at ambient conditions using a Bruker Multimode 8 equipped with a Nanoscope V electronics. AFM was operated in Tapping mode (300 mV target amplitude, 200 mV amplitude setpoint) with AppNano 0.6-3.7 N/m force constant silicon tips whose resonant frequency is from 43 kHz to 81 kHz. The integral gain is 1 and the proportional gain is 5 for AFM. Au(111)/mica substrates purchased from Phasis (Swiss) were used.

## III. Electrostatic force microscopy (EFM)

Electrostatic force microscopy (EFM) is a type of dynamic non-contact atomic force microscopy where the electrostatic force is probed. This force arises due to the attraction or the repulsion of separated charges. It is a long-range force and can be detected 100 nm or more from the sample. For example, consider a conducting cantilever tip and sample which are separated a distance z usually by a vacuum. A bias voltage between tip and sample which are separated a distance z usually by a vacuum. A bias voltage between tip and sample is applied by an external battery forming a capacitor, C, between the two. The capacitance of the system depends on the geometry of the tip and sample. The total energy stored in that capacitor is $U = (1/2)C \cdot \triangle V^2$. The work done by the battery to maintain a constant voltage, $\triangle V$, between the capacitor plates (tip and sample) is -2U. Taking the negative gradient of the total energy $U_{total}$=-U gives the force. Let $\Delta V$ the potential difference between the $V_{CPD}$ and the voltage applied to the tip, $\partial C/\partial z$ the gradient of the capacitance between the tip and the sample in the z direction. The potential difference $\Delta V$ and the electrostatic force $F_{es}(z,t)$ can be written when $V_{AC}\sin(\omega t) \pm V_{DC}$ is applied to the tip (+ when $V_{DC}$ is applied to the sample and - when $V_{DC}$ is applied to the tip):

$$\Delta V = (V_{DC} \pm V_{CPD}) + V_{AC}\sin\omega t$$

$$F_{es}(z,t) = -\frac{1}{2}\frac{\partial C}{\partial z}[(V_{DC} \pm V_{CPD}) + V_{AC}\sin\omega t]^2$$

Then the equation can be divided into three parts:

$$F_{es}(z,t) = F_{DC} + F_{\omega} + F_{2\omega}$$

$$F_{DC} = -\frac{1}{2}\frac{\partial C}{\partial z}(V_{DC} \pm V_{CPD})^2 \; for \; EFM$$

Since $\partial C/\partial z < 0$ this force is always attractive. The electrostatic force can be probed by changing the voltage, and that force is parabolic with respect to the voltage, as can be seen by the part of the $F_{DC}$. One note to make is that $\triangle V$ is not simply the voltage difference between the tip and sample. Since the tip and sample are often not the same material, and furthermore can be subject to trapped charges, debris, etc., there is a difference between the work functions of the two. This difference, when expressed in terms of a voltage, is called the contact potential difference, $V_{CPD}$ This causes the apex of the parabola to rest at $\triangle V = V_{tip} - V_{sample} - V_{CPD} = 0$. Typically, the value of $V_{CPD}$ is on the order of a few hundred millivolts. Forces as small as piconewtons can routinely be detected with this method.

EFM is adopted to check whether charged molecules are adsorbed on the surface. EFM measurements were performed at ambient conditions using a Bruker Multimode 8 equipped with a Nanoscope V electronics. EFM was operated in Tapping mode with no bias on the tip (300 mV target amplitude, 200 mV amplitude setpoint) with NANO*SENSORS*™ 0.5-9.5 N/m force constant silicon tips whose resonant frequency is from 45 kHz to 115 kHz. The integral gain is 1 and the proportional gain is 5 for EFM. The tip is coated by a Platinum/Iridium coating for

the special use of cantilever for electrical force microscopy. Au(111)/mica substrates purchased from Phasis (Swiss) were used.

EFM analyses were operated in the so-called lift mode: first the topographic image is recorded, then the tip is lifted and scan the surface following the recorded topography to be sensible only to the electrical features.

# 3. Self-assembled monolayer of push-pull chromophore using ferrocene as the electron donating group on different surfaces for the potential modulation

In the field of molecular electronics, ferrocene derivatives are used as the basic unit of the molecular rectifier[177], due to their intrinsic electrical dipole structure. The electrical property and the electronic structure of the rectifier based on the ferrocene derivatives are strongly impacted by the symmetry of the molecular structure around the central ferrous ion and by morphology property of the self-assembled monolayer[178]. Besides, the central metal ion can be used as the charge storage of holes unit in the application of solar cells to slow down the recombination process[179].

Organometallic compounds are becoming the popular trend in the structure of the push-pull chromophore[180]. The macrocyclic porphyrin and phthalocyanine belongs to this range, however, this is the part of the π-conjugated spacer or electron donating group[181,182]. A new trend is to use the organometallic compound as an electron-donating group. The most outstanding organometallic compound as an electron-donating group for now is the ferrocene[183]. Compared to the conventional push-pull chromophore, the thermal stability is greatly enhanced because ferrocene is a stable 18 electrons organometallic compound[180]. During this PhD work, I have been interested firstly in a simple organometallic push-pull chromophore which is 3-ferrocenoylpropionic acid. In the structure of the compound, the electron-donating part is the cyclopentadienyl linked to the rest of the molecule. The electron-withdrawing group is the α-carbonyl of the cyclopentadienyl, and they are linked by a simple spacer. 3-ferrocenoylpropanoic acid has a carboxylic acid group as the grafting unit and a small aliphatic linker.

The goal of this chapter is to show that the idea of tuning the electrical response of an electro-active molecular layer through an intermediate dipolar self-assembled monolayer is feasible by showing an analogue experiment.

For this purpose, I have chosen three molecules to act as a first self-assembled monolayer promoting the potential modulation effect on a molecular layer deposited on top: cysteamine, para-aminothiophenol and 3-amino-5-mercapto-1,2,4-triazole. These three molecules have been selected since they have different intrinsic electrical dipole moment due to different molecular structures. Once the first self-assembled monolayer is characterized, the second self-assembled monolayer will be made using the adsorption of the 3-ferrocenoylpropanoic acid on the self-assembled monolayer of aminothiol molecules.

The specific goal is to highlight the relationship between the electron transport process during the redox reaction of central ferrous atom and the molecular structure between the substrate and the central ferrous atom.

In fact, due to the additional aminothiol molecular monolayer, the potential of the electrochemical reaction is expected to change. This phenomenon is called potential modulation, and the origin of the shift is due to the intrinsic electrical dipole moment of the intermediate SAM of aminothiol on the surface. To do this, we combined the information by a variety of characterization method. We used cyclic voltammetry as the main characterization method for the electron transport property and the coverage of the molecule on the surface. Atomic force microscopy and scanning tunnelling microscopy are used to reveal the morphology of molecules on the surface. X-ray photoelectron spectroscopy and surface-enhanced Raman spectroscopy is adopted to see the chemical composition of the molecules on the substrate.

# A. Self-assembled monolayer of different aminothiols on gold

The self-assembled monolayer of aminothiol molecules should act as a potential modulation layer. For the study in this section, cysteamine, para-aminothiophenol and 3-amino-5-mercapto-1,2,4-triazole have been chosen (figure 1).

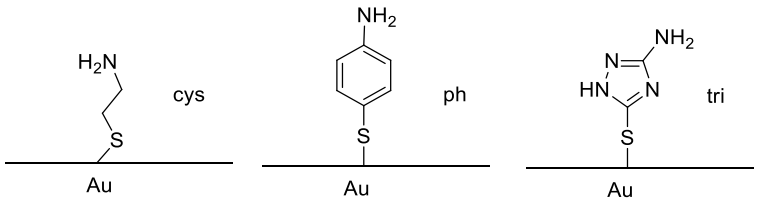


**Figure 1**: different structure of aminothiol molecules on gold

These molecules possess all the thiol functional group to be grafted on gold and an amino group which can be further modified to attach 3-ferrocenoylpropionic acid. Such molecules have different molecular structures between the thiol group and the amino group: alkyle for cysteamine, benzene for para-aminothiophenol and triazole for 3-amino-5-mercapto-1,2,4-triazole. Taking the structure of the benzene, each carbon atom is in $sp^2$ hybridization to form the molecule. The electronic configuration of carbon atom is $1s^2 2s^2 2p^2$ with $2s^2 2p^2$ four valence electrons. To form the benzene molecule, the wavefunction of a 2s electron and two 2p electron of the carbon atom in the benzene ring are fused and they form three hybridized $sp^2$ electrons to form the $\sigma$ bond with two neighbouring carbon atoms and a hydrogen atom. The only unhybridized electron interact with another unhybridized electron in the neighbouring atom and they form a π bond and these

electrons are called π electrons. To maximize the interaction of π bonds, these π electrons are perpendicular to the benzene ring and the electronic density is very positive on one side and very negative on the other side. This makes the π-π interaction an electrostatic interaction. There are some configurations, and the most stable configuration is T-shape. The hybridization station of nitrogen atoms and carbon atoms in the molecular ring of 3-amino-5-mercapto-1,2,4-triazole is all $sp^2$ hybridization. Since nitrogen atom has one more valence electron than carbon atom, its hybridized 2p orbital is fully filled without any electron sharing of π bonds and they can interact with other π electrons. Compared to the benzene ring, the electronic density of the ring of 3-amino-5-mercapto-1,2,4-triazole is stronger due to the more compact geometry and higher electronegativity of nitrogen atom. This should increase the electronic density out of the potential well of the atom and make the molecule more conductive. This is the reason why 3-amino-5-mercapto-1,2,4-triazole is interesting to be used to facilitate the electron transfer across the interface than cysteamine and para-aminothiophenol. Each self-assembled monolayer is characterized by Contact angle, AFM and STM.

# I. Self-assembled monolayer preparation

For surface functionalization, 4-aminothiophenol (CAS 1193-02-8) and 2-aminoethanethiol (CAS 60-23-1) come from Across Organics; 3-amino-5-mercapto-1,2,4-triazole (CAS 16691-43-3) comes from Alfa Aesar and anhydrous sodium hydroxide pellets (CAS 1310-73-2) come from Carlo Erba.

Prior to the functionalization of a thiol monolayer, the Au electrode surface was cleaned by UV-ozone (in air) for 10 min. For gold samples, the cleaning procedure was to put the gold surface in a plastic chamber within half a centimetre from a UV lamp emitting at $\lambda_1$ = 185 nm and $\lambda_2$ = 254 nm. The shorter wavelength $\lambda_1$ dissociates $O_2$ molecules to form ozone $O_3$ with another $O_2$ molecule and a very reactive radical $O^{\cdot}$. Under UV illumination at $\lambda_2$, $O^{\cdot}$ oxidizes all organic compounds present at the sample surface to form gas products leaving the surface clean. The surface functionalization was formed by immersing the precleaned Au electrode once the UV-ozone is finished in a freshly prepared solution for 24h at room temperature. The solution is 10 mM cysteamine or para-aminothiophenol or 3-amino-5-mercapto-1,2,4-triazole and 10 mM sodium hydroxide in absolute ethanol (99%) and distilled water (1%). In addition, NaOH is used to deprotonate the thiol to help the physical and the chemical adsorption. Then the substrate will be rinsed by acetone and water and dried using nitrogen gas after the functionalization. To ensure the reproducibility, three functionalized substrates are prepared. For the adsorption of the thiol on gold, the addition of base like sodium hydroxide can be beneficial because protons formed on the surface can be extracted from the surface by the base[184].

## II. Contact angle measurement

Firstly, the characterization is started with the water contact angle measurements for each self-assembled monolayer. Since the three molecules have a same amino group, then the value of the contact angle measurement should be the same. The value is 48.5±7.6° for the substrate after the same procedure using the same solvent without aminothiol molecule. The measured water contact angles for the self-assembled monolayer of cysteamine and para-aminothiophenol are very close: 54.2±8.0° and 54.4±5.8° respectively. For 3-amino-5-mercapto-1,2,4-triazole, there are two measured values: 50.4±5.6° or 27.3±6.9°. An assumption for these two values may be two different modes of molecular adsorption on the surface, perpendicular for the higher value, and lying flat on the surface for the lower. Indeed, the similar water contact angles around 46-50° show that the functional group on the surface should be amino group[77]. For self-assembled monolayer of cysteamine on gold, Yu et al. found 46° after the water contact angle measurement[185]. Ouerghi et al. confirmed this conclusion[186]. The reason for the higher value may be an indication of not perfectly organized layers. Unfortunately, there is little information about the contact angle value for the self-assembled monolayer of para-aminothiophenol and 3-amino-5-mercapto-1,2,4-triazole.

## III. Scanning probe microscopy

Then self-assembled monolayers of aminothiol molecules were imaged. The STM images of all the self-assembled monolayer of cysteamine on gold, self-assembled monolayer of para-aminothiophenol on gold and self-assembled monolayer of 3-amino-5-mercapto-1,2,4-triazole on gold are in figure 2. The AFM images of self-assembled monolayer of cysteamine on gold, para-aminothiophenol on gold and 3-amino-5-mercapto-1,2,4-triazole on gold are in figure 3, 4 and 5 respectively. In terms of the roughness determined by scanning tunnelling microscope, the value of $R_q$ for the self-assembled monolayer of cysteamine on gold is 1.16 nm, 0.199 nm for the self-assembled monolayer of para-aminothiophenol on gold and 0.146 nm for the self-assembled monolayer of 3-amino-5-mercapto-1,2,4-triazole on gold. The clear presence of aggregation and high roughness show the multilayer formation in the case of cysteamine. For cysteamine, the ordered structure cannot be reached under scanning tunnelling microscope, however, amorphous surface functionalization of gold by these molecules can be done. For the self-assembled monolayer of aliphatic aminothiol, the Van der Waals interaction is the key factor to form the ordered structure and the longer the chain, the stronger the Van der Waals forces. Therefore, cysteamine based self-assembled monolayer on gold cannot form ordered structure because the length of the carbon chain is short. For the benzylic and unsaturated heterocyclic structure, the structure of its self-assembled monolayer is determined by π-π interaction. This interaction comes from the π electrons.

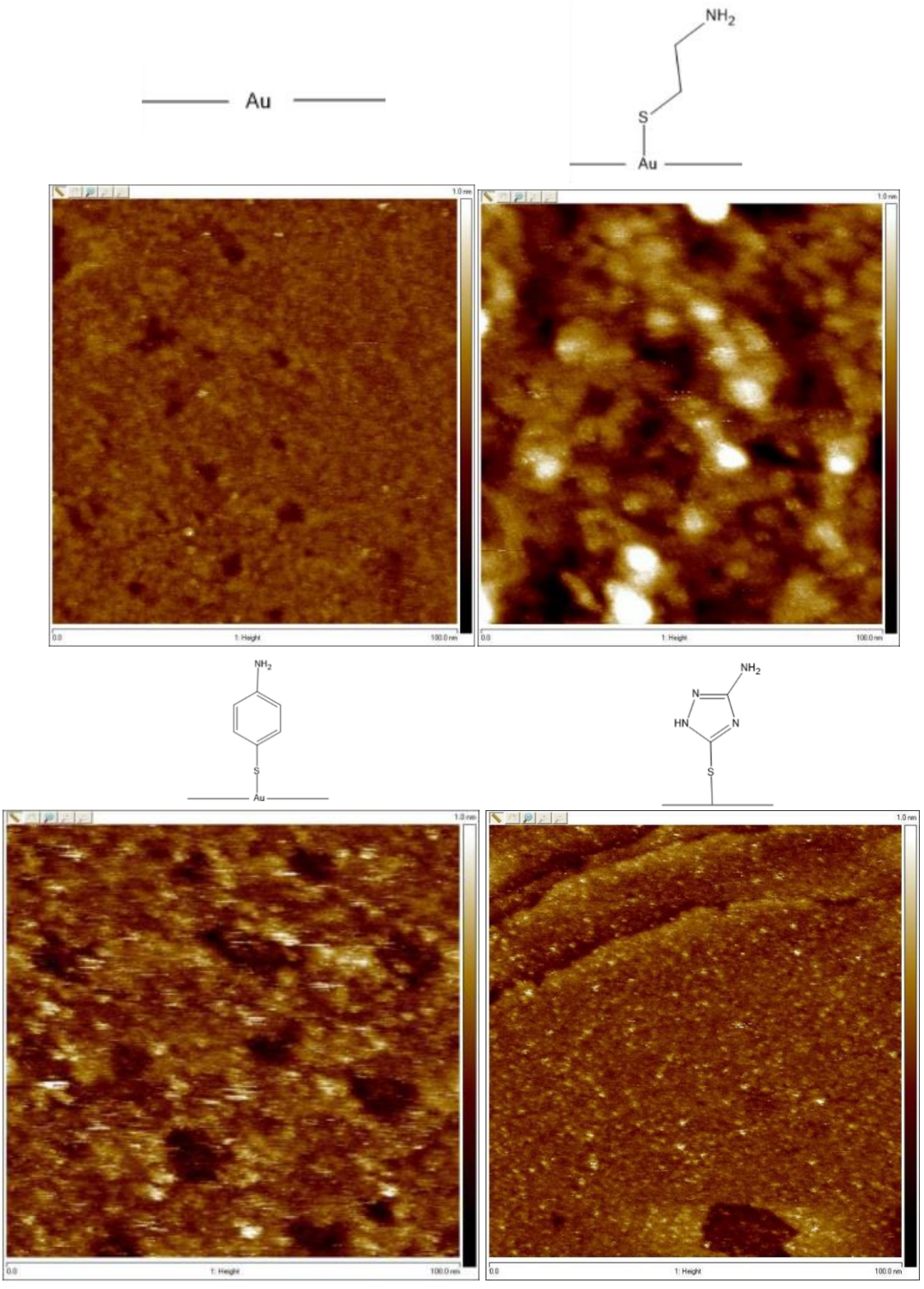


**Figure 2**: (top left) STM (5pA, -200mV) image (100*100 $nm^2$) of Au(111)/mica; (top right) STM (5pA, -200mV) image (100*100 $nm^2$) of cysteamine self-assembled monolayer on Au(111)/mica (10 mM, RT, 24h, ethanol); (bottom left); (top right) STM (5pA, -200mV) image (100*100 $nm^2$) of para-aminothiophenol self-assembled monolayer on Au(111)/mica (10 mM, RT, 24h, ethanol); (bottom right) STM (5pA, -200mV) image (100*100 $nm^2$) of 3-amino-5-mercapto-1,2,4-triazole self-assembled monolayer on Au(111)/mica (10 mM, RT, 24h, ethanol)

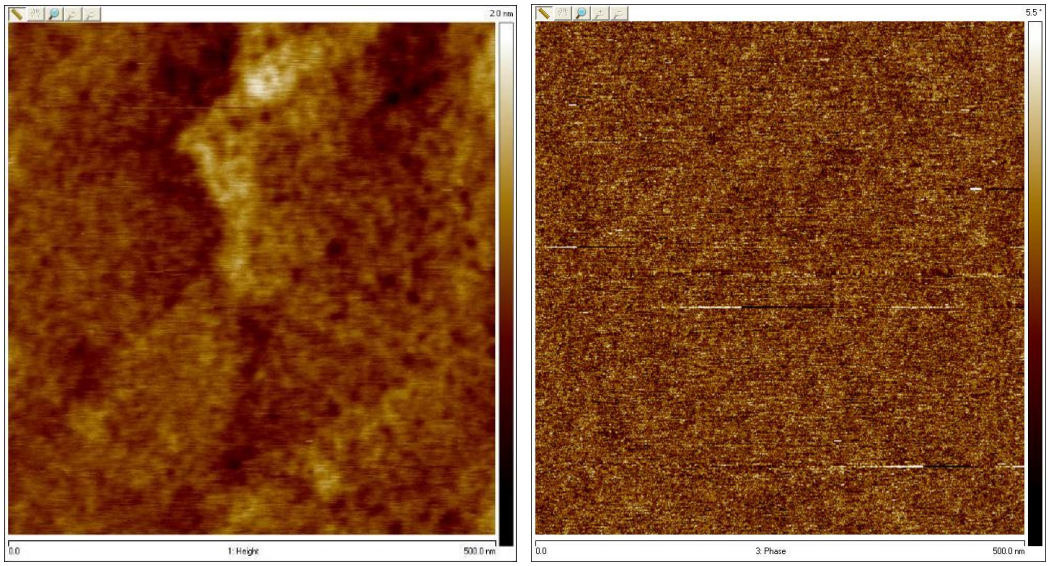


**Figure 3**: the AFM tapping mode (left) topography and (right) phase image (500*500 $nm^2$) of Au(111)/mica (10 mM, RT, 24h, ethanol).

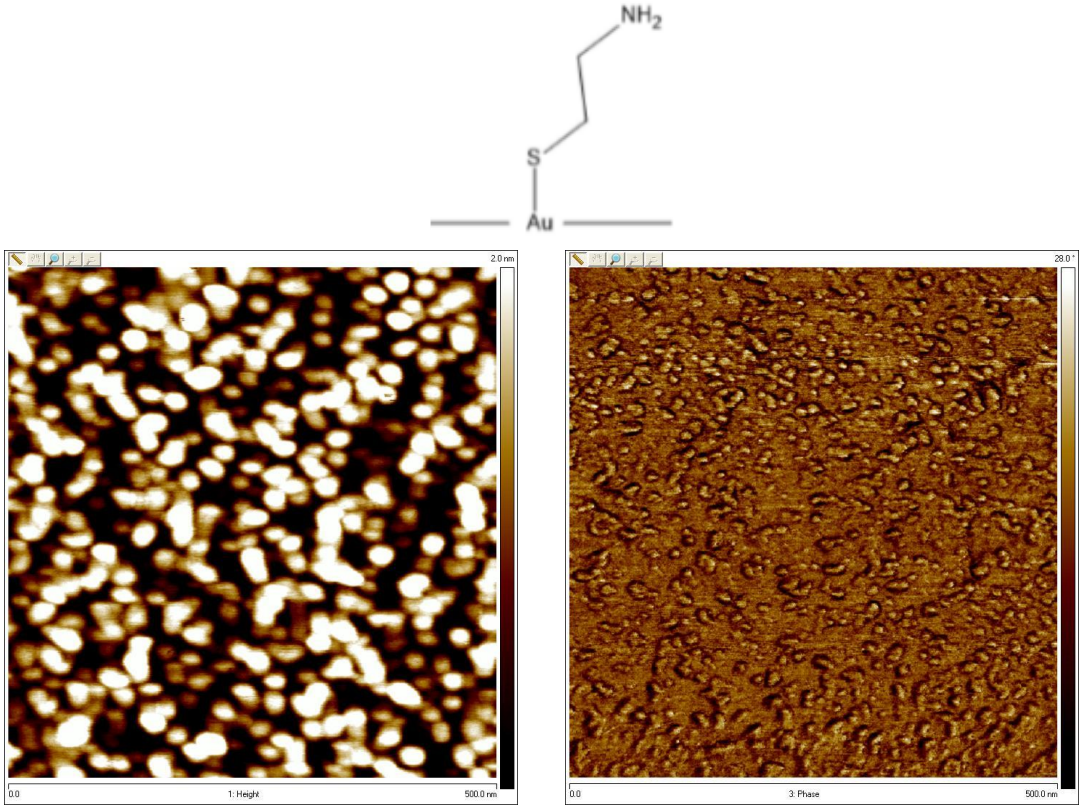


**Figure 4**: the AFM tapping mode (left) topography and (right) phase image (500*500 $nm^2$) of self-assembled monolayer of cysteamine on Au(111)/mica (10 mM, RT, 24h, ethanol).

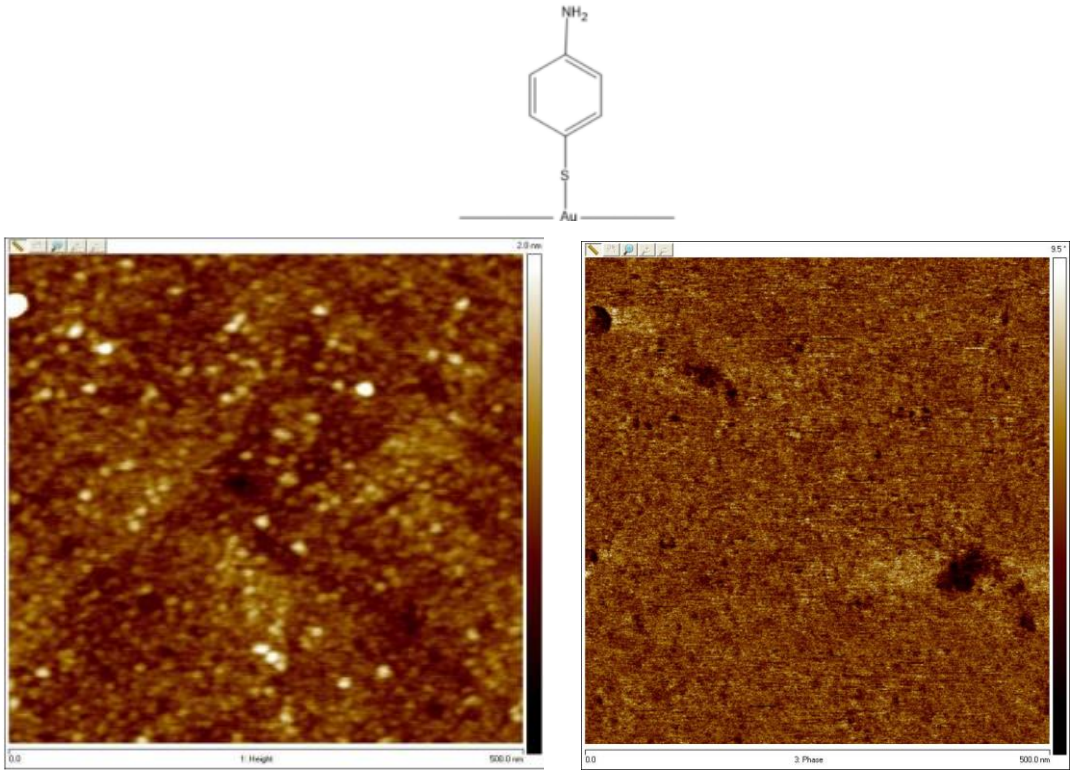


**Figure 5**: the AFM tapping mode (left) topography and (right) phase image (500*500 $nm^2$) of self-assembled monolayer of para-aminothiophenol on Au(111)/mica (10 mM, RT, 24h, ethanol).

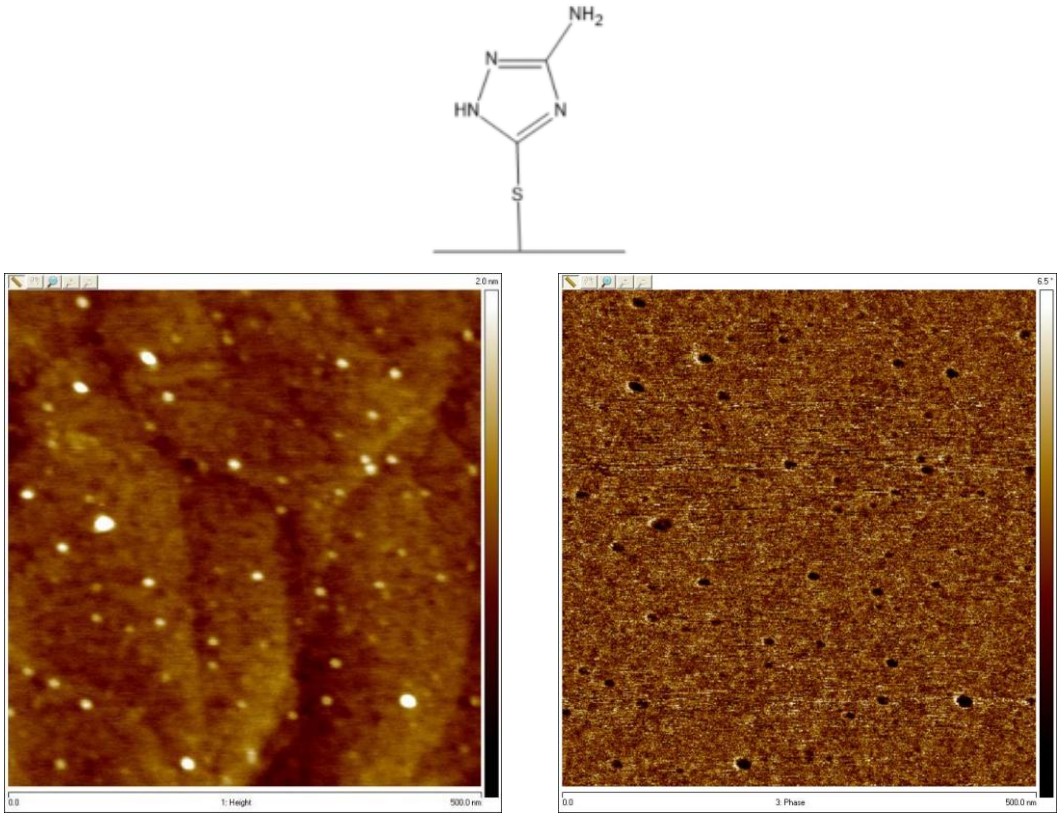


**Figure 6**: the AFM tapping mode (left) topography and (right) phase image (500*500 $nm^2$) of self-assembled monolayer of 3-amino-5-mercapto-1,2,4-triazole on Au(111)/mica (10 mM, RT, 24h, ethanol).

Sun et al. used scanning tunnelling microscope to probe the surface structure of the para-aminothiophenol on Au(111) substrate[187]. The formation of the etch pit according to the sectional analysis in the article shows the good coverage of the surface by the molecule. Unfortunately, to the best of my knowledge, no scanning probe microscopy images analyses of the self-assembled monolayer of cysteamine and 3-amino-5-mercapto-1,2,4-triazole were found in the literature.

As can be seen in the STM in figure 2 and AFM images in figure 3, the Au(111)/mica substrate is flat and there are some small pits in the image, and they are the defects of the structure of the surface. Also, there are almost no white spots on the surface. Compared with STM and AFM images of the Au(111)/mica substrate, there are additional round spots appeared on the STM images in figure 2 and AFM images in figure 4 of self-assembled monolayer of cysteamine on the surface. Also, the size of the pits increased a little bit, and this is due to the etching process. In fact, there are several steps for the growth of the self-assembled monolayer. The first process is the transfer of the amphiphilic molecules from the solution to the surface. Then the molecule is physically adsorbed, followed by chemisorption, after which the growth of the surface functionalization starts from this point. After the full coverage, the transformation from the laying down phase to the standing up phase may occur, and the structure of the self-assembled monolayer is optimized spontaneously in the solution. It seems that the organization of the self-assembled monolayer of cysteamine is less ordered than the self-assembled monolayer of para-aminothiophenol, though the full coverage of the surface is attained for two systems.

However, the interaction of the gold-thiolate is so strong that the thiol-Au complex will leave the surface, and this process is faster on the edge of the defect on the gold. This is the reason the pit becomes larger after the surface functionalization. In the view of the chemistry, it is also a redox reaction where the hydrogen of the thiol (oxidation number +I) is reduced to hydrogen gas (oxidation number 0) and the gold (oxidation number 0) is oxidized to form gold-thiolate complex (oxidation number +I). This process will continue until the full coverage of the surface. As the Au(111)/mica substrate is immersed in the solution, bubbles can be seen, and they leave the surface.

Here is the process of the chemical functionalization. Firstly, the thiol will be transferred from the solution to the clean gold surface and the thiol will be physically adsorbed on the surface and chemically adsorbed by oxidative addition to form R-S(-I)-Au(+II)-H(-I). At last, the molecule of dihydrogen gas was generated by quenching using a protic hydrogen.

The bonding situation is different for aliphatic thiol and aromatic thiol. The sulphur atom in the aliphatic thiol is in $sp^3$ or sp hybridization. The sulphur atom in the aromatic thiol is in sp hybridization. This difference could have an impact in the

geometrical structure of the self-assembled monolayer and explain the difference observed from images.

In fact, it seems like there are less surface coverage of 3-amino-5-mercapto-1,2,4-triazole on the surface. One explanation is that 3-amino-5-mercapto-1,2,4-triazole has a $pK_a$ about 10-12 for the hydrogen of the nitrogen atom of position 1. Since this $pK_a$ is similar as the $pK_a$ of thiol, the solution has two components: the one is the thiolate of position 5 for 3-amino-5-marcapto-1,2,4-triazole and the other one is the deprotonated triazole of position 1. For the adsorption of the thiol on gold, the addition of base like sodium hydroxide can be beneficial because protons formed on the surface can be extracted from the surface by the base[184]. Therefore, for a good grafting, it is better to use base like sodium hydroxide. If the protonation on the position 1 occurs, the resonance makes the charge stabilized in the ring of 5 atoms, and this seems as same as the case of cyclopentadiene. In terms of the stability, the complexation coefficient $\beta$ is higher for $\eta^5$ coordination than $\eta^1$. If the molecule is lying flat, it is possible to have lower coverage. But the scanning tunnelling microscope is a localized investigation method, the possibility to see the grafting undeprotonated 3-amino-5-mercapto-1,2,4-triazole cannot be excluded.

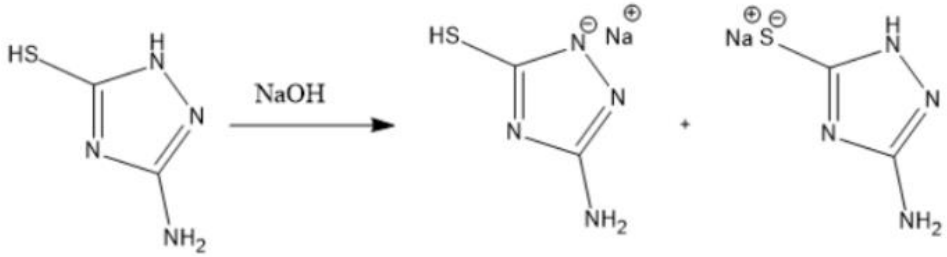


**Figure 7**: the scheme of the reaction of 3-amino-5-mercapto-1,2,4-triazole

The coexistence of the adsorption of deprotonated 1-position and undeprotonated 1-position 3-amino-5-mercapto-1,2,4-triazole is predicted based on the acido-basic property of the molecule in figure 7. According to the STM images, the phases of undeprotonated and deprotonated 3-amino-5-mercapto-1,2,4-triazole are both observed in figure 8. These two phases have two differences. The first difference is the different vertical contrast to the substrate. The undeprotonated phase has a higher vertical island contrast to the substrate than the deprotonated phase. The other difference is the horizontal and/or lateral contrast to the substrate. In other word, apart from the different contrast along z-axis, the different contrast on the xy plane is also apparent for the two phases. The size of the island for a typical undeprotonated 3-amino-5-mercapto-1,2,4-triazole is about 10*10 $nm^2$ and the size of the island for a typical deprotonated 3-amino-5-mercapto-1,2,4-triazole is about 2*2 $nm^2$.

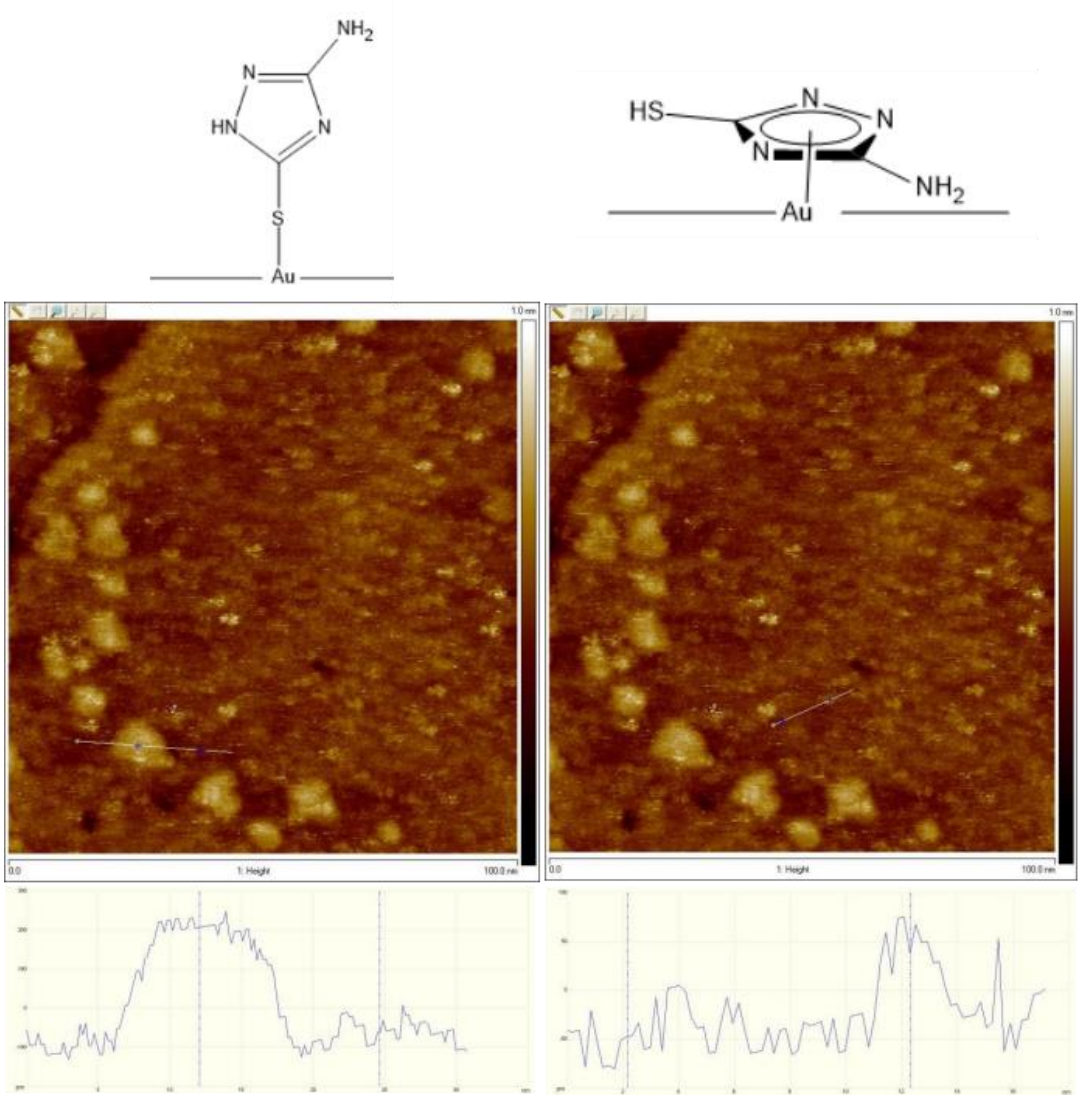


**Figure 8**: $\eta^1$-3-amino-5-mercapto-1,2,4-triazole-gold complex structure (left top) and $\eta^5$-3-amino-5-mercapto-1,2,4-triazole-gold complex structure (left down); the molecular island of undeprotonated $\eta^1$-3-amino-5-mercapto-1,2,4-triazole on the STM image (middle left) and the molecular island of deprotonated $\eta^5$-3-amino-5-mercapto-1,2,4-triazole on the STM image (middle right); the sectional analysis of the molecular island of undeprotonated $\eta^1$-3-amino-5-mercapto-1,2,4-triazole on the STM image (bottom left) and the sectional analysis of the the molecular island of deprotonated $\eta^5$-3-amino-5-mercapto-1,2,4-triazole on the STM image (bottom right)

# IV. Conclusion

In this section, a series of aminothiol based self-assembled monolayers is prepared and they are checked by contact angle measurement, tapping-mode atomic force microscopy and scanning tunnelling microscopy. The STM and AFM doubly confirmed the good adsorption of the three different aminothiol molecules on top of the gold substrate. The result of the contact angle measurement shows that the functional group on top is $NH_2$ for cysteamine and para-aminothiophenol SAMs, whereas for the triazole-based SAM there may be two configurations : molecules perpendicular or lying flat on the surface. That is the reason why in the following we discarded triazole-based SAM as a sticking layer for the additional SAM on top. These results will be used as the preliminary section for the next section: preparation and characterization of self-assembled monolayer using the ferrocene-based chromophore by surface synthesis.

# B. Ferrocene derivative molecule on the aminothiol self-assembled monolayer for the effect of potential modulation

## I. Self-assembled monolayer preparation

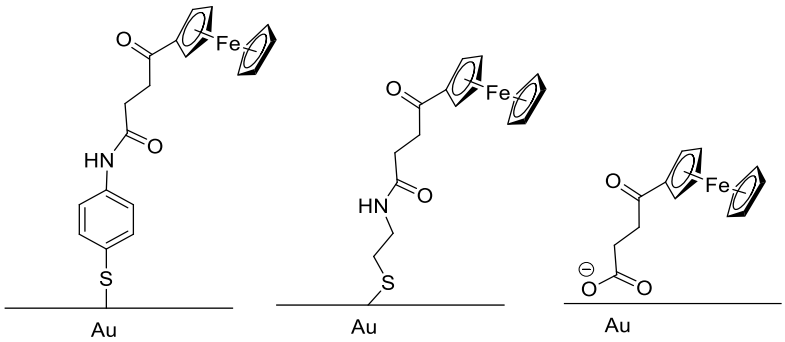


**Figure 9**: the structure of different self-assembled monolayer on gold.

This section is dedicated to show the potential modulation of electrochemical reaction of ferrocene-based derivatives caused by the intrinsic electrical dipole of the aminothiol molecules using cyclic voltammetry. To prepare the self-assembled monolayer on gold in figure 9, 3-ferrocenoylpropionic acid (CAS 1291-72-1) comes from TCI Europe; 4-Aminothiophenol (CAS 1193-02-8) and 2-Aminoethanethiol (CAS 60-23-1) come from Across Organics; 1,1'-Carbonyldiimidazole (CAS 530-61-2) comes from Fluka. All solvents were bought from Fisher Chemicals. The self-assembled monolayer preparation process is in figure 10.

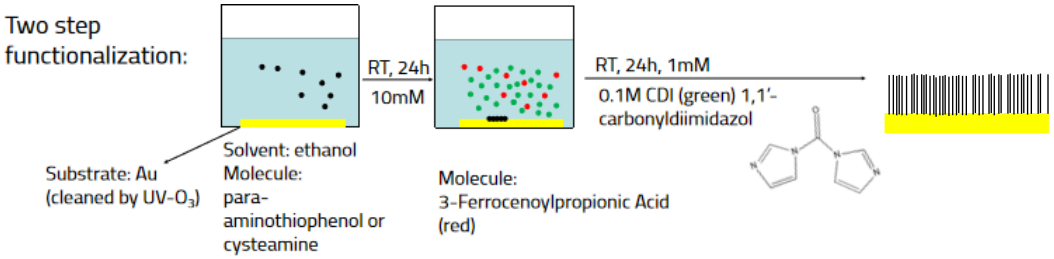


**Figure 10**: two-step preparation process of the ferrocene-based self-assembled monolayers

Gold substrate on quartz from OpenQCM and Dropsens 220AT were used throughout all electrochemical studies whereas Au(111) on mica for atomic force microscopy and scanning tunnelling microscopy. Prior to the functionalization of a thiol monolayer, the Au electrode surface was rinsed by absolute ethanol, UV-ozone (in air) processed for 10 min, rinsed by absolute ethanol and dried using nitrogen gas. The surface functionalization was formed by immersing the precleaned Au electrode in a freshly prepared solution with a concentration of 10 mM of cysteamine or para-aminothiophenol in absolute EtOH or 1 mM 3-

ferrocenoylpropionic acid in DMF for 48h. After the first step functionalization, the substrate will be immersed in a solution of 1 mM 3-ferrocenoylpropionic acid and 0.1M 1,1′-carbonyldiimidazol in dimethylformamide for 24h or 48h. The goal is to use 1,1′-carbonyldiimidazole to make peptide bond coupling. For this, large amount of 1,1′-carbonyldiimidazole is used. It can deprotonate the carboxylic acid to start the nucleophilic addition on the electrophile of the carbon of the carbonyl but also make the proton exchange to replace the ammonium to amine group on the surface to facilitate the final nucleophilic substitution toward the activated ester. At the end, the substrate is rinsed by absolute ethanol and dried using nitrogen gas after the second step functionalization.

## II. Atomic force microscopy

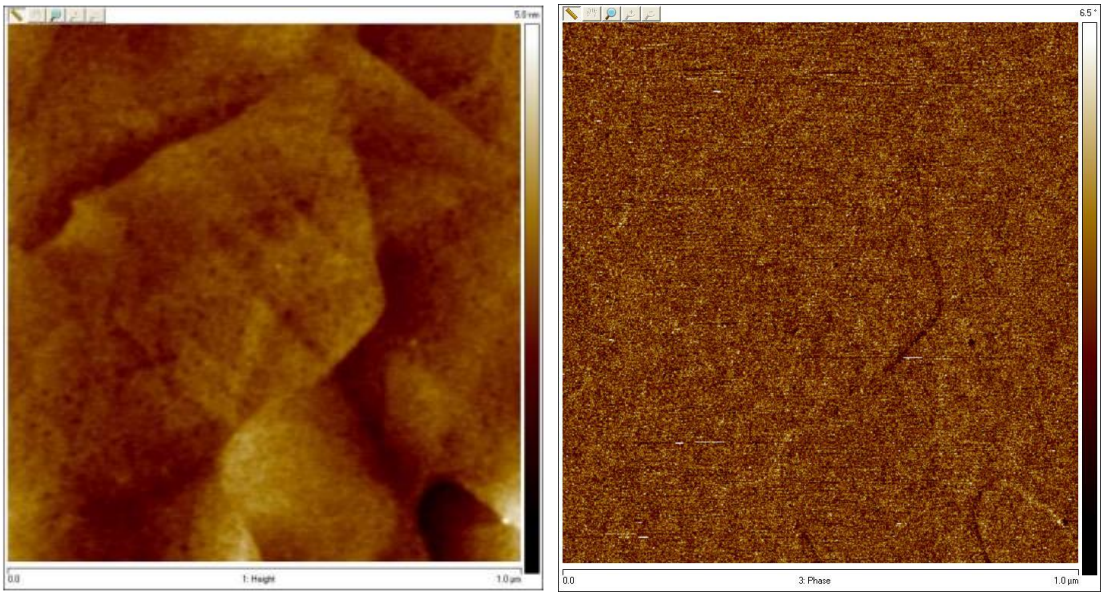

**Figure 11**: AFM topography (left) and phase (right) images on Au(111)/mica

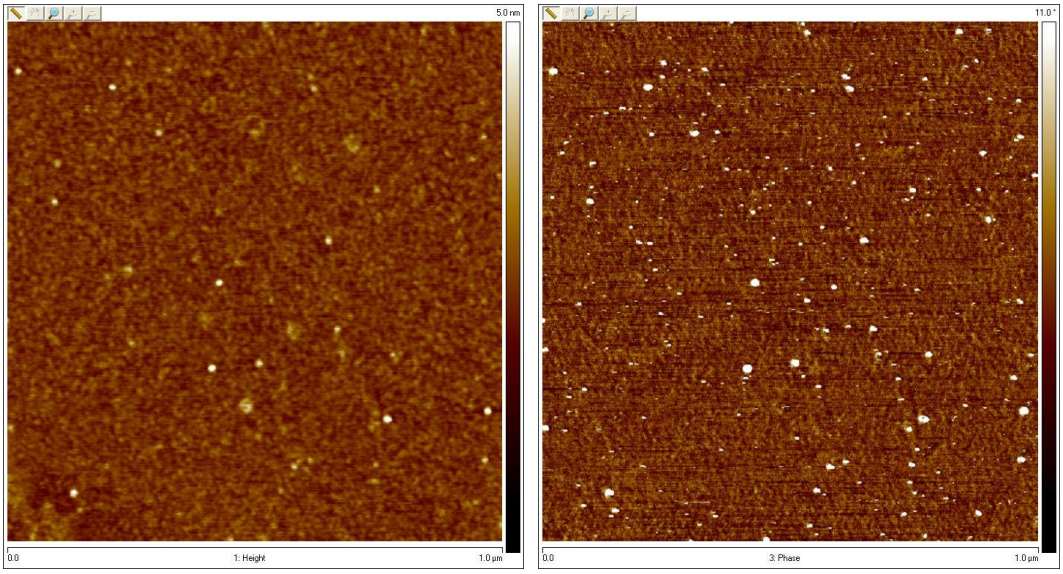

**Figure 12**: AFM topography (left) and phase (right) images of self-assembled monolayer of 3-ferrocenoylpropionic acid on Au(111)/mica

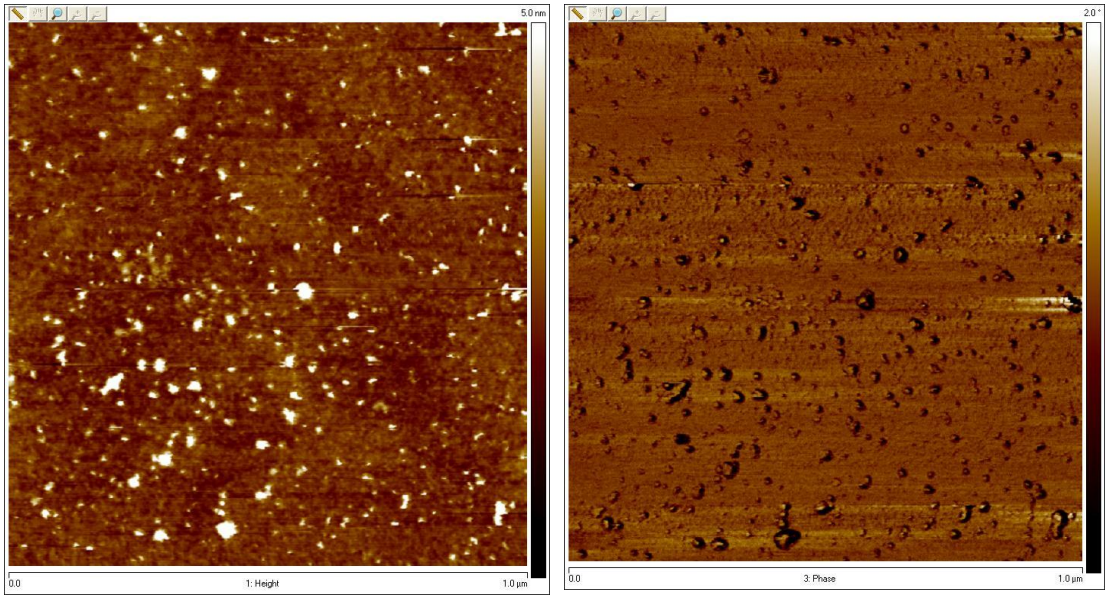


**Figure 13**: AFM topography (left) and phase (right) images of self-assembled monolayer of cys+ferro system on Au(111)/mica

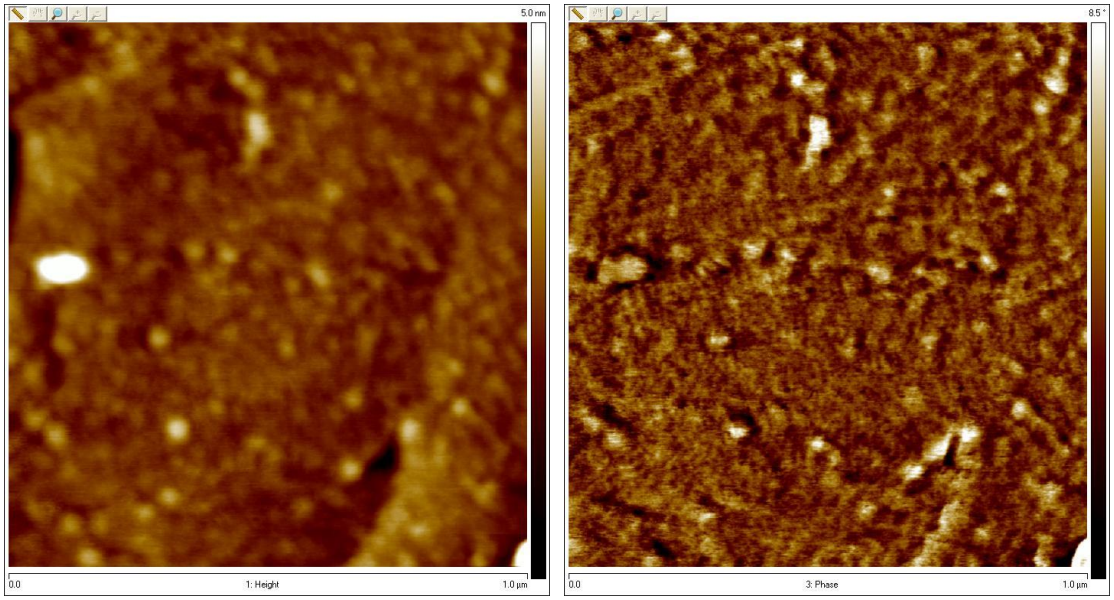


**Figure 14**: AFM topography (left) and phase (right) images of self-assembled monolayer of ph+ferro system on Au(111)/mica

Figures 11, 12, 13 and 14 show the AFM images (topography and phase) of the Au(111) substrate, the self-assembled monolayer of 3-ferrocenoylpropanoic acid on Au(111), the self-assembled monolayer of cys+ferro system on Au(111) and the self-assembled monolayer of ph+ferro system on Au(111) respectively. Due to the flat surface of the substrate, the structure contrast in these AFM images is mainly caused by the molecules. The roughness of the self-assembled monolayer is recorded using the $R_q$ value. This value is 0.162 nm for the gold substrate, 0.231 nm for the surface of the self-assembled monolayer of 3-ferrocenoylpropanoic acid on gold, 0.268 nm for the self-assembled monolayer of ph+fc system and 0.305 nm for the self-assembled monolayer of cys+fc system. For ferro system, the main

reaction is the equilibrium of acid-carboxylate, and the surface is the flattest because there is only one layer of molecule on the surface. The structural difference can be distinguished using AFM between a functionalized substrate and bare substrate. The AFM images show the roughness increased after the formation of the self-assembled monolayer with two steps because the vertical scale is bigger than the vertical scale in the AFM image of self-assembled monolayer before the grafting of 3-ferrocenoylpropionic acid. So, the 3-ferrocenoylpropionic acid is successfully grafted on the surface. Moreover, there are same content of white stuff before and after the step of the immersion in the solution containing 3-ferrocenoylpropionic acid when the substrate is functionalized by the cysteamine firstly. Therefore, the self-assembled monolayer of ph+ferro system seems to have a better quality than the self-assembled monolayer of cys+ferro system.

There is something to be discussed in the phase imaging. The phase imaging can be used to distinguish the difference of the mechanical property on the surface. The surface is homogenous in the figure 11, in the figure 13 and in the figure 14. It means that the surface is either fully covered by the molecule or completely empty. Therefore, the Au(111) substrate in figure 11 is fully empty on the surface. Moreover, the Au(111) surface is fully covered by the molecules for the cys+ferro system in figure 13 and ph+ferro system in figure 14. However, there is an interesting point in the figure 12 for the self-assembled monolayer of 3-ferrocenoylpropanoic acid on Au(111). Some white spots can be seen on the phase image, and they are correlated with the white spots on the topography image. The white spots appeared on the AFM image is often considered as the aggregates of the molecules on the surface, but the white spots appeared in the figure 12 can be attributed to the ferrocene terminal in the molecular structure. The ionic bond in the ferrocene makes the molecule more rigid to the external mechanic force. The adsorption of the 3-ferrocenoylpropanoic acid on the surface is via the carboxylic acid and the well prepared self-assembled monolayer of 3-ferrocenoylpropanoic acid should have all the ferrocene terminal at the top of the surface. The appearance of the white spots shows the existence of the adsorbed 3-ferrocenoylpropanoic acid whose ferrocene terminal is at the top of the surface. However, more attempts are required so that the top of the surface is fully the ferrocene terminal of the molecule.

In the literature, Fontanesi et al. struggled to record an AFM image of the self-assembled monolayer of ferrocene-terminated molecule on the Si(111) surface[188]. However, Yokota et al. prepared the self-assembled monolayer of three different ferrocene-based alkylthiol on gold and characterized them using atomic force microscopy[189]. Our result is like the images in the article of Yokota et al. where the surface is covered by the patterns created by the molecule.

## III. Scanning tunnelling microscopy

Due to the flat surface of the substrate and the high resolution provided by STM, the structure details on the surface can be observed. For ferro system in figure 15, the main reaction is the equilibrium of acid-carboxylate and the physical adsorption of the carboxylate on the surface. The surface is the flattest because there is only one layer of molecule on the surface. However, some new things happen to better understand this grafting process.

Apart from the structure contrast caused by the gold terrasse, etch pits can be observed and confirmed by further sectional analysis. This showed the good grafting process because it showed the existence of etching on the surface. The depth of the pit is 2.5 Å, which is the diameter of the gold atom. This is caused by the desorption of the gold-thiolate complex molecule. For cys+ferro system in figure 16. However, the structure contrast caused by the gold terrasse cannot be seen and the surface roughness increases, this shows the uncompleted two-layer structure. The sectional analysis found the existence of etch pits caused by the grafting using cysteamine. This showed the good first step of grafting process because it showed the existence of thiolate- gold complex by the etch pits resulted by reversible process of molecule grafting on the surface.

Figure 17 shows the scanning tunnelling microscopy (STM) images on the mica/Au(111) with ph+ferro system. For ph+ferro system, the preparation has two steps. The structure contrast is like the cys+ferro system, but the quality of the image is always not optimal. This showed the good first step of grafting thanks to the sectional analysis but the arrangement of the molecule on the surface is not very good. The origin of the instability comes from the intrinsic electrical conductivity of the benzene ring. According to the basic function of the scanning tunnelling microscope, the height will be larger than the real height if the tip encounters a more conductive material. The roughness $R_q$ is also interesting to discuss. This value is 0.131 nm for the self-assembled monolayer of 3-ferrocenoylpropanoic acid, 0.152 nm for the self-assembled monolayer of ph+fc system and 0.236 nm for the self-assembled monolayer of cys+fc system. It is not strange that the more complex the molecular system of the surface the higher the roughness. For ph+fc system, the increase of the roughness is not as big as the one for the cys+fc system.

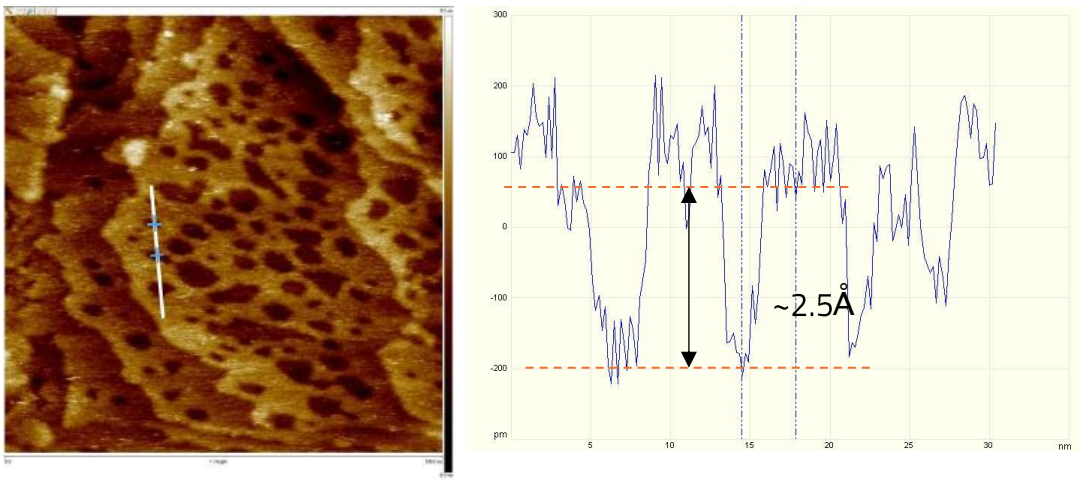


**Figure 15**: Comparison of STM images (5 pA, -200 mV) on Au(111)/mica with ferro system (left: STM image; right: STM sectional analysis)

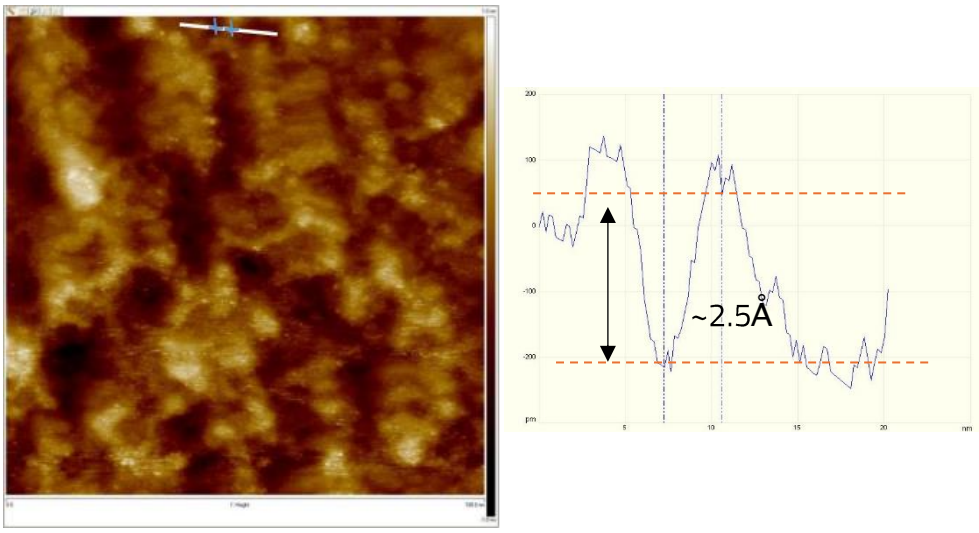


**Figure 16**: Comparison of STM images (5 pA, -200 mV) on Au(111)/mica with cys+ferro system (left: STM image; right: STM sectional analysis)

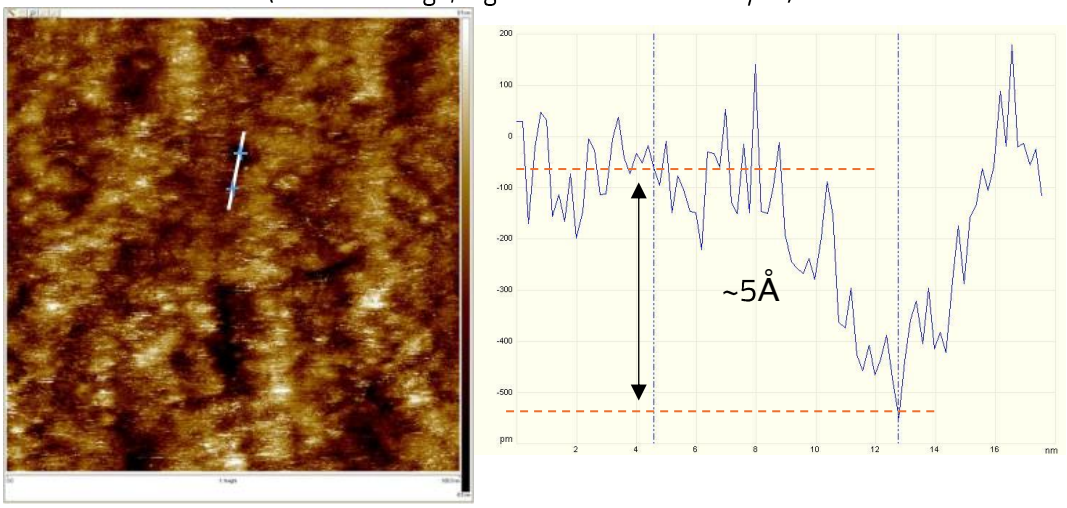


**Figure 17**: Comparison of STM images (5 pA, -200 mV) on Au(111)/mica with ph+ferro system (left: STM image; right: STM sectional analysis)

## IV. X-ray photoelectron spectroscopy

Among the studies for the self-assembled monolayer of ferrocene-terminated molecules on gold, the iron element is often chosen as the unique signature due to ferrous ion[190–192]. We chose C 1s, S 2p, Fe 2p and N 1s spectrum. The horizontal axis is the binding energy, and the vertical axis is counts per second (counts in the graph).

The XPS spectrum of surface functionalization using 3-ferrocenoylpropionic acid on the gold substrate on quartz is presented in figure 18. The deconvolution of signal of carbon C 1s according to the database shows at least the existence of $sp^2$ hybridized carbon for alkene bond (C=C, 284.9 eV) signal for cyclopentadiene ligand, $sp^2$ hybridized carbon for the carbonyl adjacent to the ferrocene group (C=O, 288.1 eV), $sp^3$ hybridized carbon for alkane bond (C-C, 285.3 eV), the $sp^2$ hybridized carbon for carboxylate on the surface ($^-$O-C=O, 288.7 eV) and $sp^2$ hybridized carbon for iron-ligand bond signal (Fe-$L_{cp}$, 286.3 eV). Watcharinyanon et al.[193] prepared self-assembled monolayers of decanethiol and 11-ferrocene-1-undecanethiol on gold. They are characterized by X-ray photoelectron spectroscopy. For C 1s spectra, a peak of 284.8 eV was found for $sp^3$ hybridized C-C carbon in the self-assembled monolayer of decanethiol and a peak of 284.2 eV for $sp^3$ hybridized C-C carbon and $sp^2$ hybridized C-C carbon was found for self-assembled monolayer of 11-ferrocene-1-undecanethiol on gold. There is a mutual shift towards higher binding energy in our result and the reason is attributed to the instrumental setup rather than the chemical composition of the self-assembled monolayer. For Fe 2p spectrum, Watcharinyanon et al.[193] found a signal at 708.5 eV and we have 710.8 eV for Fe $2p_{3/2}$ and 715.8 eV for Fe $2p_{1/2}$. The noise in the Fe 2p spectrum is caused by the difficulty to detect the iron.

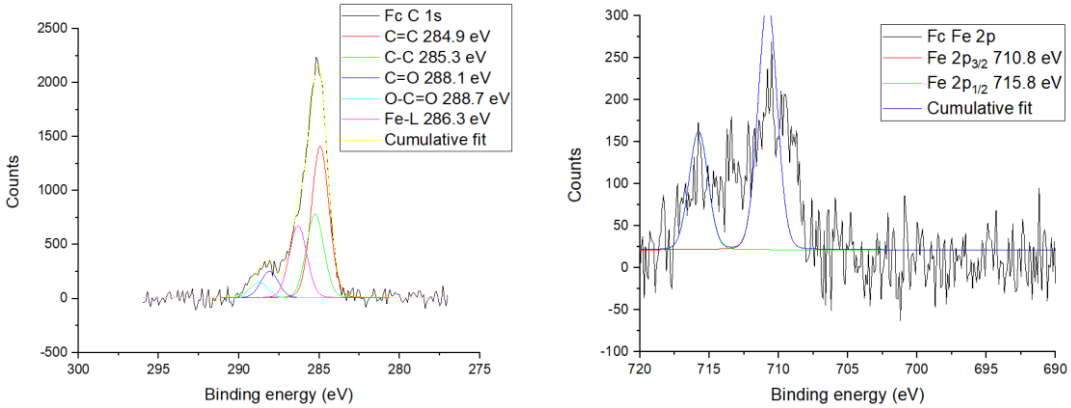


**Figure 18**: The XPS spectrum (left C 1s and right Fe 2p) of surface functionalization using 3-ferrocenoylpropionic acid on the gold substrate on quartz.

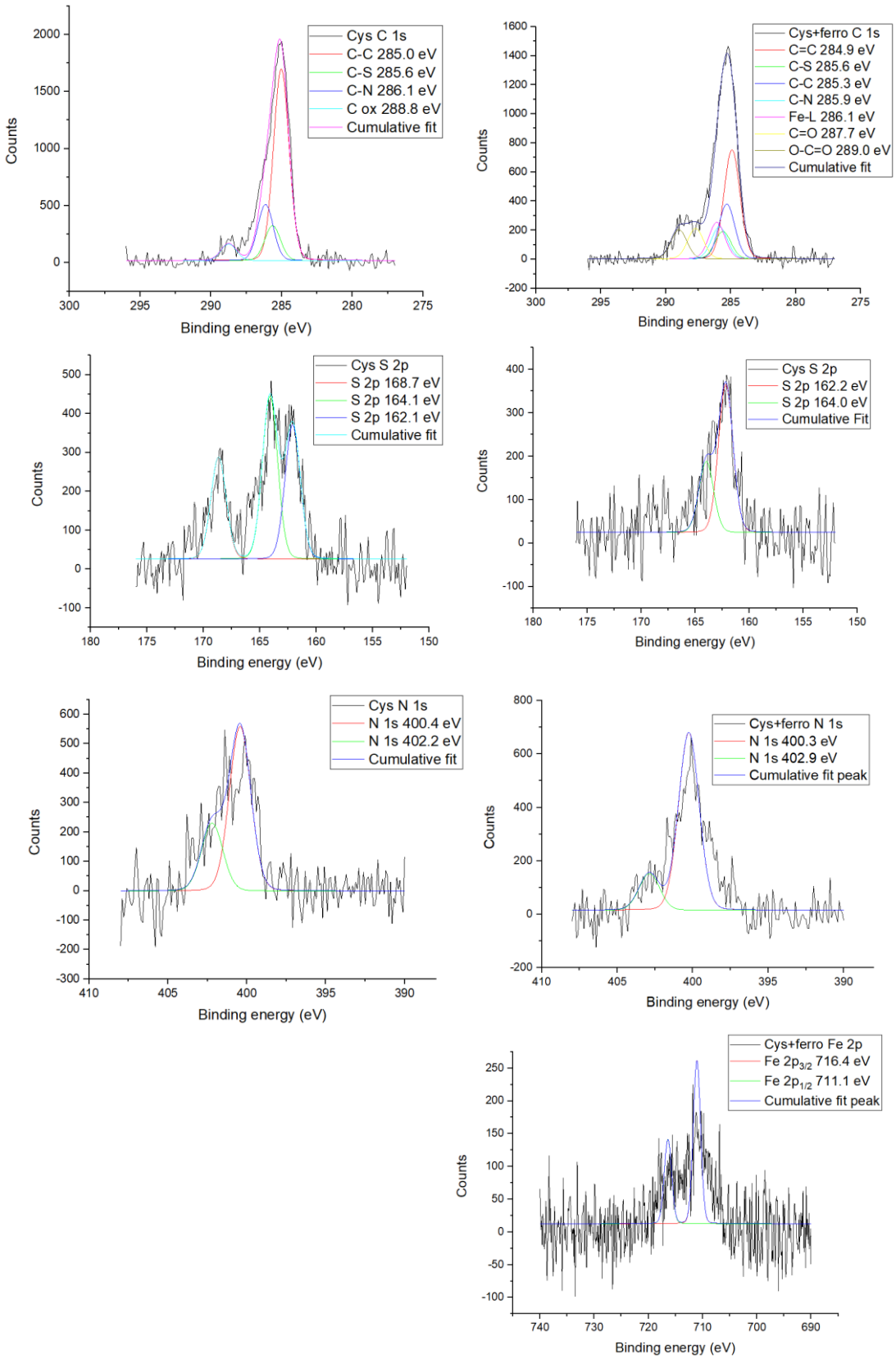


**Figure 19**: (left) the XPS spectrum (C 1s, S 2p and N 1s) of surface functionalization using cysteamine on the gold substrate on quartz; (right) the XPS spectrum (C 1s, S 2p, N 1s and Fe 2p) of surface functionalization using cys+ferro system on the gold substrate.

The XPS spectra of surface functionalization using cysteamine on the gold substrate on quartz is shown in figure 19. The data were replotted using Origin software using Pseudo-Voigt model (90% Gaussian profile). Three peaks were found for cysteamine on gold and two peaks were found to para-aminothiophenol on gold. For SAM of cysteamine on gold, 161.9 eV is for chemically adsorbed gold-thiolate complex, 163.8 eV is for physically adsorbed thiol and 168.9 eV is attributed to functionalization of gold using 'sulfinic acid' caused by UV-ozone processing or direct oxidation by air. For SAM of para-aminothiophenol, 164.1 eV is for physically adsorbed thiol and 170.0 eV is attributed to functionalization of gold using 'sulfonic acid' caused by UV-ozone processing. According to the references[194,195], the binding energy should be 170.3 eV, 168.8 eV, 167.2 eV, 164.0 eV, 162.8 eV and 160.8 eV for S(+VI) 2p, S(+IV) 2p, S(+II) 2p, S(0) 2p, S(-I) 2p and S(-II) 2p respectively. The shift towards higher value may be due to the UV-ozone processing in air or direct oxidaztion by air. In fact, the UV-ozone processing is used to make the physical and chemical adsorption of oxygen gas[196]. Wirde et al.[197] recorded the S 2p spectrum of the self-assembled monolayer of cysteamine and para-aminothiophenol on gold. They found 162.1 eV is attributed to a normal S-Au bond as the result of the chemical adsorption while the second component located at about 163-164 eV is for physical adsorption. This shows similar values to our results. They found also a component with lower binding energy that corresponds to sulfur atoms with a higher degree of coordination to gold atoms than that for the initially adsorbed thiols.

The chemical shift in the signal of the XPS is a common phenomenon. If a thiol group adsorbed on a surface site surrounded by lots of adsorbed oxygen gas, the signal will shift as if the molecule is oxidized.

The C 1s spectrum gives the information of several chemical bonds after the fitting: C-C bond at 285.0 eV, C-S bond at 285.6 eV, C-N bond at 286.1 eV and a signal at 288.8 eV for the oxidized species. For the N 1s spectrum, two peaks are found for the self-assembled monolayer of cysteamine on gold (400.4 eV and 402.2 eV). There is a small deviation in terms of the binding energy value for the cysteamine in the literature of Wirde et al.[197].

For the cys+ferro system (figure 19), the C 1s spectrum exhibits C=C bond at 284.9 eV, C-C bond at 285.3 eV, C-S bond at 285.6 eV, C-N bond at 285.9 eV, iron-ligand ionic bond at 286.1 eV, C=O bond at 287.7 eV and carboxylic acid at 289.0 eV. Compared to the spectrum of cys, new contributions of C=O and Fe-L ionic bond can be seen in the spectrum of cys+fc. The N 1s spectrum shows two peaks: 400.3 eV and 402.9 eV. The two peaks at 716.4 eV and 711.1 eV in Fe 2p spectrum confirmed the existence of attachment of 3-ferrocenoylpropanoic acid on the surface.

For the S 2p spectrum, only a strong peak can be seen at 162.2 eV for the chemical adsorption with gold-thiolate formation and 164.0 eV for physical adsorption. The peak for the oxidized species almost disappeared (168.7 eV), the intensity of the peak of physical adsorption decreased relatively to the intensity of

the peak of chemical adsorption. This observation can be explained by the desorption of aggregated cysteamine from the surface and the part in the 164 eV decreased. The part at 169 eV decreased also but the reason is not clear.

For the Ph system in figure 20, C 1s spectrum gives the signal of C=C bond at 284.9 eV, C-S bond at 285.4 eV, C-N bond at 286.1 eV, and additional bond at 289.5 eV for oxidized species. For S 2p spectra, 170.0 eV for oxidized species, 165.3 eV for the physical adsorption and 163.6 eV for the chemical adsorption. For the N 1s spectrum, only one peak can be seen at 399.9 eV for the self-assembled monolayer of para-aminothiophenol on gold. Also, there is a small deviation in terms of the binding energy value for the cysteamine in the literature of Wirde et al.[197].

For the ph+ferro system in figure 20, the C 1s spectrum exhibits C=C bond at 284.6 eV, C-C bond at 284.7 eV, C-S bond at 285.4 eV, C-N bond at 285.8 eV, iron-ligand ionic bond at 286.7 eV, C=O bond at 287.9 eV and carboxylate at 289.0 eV. Concerning the S 2p spectrum, the fits give 170.6 eV for oxidized species, 163.2 eV for physical adsorption and 162.0 eV for chemical adsorption. Compared to the spectrum of ph, the contribution of C=O and Fe-L ionic bond can be seen in the spectrum of ph+fc. The N 1s spectrum shows only one peak at 400.2 eV and Fe 2p spectrum show a tiny peak at 710.8 eV. Compared to the spectra for cys+ferro system, the relatively low intensity in the Fe 2p spectrum can infer the less coverage of the attachment due to 3-ferrocenoylpropanoic acid in the second step.

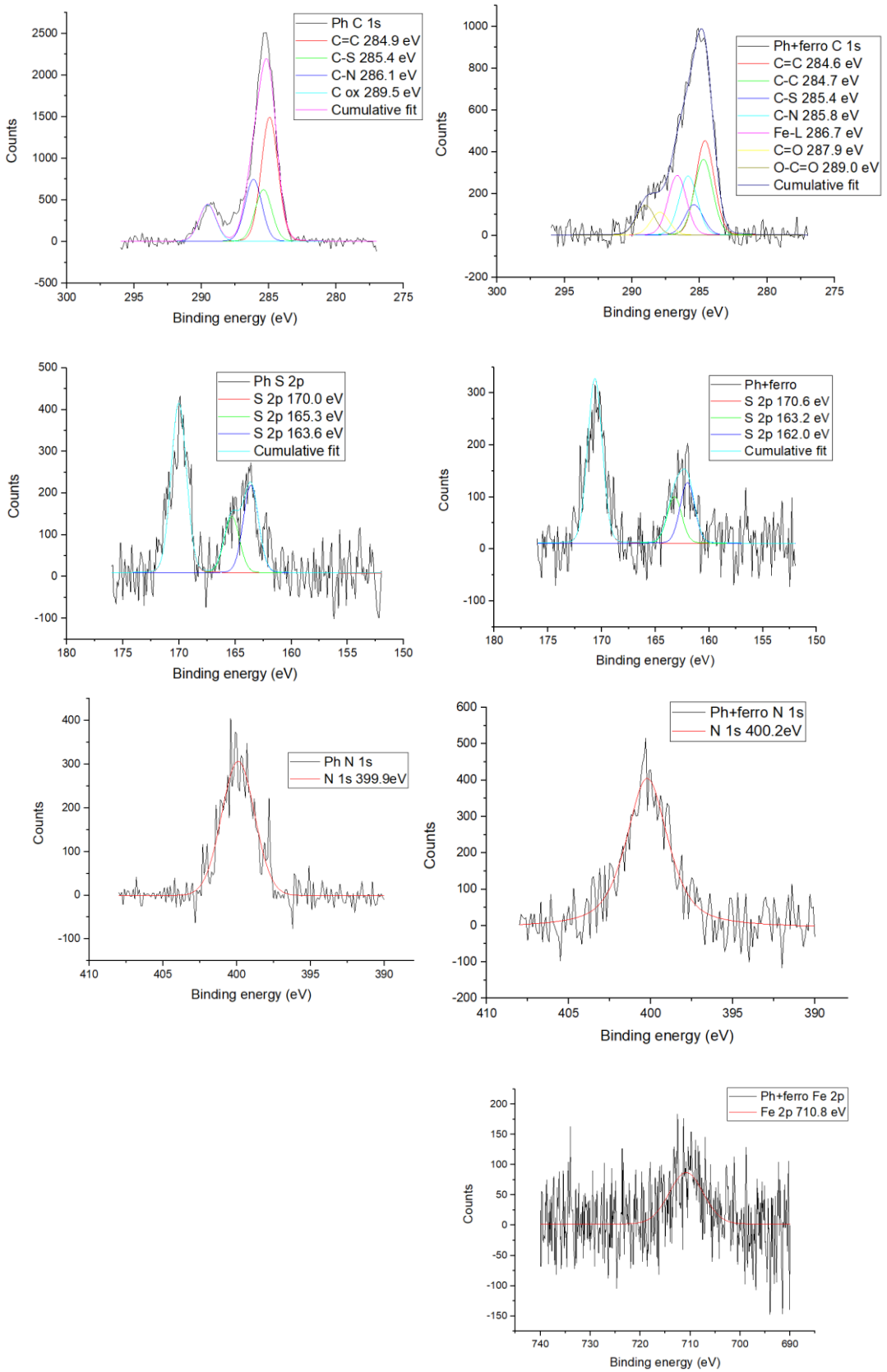


**Figure 20**: (left) the XPS spectrum (C 1s, S 2p and N 1s) of surface functionalization using para-aminothiophenol on the gold substrate on quartz. (right) the XPS spectrum (C 1s, S 2p, N 1s and Fe 2p) of surface functionalization using cysteamine and 3-ferrocenoylpropionic acid on the gold substrate on quartz.

# V. Surface-enhanced Raman spectroscopy

A special nanostructured gold substrate with LSPR (localized surface plasmon resonance) effect[198] was used to prepare the sample for SERS spectra. The Raman spectrum (Figure 21) of 3-ferrocenoylpropionic acid powder was recorded (1068, 1109 and 1659 $cm^{-1}$) as the reference for the SERS spectra of three different systems and the peak at 1110 $cm^{-1}$ (1 $cm^{-1}$ difference can be neglected due to uncertainty) is for the strong symmetrical breathing of ferrocene ring in the molecule[199]. For the result of ferro system, 2 peaks (1347 and 1549 $cm^{-1}$) can be found, and they are the signature of 3-ferrocenoylpropionic acid on the surface (Figure 22 left). For ph+ferro system on the SERS spectra, five peaks can be seen (1076, 1140, 1395, 1443 and 1585 $cm^{-1}$) (Figure 22 right). However, the SERS of cys+ferro system wasn't acquired successfully. The grafting of the cysteamine layer seems to destroy the nanostructuration of SERS substrate.

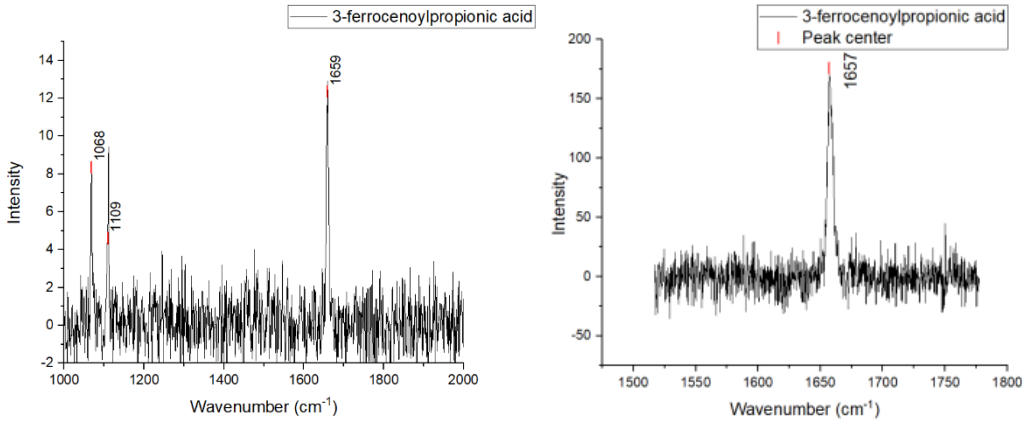


**Figure 21**: The Raman spectrum of 3-ferrocenoylpropionic acid powder (left Raman, right zoomed Raman)

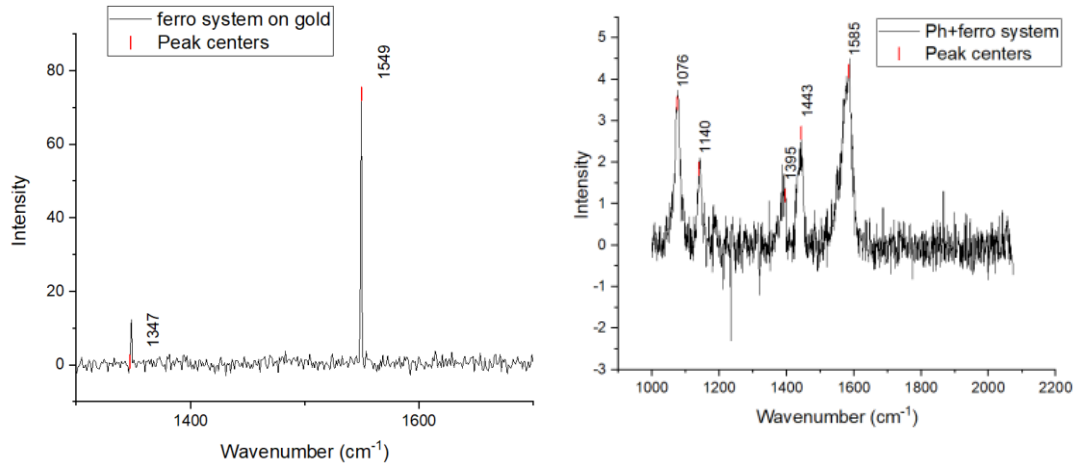


**Figure 22**: The SERS spectrum of self-assembled monolayer of ferro system (left) and ph+ferro system (right)

Sun et al.[187] used tip-enhanced Raman spectroscopy where the tip of the scanning probe microscopy is decorated with nanostructured gold to have the

plasmonic effect for the enhancement of the signal. TERS spectra acquired at the terrace site of Au(111) under irradiation by a 632.8 nm laser. In our experiments we used the same laser wavelength. They found the characteristic features of para-aminothiophenol, with the C–S stretching mode at 1082 $cm^{-1}$ and the C–C stretching mode at 1594 $cm^{-1}$. We have assigned 1076 (C-S stretching), 1140 (C-H bending), 1395 (C-C stretching, C-H rocking, phenyl ring deformation) and 1585 $cm^{-1}$ (C-C stretching) for para-aminothiophenol[200]. It seems that the peaks at 1443 $cm^{-1}$ and 1585 $cm^{-1}$ have a weak contribution of 3-ferrocenoylpropanoic acid.

## VI. Cyclic voltammetry

The surface functionalization using three systems were checked by cyclic voltammetry. As a preliminary study, 5 mM 3-ferrocenoylpropionic acid in anhydrous acetonitrile with 0.1M tetra-n-butylammonium hexafluorophosphate as the electrolyte was tested by cyclic voltammetry. The oxidation potential is $E_{ox}$=0.72V and the reduction potential is $E_{red}$=0.64V. This system is reversible and the current proportional to the square root of scan rate. The result is presented in the figure 23.

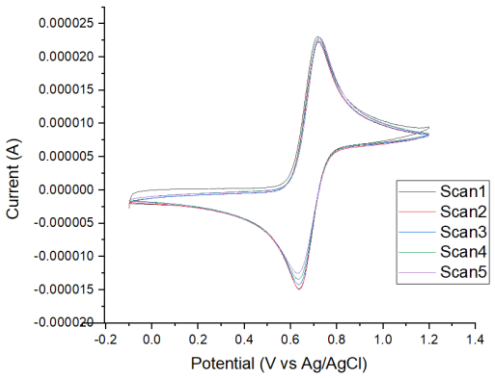


**Figure 23**: Cyclic voltammetry graph of 5mM 3-ferrocenoylpropionic acid in anhydrous acetonitrile with 0.1 M tetra-n-butylammonium hexafluorophosphate as the electrolyte with the scan rate of 50 mV/s.

The redox reaction can be represented by the following equation:

$$(L_1Fe^{+III}L_2)^+ + e^- = L_1Fe^{+II}L_2$$

The figure 24 show the voltammetry measurement obtained on ferrocene derivative-based SAM. Before talking about the difference between the chain using two different linkers, it is important to talk about the reason why an extra peak appeared with a smaller potential. Two peaks can be seen in the Figure 24 (a): first peak centred at 0.2V ($E_{ox}$=0.28V, $E_{red}$=0.12V) and second peak at 0.875V ($E_{ox}$=1.00V, $E_{red}$=0.75V). The origin of the first peak can be illustrated by the difference of the local environment of the ferrocene derivative molecule on the surface. The result of a similar experiment prepared with 48h during the second step functionalization for

cys+ferro system as shown in the Figure 24 (b), the redox peaks shifted, inversed, and centred at 0.75 V ($E_{ox}$=0.6V and $E_{red}$=0.9V). Here is one possible explanation of this evolution: The first 24 h during the second step functionalization, the main process is the reaction of amide bond formation. The peak at 0.875V ($E_{ox}$=1.00V, $E_{red}$=0.75V) reflects the clustered ferrocene group on the surface while the peak centred at 0.2V ($E_{ox}$=0.28V, $E_{red}$=0.12V) reflects isolated ferrocene on the surface. During the second 24 h, the second functionalization continues with higher coverage of ferrocene derivative on the surface. The introduction of the amide bond can increase the stability by interchain hydrogen bond formation. The desorption also happens due to the shift of the clustered ferrocene derivatives.

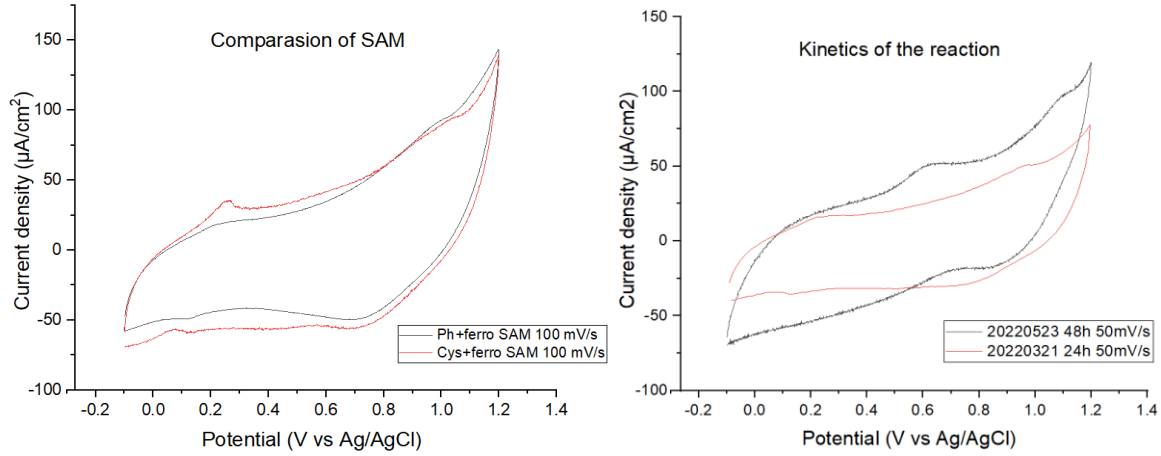


**Figure 24** (a): Cyclic voltammetry graph of ferrocene-terminated monolayer using cysteamine and para-aminothiophenol using 24 h second step functionalization with the scan rate of 100 mV/s (b) Cyclic voltammetry graph of ferrocene-terminated monolayer using cysteamine using 24 h and 48 h second step functionalization with the scan rate of 50 mV/s.

For a global view of comparison of surface functionalization with ferrocene-terminated structure on the surface with different systems and different scanning rate, we used Dropsens 220AT as the substrate to facilitate the measurement. The figure 25 shows the cyclic voltammetry curve of the bare Dropsens substrate in the electrolyte solution. There is no electrochemical reaction when no molecules are adsorbed on the surface. The situation for 3-ferrocenoylpropionic acid on the substrate in figure 26 has two sets of redox reactions. This phenomenon is recorded in various references due to different arrangement of the ferrocene-terminated molecule on the surface[78,201,202].

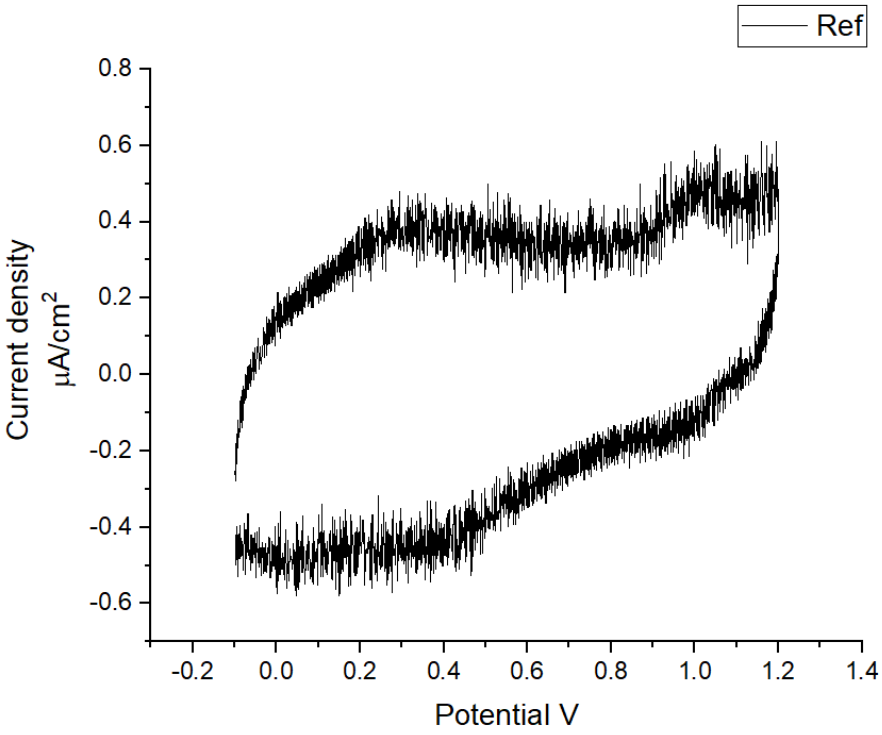


**Figure 25**: Cyclic voltammetry results on bare Dropsens 220AT as the reference

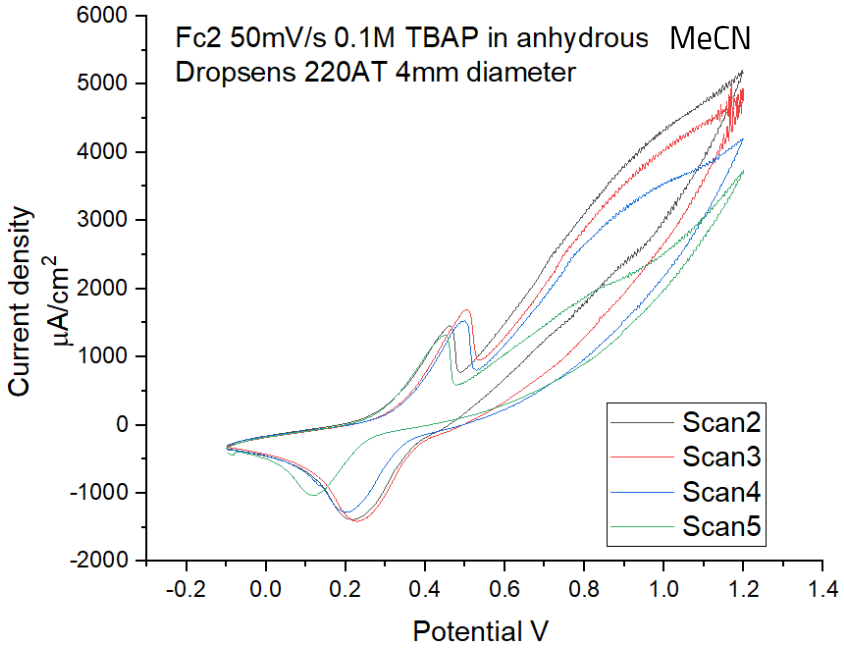


**Figure 26**: Cyclic voltammetry results on Dropsens 220AT with Fc systems.

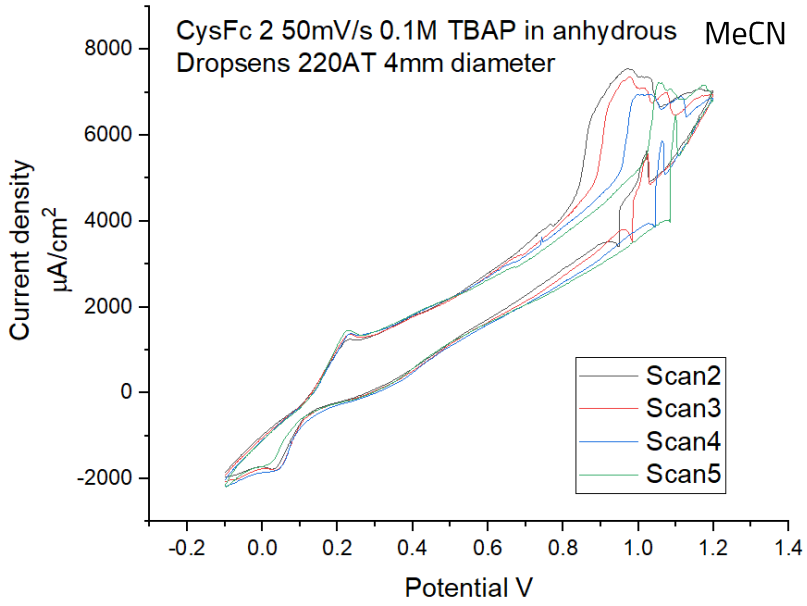


**Figure 27**: Cyclic voltammetry results on Dropsens 220AT with Cys+Fc systems

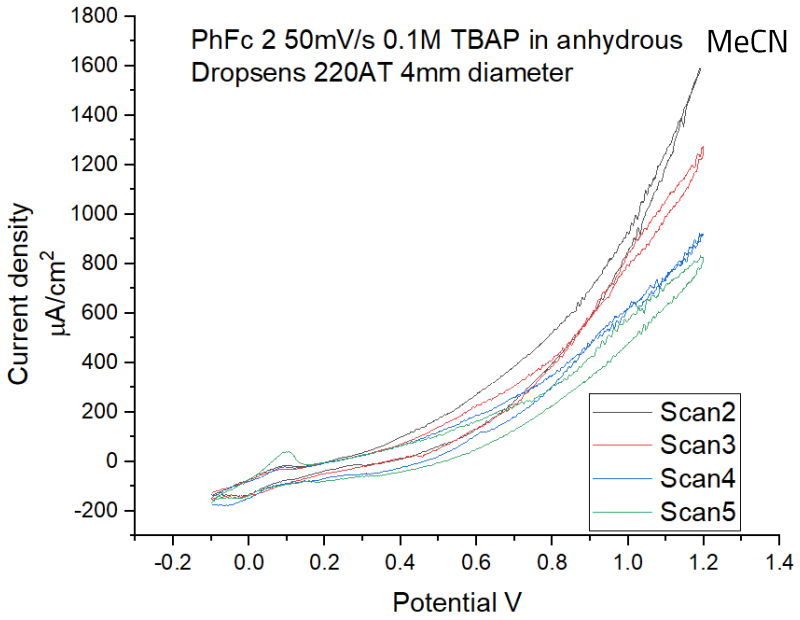


**Figure 28**: Cyclic voltammetry results on Dropsens 220AT with Ph+Fc systems

| | Fc (V/vs Ag/AgCl) | Cys+Fc (V/vs Ag/AgCl) | Ph+Fc (V/vs Ag/AgCl) |
|---|---|---|---|
| 50mV/s | $E_{ox1}$: 0.4 V $E_{red1}$: 0.25 V<br>$E_{ox/red2}$: 0.7-0.9 V | $E_{ox1}$: 0.25 V $E_{red1}$: 0.05 V<br>$E_{ox2}$: 1.1 V $E_{red2}$: 1.0 V | $E_{ox1}$: 0.1 V $E_{red1}$: 0.00 V<br>$E_{ox2}$: 0.95 V $E_{red2}$: 0.75 V |

**Table 1**: Comparison of cyclic voltammetry results on Dropsens 220AT with different systems

When the scan rate is 50mV/s, the oxidation occurs at 0.4V and reduction at 0.1V with a current density 1.5mA/cm$^2$. The second set is at about 0.7-0.9V. The current density is proportional to the scan rate of cyclic voltammetry. For cys+fc system in figure 27 with 50mV/s as the scan rate, there are also two sets of redox reaction. The first redox reaction is centred at 0.15 V ($E_{red}$= 0.05V and $E_{ox}$= 0.25V) and the second at 1.05V ($E_{red}$= 1.00V and $E_{ox}$= 1.1V). The current density for each redox reaction is 2 mA/cm$^2$. The lower redox potential is for isolated ferrocene derivative on the surface and the higher redox potential is for clustered ferrocene derivative on the surface.

The situation for the ph+ferro system in figure 28 with 50 mV/s as the scan rate is a little bit different. The first redox reaction is centred at 0.05 V ($E_{red}$= 0.00 V and $E_{ox}$= 0.1 V) and the second at around 0.4-0.8 V. The current density for each redox reaction is 0.2 mA/cm$^2$. Several information can be extracted by looking at these data. By looking at the absolute value of redox current density, the cys+fc system has the highest ferrocene derivative density on the substrate since the signal we see from the cyclic voltammetry comes from the redox reaction of ferrocene derivative. There are two sets of redox reaction indicating different local environment for the ferrocene derivative for cys+ferro and ph+ferro systems and there are only one for ferro system. The reason for this is that the functionalization reaction is maybe linked to uncompleted coverage and/or due to the structure of underlayer of aminothiol molecule.

By looking at the potential of the reduction of redox reaction 1, the Fc system is centred at 0.25 V, Cys+ferro system is centred at 0.05 V and 0.00 V for the Ph+ferro system. Consequently, it appears that the first layer of para-aminothiophenol has an effect of potential modulation of 0.25 V and 0.20 V towards lower potential for the first layer of cysteamine. It appears that the shift caused by the layer of cysteamine is less.

# VII. Conclusion

The three different ferrocene-terminated surface functionalization on gold were carefully prepared and the quality was checked by cyclic voltammetry, atomic force microscopy, scanning tunnelling microscopy, X-ray photoelectron spectroscopy and surface-enhanced Raman spectroscopy. By changing the experimental conditions and the molecule, the structural, chemical composition and electrochemical properties of ferrocene-terminated surface functionalization exhibit a modification. For the surface functionalization, ferro system has the highest coverage and the best electrochemical property but the surface density is not very high. Cys+ferro system has the highest ferrocene derivative density but the coverage can be increased due to the existence of the signal for isolated ferrocene derivatives. Ph+ferro system shows similar structural and chemical composition properties than cys+ferro system, however, the current density for Ph+ferro system is smaller maybe due to the organisation of the self-assembled monolayer. Two redox peaks were observed which could suggest two possible organizations for the ferrocene. Importantly, cyclic voltammetric characterization revealed a shift in the redox peak values depending on the nature of underneath SAM, which represents the expected polarization modulation effect exerted by the first layer.

# C. Conclusion

In this chapter, the goal was to show the feasibility of the potential modulation using the self-assembled monolayer of aminothiol molecules due to their intrinsic electrical dipole. Cysteamine, para-aminothiophenol and 3-amino-5-mercapto-1,2,4-triazole were adopted to prepare the self-assembled monolayer. The potential modulation effect can be seen according to the result of cyclic voltammetry. The first layer of para-aminothiophenol has an effect of potential modulation of 0.25 V and 0.20 V for the first layer of cysteamine to shift the signal of the electrochemical reaction towards higher potential for the first layer of cysteamine. This phenomenon shows the feasibility of the self-assembled monolayer of dipolar molecule like push-pull chromophore to achieve the modification of the electrical properties.

The latter point will be the scope of the next chapter addressing the synthesis of a novel non-charged push-pull chromophore whose intrinsic dipole should modify the electrical signal applied to the active top layer.

# 4. Push-pull chromophore

Once the principle of polarization modulation has been observed using model molecules, we can now consider applying it using a more efficient push-pull chromophore. For this purpose, the first step is to synthesize such a novel non-charged push-pull chromophore. This is addressed in the present chapter presenting the synthesis work that I have carried out in CINaM.

## A. Synthesis of the push-pull chromophore

All chemicals were purchased from Sigma-Aldrich, Alfa Aesar, Fluorochem, Abcr, TCI-Europe and Acros Organic and used as received from the commercial sources, unless otherwise stated, without further purification. Infrared spectra were recorded on an Agilent Cary 630 FTIR spectrometer. UV-visible absorption spectra were obtained on a Varian Cary 1E spectrophotometer. The electronic absorption maxima ($l_{max}$) are directly extracted from absorption spectra of the chromophore-based solution. $^{1}H$ and $^{13}C$ NMR spectra were recorded on JEOL-400 at 400 MHz, and 101 MHz respectively. The starting pulse of NMR is 45° and the signal is recorded with a 5s delay to the starting pulse. The accumulation of the spectrum is at most 128 for the NMR spectroscopy except $^{13}C$ (4096 accumulation). The low-resolution mass spectroscopy and CHNS elemental analysis were made in the Spectropôle facility of Aix-Marseille University. All reactions were magnetically stirred and monitored by thin-layer chromatography (TLC) using E. Merck silica gel 60 F254 precoated plates (0.25 mm) and flash chromatography was performed on silica gel 60 (230–400 mesh) from Macherey-Nagel EURL.

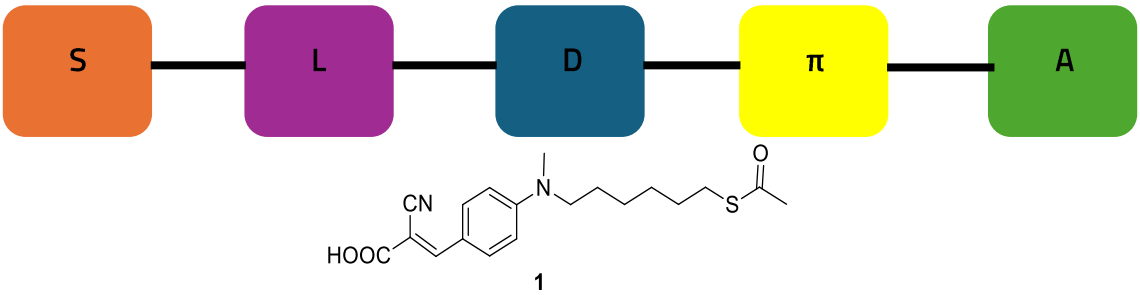


**1**

**Figure 1**: (top) the structure of the push-pull chromophore to form self-assembled monolayer on the surface and (**1** bottom) the push-pull chromophore structure in the PhD work. D in blue box is for the electron-donating group, π in yellow box is for the π-conjugated spacer, A in green box is for the electron-withdrawing group, L in purple box is for the alkyl chain linker and the S in red box is for the surface grafting group.

The push-pull chromophore has three parts in the structure: the electron-donating group, the π-conjugated spacer, and the electron-withdrawing group. In our case, the push-pull chromophore is added by the surface grafting group to enable the functionalization of the molecule on the surface, the alkyl chain which helps the reorganization of the structure for the molecules on the surface. The

electron-donating group is dialkylamine (-$NR_2$), the electron-withdrawing group is based on cyano group (-CN). The length for the alkyl linker chain must be long enough (at least six carbons) to form a self-assembled monolayer on the surface. This is the reason why the length of the alkyl chain is six in the structure of the push-pull chromophore. The thioacetate group is to enable the functionalization of gold. It will be deprotected on the surface to start the surface functionalization. The organosulfur group is very common for the surface functionalization of the substrate.

The final goal to synthesize the push-pull chromophore is to use its intrinsic electrical dipole to achieve the potential modulation on the surface. In the final part of the development of the biosensor, the additional layer of the self-assembled push-pull chromophore can shift the potential of the electrochemical reaction and the potential to induce the change of the conformation of the oligopeptide chain. This shift can be tailored with different combination of the components. The electron-withdrawing group is based on cyanoacetic acid. Compared to the electron-withdrawing group in the article of Malytskyi *et al.*[6], and the cyanoacrylic acid is special with the carboxylic acid. This is a trade-off because the electron-withdrawing ability is weaker using cyanoacrylic acid because one of the nitriles is replaced by carboxylic acid. However, the push-pull chromophore has a new functional group. The cyanoacrylic acid can be used for further extension by forming ester or activated ester group. It is good to graft biomolecules like proteins (amino group) onto the push-pull chromophore on the surface.

The first reaction to form **3** (figure 2) is the nucleophilic substitution of N-methylaniline (CAS 100-61-8) **2** (figure 2) with 6-bromohexanol (CAS 4286-55-9) in the anhydrous THF using triethylamine as the base rather than aqueous sodium hydroxide solution under reflux condition. Also, tetrabutylammonium bromide is no longer needed as the phase transfer catalyst since the reaction medium has only one phase. After the column chromatography using silica gel, the best yield is about 72%.

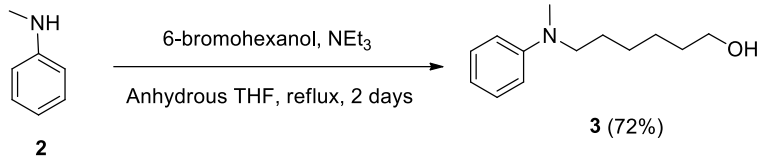


**2** **3** (72%)

**Figure 2**: the scheme for the nucleophilic substitution to form **3** from **2** for the novel push-pull chromophore in the PhD work.

The use of the alcohol functional group is with the aim to graft on the metal oxides surface by M-O-M condensation reaction. However, the alcohol functional group is very reactive under the reaction condition for the further synthesis. The strategy to turn the alcohol group to thioacetate in the article of Malytskyi *et al.* Is the following: the first reaction is the bromation reaction of alcohol group using $PBr_3$ to form **4** (figure 3) in chloroform at 0°C. The second reaction is the nucleophilic

substitution using potassium thioacetate in N,N-dimethyl formaldehyde at room temperature to form **5** (figure 3).

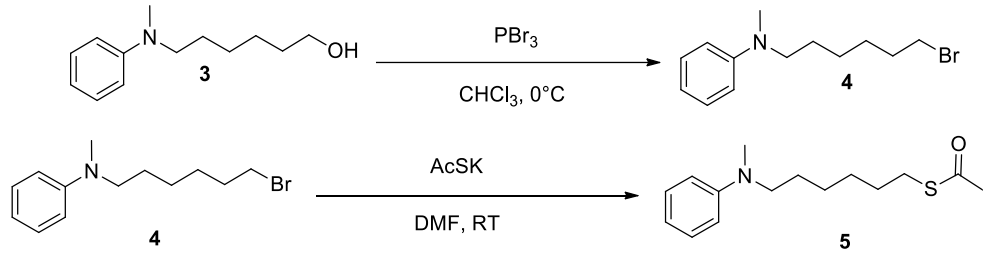


**Figure 3**: the scheme for the transformation of alcohol to thioacetate in the PhD thesis of Malytskyi *et al.*

There are other ways to activate the alcohol group by using tosylate chloride and triflate chloride. To avoid the use of highly toxic $PBr_3$, the thioacetate group is directly added in the push-pull chromophore considering the relative inertness of thioacetate group. The new strategy to form thioacetate from alcohol is here: the first reaction is the nucleophilic substitution of mesylate chloride (CAS 124-63-0) using alkyl alcohol in anhydrous THF and triethylamine as the base at 0°C to form **6** (figure 4). And then the nucleophilic substitution of mesylate using potassium thioacetate (CAS 4286-55-9) in ethanol under reflux condition to form **5** (figure 4). This new strategy compared to the way in the work of Malytskyi et al.[6] has less steps and a higher overall yield (92%). Lee et al.[203] and Hoang et al.[204] used also mesylate chroride for the activation of the alcohol and the yield is 94% for the crude product and 88% respectively.

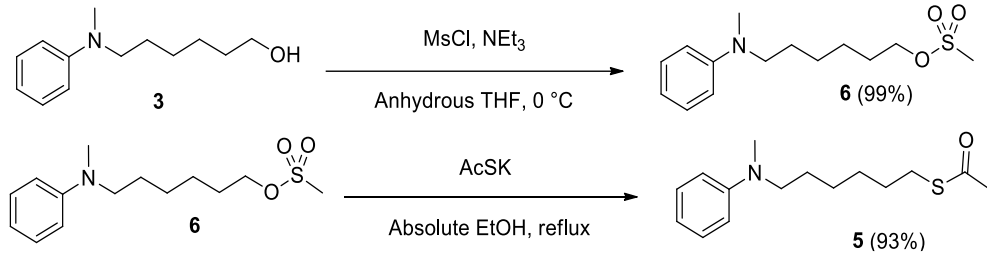


**Figure 4**: the scheme for the transformation of alcohol to thioacetate during the PhD work

The next step is the Vilsmeier-Haack reaction to add a formyl at the para position of the dialkylaniline. This reaction uses Vilsmeier-Haack reagent, which is the product of DMF (CAS 68-12-2) and the phosphoryl chloride (CAS 10025-87-3). The yield for this reaction is 64% after the silica-gel chromatography (reaction from **5** to **7** in figure 5). Jiao et al.[205] used this reaction to prepared boron-dipyrromethene based dye with a yield of 72%-84% whereas Baert et al.[206] used this reaction for the thieo[2,3-b]indole-based substrate and the yield is from 72% to 99%.

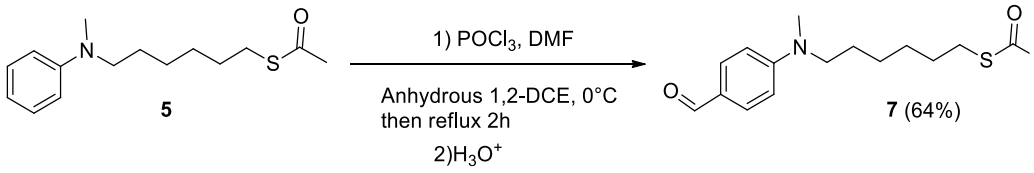


**Figure 5**: the scheme for the Vilsmeier-Haack reaction (64%) during the PhD work

Then the following reaction is to take the Knoevenagel reaction using piperidine in ethanol under reflux condition to form **8** (figure 6) from **7** (figure 6). The piperidine (CAS 110-89-4) can absorb the proton of carboxylic acid (not catalytic) and make its salt, activate the aldehyde group, and render it more electrophilic (catalytic effect). Also, the salt of piperidine and carboxylic acid increases the probability to get the final product with E configuration for the carbon-carbon double bond according to the E1 mechanism. Moreover, the reaction condition becomes less harsh, and the yield is 54% after the precipitation, washing and drying process. For this step, Fauvel et al.[207] found a yield from 21%-63%, Kang et al.[208] had a yield of 80% and Lu et al.[209] found 50%-72%.

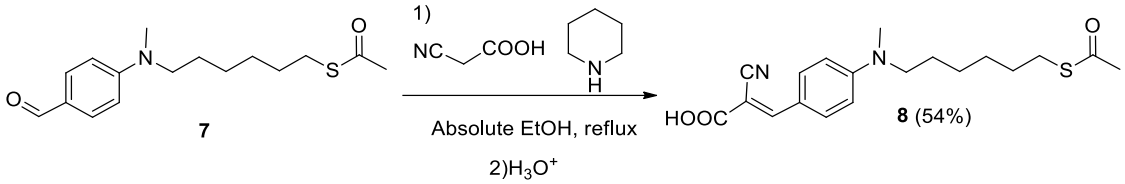


**Figure 6**: the scheme for the Knoevenagel reaction for the push-pull chromophore synthesis.

However, the thioacetate can be oxidized to form disulfide structure after using cyanoacetic acid in excess, as can be seen in the mass spectrum (Figure 7) of a batch with a peak at m/z=634.3. To avoid misunderstanding, the compound used for further characterization will be shown clearly and no reason to mix the result and the structure of the push-pull chromophore for the sake of the rigor in scientific research. Compound **9** in figure 7 is formed with the disulfide structure. The reason for this is due to the excess of the cyanoacetic acid which ethanolysed the thioacetate and the oxidation occurs at reflux condition.

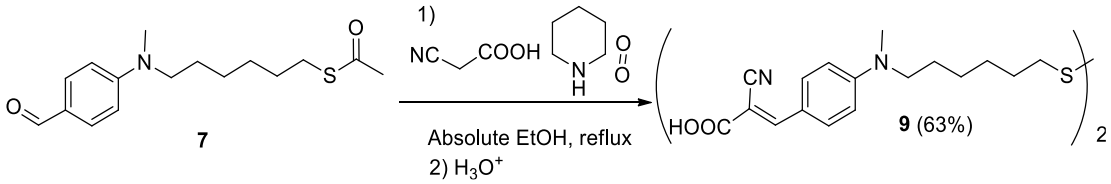


**Figure 7**: the scheme for the formation of disulfide via the Knoevenagel reaction for the push-pull chromophore synthesis during PhD work.

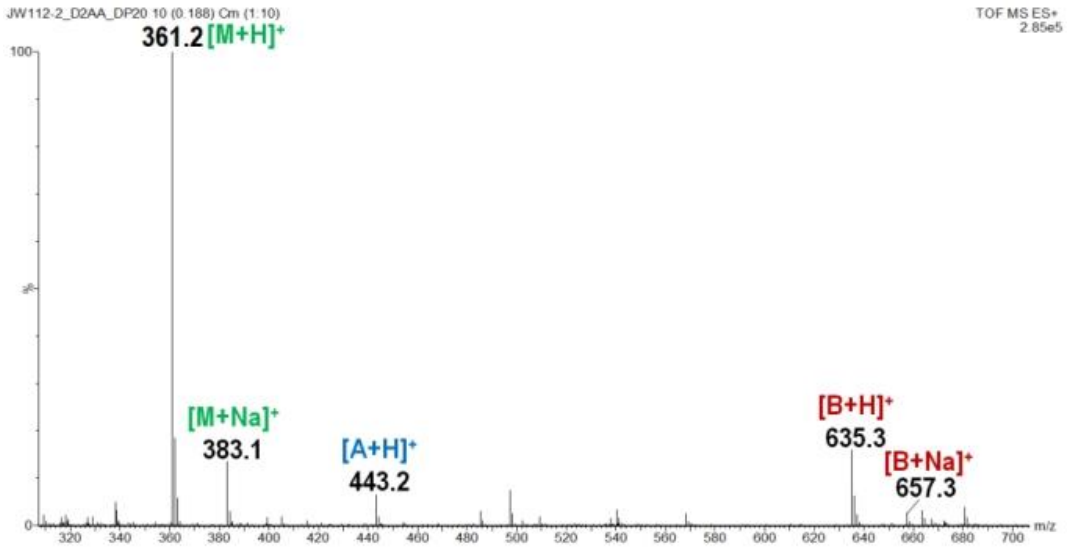


**Figure 8**: positive electrospray mass spectrum of a batch of compound 6 after 3 months storage in air

Apart from the targeted push-pull chromophore, there is a push-pull chromophore with disulfide structure. To make the push-pull chromophore with the disulfide structure, the N,N-bis(2-chloroethyl)aniline (**10**) precursor (CAS 553-27-5, Fluorochem) was dissolved in the ethanol to make the substitution using potassium thiocyanate[210,211] (CAS 333-20-0, Alfa Aesar) in figure 9. The reaction to form **11** has a yield of 73.4%.

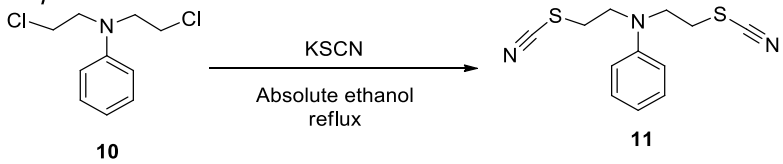


**Figure 9**: the scheme for the nucleophilic substitution using potassium thioacetate.

The second reaction is the reduction of the thiocyanate (oxidation state number is 0 for the sulphur) to form the molecule with disulfide **12** (oxidation state number -I for the sulphur) by using sodium hydroxide (CAS 1310-73-2) in absolute ethanol in figure 10[212]. The reaction works with a lower yield after the purification by column chromatography (50.4%).

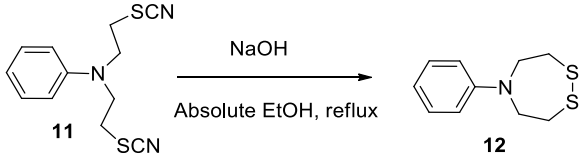


**Figure 10**: the scheme for the disulfide formation

The final reaction to form disulphide-based push-pull chromophore **13** is the Vilsmeier-Haack reaction in figure 11, however, the yield is 12.6% after the purification by column chromatography.

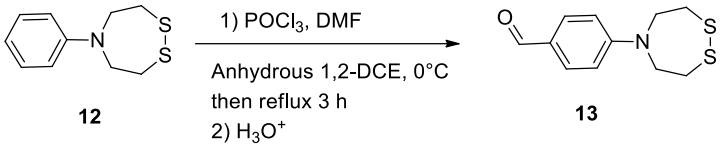


**Figure 11**: the scheme of Vilsmeier-Haack reaction for the disulfide-based push-pull chromophore

Moreover, in terms of the push-pull chromophore using rhodanine-N-acetic acid, the reaction is as same as the aldol condensation reaction using 4-(dimethylamino)benzaldehyde (CAS 100-10-7), rhodanine-N-acetic acid (CAS 5718-83-2) and piperidine as the base. The yield of the reaction is almost quantitative after the acidification, filtration under the reduce pressure and washing (99%). For the structure, this unconventional Z-configuration molecule is thermodynamically more stable because of the strong hydrogen bonds. The planar molecular structure ensures a good efficiency for the electron transport during the internal charge transfer process. **15** in figure 12 is the first pyrene-like molecule for the crystalline molecular crystal on the surface. For this step, Avhad et al.[213] found a yield of 81%-89% and 24%-69% for Fernandes et al.[214].

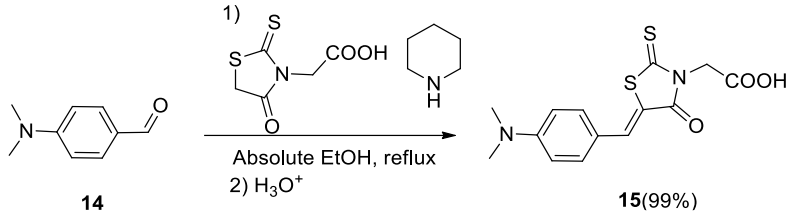


**Figure 12**: the scheme for the reaction to form push-pull chromophore using rhodanine-N-acetic acid

After all the synthesis, we think that there is a huge space to not only optimize the reaction condition to increase the yield and to increase the purity (the spectrum is not clean, fortunately, the major part is the target molecule as the spectroscopy is also quantitative), but also to optimize the structure of the push-pull chromophore for a stronger electrical dipole for the further PhD work about the functionalization of the surface.

# B. Push-pull chromophore characterization by UV-vis spectroscopy

The UV-visible spectrophotometry is the basic method to characterize the electronic transition of the molecule, especially used in the domain of dyes and pigments. Here, we dissolve our synthesized push-pull chromophore in a solvent in a glass cuvette and the spectrum is recorded. Three solvents (THF, DMF and ethanol) were adopted to see the influence of the solvent on the photophysical properties of the push-pull chromophore, such as the wavelength of the absorption maximum and the molar extinction coefficient. All the spectra were recorded from 800 nm to 300 nm with a scanning speed of 300 nm/min.

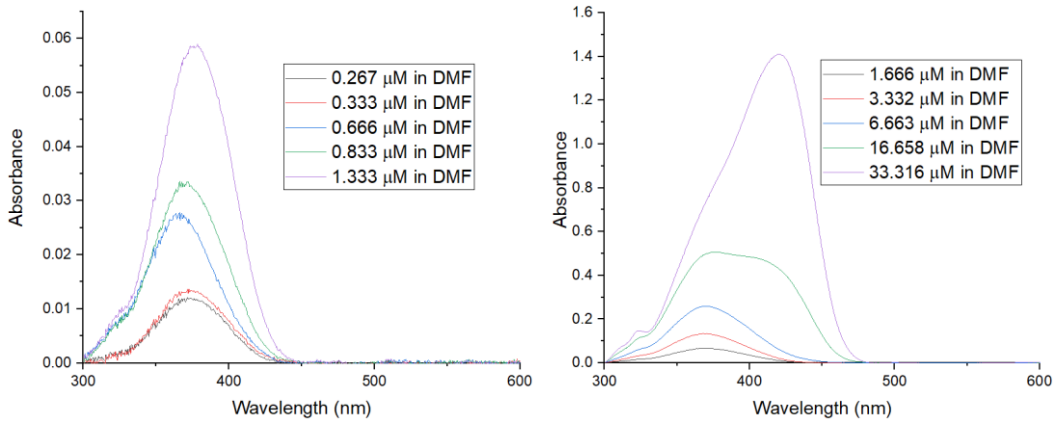


**Figure 13**: the UV-vis spectrum of compound 9 with different concentrations in DMF

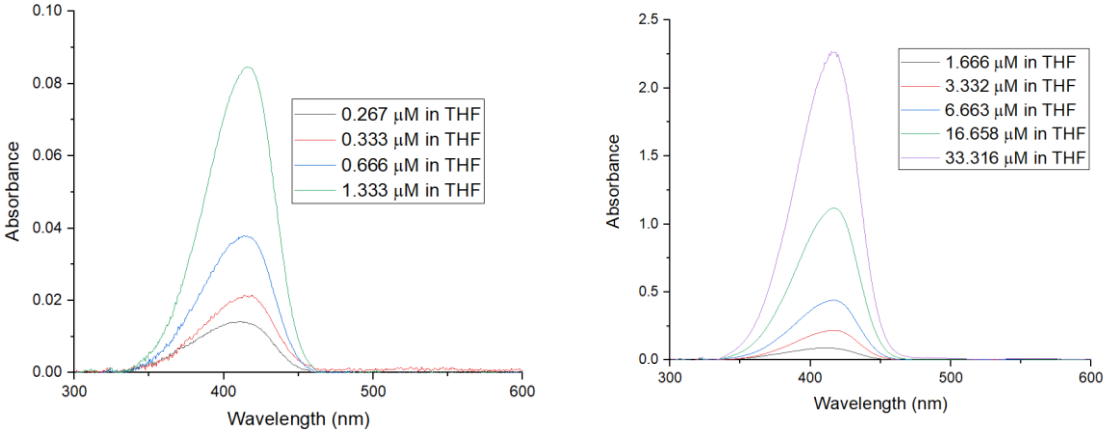


**Figure 14**: the UV-vis spectrum of compound 9 with different concentrations in THF

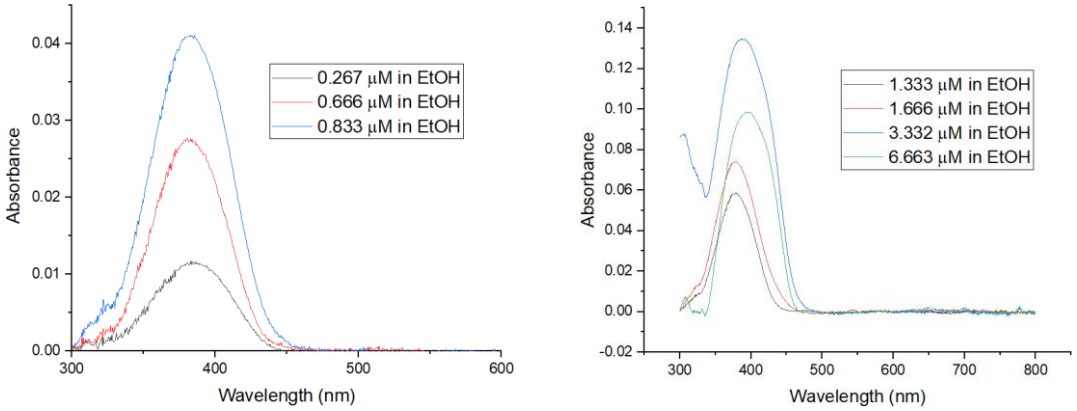


**Figure 15**: the UV-vis spectrum of compound 9 with different concentrations in EtOH

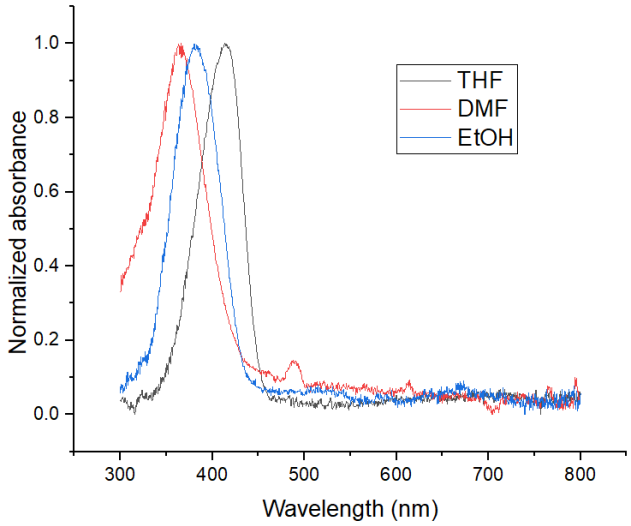


**Figure 16**: the normalized spectrum of the compound 9 in different solvents

After plotting all the spectra, the wavelength for the absorption maxima is recorded for different concentrations, also the value for the absorbance at this wavelength. Then, a series of linear regression using Beer-Lambert law[215,216] is done to determine the value of molar extinction coefficient.

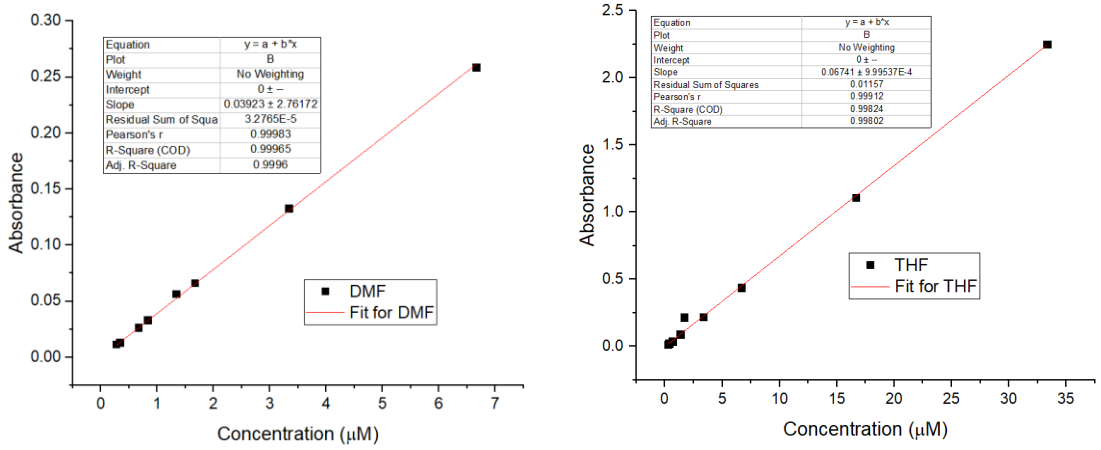


**Figure 17**: (left) the linear regression for the compound 9 in DMF; (right) the linear regression for the compound 9 in THF.

The push-pull chromophore represents the strongest electrical dipole in THF. In the UV-vis spectrum, the higher the value of the absorption in the spectrum, the stronger the electrical dipole. The HOMO-LUMO transition is a π-π* electronic transition. The maximum of the optical absorption is 371nm in DMF, 382nm in EtOH and 415nm in THF. Also, the highest molar extinction coefficient is recorded in figure 18 in THF as the solvent.

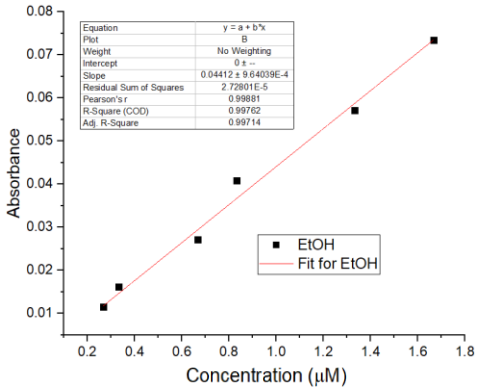


| Solvent | log ε(λ) ($cm^2$/mol) |
|---|---|
| EtOH | 7.64 (382nm) |
| DMF | 7.59 (371nm) |
| THF | 7.83 (415nm) |

**Figure 18**: (left) the linear regression for the compound 7 in EtOH; (right) the table for the summary.

Another discussion point is the aggregation situation of the push-pull chromophore in different solvent. For all the experiments conducted, the push-pull chromophore is solubilized in the solvent; however, the solvation situation is not the same for the concentrations. The aggregation occurs if the molecules is not well solvated, or the concentration of the molecule is too high. Fortunately, the validity of the Beer-Lambert law is ensured for our data and no concentration is out of the linear region. However, as the concentration increases, the maxima of the absorption redshifts or two peaks appear at the same. The validity of the Beer-

Lambert law is no longer here if this situation is encountered. This is the evidence of the formation of aggregation. As in the aggregation, two molecules are so close that their electronic structure changes and they represent a common electronic behaviour. The is called the J-aggregation and in this case, the push-pull chromophore has a head to tail structure in the solution. The other one is called the H-aggregation and a blue-shift of the maxima of the absorption can be observed and, in this case, the push-pull chromophore has a parallel structure in the solution[217,218].

As the concentration is very low, no aggregation occurs, and the maxima of the absorption doesn't move. In ethanol, the appearance of the H-aggregation when the concentration is below than 4 μM. When the concentration reaches about 6 μM, the appearance of the J-aggregation is evidenced by the redshift of the absorption maxima about 10 nm. For DMF, the J-aggregation happened as the concentration is higher than 30 μM, as a peak with a redshift about 30 nm appeared and replaced the initial absorption peak. THF is the best solvent in terms of the solubility and the solvation of the push-pull chromophore. The validity of the Beer-Lambert law is ensured, and this value of the upper limit of the concentration for the validity of Beer-Lambert law is limited by the saturation of the detector of the UV-vis spectrophotometry.

At the same concentration of the push-pull chromophore, the absorption maxima are 371nm in DMF, 382nm in EtOH and 415nm in THF. Moreover, the differences of transition energy in the different solvents are 2082 $cm^{-1}$ and 776 $cm^{-1}$, which corresponds to the transition energy in the vibrational transition. Due to the limitation of the spectrophotometry for the resolution, all the peaks cannot be resolved. However, the tendency is still here for the further interpretation. Here is a possible assumption: the property of the HOMO-LUMO electronic transition[219] is influenced by the local environment which is composed by the surrounding solvent molecules. Different surroundings can shift the electronic density of the HOMO and LUMO level[220], which results in the difference of the distance between the electron-donating group and the electron-withdrawing group. In fact, the electronic transition is a vertical transition and there is a factor called Franck-Condon overlap. Since only the vertical transition is allowed, for the same electronic transition, the vibronic transition is allowed only for vibrational energy states whose vertical overlap is not zero. Also, according to the Maxwell-Boltzmann distribution[221,222], there is a not negligible probability to find the electron on the excited vibrational energy states for the fundamental energy states for the electronic transition. In the figure 16, the horizontal axe represents the interatomic distance.

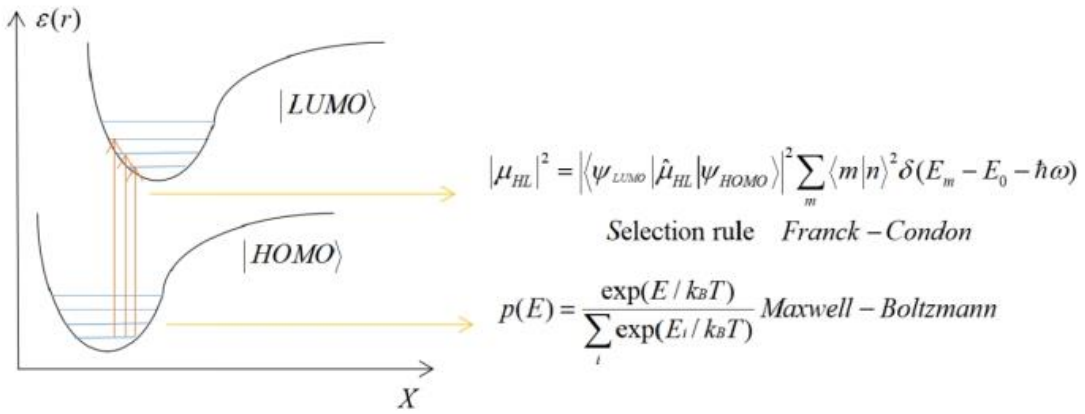


**Figure 19**: the principle of the different vibronic transitions

For our push-pull chromophore molecules, the X is the distance between the electron-donating group and the electron-withdrawing group. In fact, the electronic density of the HOMO is in the part of the electron-donating group and the LUMO is in the part of the electron-withdrawing group. If the system is an atom or an ion, the HOMO-LUMO transition is vertical since it is a transition from the inner shell to an outer shell or even thin the same shell. For the push-pull chromophore, the distance X is very large. The high value of molar extinction coefficient comes from the phenomenon called internal charge transfer (ICT)[223,224] from the electron-donating group to the electron-withdrawing group along the π-conjugated carbon skeleton with a high electron mobility.

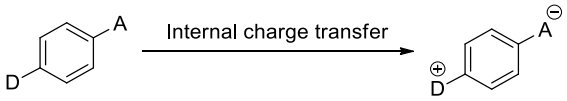


**Figure 20**: the scheme for the internal charge transfer process

In this case, the schema in figure 16 for the vibronic transitions is different in different solvents. This induces different Franck-Condon overlap for different vibronic transitions. It is the interpretation for the different absorption maxima for the same push-pull chromophore in different solvents. Besides, the molar extinction coefficient is the highest in THF and the surrounding media constructed by THF molecules can induce a better linearity and a better coplanarity between the electron-donating group and the electron-withdrawing group for a better internal charge transfer process. The similar phenomenon is observed also for the aggregation process of the formation of the primary aggregates of polythiophene chains.

# C. Conclusion

In this chapter, several novel push-pull chromophores (**8**, **9**, **13** and**15**) have been synthesized with innovative structure having potential for many fields. Then a thorough chemical analysis was done to determine the structure of the push-pull chromophore and the photophysical properties of the push-pull chromophore with several characterization methods. Our novel push-pull chromophore attained all the requirements to be considered as a push-pull chromophore for the functionalization for the next stage of the PhD.

# D. Experimental part

6-(methyl(phenyl)amino)hexan-1-ol

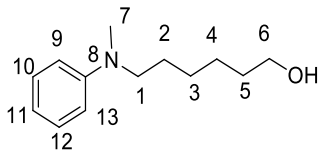


6.0 mL N-methylaniline was dissolved in 30 mL anhydrous THF under argon atmosphere. 7.4 mL 6-bromohexanol and 9 mL triethylamine were added. The mixture was heated to reflux for at least 2 days. The reaction is stopped, and the product was extracted by DCM for 3 times after the cooling. The organic phase was washed by distilled water for two times. The solvent was removed by rotary evaporator after drying by anhydrous sodium sulphate. After the column chromatography using ethyl acetate and petroleum ether as the eluent (1:9 and 1:2), 8.206g product was obtained (72%).

NMR spectrum:

$^{1}$H NMR (400 MHz, $CDCl_3$) δ, ppm: 7.28 (2 H, H-$C_{10}$ and H-$C_{12}$, t), 6.74 (3 H, H-$C_9$,H-$C_{11}$ and H-$C_{13}$, m), 3.67 (2 H, $H_2$-$C_6$, t, J = 6.37 Hz), 3.36 (2 H, $H_2$-$C_1$, t, J = 7.65 Hz), 2.97 (3 H, $H_3$-$C_7$, s), 1.63 (4H, $H_2$-$C_2$ and $H_2$-$C_5$, m),1.43 (4 H, $H_2$-$C_3$ and $H_2$-$C_4$, m).

$^{13}$C NMR (101 MHz, $CDCl_3$) δ, ppm: 149.45, 129.27, 115.98, 112.22, 63.02, 52.84, 38.42, 32.86, 27.10, 26.76, 25.80.

ESI-MS+ spectrum:

m/z=208.2 for $[M+H]^+$, thus M = 207.2 g/mol.

$^{1}H$:

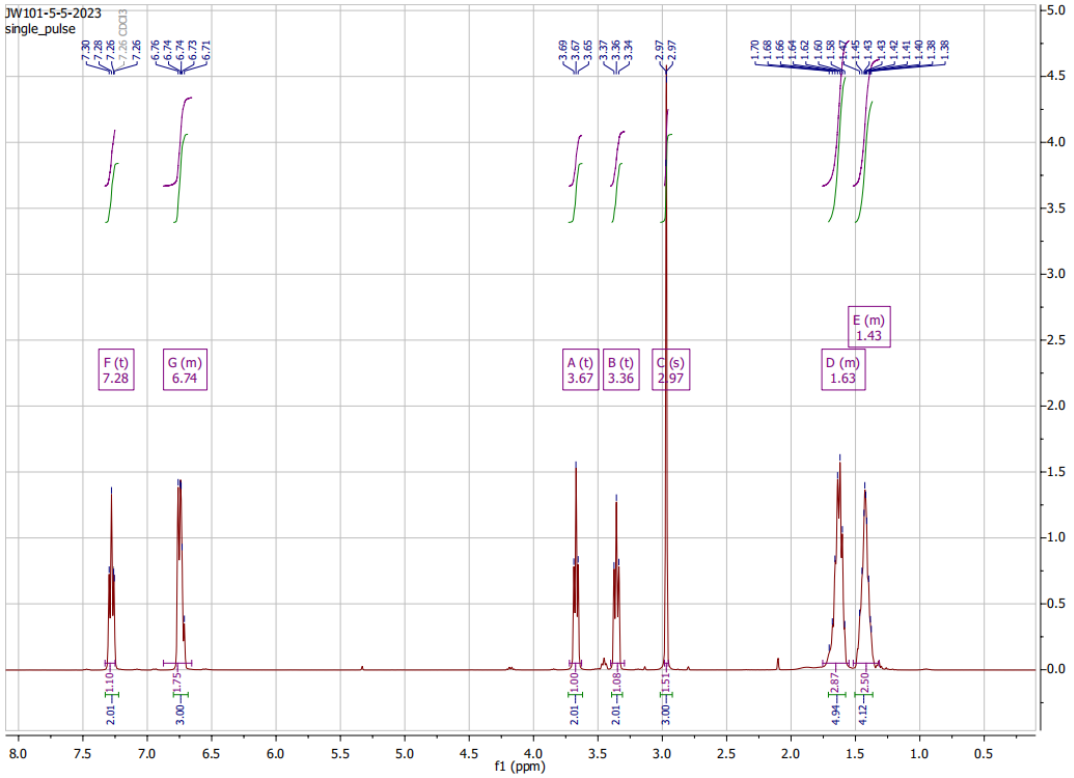
JW101-5-5-2023
single_pulse
F (t)
7.28
G (m)
6.74
A (t)
3.67
B (t)
3.36
C (s)
2.97
D (m)
1.63
E (m)
1.43
f1 (ppm)

$^{13}C$:

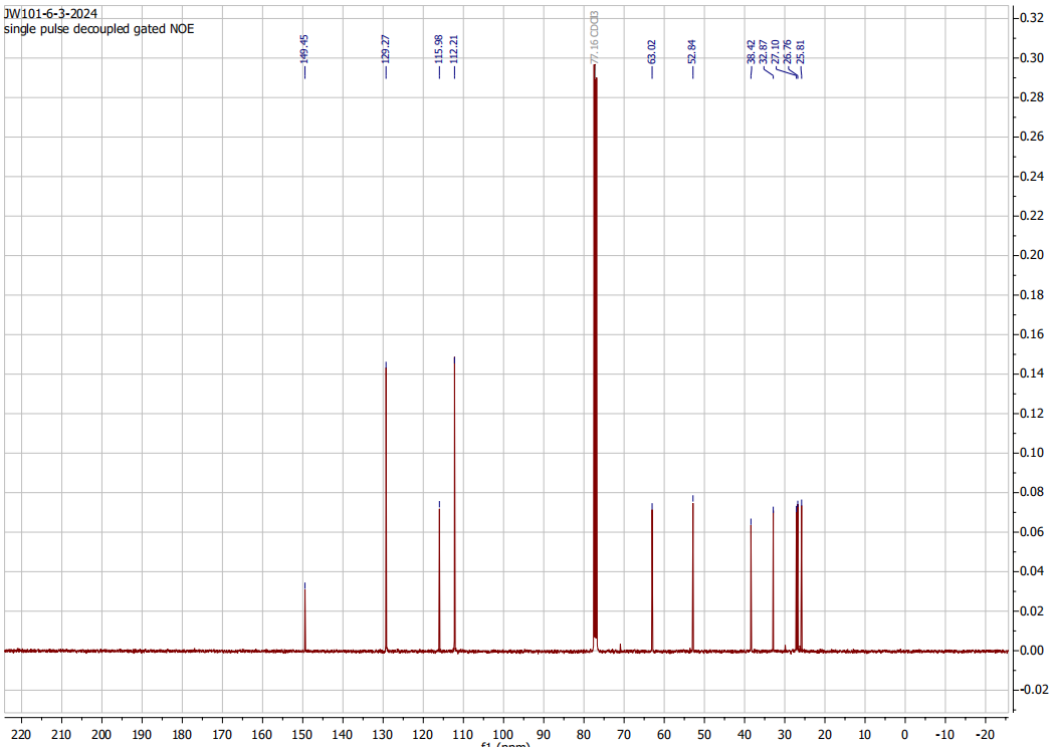
JW101-6-3-2024
single pulse decoupled gated NOE
149.45
129.27
115.98
112.21
77.16 CDCl3
63.02
52.84
38.42
32.87
27.10
26.76
25.81

ESI-MS+ :

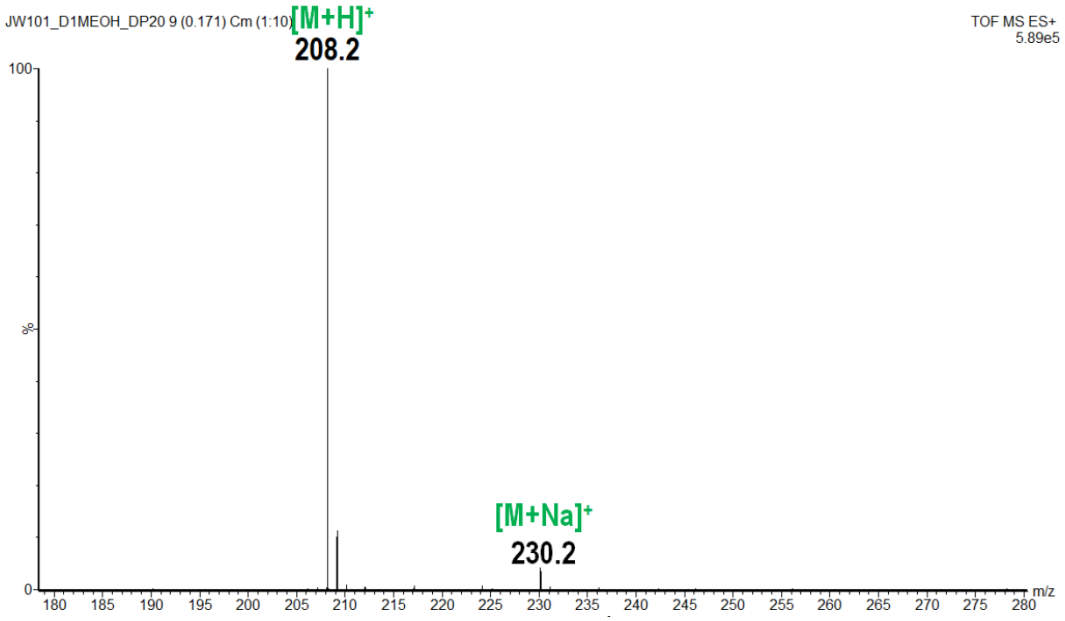
JW101_D1MEOH_DP20 9 (0.171) Cm (1:10)
TOF MS ES+
5.89e5
[M+H]+
208.2
[M+Na]+
230.2
100
%
0
180 185 190 195 200 205 210 215 220 225 230 235 240 245 250 255 260 265 270 275 280
m/z

6-(methyl(phenyl)amino)hexyl methanesulfonate

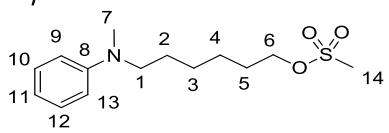


To a stirring solution of 2.012 g 6-(methyl(phenyl)amino)hexan-1-ol in 25 mL anhydrous THF, 2.70 mL triethylamine was added and stirred for 40 min under argon atmosphere. To a stirring solution of 1.50 mL mesylate chloride in 25 mL anhydrous THF under argon atmosphere, the solution of 6-(methyl(phenyl)amino)hexan-1-ol and triethylamine in anhydrous THF was added by using cannulation very slowly at 0 °C. The solution was stirred for 3 h. The reaction was stopped by 5 mL distilled water. The compound was extracted by DCM, washed by distilled water, and dried by anhydrous sodium sulphate. The solvent was removed by rotary evaporator and the mass is 2.73 g (99%).

NMR spectrum:

$^{1}$H NMR (400 MHz, $CDCl_3$) δ, ppm: 7.24 (2 H, H-$C_{10}$ and H-$C_{12}$, t), 6.70 (3 H, H-$C_9$,H-$C_{11}$ and H-$C_{13}$, m), 4.23 (2 H, $H_2$-$C_6$, t, J = 6.57 Hz), 3.32 (2 H, $H_2$-$C_1$, t, J = 7.38 Hz), 3.00 (3 H, $H_3$-$C_{14}$, s), 2.94 (3 H, $H_3$-$C_7$, s), 1.67 (2H, $H_2$-$C_5$, p, J=6.75 Hz), 1.61 (2H, $H_2$-$C_2$, p, J=7.39 Hz), 1.45 (2 H, $H_2$-$C_4$, m), 1.38 (2 H, $H_2$-$C_3$, m).

$^{13}$C NMR (101 MHz, $CDCl_3$) δ, ppm: 149.55, 129.60, 129.51, 116.53, 112.61, 70.39, 68.38, 53.07, 38.82, 37.74, 31.96, 29.51, 26.90, 25.81.

$^{1}H$:

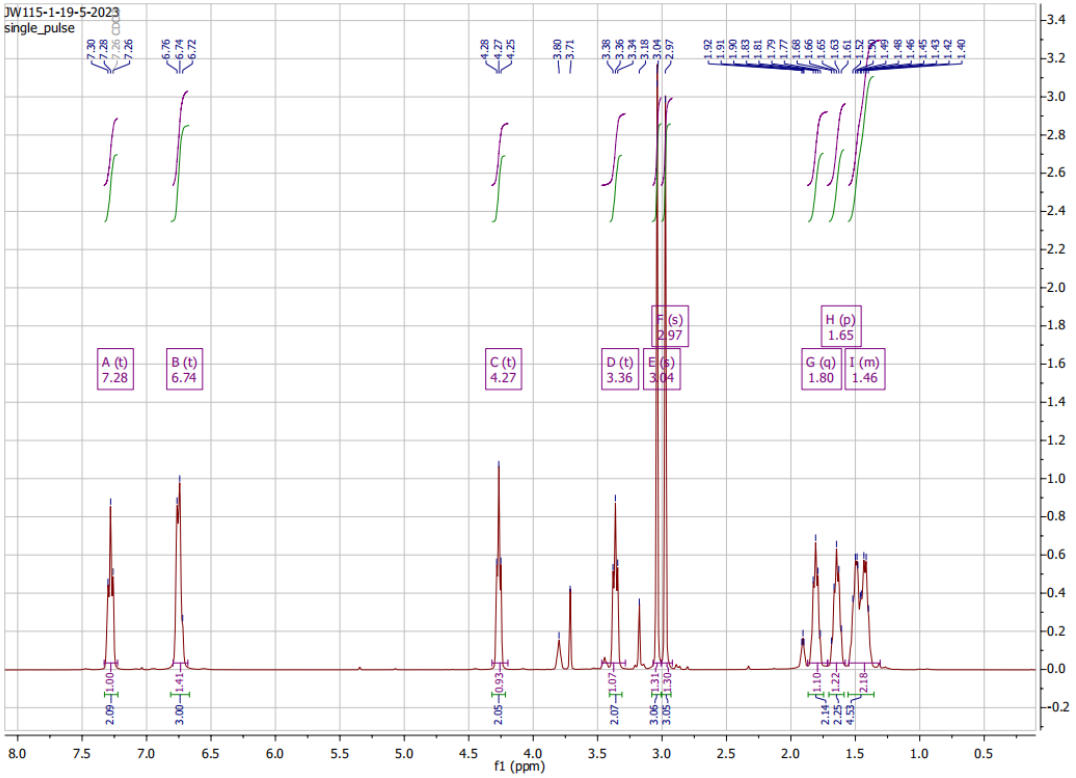
JW115-1-19-5-2023
single_pulse
A (t) 7.28
B (t) 6.74
C (t) 4.27
D (t) 3.36
E (s) 3.04
F (s) 2.97
G (q) 1.80
H (p) 1.65
I (m) 1.46
f1 (ppm)

$^{13}C$:

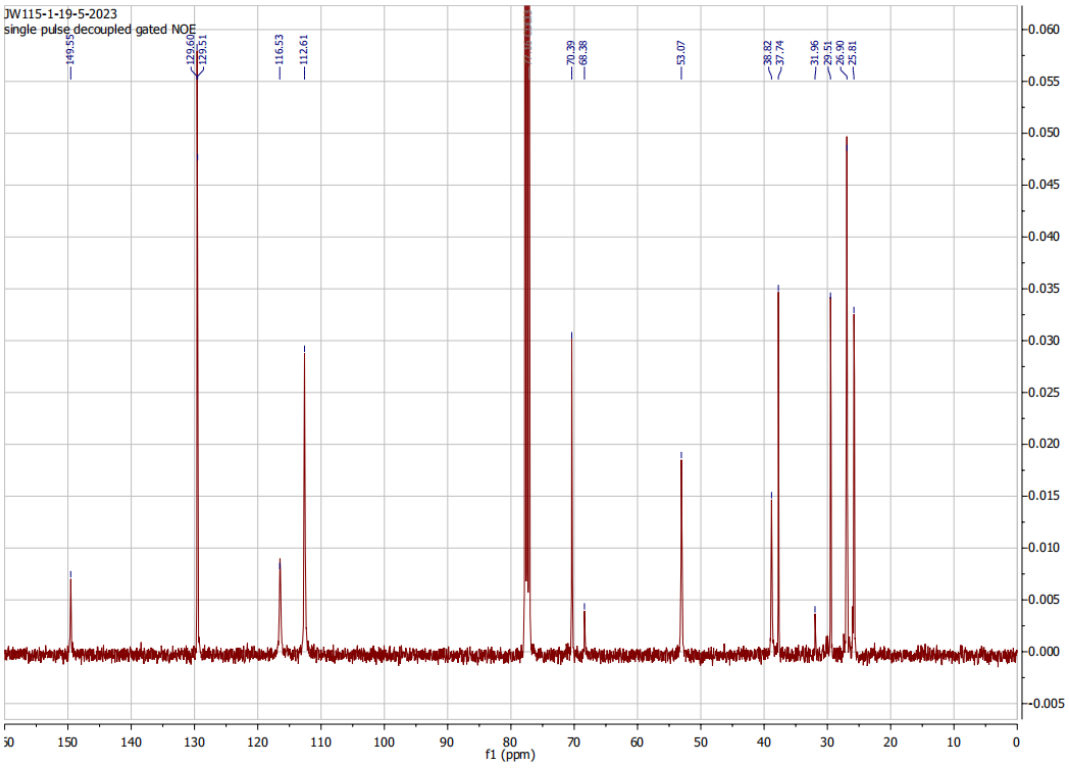
JW115-1-19-5-2023
single pulse decoupled gated NOE
149.55
129.60
129.51
116.53
112.61
77.32
77.00
76.68
70.39
68.38
53.07
38.82
37.74
31.96
29.51
26.90
25.81
f1 (ppm)

(6-(methyl(phenyl)amino)hexyl) ethanethioate

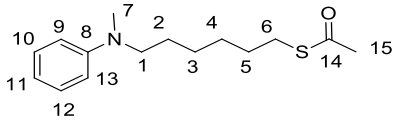


2.483g 6-(methyl(phenyl)amino)hexyl methanesulfonate and 2.38 g potassium thioacetate were suspended in the 50 mL absolute ethanol and refluxed for at least overnight under argon atmosphere. The product was extracted after cooling. The organic phase was washed by water and dried over anhydrous sodium sulphate. The solvent was removed by rotary evaporator to give 2.126 g (92.0%) product.

NMR spectrum:

$^{1}$H NMR (400 MHz, $CDCl_3$) δ, ppm: 7.22 (2 H, H-$C_{10}$ and H-$C_{12}$, t, J=7.90 Hz), 6.68 (3 H, H-$C_9$,H-$C_{11}$ and H-$C_{13}$, m), 3.29 (2 H, $H_2$-$C_1$, t, J = 7.57 Hz), 2.92 (3 H, $H_3$-$C_7$, s),2.86 (2 H, $H_2$-$C_6$, t, J = 7.45 Hz), 2.33 (3 H, $H_3$-$C_{15}$, s), 1.58 (4H, $H_2$-$C_2$ and $H_2$-$C_5$, m),1.37 (4 H, $H_2$-$C_3$ and $H_2$-$C_4$, m).

$^{13}$C NMR (101 MHz, $CDCl_3$) δ, ppm: 196.16, 149.41, 129.27, 115.98, 112.20, 52.80, 38.42, 30.78, 29.62, 29.15, 28.80, 26.79, 26.62.

ESI-MS+ spectrum:

m/z=266.2 for $[M+H]^+$, thus M = 265.2 g/mol.

$^{1}$H:

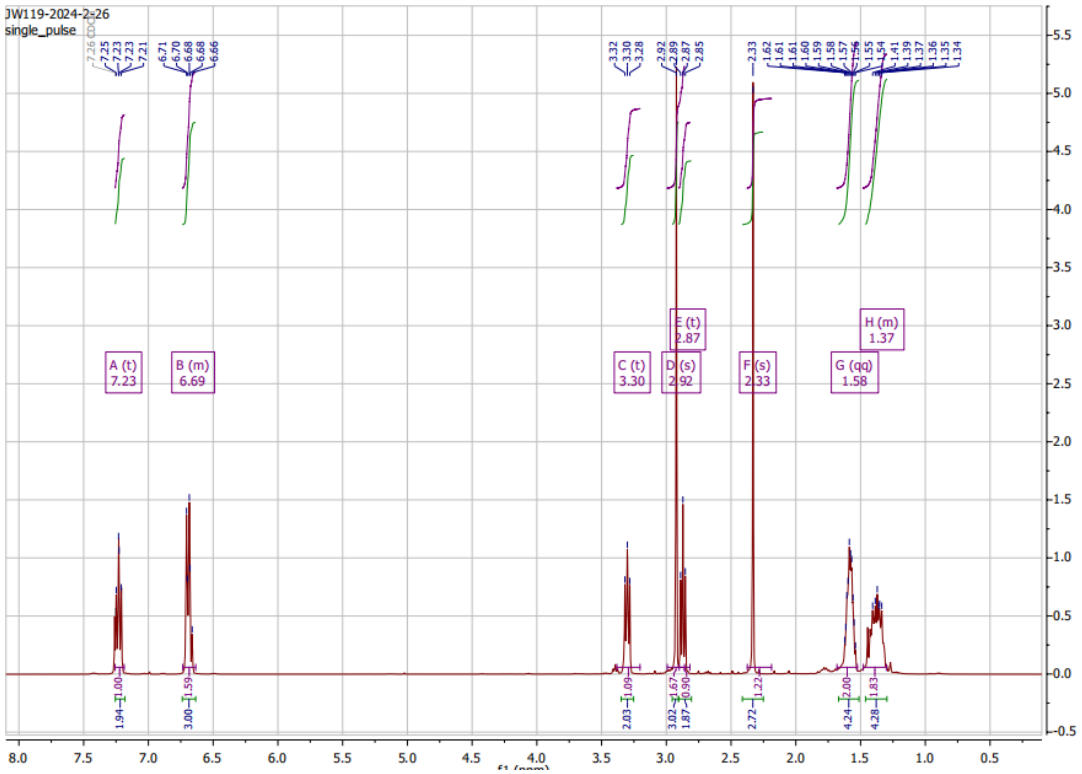

$^{13}C$:

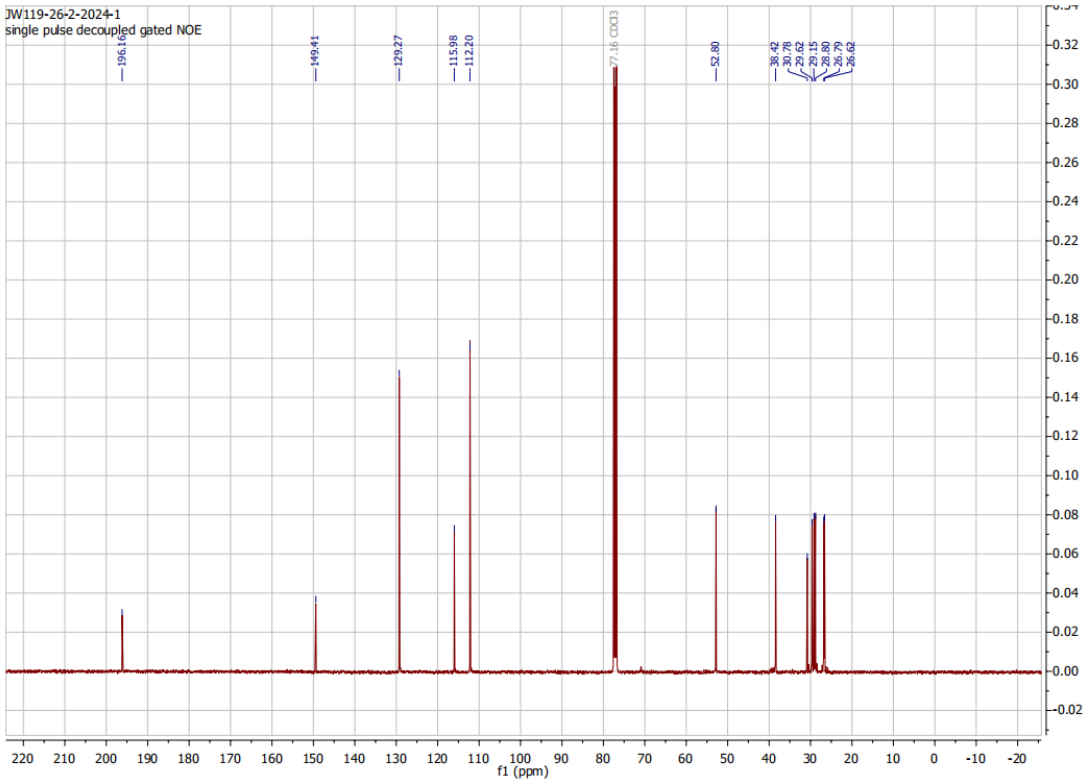


ESI-MS+ :

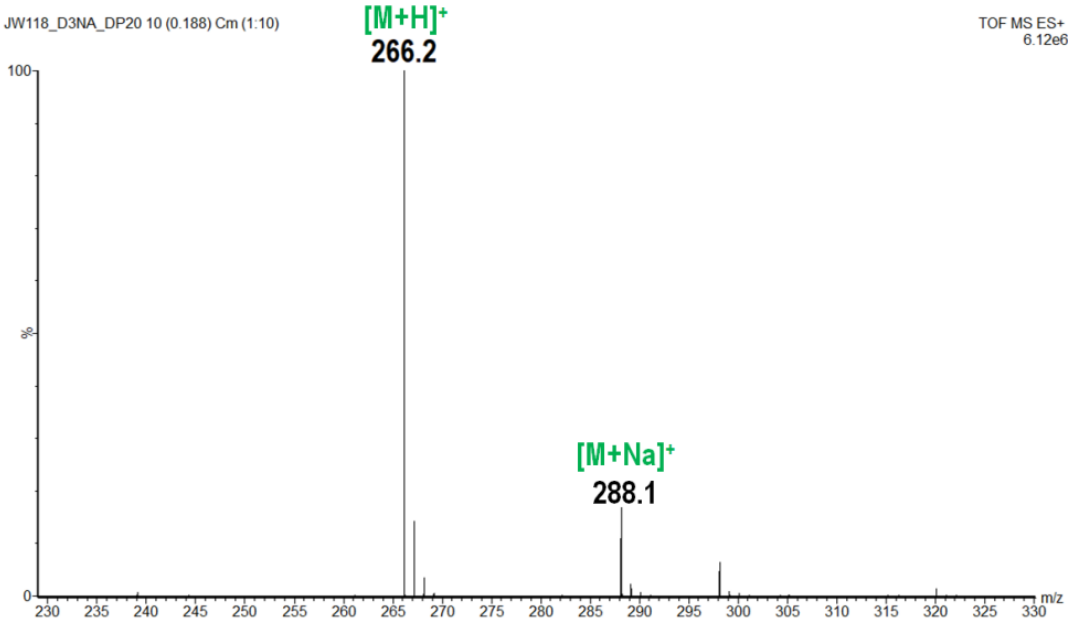


Figure 1 – Spectre de masse en mode electrospray positif de l'échantillon JW118.

S-(6-((4-formylphenyl)(methyl)amino)hexyl) ethanethioate

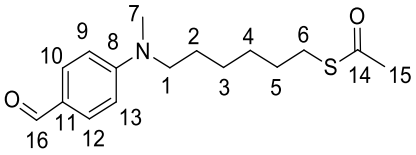


In the dried glassware under argon atmosphere at 0 °C, 3.48 mL DMF and 4.30 mL phosphoryl chloride were added together dropwise. Next, 3.978 g S-(6-(methyl(phenyl)amino)hexyl) ethanethioate in 75 mL anhydrous DCE solution was added by cannulation. The mixture was heated to reflux for 4 h. After cooling to RT, 100 mL cold $NaHCO_3$ solution was added at 0 °C. After 30 min, at room temperature, the mixture was diluted by DCM. The whole was transferred into separatory funnel and the product was extracted by dichloromethane. Then, the organic phase was washed by distilled water for 2 times, dried by anhydrous sodium sulphate. 3.996 g crude product was obtained after the evaporation under reduced pressure. The product was purified by silica-gel chromatography using the eluent (petroleum ether 3 and ethyl acetate 1). The mass of the product is 2.829 g (64.4%).

NMR spectrum:

$^{1}H$ NMR (400 MHz, $CDCl_3$) δ, ppm: 9.72 (1 H, H-$C_{16}$, s), 7.72 (2 H, H-$C_{10}$ and H-$C_{12}$, d, J= 8.93 Hz), 6.67 (2 H, H-$C_9$ and H-$C_{13}$, d, J= 8.22 Hz), 3.40 (2 H, $H_2$-$C_1$, t, J = 7.53 Hz), 3.04 (3 H, $H_3$-$C_7$, s),2.86 (2 H, $H_2$-$C_6$, t, J = 7.36 Hz), 2.32 (3 H, $H_3$-$C_{15}$, s), 1.59 (4H, $H_2$-$C_2$ and $H_2$-$C_5$, m),1.38 (4 H, $H_2$-$C_3$ and $H_2$-$C_4$, m).

$^{13}C$ NMR (101 MHz, $CDCl_3$) δ, ppm: 196.85, 191.03, 154.27, 132.98, 125.75, 111.65, 53.21, 39.42, 31.51, 30.31, 29.78, 29.40, 27.59, 27.34.

$^{1}H$:

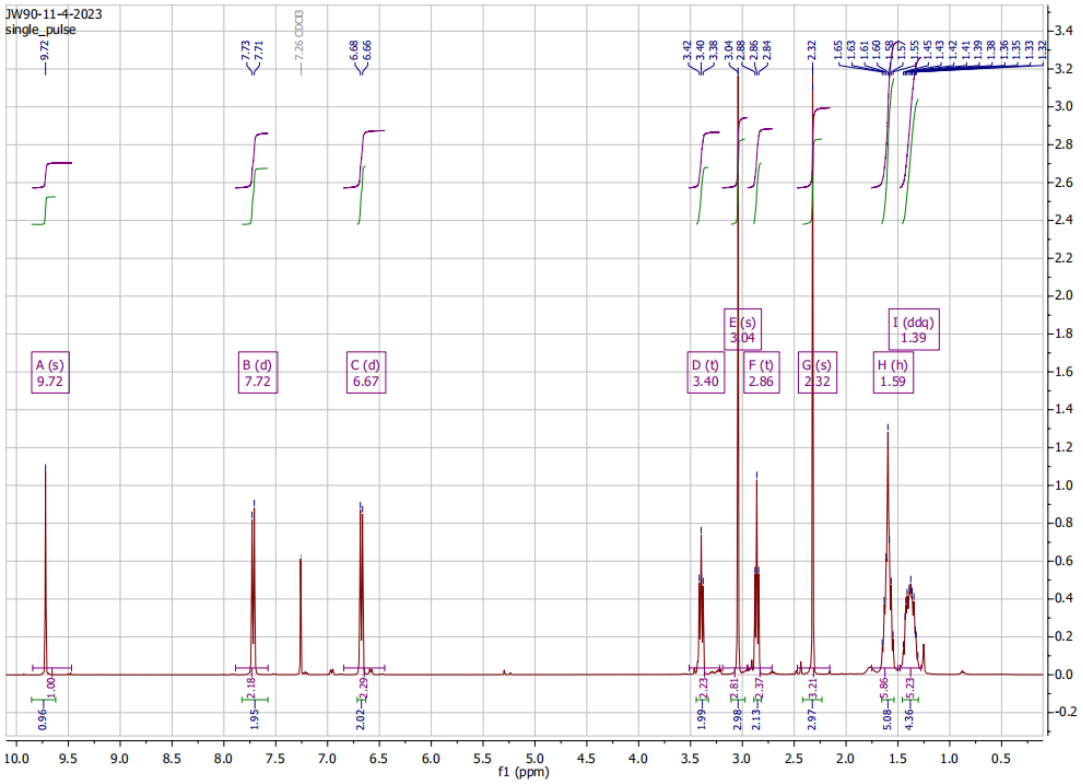


$^{13}C$:

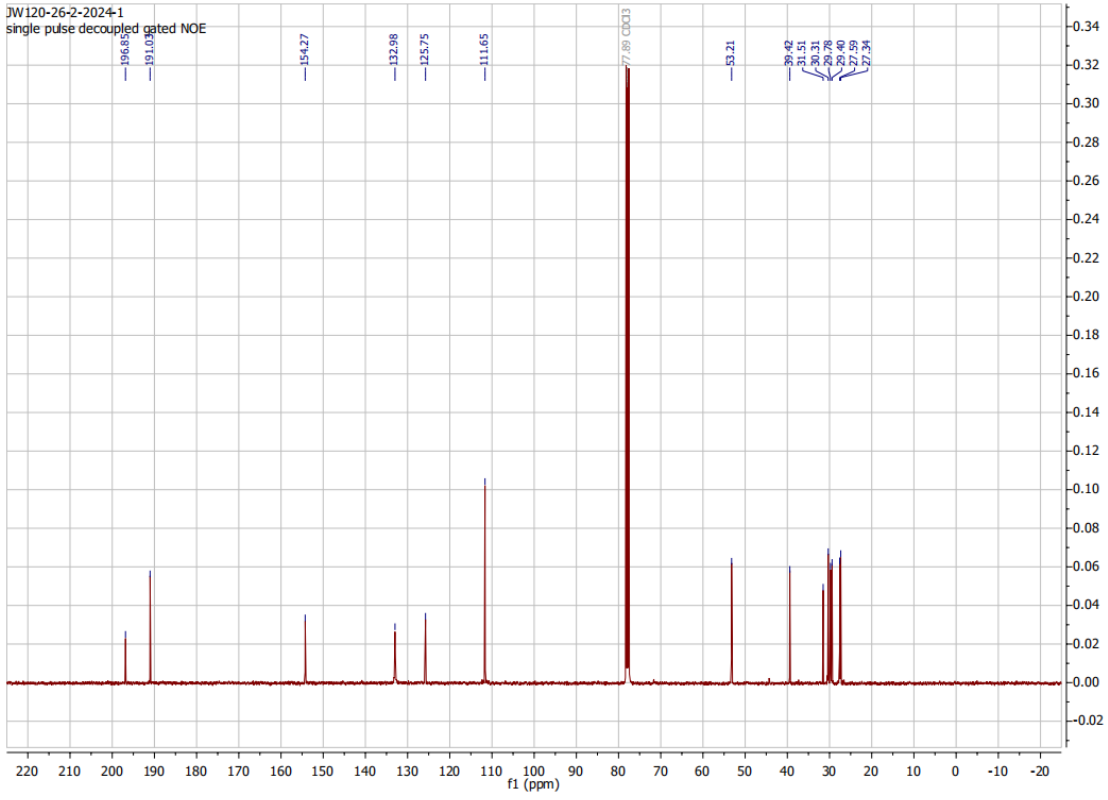


(E)-3-(4-((6-(acetylthio)hexyl)(methyl)amino)phenyl)-2-cyanoacrylic acid

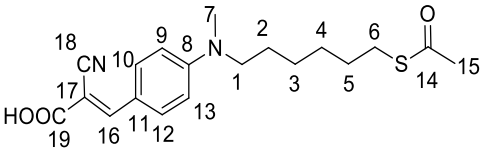


0.174 g S-(6-((4-formylphenyl)(methyl)amino)hexyl) ethanethioate was dissolved in 10 mL absolute ethanol and 0.15 mL piperidine and 0.070 g cyanoacetic acid was added. The reaction will undergo at reflux temperature for 24 h. After cooling to 0 °C, 10 mL 3M HCl aqueous solution was added. The product was collected using conical sintered glass funnel and washed by cold distilled water and cold ethanol. The product is yellow, and the mass is 0.115g (53.9%).

NMR spectrum:

$^1$H NMR (400 MHz, THF-$d_8$) δ, ppm: 8.02 (1 H, H-$C_{16}$, s), 7.94 (2 H, H-$C_{10}$ and H-$C_{12}$, d), 6.78 (2 H, H-$C_9$ and H-$C_{13}$, d), 3.46 (2 H, $H_2$-$C_1$, t), 3.07 (3 H, $H_3$-$C_7$, s),2.85 (2 H, $H_2$-$C_6$, t), 2.26 (3 H, $H_3$-$C_{15}$, s), 1.60 (4H, $H_2$-$C_2$ and $H_2$-$C_5$, m),1.40 (4 H, $H_2$-$C_3$ and $H_2$-$C_4$, m).

ESI-MS+ spectrum:

m/z=361.2 for $[M+H]^+$, thus M = 360.2 g/mol.

$^1$H:

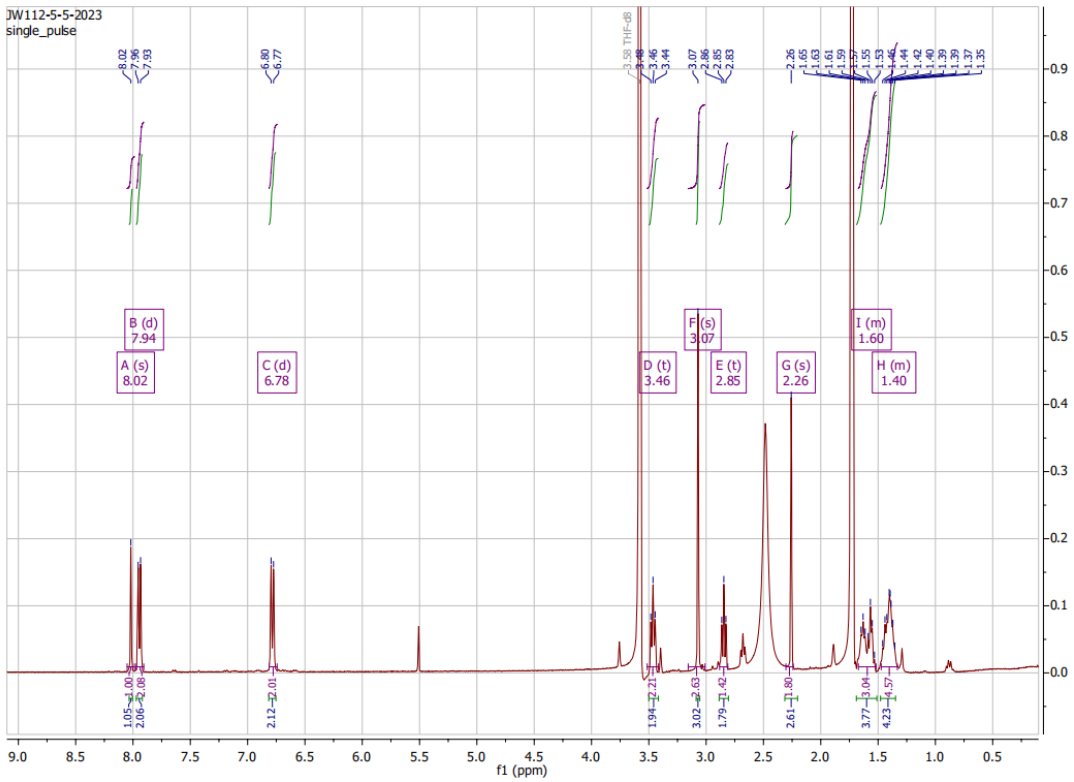

ESI-MS+:

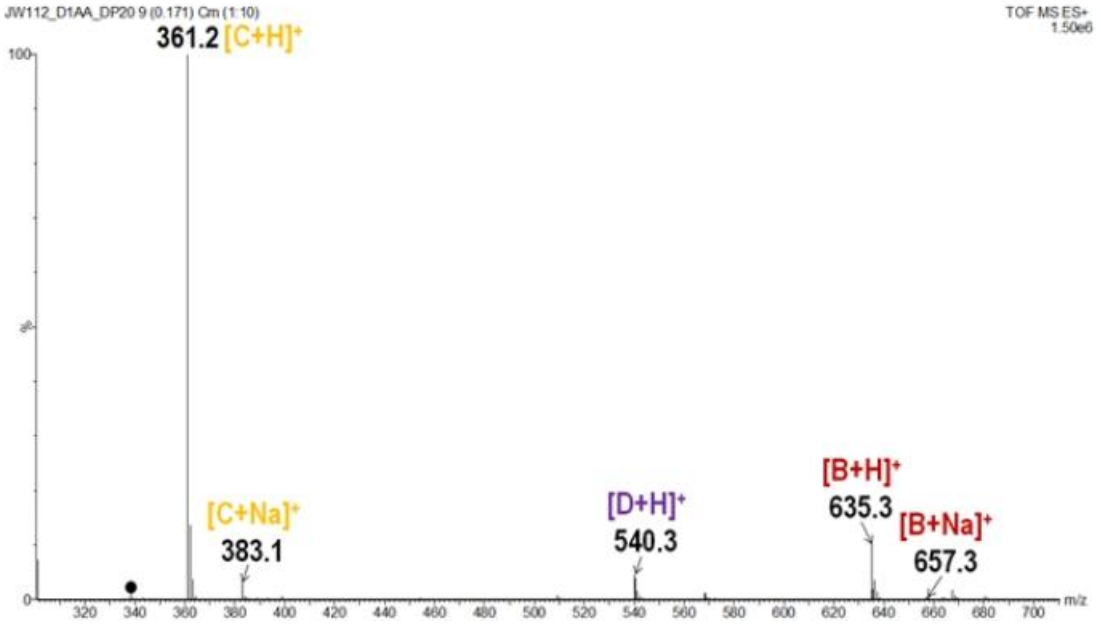


(2E,2'E)-3,3'-(((disulfanediylbis(hexane-6,1-diyl))bis(methylazanediyl))bis(4,1-phenylene))bis(2-cyanoacrylic acid)

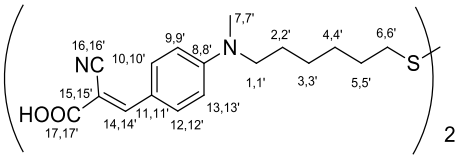


0.098 g S-(6-((4-formylphenyl)(methyl)amino)hexyl) ethanethioate and 0.057 g cyanoacetic acid were dissolved in EtOH, 0.2 mL piperidine was added and the mixture was in reflux for 24 h. After cooling at 0 °C, 10 mL 3M HCl aqueous solution was added. The product was collected using conical sintered glass funnel and washed by cold EtOH and cold water. The product is red oily sticky solid, and the mass is 0.0558 g (63.2 %).

NMR spectrum:

$^{1}$H NMR (400 MHz, THF-$d_8$) δ, ppm: 8.02 (2 H, H-$C_{14}$ and H-$C_{14'}$, s), 7.94 (4 H, H-$C_{10}$, H-$C_{10'}$, H-$C_{12}$ and H-$C_{12'}$, d), 6.78 (4 H, H-$C_9$, H-$C_{9'}$, H-$C_{13}$ and H-$C_{13'}$, d), 3.47 (4 H, $H_2$-$C_1$ and $H_2$-$C_{1'}$, t), 3.07 (6 H, $H_3$-$C_7$ and $H_3$-$C_{7'}$, s), 2.68 (4 H, $H_2$-$C_6$ and $H_2$-$C_{6'}$, t), 1.66 (8H, $H_2$-$C_2$, $H_2$-$C_{2'}$, $H_2$-$C_5$ and $H_2$-$C_{5'}$, m),1.42 (8 H, $H_2$-$C_3$, $H_2$-$C_{3'}$, $H_2$-$C_4$ and $H_2$-$C_{4'}$, m).

$^{13}$C NMR (101 MHz, THF-$d_8$) δ, ppm: 165.57, 154.63, 154.04, 134.91, 120.69, 118.26, 112.62, 95.96, 53.21, 39.66, 38.89, 30.35, 29.54, 28.08, 27.79.

ESI-MS- spectrum:

m/z=633.3 for $[M-H]^-$, thus M = 634.3 g/mol.

FTIR spectrum:

FTIR in $cm^{-1}$: 2928 (m), 2845 (m), 2500 (m,b), 2218 (m), 2119 (w), 1668 (s), 1601 (s), 1566 (s), 1505 (s), 1434 (w), 1395 (w), 1323 (w), 1279 (m), 1239 (m), 1160 (m,b), 931 (w), 811 (m), 757 (w), 689 (w), 626 (w), 574 (w), 451 (w).

$^{1}H$:

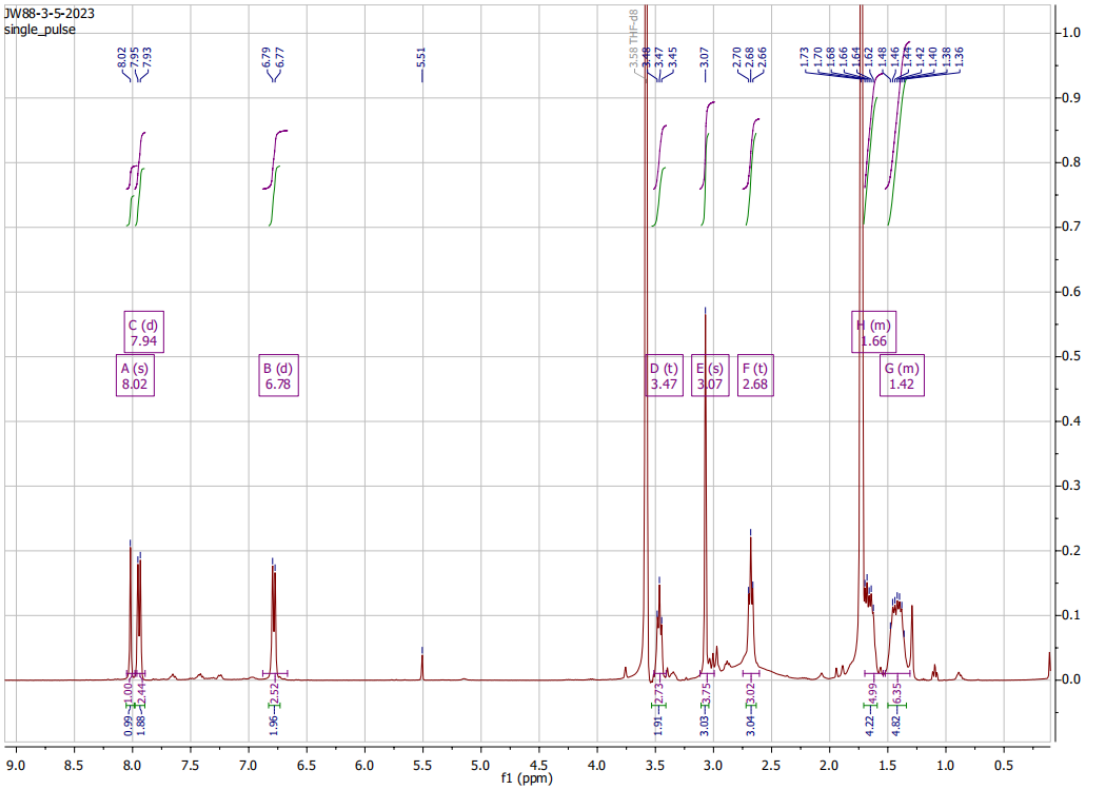
JW88-3-5-2023
single_pulse
C (d)
7.94
A (s)
8.02
B (d)
6.78
D (t)
3.47
E (s)
3.07
F (t)
2.68
H (m)
1.66
G (m)
1.42
f1 (ppm)

$^{13}C$:

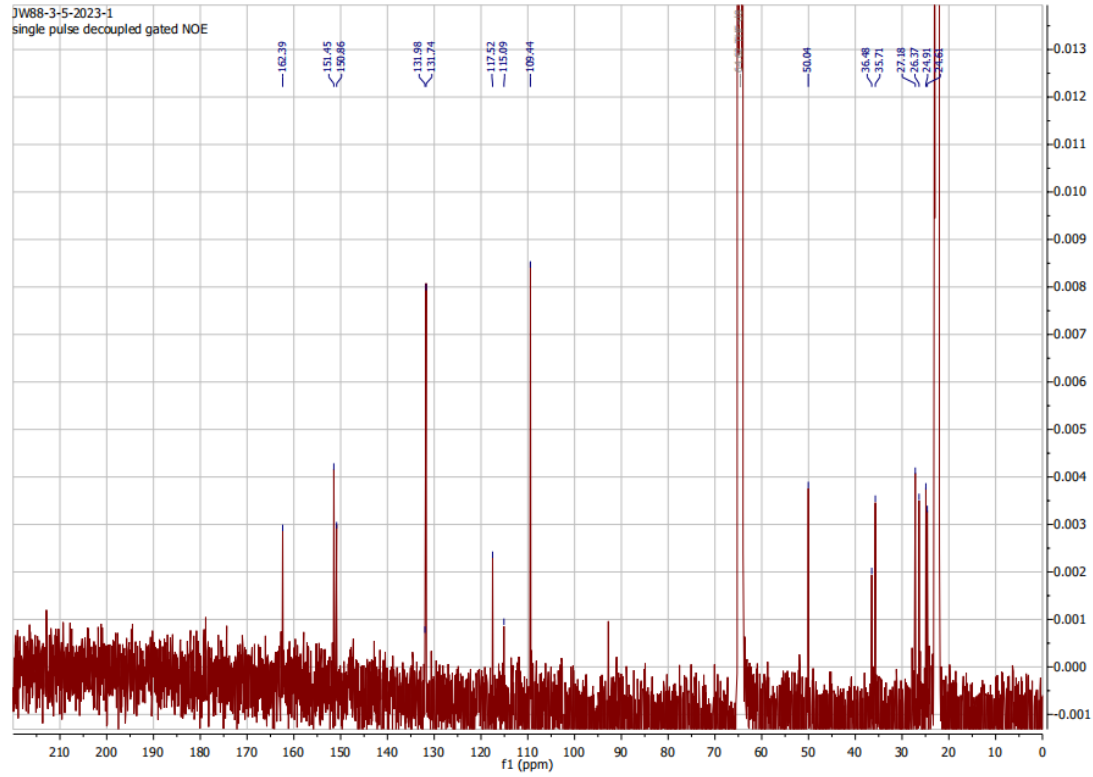
JW88-3-5-2023-1
single pulse decoupled gated NOE
f1 (ppm)

ESI-MS-:

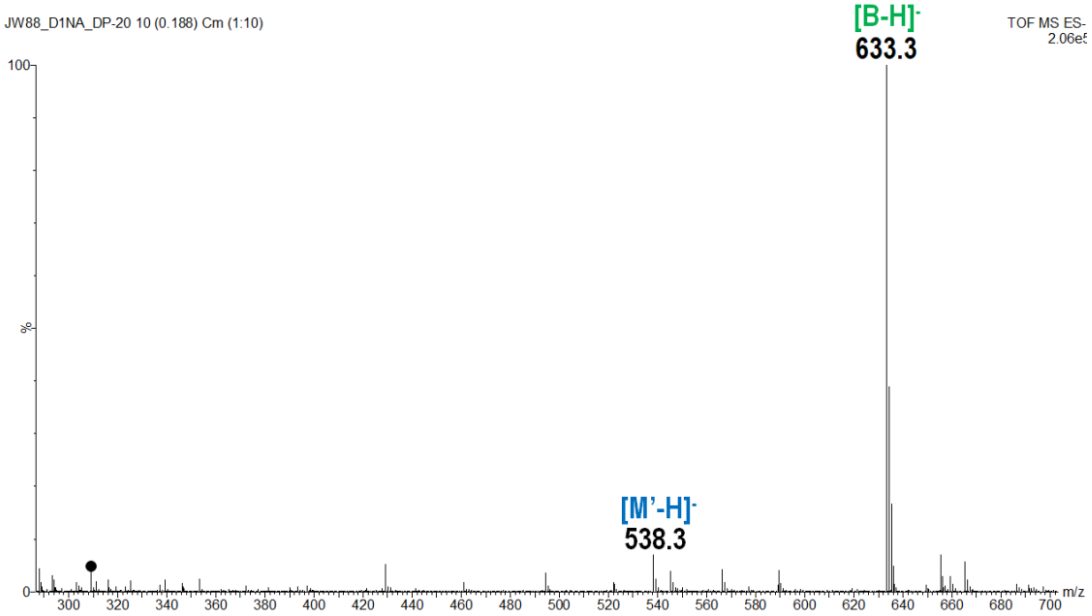


FTIR:

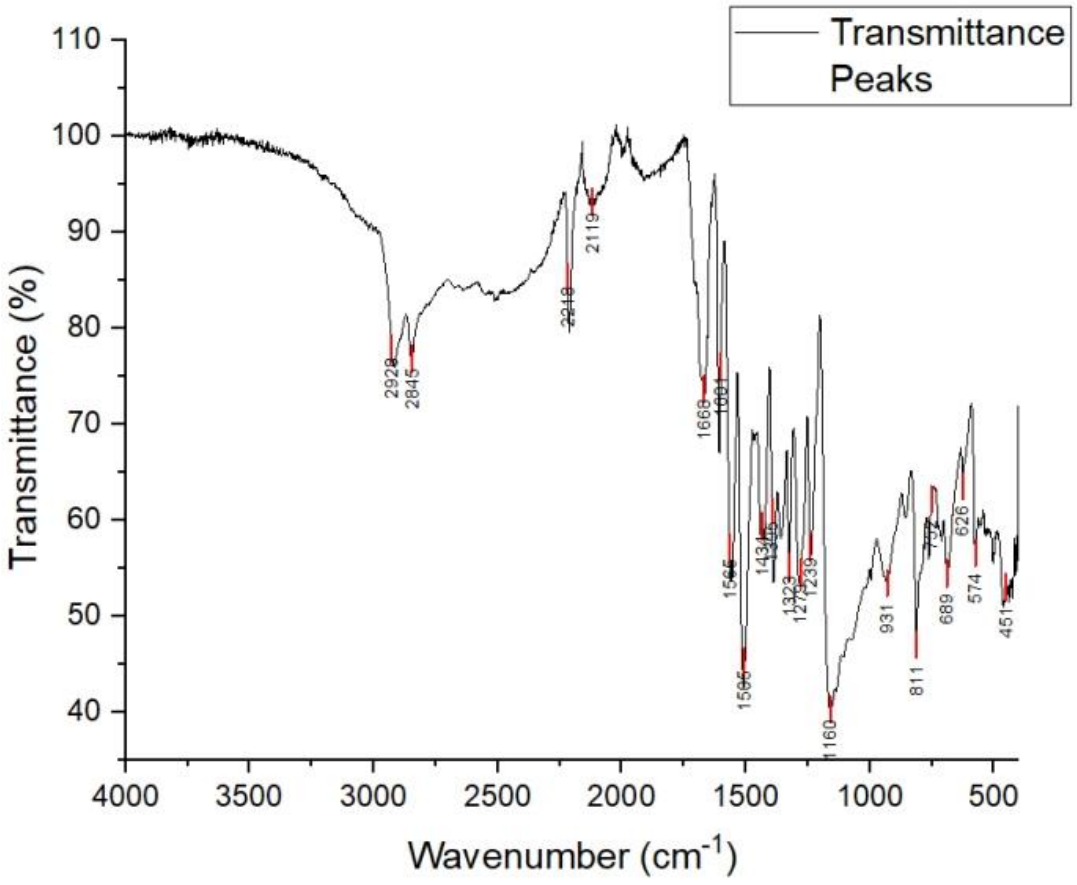


N,N-bis(2-thiocyanatoethyl)aniline

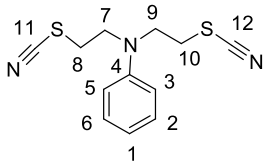


To 2.187 g N,N-bis(2-thiocyanatoethyl)aniline in absolute EtOH, 9.743g KSCN is added. The mixture will be refluxed for 24 h. After cooling, 40 mL $H_2O$ was added. The white precipitation was filtered as crude product. The crude product was dissolved in dichloromethane, dried by anhydrous $Na_2SO_4$. After filtration and evaporation of the solvent, 1.930 g (73.4 %) product is obtained.

NMR spectrum:

$^1$H NMR (400 MHz, $CDCl_3$) δ, ppm: 7.31 (2 H, H-$C_2$ and H-$C_6$, t), 6.88 (1 H, H-$C_1$, t), 6.80 (2 H, H-$C_3$, and H-$C_5$, d), 3.82 (4 H, $H_2$-$C_7$ and $H_2$-$C_9$, t), 3.13 (4 H, $H_2$-$C_8$ and $H_3$-$C_{10}$, t).

$^{13}$C NMR (101 MHz, $CDCl_3$) δ, ppm: 145.33, 130.15, 119.81, 114.23, 111.80, 52.00, 31.09.

ESI-MS+ spectrum:

m/z=286.0 for $[M+Na]^+$, thus M = 263.1 g/mol.

$^1$H:

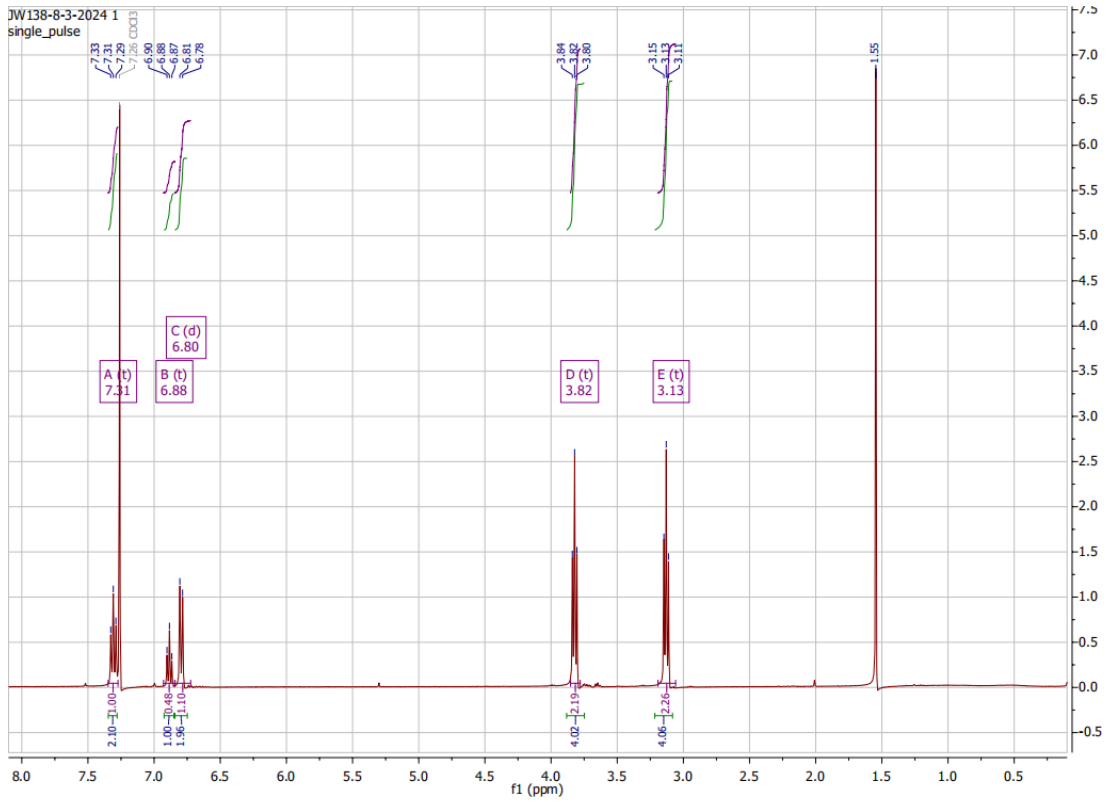

$^{13}C$:

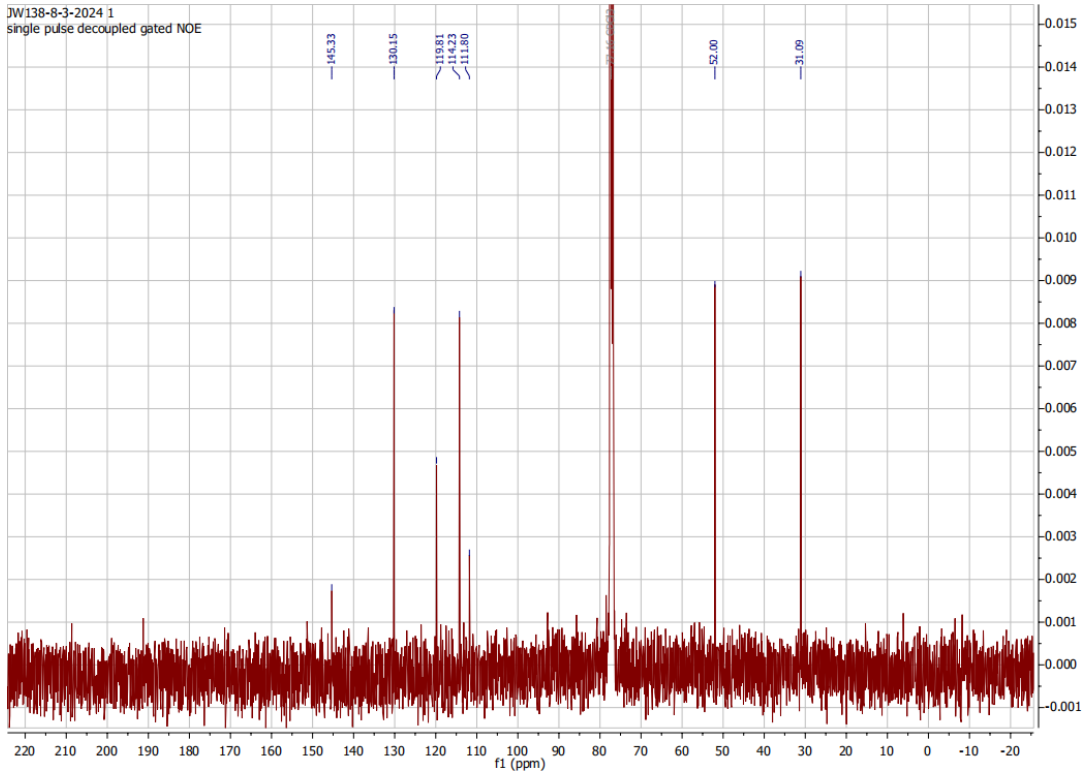
JW138-8-3-2024 1
single pulse decoupled gated NOE
145.33
130.15
119.81
114.23
111.60
52.00
31.09
f1 (ppm)

ESI-MS+:

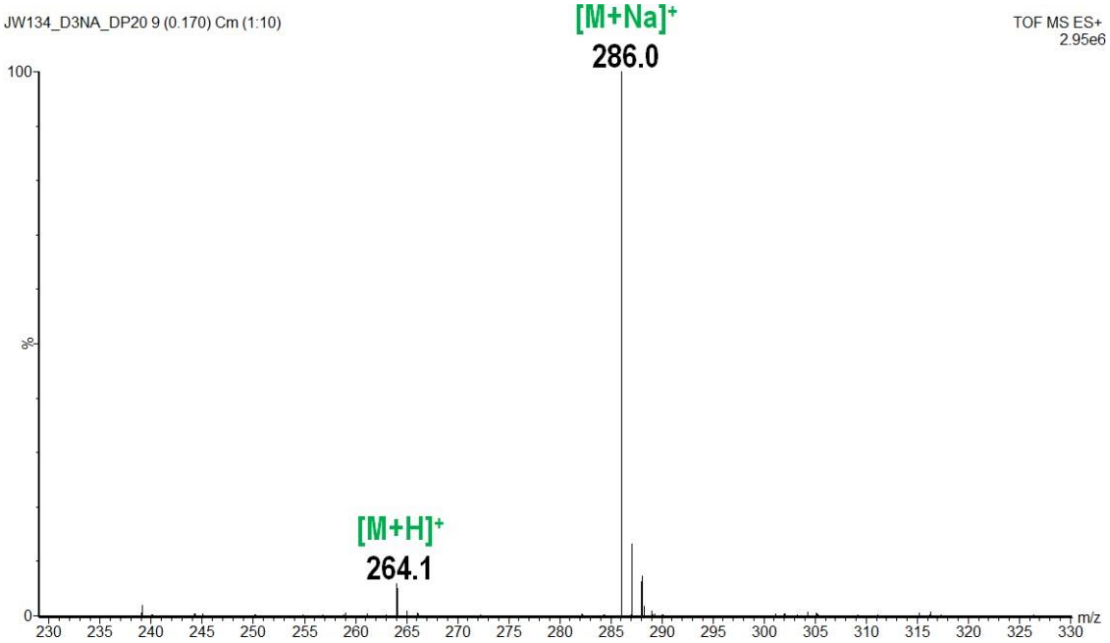
JW134_D3NA_DP20 9 (0.170) Cm (1:10)
TOF MS ES+
2.95e6
[M+Na]+
286.0
[M+H]+
264.1
100
%
0
m/z

5-phenyl-1,2,5-dithiazepane

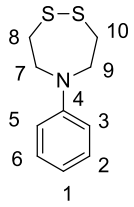


To 2.475 g N,N-bis(2-thiocyanatoethyl)aniline in 40 mL absolute ethanol, 2 equivalents of NaOH was added. The mixture was heated under reflux for 5 h. After cooling, the solvent was collected to get crude product. After purification by column chromatography (petroleum ether 9, dichloromethane 1), 1.381 g (69.5 %) product was obtained.

NMR spectrum:

$^1$H NMR (400 MHz, $CDCl_3$) δ, ppm: 7.22 (2 H, H-$C_2$ and H-$C_6$, t), 6.69 (1 H, H-$C_1$, t), 6.63 (2 H, H-$C_3$, and H-$C_5$, d), 3.96 (4 H, $H_2$-$C_7$ and $H_2$-$C_9$, t), 3.09 (4 H, $H_2$-$C_8$ and $H_3$-$C_{10}$, t).

ESI-MS+ spectrum:

m/z=212.1 for $[M+H]^+$, thus M = 211.0 g/mol.

$^1$H:

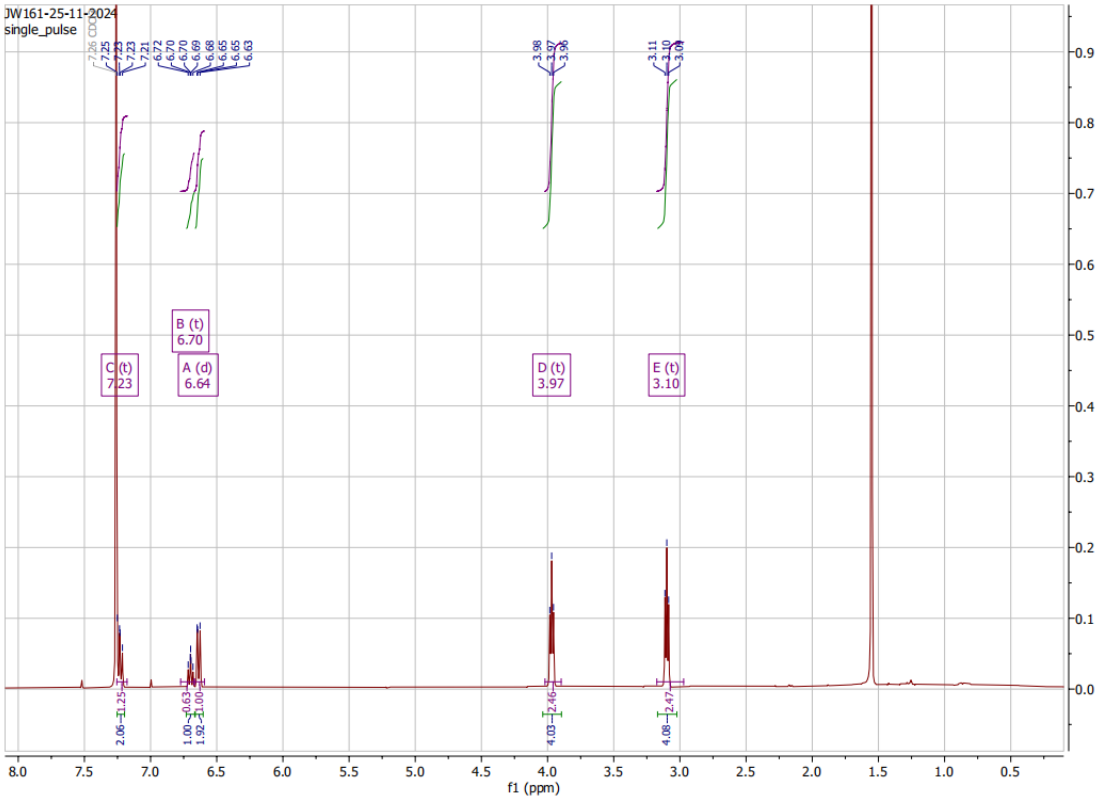

ESI-MS+:

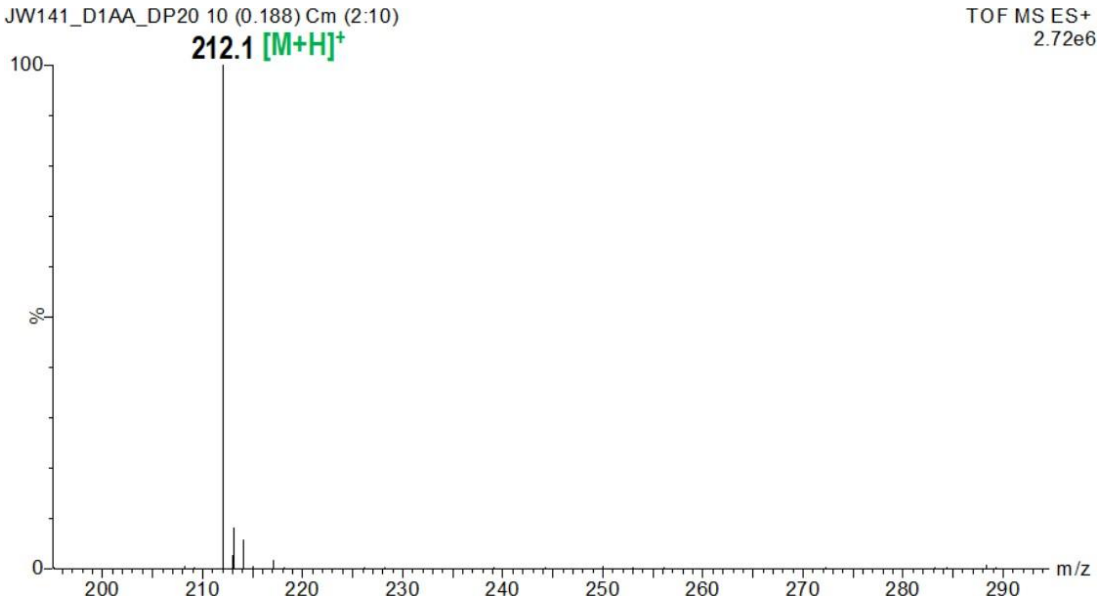
JW141_D1AA_DP20 10 (0.188) Cm (2:10)
TOF MS ES+
2.72e6
212.1 [M+H]+
100
%
0
200
210
220
230
240
250
260
270
280
290
m/z

4-(1,2,5-dithiazepan-5-yl)benzaldehyde

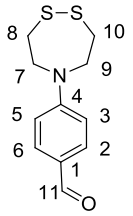


At 0 °C and under Ar, $POCl_3$ was dissolved in DMF in the very dry glassware. The mixture was heated to reflux for 4 h after adding 3.024 g 5-phenyl-1,2,5-dithiazepane. The mixture was heated to 0 °C and the 100 mL distilled water was added. Then the mixture was stirred for 30 min at room temperature. The precipitation is formed at 0 °C. The precipitation was collected, and it was dissolved in dichloromethane after drying. For the same reason, another part of the product was collected by extraction. The organic phase was collected and washed by water for several times. After drying by anhydrous $Na_2SO_4$, the solvent was removed by rotary evaporator to give crude product. 0.430 g (12.6 %) viscous product was obtained after the column chromatography (petroleum ether 7, ethyl acetate 3). After the recrystallization in ethanol, 88.8 mg crystal was collected (2.61 %).

NMR spectrum:

$^1$H NMR (400 MHz, $CDCl_3$) δ, ppm: 9.76 (1 H, H-$C_{11}$, s), 7.76 (2 H, H-$C_2$ and H-$C_6$, t), 6.70 (2 H, H-$C_3$, and H-$C_5$, d), 4.05 (4 H, $H_2$-$C_7$ and $H_2$-$C_9$, t), 3.10 (4 H, $H_2$-$C_8$ and $H_3$-$C_{10}$, t).

$^{13}$C NMR (101 MHz, $CDCl_3$) δ, ppm: 190.40, 151.72, 132.55, 126.14, 111.12, 53.11, 36.30.

ESI-MS+ spectrum:

m/z=240.1 for $[M+H]^+$, m/z=262.0 for $[M+Na]^+$ thus M = 239.1 g/mol.

CHNS/O characterization:

Experimental: m(N)%=5.71%, m(C)%=54.75%, m(H)%=5.38%, m(S)%=27.05%

Theoretical: m(N)%=5.86%, m(C)%=55.23%, m(H)%=5.44%, m(S)%=26.8%

$^{1}H$:

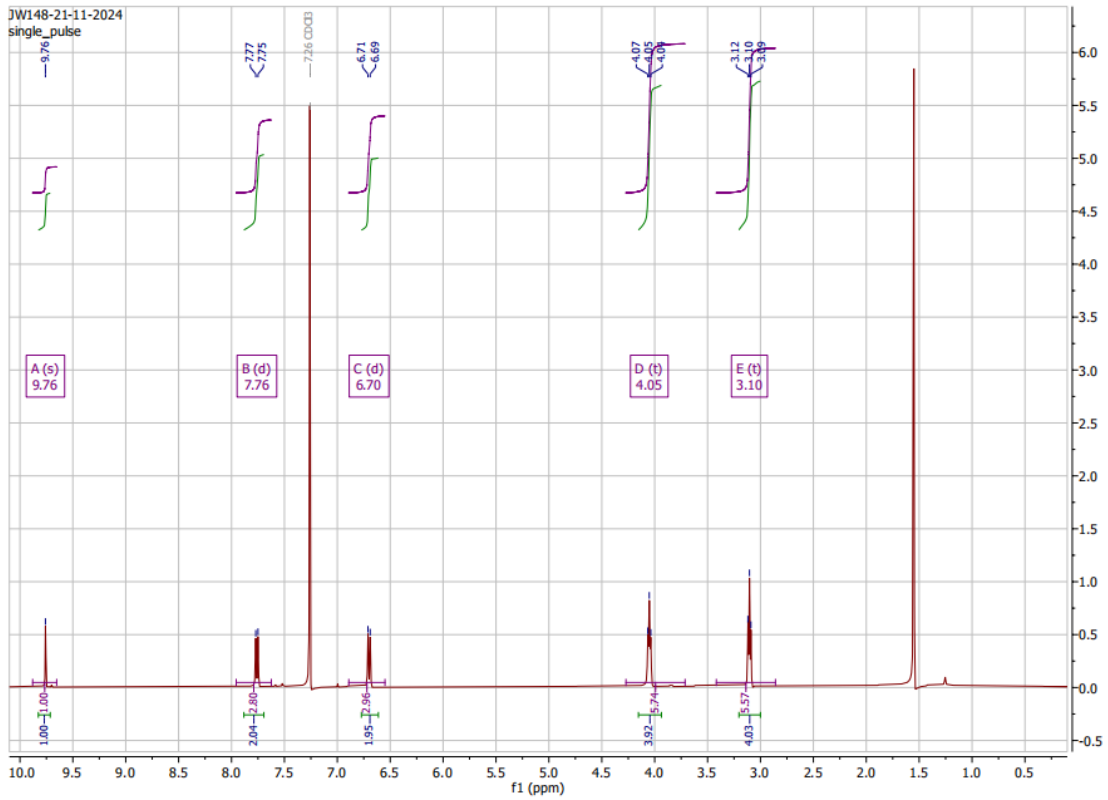
JW148-21-11-2024
single_pulse
A (s)
9.76
B (d)
7.76
C (d)
6.70
D (t)
4.05
E (t)
3.10
f1 (ppm)

$^{13}C$:

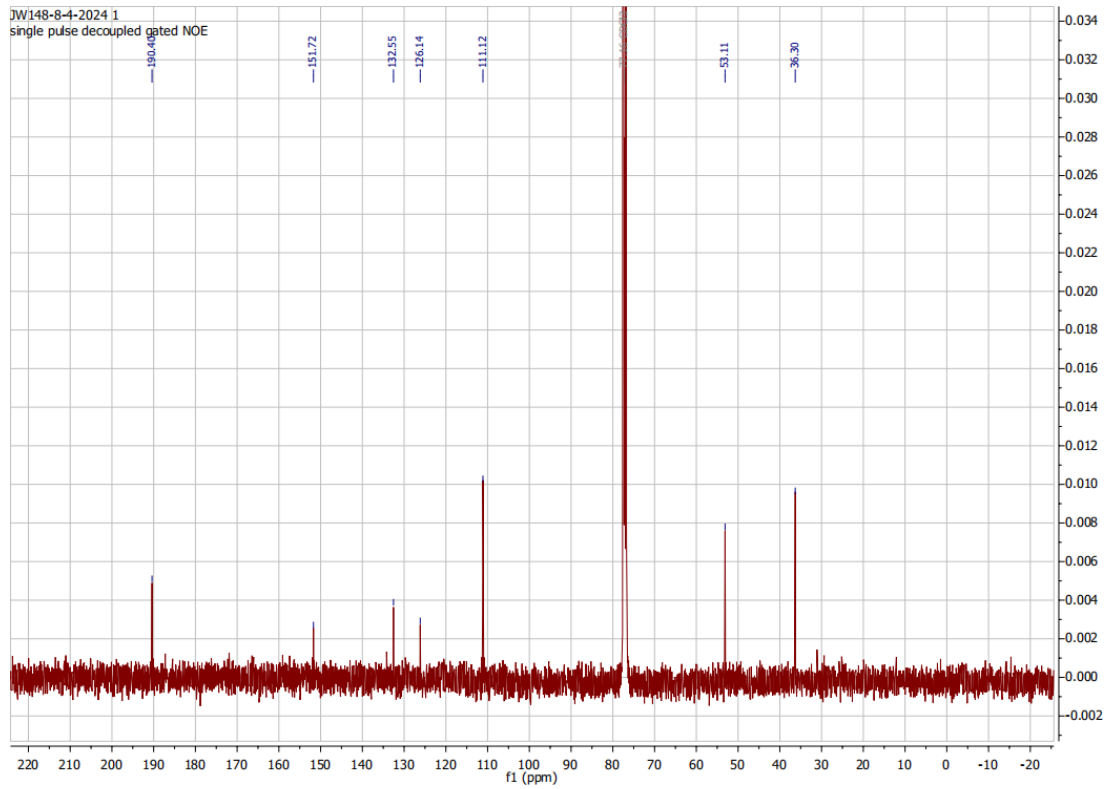
JW148-8-4-2024 1
single pulse decoupled gated NOE
190.48
151.72
132.55
126.14
111.12
53.11
36.30
f1 (ppm)

ESI-MS+:

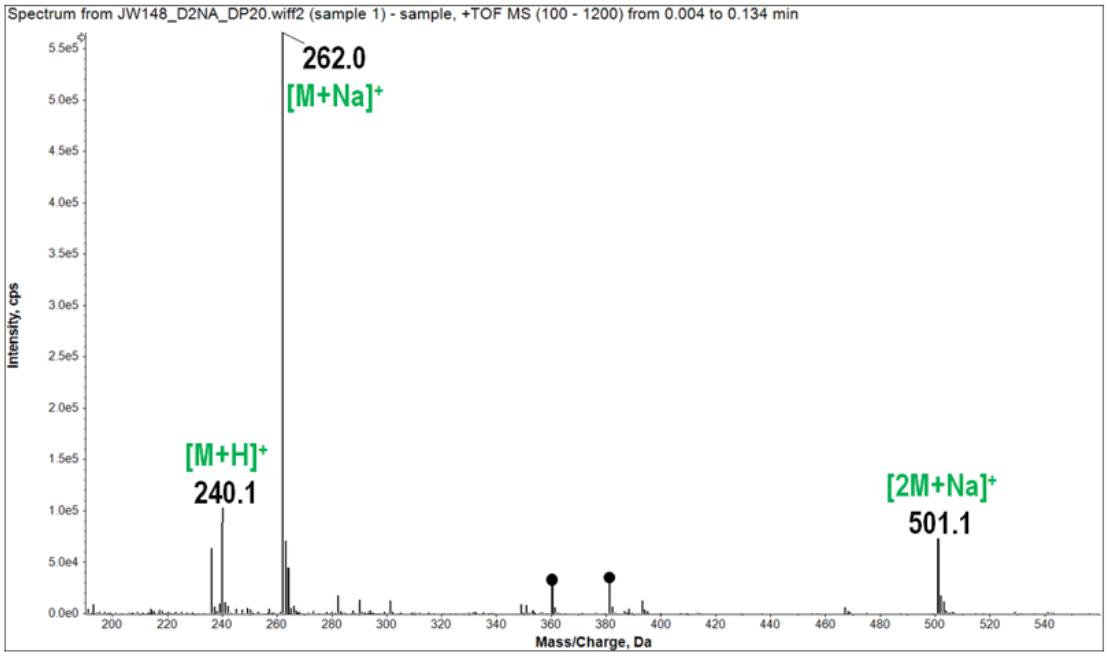
Spectrum from JW148_D2NA_DP20.wiff2 (sample 1) - sample, +TOF MS (100 - 1200) from 0.004 to 0.134 min
262.0
[M+Na]+
[M+H]+
240.1
[2M+Na]+
501.1
Intensity, cps
Mass/Charge, Da

CHNS:

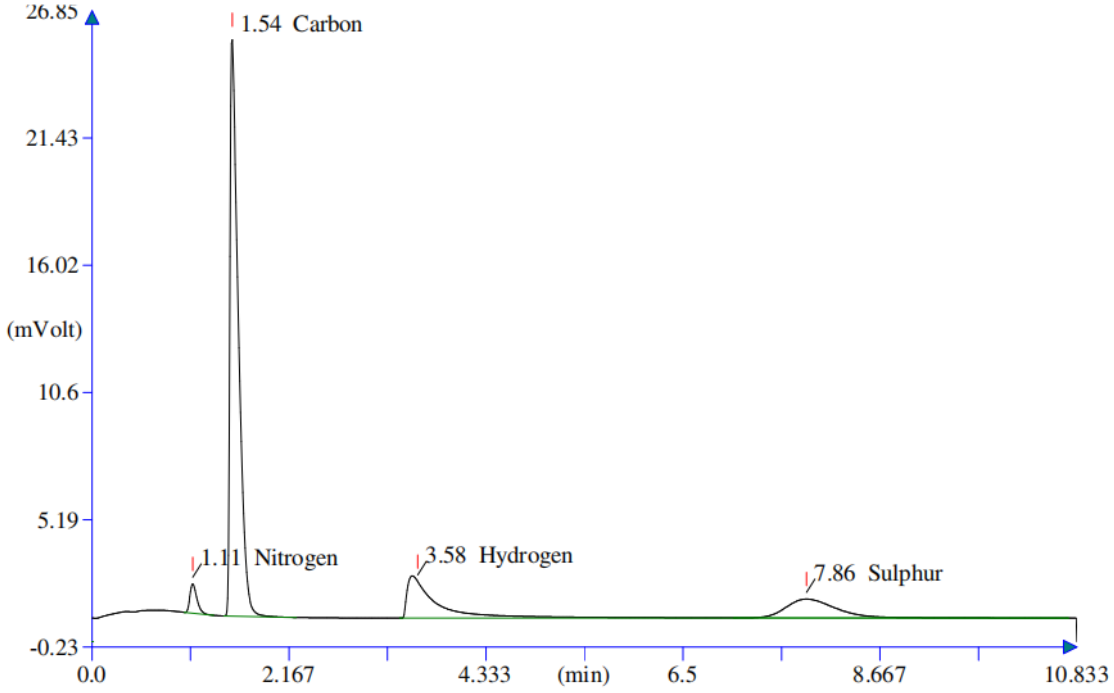
26.85
21.43
16.02
(mVolt)
10.6
5.19
-0.23
1.54 Carbon
1.11 Nitrogen
3.58 Hydrogen
7.86 Sulphur
0.0
2.167
4.333
(min)
6.5
8.667
10.833

(Z)-2-(5-(4-(dimethylamino)benzylidene)-4-oxo-2-thioxothiazolidin-3-yl)acetic acid

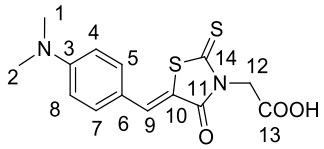


0.6934 g rhodanine-N-acetic acid was dissolved in the absolute EtOH and 0.66 mL piperidine was added. 5 min later, 0.5351 g 4-(dimethylamino)benzaldehyde was added, and the mixture is heated to reflux. 30 min later, the red precipitation formed. The temperature was cooled to 0 °C and 3M HCl in water was added. 5 min later, the precipitation was collected by conical sintered glass funnel and washed by cold distilled water and cold ethanol. The mass of the product is 1.156 g (> 99 %).

NMR spectrum:

$^1$H NMR (400 MHz, TFA) δ, ppm: 7.88 (1 H, H-$C_9$, s), 7.77 (2 H, H-$C_5$ and H-$C_6$, t), 7.71 (2 H, H-$C_4$, and H-$C_8$, d), 5.04 (2 H, $H_2$-$C_{12}$, s), 3.42 (4 H, $H_3$-$C_1$ and $H_3$-$C_2$, s).

ESI-MS+ spectrum:

m/z=323.1 for $[M+H]^+$, thus M = 322.0 g/mol.

$^1$H:

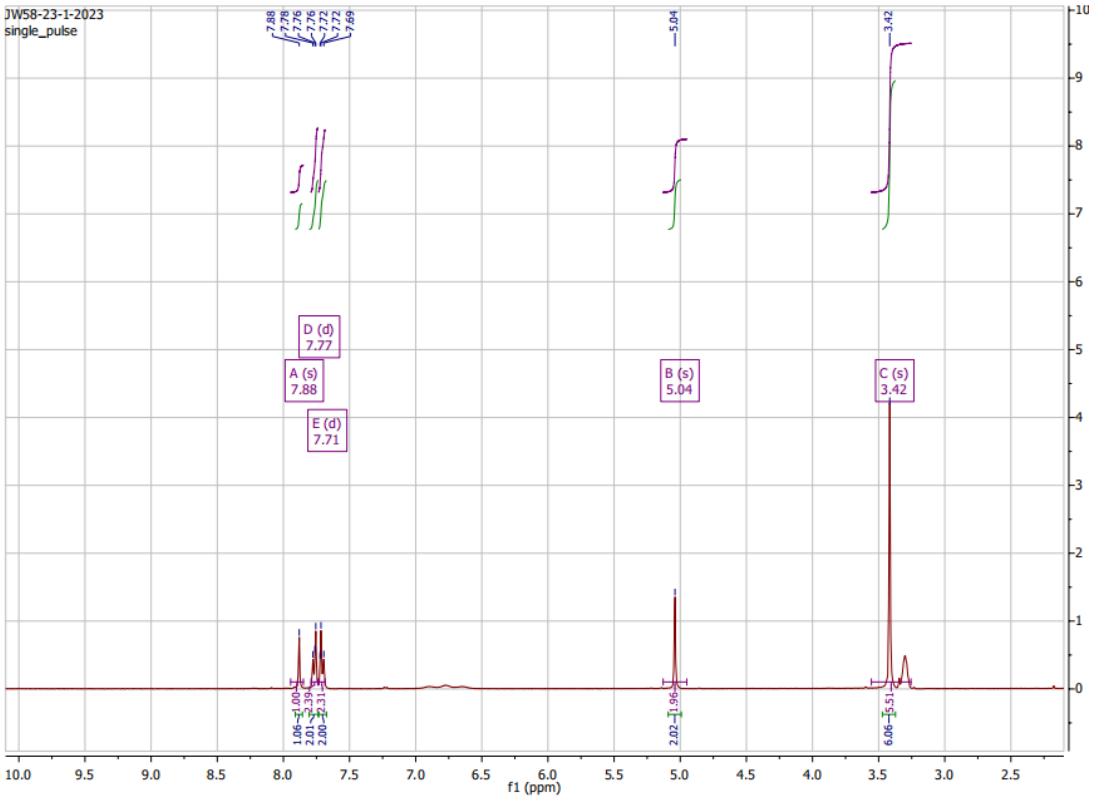

ESI-MS+:

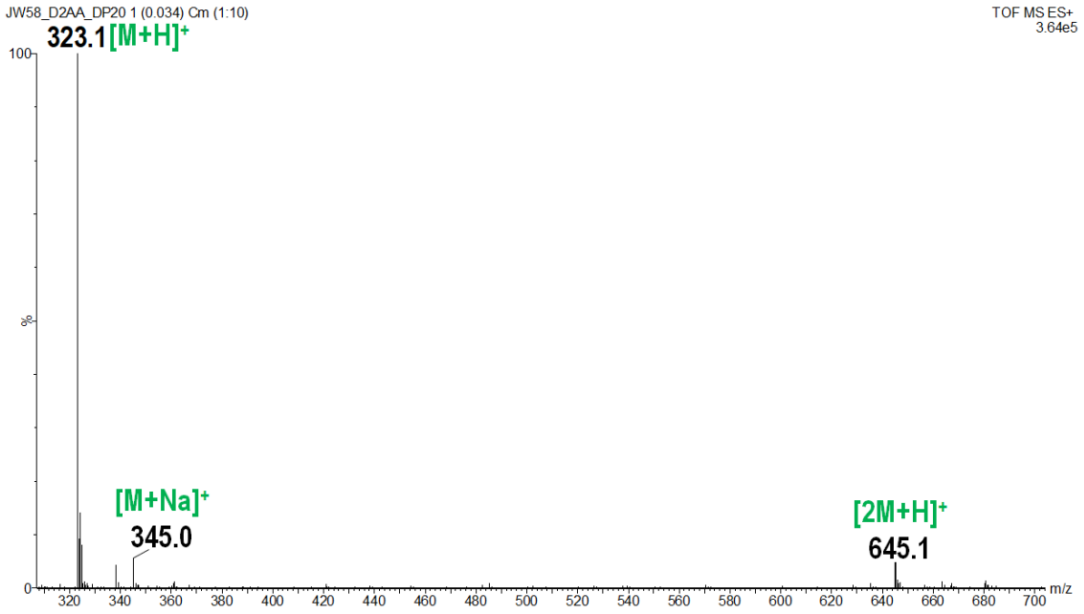
JW58_D2AA_DP20 1 (0.034) Cm (1:10)
TOF MS ES+
3.64e5
323.1 [M+H]+
100
%
0
[M+Na]+
345.0
[2M+H]+
645.1
320
340
360
380
400
420
440
460
480
500
520
540
560
580
600
620
640
660
680
700
m/z

# 5. Self-assembled monolayer of push-pull chromophore and oligomers on gold

## A. Self-assembled monolayer of synthesized push-pull chromophore on gold

After the successful synthesis of novel push-pull chromophore with the cyanoacrylic acid as the electron-withdrawing group, it is possible to graft such molecule on the substrate. In the case of the aggregation, the electronic structure changes because of the excitonic interaction, showing the different properties between the molecule and the aggregates. The self-assembly of the push-pull chromophore is the intentional aggregation to form the structure as ordered as possible to create an interface where the intrinsic electrical dipole is aligned in good organisation. Such alignment of dipoles will modify the electrical stimuli so that the activation and/or inhibition potential of the deployment of the electro-responsive oligopeptide chain can be shifted, resulting a new activation potential.

We will graft the novel push-pull chromophore in the solution because it is believed that the thioacetate can be hydrolysed on the surface site of the gold and then it can be grafted on the gold. Then, this direct functionalization will be done in different solvents and different concentrations because the choice of the solvent and the concentration can have a direct impact of the quality of the self-assembled monolayer. It is believed to have higher solubility to facilitate the self-assembled monolayer formation. If the solution contains too much J-aggregates, it is detrimental for the formation of the self-assembled monolayer. The first reason is that the aim is to create an interface covered by well-oriented electrical dipoles and the head-tail structure of the electrical dipole of the J-aggregation makes it unappealing for the final objective. The second reason is that the low solubility of the push-pull chromophore is a solvent can leave lots of molecular aggregates on the surface, which leads misleading and even incorrect result for the analysis. The prepared SAMs will be checked by contact angle measurement, AFM and STM to see whether the push-pull chromophore is grafted on the gold surface or not.

### I. Self-assembled monolayer preparation

For surface functionalization, the push-pull chromophore has been synthesized and characterized in the chapter 4. The gold substrate for the contact angle measurement was made by the evaporation of gold under the vacuum on a gallium arsenide substrate. The Au(111) on mica for scanning tunnelling microscopy and tapping-mode atomic force microscopy from Phasis Geneva Switzerland. All solvents were bought from Fisher and Sigma-Aldrich. Prior to the functionalization, the Au electrode surface was UV-ozone (in air) processed for 10 min.

The surface functionalization was formed by immersing the precleaned Au substrate in a freshly prepared solution. Three different molecules are used: (E)-3-(4-((6-(acetylthio)hexyl)(methyl)amino)phenyl)-2-cyanoacrylic acid (JW112), (2E,2'E)-3,3'-(((disulfanediylbis(hexane-6,1-diyl))bis(methylazanediyl))bis(4,1-phenylene))bis(2-cyanoacrylic acid) (JW88) and (Z)-2-(5-(4-(dimethylamino)benzylidene)-4-oxo-2-thioxothiazolidin-3-yl)acetic acid (JW58). They are shown in figure 1.

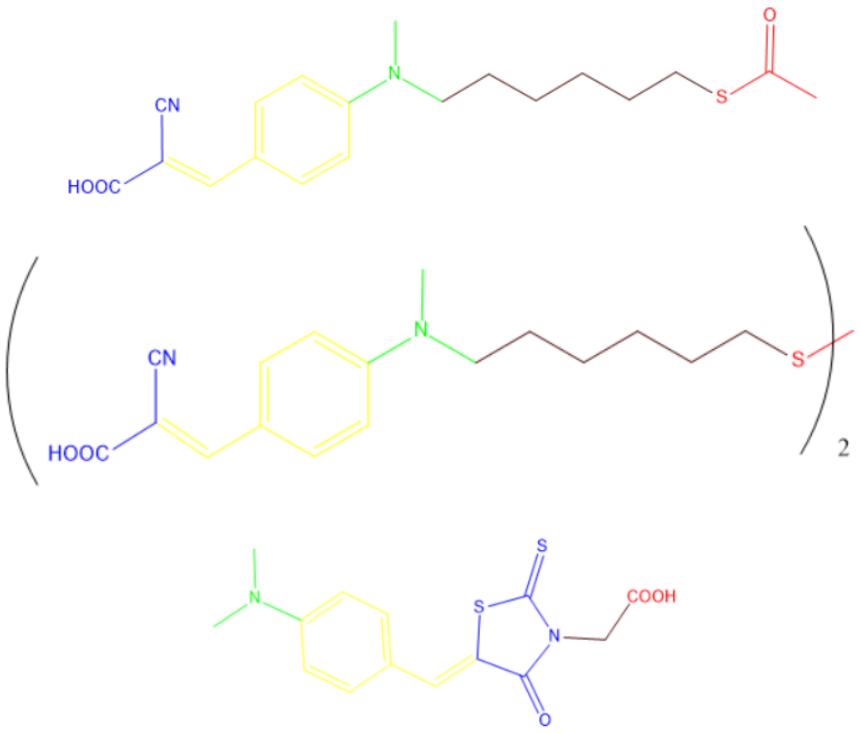


**Figure 1**: molecular structure of (from top to bottom) JW112, JW88 and JW58

The first series of the samples used the solution with a concentration of 0.001 mM, 0.01 mM, 0.1 mM and 1 mM of JW112 in tetrahydrofuran at room temperature for 48h. The substrate will be rinsed by the bath of tetrahydrofuran for twice, the bath of acetone for twice and dried using nitrogen gas. The stuff is in the vacuum of glove box for 1 min after the functionalization. These samples were characterized by contact angle measurements, scanning tunnelling microscopy and atomic force microscopy. The goal is to determine the best concentration.

The second series of the samples used the solution with a concentration of 1mM JW112 and $10^{-4}$ M $NaOH_{(aq)}$ in 10 mL different mixed solution (1 % $H_2O$ + 99 % absolute EtOH, 1 % $H_2O$ + 99 % tetrahydrofuran and 1 % $H_2O$ + 99 % N,N-dimethyl formaldehyde). The substrate is the nanostructured gold on glass slide for SERS analyses. The substrate is immersed in the solution for 24 h at room temperature. The sample preparation is finished by rinsing by absolute ethanol for three times and dried by nitrogen gas. The goal is to determine the best solvent.

The third series of the samples used the solution with a concentration of 0.005 mM, 0.05 mM and 0.5 mM of JW88 in tetrahydrofuran, absolute ethanol and N,N-dimethyl formaldehyde at room temperature for 48h. The self-assembled monolayers are collected, rinsed by absolute ethanol for two times and dried by nitrogen gas. They are characterized by contact angle measurement, atomic force microscopy and scanning tunnelling microscopy. The substrate for AFM is Au/mica. The goal is to determine the best solvent and the best concentration.

For JW58, the solution is 10 mM JW58 and 5 mM $Na_2CO_3$ in THF/$H_2O$ (49.5%/50.5%) solution. The immersion condition is all at room temperature for 48 h. After the immersion, the prepared self-assembled monolayer on the substrate is rinsed by absolute ethanol, distilled $H_2O$ and absolute ethanol and dried by nitrogen gas. This self-assembled monolayer is checked by contact angle measurement, scanning tunnelling microscopy, atomic force microscopy and attenuated total reflection-Fourier transform infrared spectroscopy.

The fifth series of the samples used to further analyse the structure and the chemical composition of the self-assembled monolayer on gold. Two further spectroscopic methods are used: ATR-FTIR and XPS. The composition of the solution to prepare the SAM is the following. For the SAM of disulfide based push-pull chromophore on gold, it is a solution of 1mM JW88 in absolute ethanol. The gold substrate was immersed in the solution for 48h. Then the self-assembled monolayer on the gold substrate is rinsed by absolute ethanol two times and dried by nitrogen gas. For the SAM of thioacetate based push-pull chromophore on gold, it is a solution of 1 mM JW112 and 1 mM $NaOH_{(aq)}$ THF/$H_2O$ solution (90% /10%). The gold substrate was immersed in the solution for 48h. Then the self-assembled monolayer on the gold substrate is rinsed by THF two times, $H_2O$ for one time and absolute ethanol two times and dried by nitrogen gas.

The last part of this chapter is to compare the asymmetrical electrical behaviour using three different push-pull chromophores using scanning tunnelling microscopy. It is known that the parameters to prepare the self-assembled monolayer are crucial because a slight change in the parameters can drastically change the quality and the property of the self-assembled monolayer. The criterion is to find the set of parameters to have the strongest asymmetrical electrical behaviour and to compare. For JW112 (with thioacetate), the solution is 1 mM JW112 and 1 mM NaOH in absolute THF/$H_2O$ (9:1) solution. The gold substrate was immersed in the solution for 48h. Then the self-assembled monolayer on the gold substrate is rinsed by THF two times, $H_2O$ one time and absolute ethanol for two times and dried by nitrogen gas. For JW88 (with disulfide), the solution is 1 mM JW88 in absolute EtOH. The gold substrate was immersed in the solution for 48h. Then the self-assembled monolayer on the gold substrate is rinsed by absolute ethanol two times and dried by nitrogen gas. For JW58 (with rhodanine-N-acetic acid), the solution is 10 mM JW58 and 5 mM $Na_2CO_3$ in THF/$H_2O$ (49.5%/50.5%) solution. The immersion condition is all at room temperature for 48 h. After the

immersion, the prepared self-assembled monolayer on the substrate is rinsed by absolute ethanol, distilled $H_2O$ and absolute ethanol and dried by nitrogen gas.

## II. Contact angle measurement

For the experiment of the water contact angle measurement, we prepared a series of the solution with different concentrations of JW112 three times using tetrahydrofuran at room temperature for 48h. The table 1 summarized the whole experimental conditions:

| Contact angle (°) | 1 mM in THF | 0.1 mM in THF | 0.01 mM in THF | 0.001 mM in THF | Reference in the solvent |
|---|---|---|---|---|---|
| Sample 1 | 69.1±1.5 | 65.1 ± 2.2 | 74.6±4.9 | 68.7 ± 3.7 | 67.5±3.9 |
| Sample 2 | 74.9±2.8 | 69.4 ± 2.9 | 69.0±7.5 | 70.1 ± 3.1 | 65.0±4.0 |
| Sample 3 | 77.8±3.9 | 73.9 ± 4.6 | 73.2±5.2 | 73.1 ± 4.3 | 67.5±3.3 |
| Average | 73.9±4.6 | 69.5 ± 4.6 | 72.3±6.2 | 70.7 ± 4.1 | 66.7±3.8 |

**Table 1**: the result of the experiment of the contact angle measurement for the series of the solution with different concentrations of JW112 using tetrahydrofuran at room temperature for 48h

According to the result of the table, the reproducibility of the sample preparation and the contact angle measurements can be ensured. A general trend is found that the increase of concentration causes the higher water contact angle, especially at 1 mM, inferring the higher coverage. It is believed that the cyanoacrylic acid group is hydrophilic, so the increase of the water contact angle is due to the contact of exposed methylene group. This shows that the self-assembled monolayer is not in standing up phase. To further study the structure of the self-assembled monolayer of push-pull chromophore on gold, it is useful to see the result of the scanning tunnelling microscopy and tapping-mode atomic force microscopy.

The structure of push-pull chromophore is based on thioacetate (JW112) for the previous paragraph, several self-assembled monolayers were done also using push-pull chromophore with disulfide structure (JW88). It is believed that the grafting of the push-pull chromophore with disulfide structure will undergo a redox reaction to give the same structure on the surface as the one using thioacetate: R-S-S-R+ Au(0) → 2 R-S(-II)-Au(+I)

Since a factor 2 is in the chemical reaction, the concentration is divided by two to assimilate the same push-pull chromophore with disulfide structure. The

aim here is to see if the choice of the solvent has an impact on the quality of the self-assembled monolayer. The first attempt is to prepare several self-assembled monolayers on gold using different solvents and different concentrations.

| Contact angle (°) | 0.5 mM | 0.05 mM | 0.005 mM |
|---|---|---|---|
| THF | 65.9±3.6 | 50.3±4.9 | 42.8±6.1 |
| EtOH | 76.4±2.1 | 76.9±0.8 | 64.7±2.1 |
| DMF | 68.5±1.6 | 56.1±2.5 | 50.1±5.4 |

**Table 2**: the result of the experiment of the water contact angle measurement for the series of the solution with different concentrations of JW88 and with different solvents at room temperature for 48h

Water contact value of dicyano-push-pull chromophore based self-assembled monolayer is 79°[6] and it confirms that the top of the self-assembled monolayer is carboxylic acid. Gold is very hydrophilic and thus the lower the concentration of the push-pull chromophore in the solution, the smaller the value of the contact angle. Thus, EtOH is the best solvent by fixing the same concentration of push-pull chromophore in the solution.

Finally, the push-pull chromophore with rhodanine-N-acetic acid (JW58) was grafted on the gold surface using carboxylic acid as the grafting unit. 67.6±1.5° is observed for water contact angle measurements.

## III. Scanning tunnelling microscopy

The first result is for the first series of the samples which used the solution with a concentration of 0.001 mM, 0.01 mM, 0.1 mM and 1 mM of JW112 in tetrahydrofuran at room temperature for 48h.

When the concentration of the push-pull chromophore is 0.01 mM in THF in figure 2, there are some white spots and dark holes from the STM image. The white spots are caused by the islands of the push-pull chromophore according to the topography. According to the sectional analysis, the dark holes are defects on the surface due to etching process (etch pits). Indeed, their size is bigger compared to the dark holes on the bare substrate. Also, the I-V curves in figure 4 were done by pointing the cursor on the white spots and the area out of the white spots.

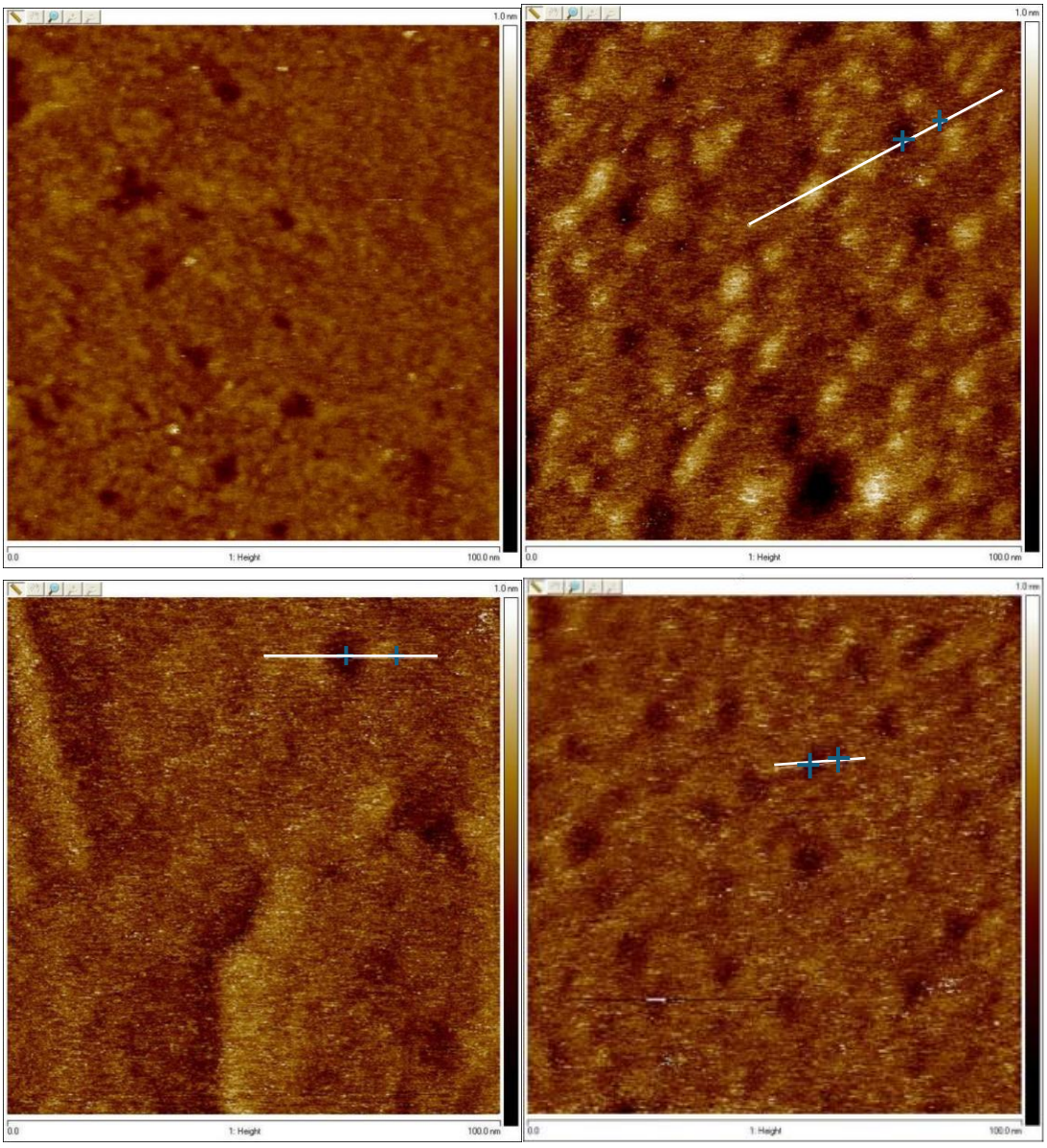

**Figure 2**: (top left) STM (5pA, -200mV) image (100*100 $nm^2$) of Au(111)/mica; (top right) STM (5pA, -200mV) image (100*100 $nm^2$) of push-pull chromophore self-assembled monolayer on Au(111)/mica (0.01 mM, RT, 48h, THF); (bottom left) STM (5pA, -200mV) image (100*100 $nm^2$) of push-pull chromophore self-assembled monolayer on Au(111)/mica (0.1 mM, RT, 48h, THF); (bottom right) the STM (5pA, -200mV) image (100*100 $nm^2$) of push-pull chromophore self-assembled monolayer on Au(111)/mica (1 mM, RT, 48h, THF)

The roughness of the image is recorded. The value is 0.051 nm for the gold substrate, 0.113 nm for the surface when the concentration is 0.01 mM. It becomes 0.098 nm when the concentration is 0.1 mM and 0.102 nm when the concentration is 1 mM. It seems that the roughness increased as the self-assembled monolayer is formed on the surface.

The I-V curves in figure 4 shows asymmetrical properties when the cursor is on the white spots whereas symmetrical properties when the cursor is out of the white spots. This confirmed the successful grafting of the push-pull chromophore since it possesses the intrinsic electrical dipole structure.

When the concentration of the push-pull chromophore is 0.1 mM in THF, there are more dark holes from the STM image in figure 2, and it seems that the surface is fully covered by the push-pull chromophore. According to the sectional analysis in figure 3, the dark holes are defects on the surface due to etching process (etch pits). Also, the I-V curves in figure 4 were done by pointing the cursor on the image. The I-V curve shows asymmetrical properties. Again, this confirmed the successful grafting of the push-pull chromophore with its intrinsic electrical dipole structure.

When the concentration of the push-pull chromophore is 1 mM in THF, there are more dark holes from the STM image in figure 2, and the surface is fully covered by the push-pull chromophore. According to the sectional analysis in figure 3, these dark holes are defects on the surface due to etching process. Also, the I-V curves in figure 4 were done by pointing the cursor on the image. This confirmed the successful grafting of the push-pull chromophore since it possesses the intrinsic electrical dipole structure. Thus, there is no big difference between the STM images when the concentration of the push-pull chromophore is 1 mM or 0.1 mM except the number of etch pits.

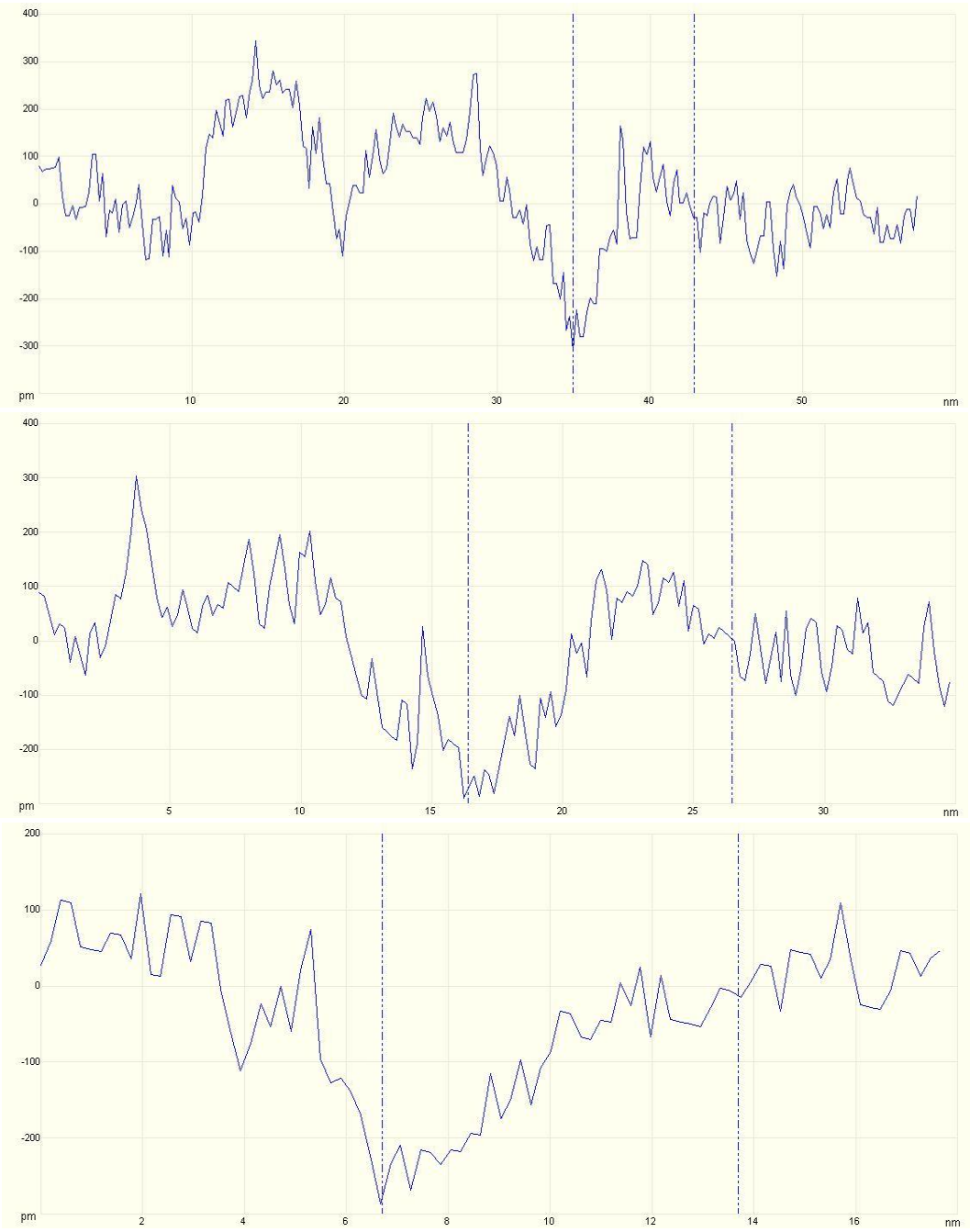


**Figure 3**: (top) the sectional analysis in the STM image when the concentration of the push-pull chromophore is 0.01 mM in THF; (middle) the sectional analysis in the STM image when the concentration of the push-pull chromophore is 0.1 mM in THF; (bottom) the sectional analysis in the STM image when the concentration of the push-pull chromophore is 1 mM in THF

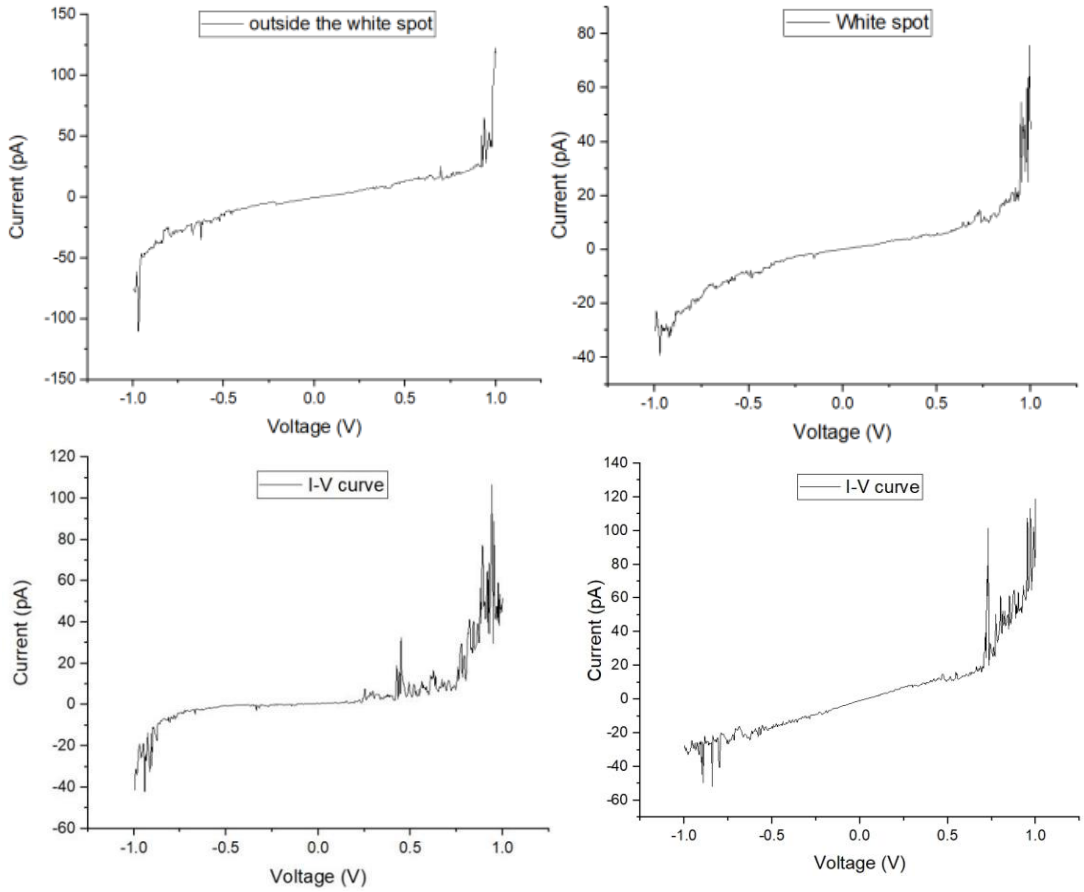


**Figure 4**: (top left) the I-V curve of a point outside the white spot in the STM image when the concentration of the push-pull chromophore is 0.01 mM in THF; (top right) the I-V curve of a point on the white spot in the STM image when the concentration of the push-pull chromophore is 0.01 mM in THF; (bottom left) the I-V curve of a point in the STM image when the concentration of the push-pull chromophore is 0.1 mM in THF; (bottom right) the I-V curve of a point in the STM image when the concentration of the push-pull chromophore is 1 mM in THF

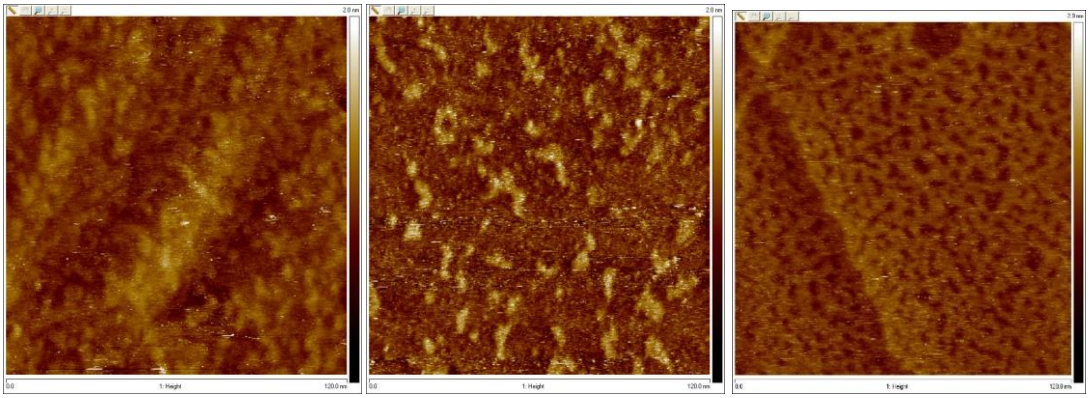

**Figure 5**: the STM images of disulfide based push-pull chromophore (JW88) in different solvents (left for DMF, middle for THF and right for EtOH) on Au(111)/mica (120nm*120nm, 2pA, -0.3V, 2 nm for height scale)

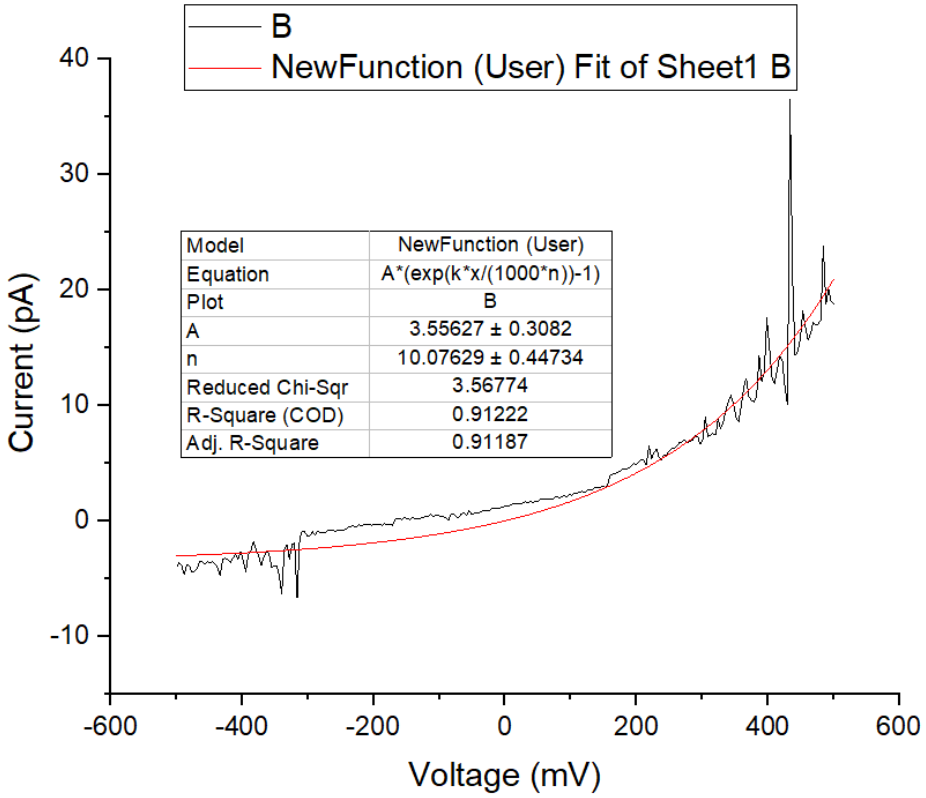


**Figure 6**: the I-V curve at a point in the STM image when the solution for the formation of self-assembled monolayer is 0.5 mM disulfide based push-pull chromophore (JW88) in absolute ethanol

For the third series of the samples which used the solution with a concentration of 0.5 mM of JW88 in tetrahydrofuran, absolute ethanol and N,N-dimethyl formaldehyde at room temperature for 48h, the STM images (high resolution) in figure 5 showed etch pits, direct evidence of R-S-Au formation since it can desorb from the surface. Asymmetrical I(V) curve proves the presence of push-pull chromophore on surface. The roughness of the surface is also recorded. The $R_q$ value is 0.130 nm when the solvent is EtOH, 0.212 nm when the solvent is THF and 0.151 nm when the solvent is DMF. Unfortunately, I cannot draw a conclusion to determine the best solvent using scanning tunnelling microscope. But the THF is not the best solvent either because the surface is not fully covered by the molecules or because of the existence of uncomplete second layer.

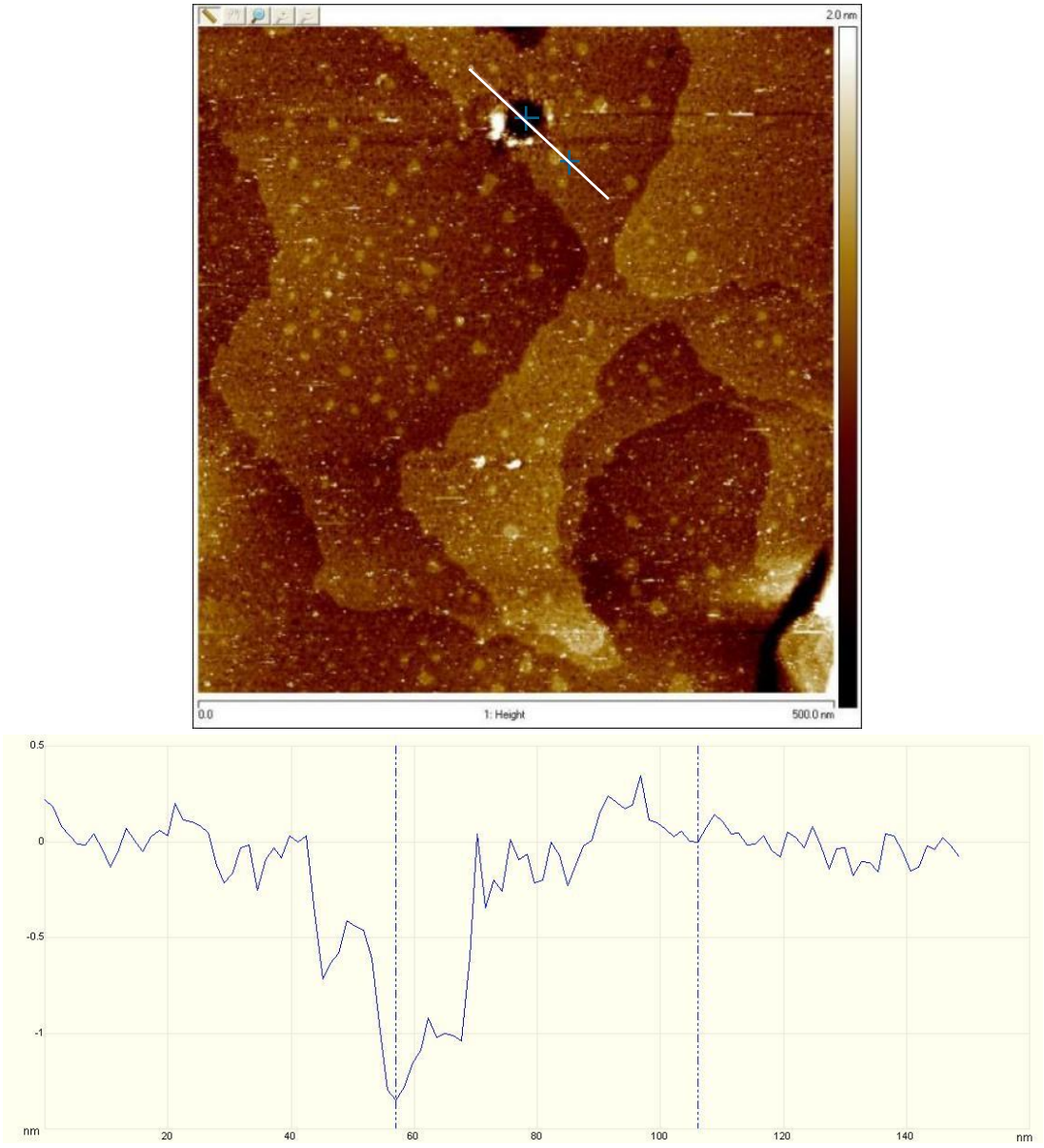


**Figure 7**: (top) the STM (5 pA, -200 mV) image (100*100 $nm^2$) push-pull chromophore (JW58) self-assembled monolayer on Au(111)/mica; (bottom) the sectional analysis of the self-assembled monolayer during the STM imaging

For the sample where the push-pull chromophore with rhodanine-N-acetic acid (JW58) was grafted on the gold surface using carboxylic acid as the grafting unit, STM images (figure 7) showed good quality for the surface functionalization. A hole was created during the STM measurements by applying locally a high voltage pulse. A depth of 1.3 nm is obtained, and it is compatible with the length of the push-pull chromophore molecule.

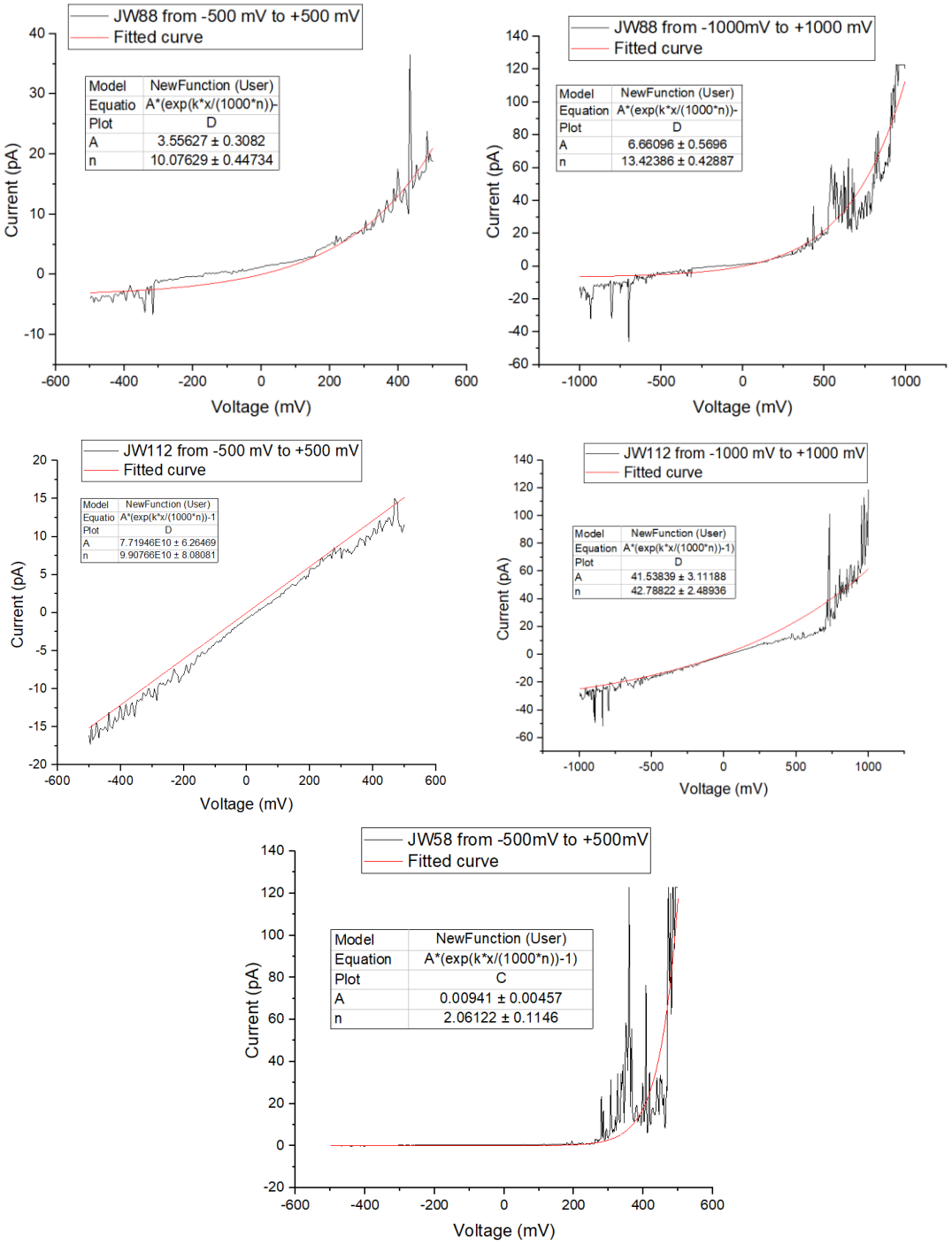


**Figure 8**: the I-V curve of a point on the self-assembled monolayer of JW88 from -500 mV to +500 mV (top left), JW88 from -1000 mV to +1000 mV (top right), JW112 from -500 mV to +500 mV (middle left), JW112 from -1000 mV to +1000 mV (middle right), JW58 from -500 mV to +500 mV (bottom) and during the STM imaging.

On I-V curves in figure 8, it is seen that there is almost no asymmetrical behaviour for JW112. For JW88 and JW58, the Schockley equation can be used (I is the current, $I_0$ is the dark current, e is the elemental charge, V is the voltage, $k_B$ is the Boltzmann constant, T is the temperature, n is the ideality coefficient):

$$I = I_0(\exp\left(\frac{eV}{nk_BT}\right) - 1)$$

The dark current is 3.56 pA for JW88 and 0.009 pA for JW58 after the fitting from -500mV to +500 mV. At ±500 mV, the rectification ratio is 0.7 for JW112, 4.7 for JW88 and $5.5\times10^3$ for JW58. At ±1000 mV, the rectification ratio is 4.3 for JW112 and 8.2 for JW88. A much significant asymmetrical behaviour is seen for JW58 due to higher asymmetrical ratio, lower dark current and narrow voltage range. The value of the rectification ratio found of JW58 is much higher compared to 100-200 in the work of Ashwell and Mohib[225] and from 2 to 19 in the work of Khalid et al.[226].

In terms of the statistics, 10% of the I-V curves show asymmetrical behaviour, the other 90% show either linear symmetrical curve due to the defects on the self-assembled monolayer or nonlinear sigmoid symmetrical curve due to the quadruple or even higher multipole formation in the self-assembled monolayer because of the strong electrostatic interaction between push-pull chromophore molecules. The high percentage of linear curves may come from laying down chromophores and/or head to tail structured push-pull chromophores.

## IV. Atomic force microscopy

For the first series of the samples which used the solution with a concentration of 0.001 mM, 0.01 mM, 0.1 mM and 1 mM of JW112 in tetrahydrofuran at room temperature for 48h, AFM images are shown in figure 9-12.

When the concentration is 0.01 mM (figure 10), tapping mode AFM image shows the existence of the molecular aggregation on the surface of the substrate as the white spots. With a phase contrast like the bare gold surface (figure 9), the surrounding surface is probably mostly coated with molecules.

When the concentration is 0.1 mM, tapping mode AFM image shows that the surface is not fully covered by the push-pull chromophore. The surface suffers a little bit the problem of the molecular aggregation. Big white aggregates can be seen in topography. The phase image reveals a homogenous network that can be assimilated to the molecules with a coverage of about 50% (figure 11).

For the topography image, the section analysis of the self-assembled monolayer of the push-pull chromophore shows that the size of molecular island is about 1.2-1.6 nm in figure 11, which is comparable to the theoretical value of the length of the push-pull chromophore (1.5 Å for the C-C bond length and assuming 16 carbons for the fully expanded shape of the push-pull chromophore molecule). However, the surface suffers from the problem of the molecular aggregation.

Tapping mode AFM images show that the surface is fully covered by the push-pull chromophore when the concentration of the push-pull chromophore is 1

mM in THF. Also, the surface suffers more from the problem of the molecular aggregation.

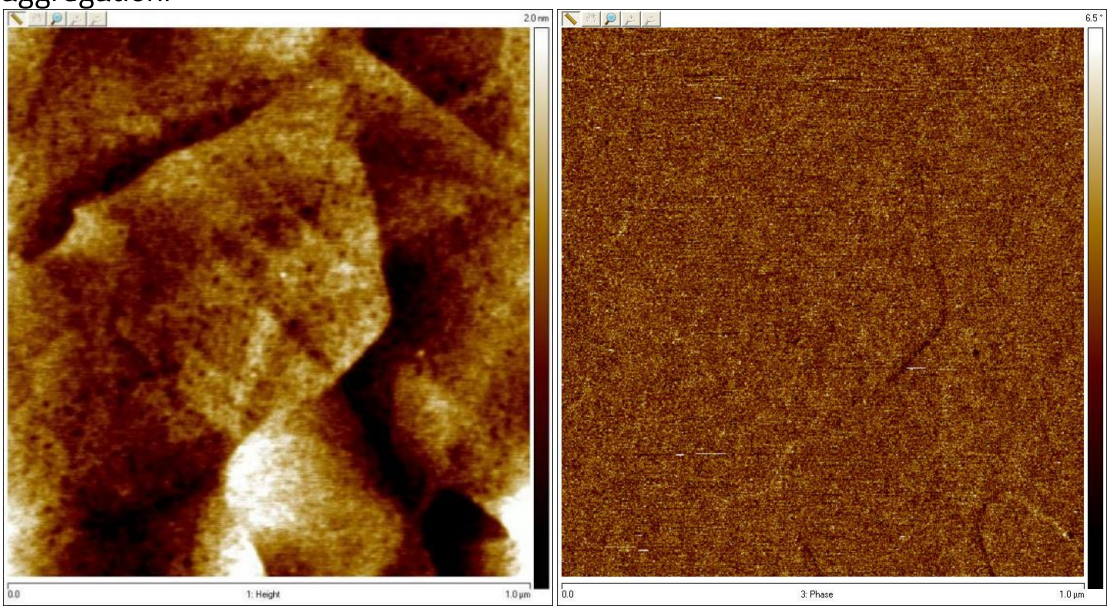


**Figure 9**: the AFM tapping mode (left) topography and (right) phase image (1*1 $\mu m^2$) of Au(111)/mica (2 nm z scale).

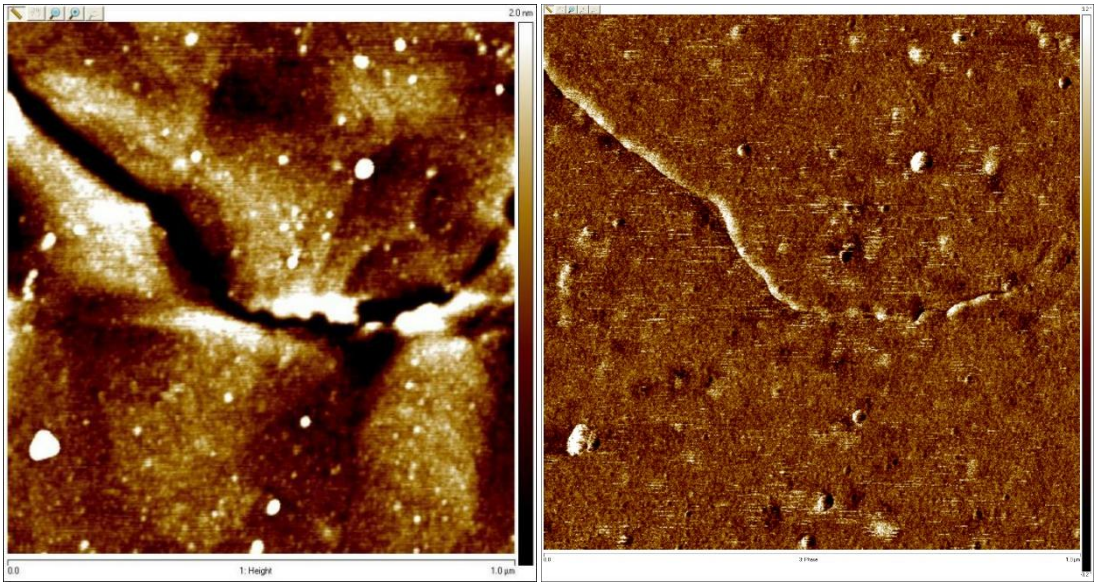


**Figure 10**: the AFM tapping mode (left) topography and (right) phase image (1*1 $\mu m^2$) of push-pull chromophore (JW112) self-assembled monolayer on Au(111)/mica (0.01 mM, RT, 48h, THF) (2 nm z scale)

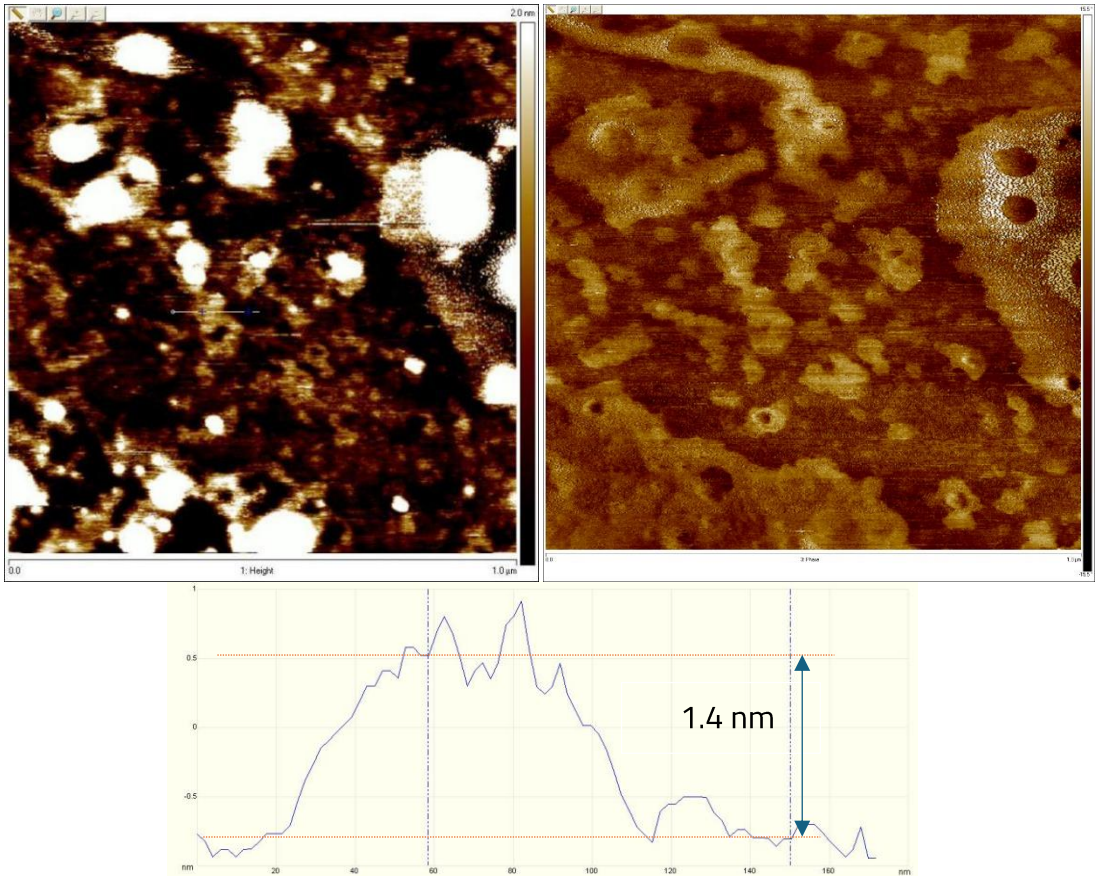


**Figure 11**: the AFM tapping mode (left) topography and (right) phase image (1*1 $\mu m^2$) of push-pull chromophore self-assembled monolayer on Au(111)/mica (0.1 mM, RT, 48h, THF) and (bottom) sectional analysis of an AFM image (2 nm z scale).

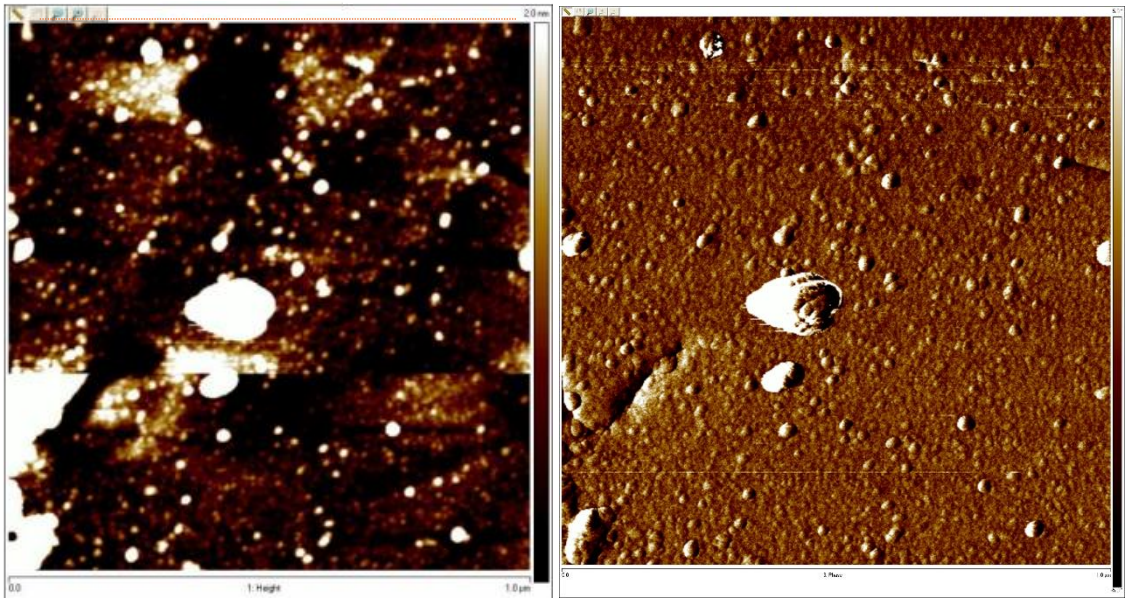

**Figure 12**: the AFM tapping mode (left) topography and (right) phase image (1*1 $\mu m^2$) of push-pull chromophore self-assembled monolayer on Au(111)/mica (1 mM, RT, 48h, THF) (2 nm z scale).

From the images, we can see that there are some drawbacks to use carboxylic acid molecules for the surface functionalization of the surface. Firstly,

due to the hydrogen bond, carboxylic acid group can form dimer, and it is easier to form aggregates in the solution than the push-pull chromophore without carboxylic acid group. Secondly, the low solubility of the carboxylic acid push-pull chromophore causes the problem of the uncleaned surface. For the scanning probe microscopy experiments, it causes a lot of big white spots in the image.

Due to different mechanical property, the phase response will be different for organic material and metallic material. When the concentration is 0.01 mM, the low coverage of the push-pull chromophore on gold cannot make any change in terms of the mechanical property (phase image). When the concentration is 0.1 mM, the contrast is clear enough to distinguish the part of the self-assembled monolayer and the other part of the gold substrate. The software showed that the coverage is 0.36. When the concentration is 1 mM, the surface is fully covered by the molecule and there is no contrast of mechanical property. In terms of the roughness $R_q$, it is 0.184 nm when the concentration is 0.01 mM, 0.406 nm when the concentration is 0.1 mM and 0.480 nm when the concentration is 1 mM.

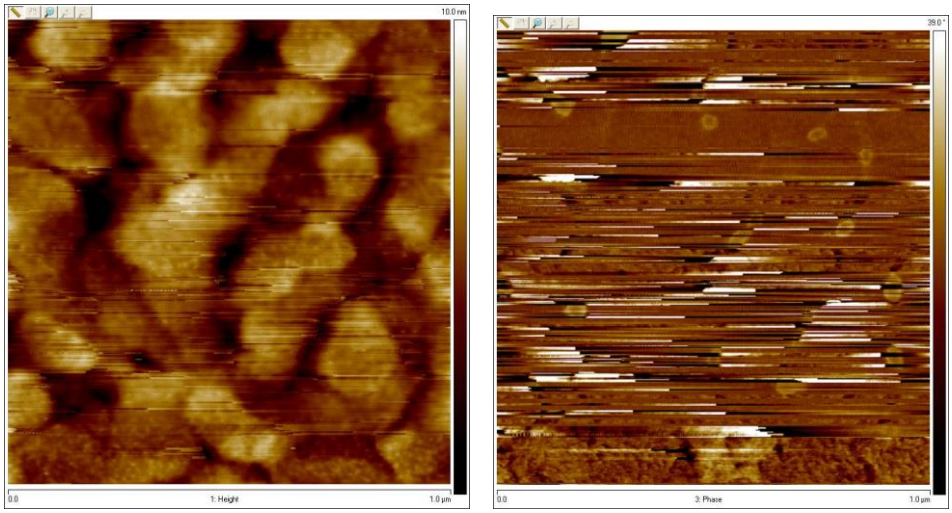

**Figure 13**: the AFM (left) topography and (right) phase images of gold substrate as the reference for self-assembled monolayer of disulfide based push-pull chromophore (JW88) on gold.

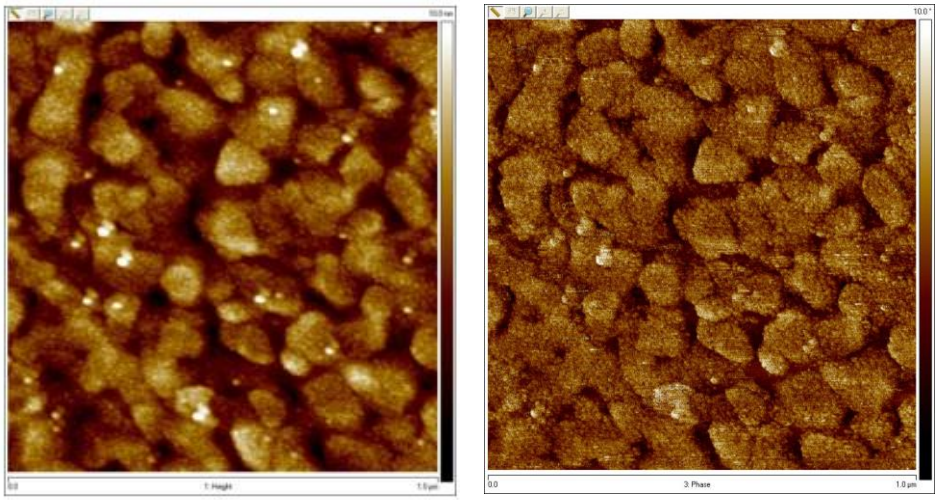

**Figure 14**: the AFM (left) topography and (right) phase images of self-assembled monolayer of disulfide based push-pull chromophore (JW88) on gold prepared in DMF.

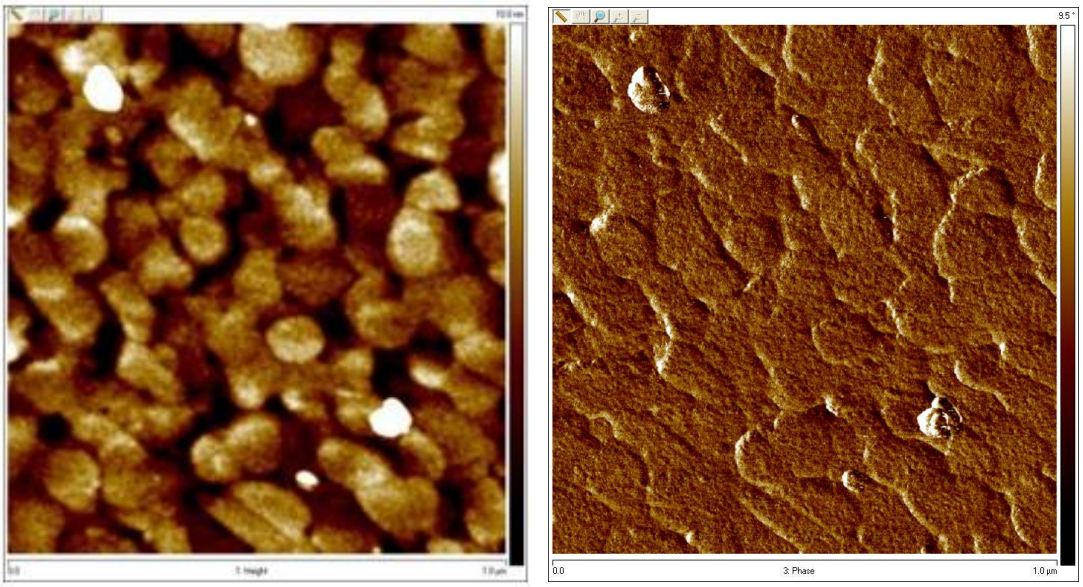

**Figure 15**: the AFM (left) topography and (right) phase images of self-assembled monolayer of disulfide based push-pull chromophore (JW88) on gold prepared in THF.

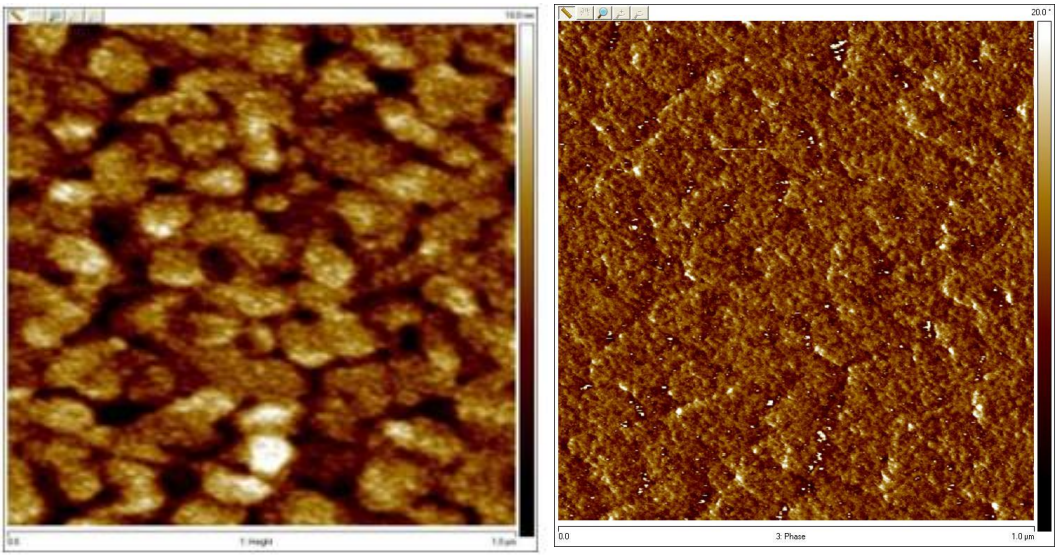

**Figure 16**: the AFM (left) topography and (right) phase images of self-assembled monolayer of disulfide based push-pull chromophore (JW88) on gold prepared in EtOH.

For the third series of the samples which used the solution with a concentration of 0.5 mM of JW88 in tetrahydrofuran, absolute ethanol and N,N-dimethyl formaldehyde at room temperature for 48h, the AFM images showed molecular domains on the surface due to the contrast with the bare substrate (figure 13). The roughness is measured in the individual gold terraces. The roughness $R_q$ value is 0.485 nm for the bare substrate, 0.835 nm when the solvent is DMF (figure 14), 0.470 nm when the solvent is THF (figure 15) and 0.617 nm when the solvent is EtOH (figure 16). The roughness of the surface is caused by the roughness of the surface of the substrate and the roughness of the surface of the self-assembled monolayer of molecules. The best solvent for the preparation of the

self-assembled monolayer of JW88 on gold is DMF due to the highest roughness modification compared to the bare substrate.

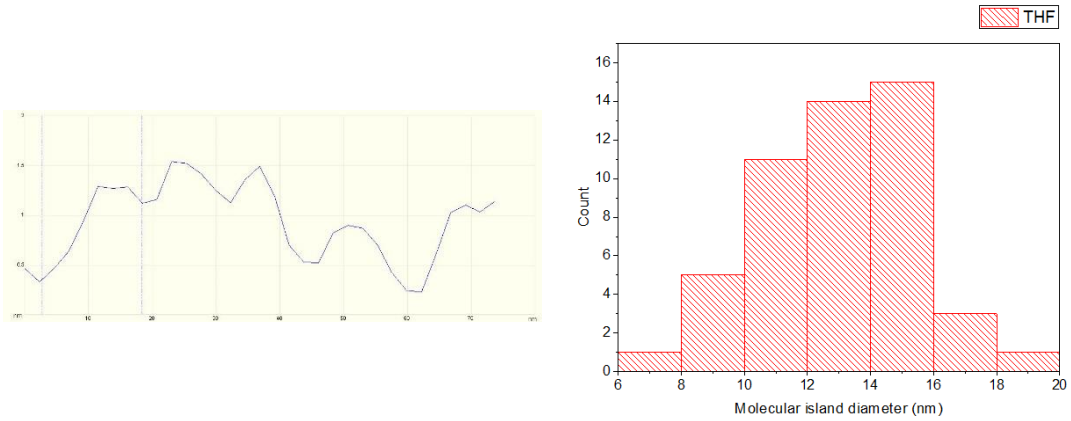


**Figure 17**: (left) the AFM topography sectional analysis and (right) phase images of self-assembled monolayer of disulfide based push-pull chromophore (JW88) on gold prepared in THF.

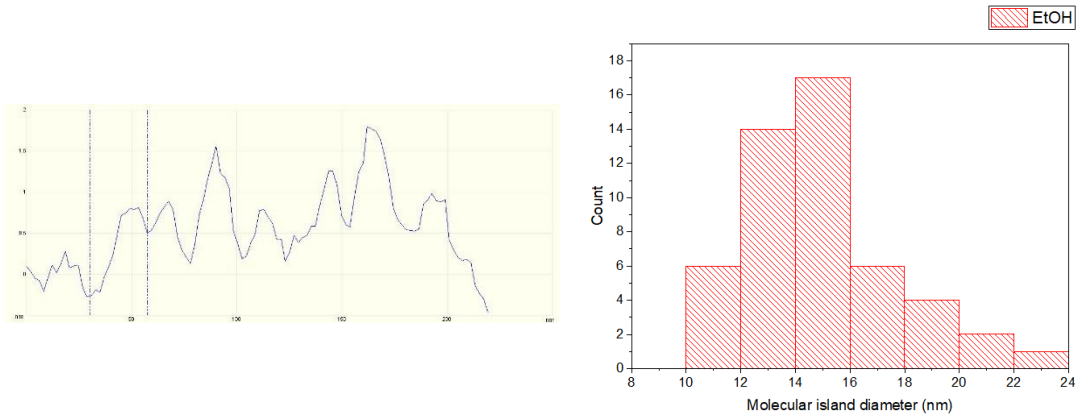


**Figure 18**: (left) the AFM topography sectional analysis and (right) phase images of self-assembled monolayer of disulfide based push-pull chromophore (JW88) on gold prepared in EtOH.

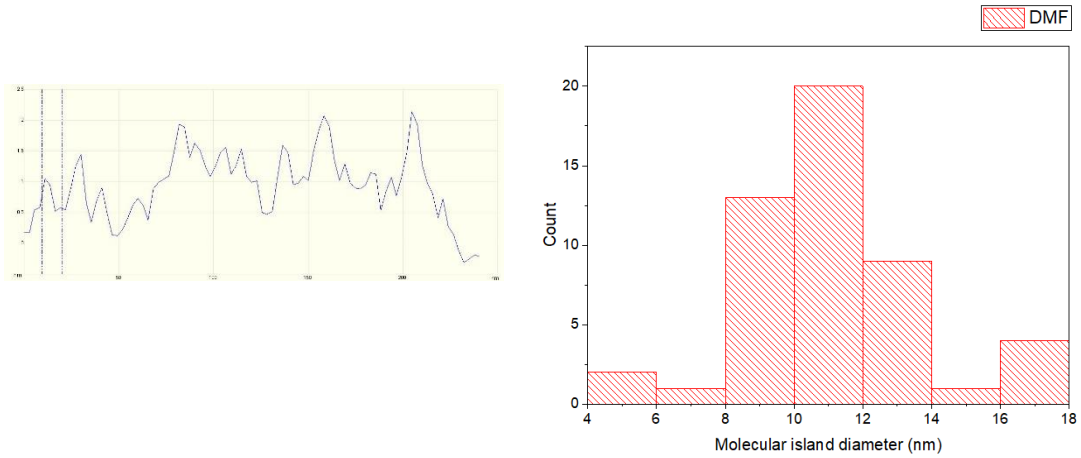


**Figure 19**: (left) the AFM topography sectional analysis and (right) phase images of self-assembled monolayer of disulfide based push-pull chromophore (JW88) on gold prepared in DMF.

The sectional analysis of and the distribution of the molecular island diameter in the self-assembled monolayer for the self-assembled monolayer of disulfide-based push-pull chromophore on gold prepared in THF, EtOH and DMF are

presented in the figure 17, 18 and 19 respectively. The sectional analysis shows that the higher the roughness, the more complex the curve in the sectional analysis. The distribution of the molecular island diameter has the form of the normal distribution. In terms of the molecular island diameter, it seems that it is biggest when the solvent is ethanol, smaller when the solvent is THF and smallest when the solvent is DMF.

Finally, the push-pull chromophore with rhodanine-N-acetic acid (JW58) was grafted on the gold surface using carboxylic acid as the grafting unit (10 mM in THF-$H_2O$ solution, 48 h at room temperature). AFM image in figure 20 (topography and phase) shows a lot of small aggregates all over the surface. The surface structure is not homogenous. The roughness $R_q$ of the self-assembled monolayer of push-pull chromophore based on rhodanine-N-acetic acid is 0.470 nm.

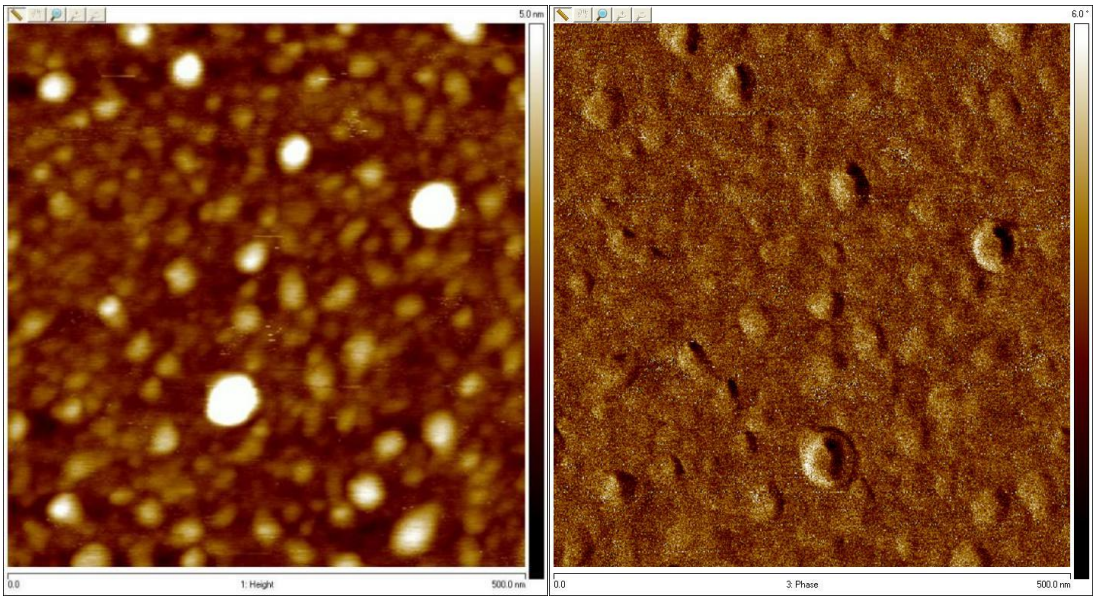


**Figure 20**: the AFM tapping mode (left) topography and (right) phase image (0.5*0.5 $\mu m^2$) of push-pull chromophore JW58 self-assembled monolayer on Au(111)/mica (10 mM, RT, 48h, THF+$H_2O$)

# V. Surface-enhanced Raman spectroscopy

A method called surface enhanced Raman spectroscopy is used to further investigate what is the best solvent for the grafting of JW112 on the surface. A good point for the surface-enhanced Raman spectroscopy is that it can detect the existence of the molecule even with a very low quantity on the surface. A special nanostructured gold substrate with LSPR effect was used to prepare the sample for SERS spectra. High resolution Raman spectra were recorded on a Horiba Jobin-Yvon HR800 LabRam, using a power of 0.005 mW with an acquisition time of 10 s and 10 accumulations, and with the wavelength of helium-neon laser $\lambda$= 632 nm.

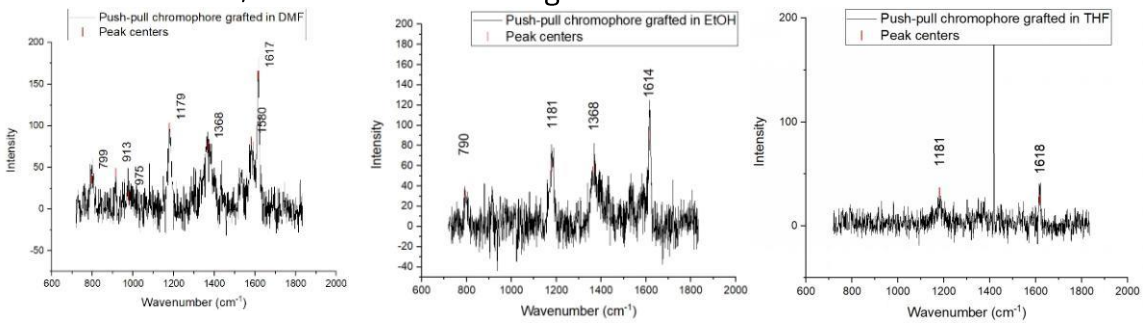


**Figure 21**: the SERS spectra of thioacetate based push-pull chromophore JW112 in different solvents on nanostructured Au/mica

The spectra in figure 21 were recorded in the same experimental conditions (preparation and spectra conditions) except the solvent to dissolve the push-pull chromophore. According to the spectra, the best solvent is dimethyl formaldehyde due to the highest counts of the band at (characteristic of push-pull) 1617 $cm^{-1}$. The signal around the 1400 $cm^{-1}$ when the solvent is tetrahydrofuran is not a signal from the molecule.

# VI. Attenuated total reflection-Fourier Transform Infrared Spectroscopy

The ATR-FTIR spectrum is recorded with Brucker Invenio with a MCT detector, and the ATR crystal is made by diamond. The number of accumulations is 32 and the resolution of the spectrum is 4 $cm^{-1}$. From the ATR-FTIR spectrum, the chemical composition information on the surface can be extracted. The SAM is grafted on the gold and the ATR crystal is on top of the SAM. The spectrum of the gold substrate as the reference shows no peaks.

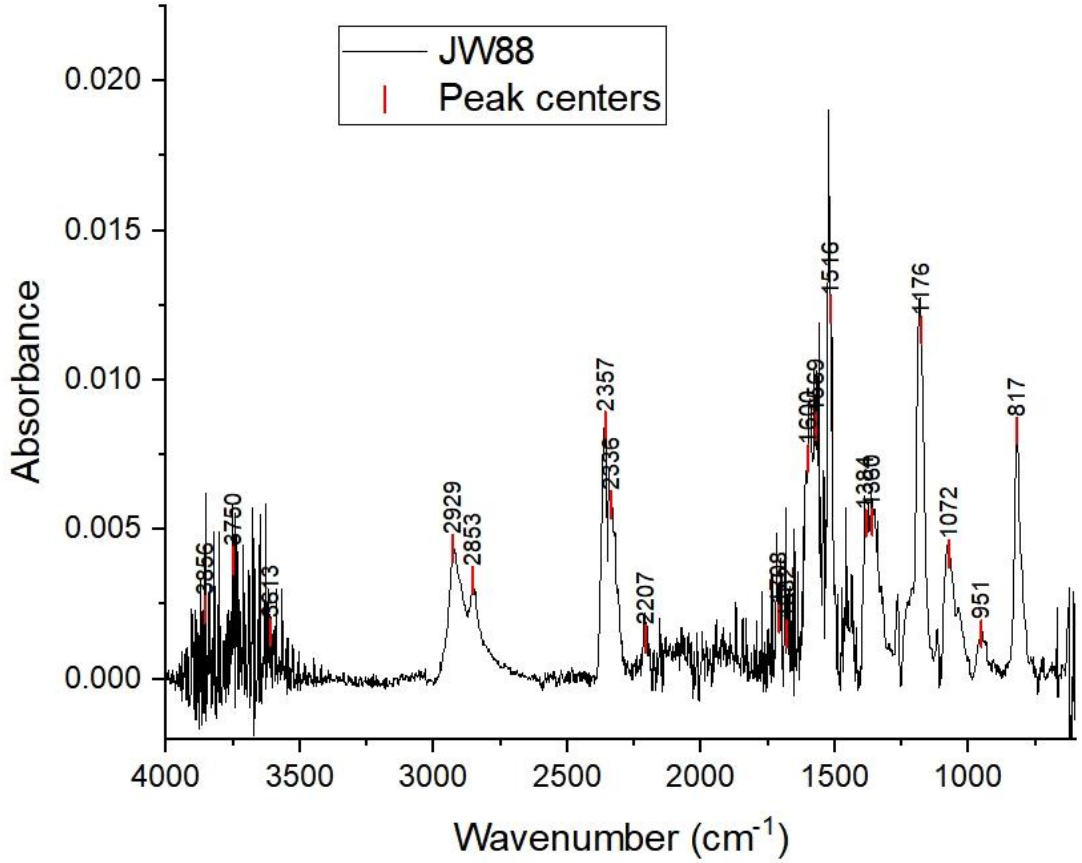


**Figure 22**: the ATR-FTIR spectrum of self-assembled monolayer of disulfide based push-pull chromophore JW88 on gold

The ATR-FTIR spectrum SAM of disulfide based push-pull chromophore JW88 on gold showed a lot of information in figure 22. The peaks at 2929 $cm^{-1}$ and 2853 $cm^{-1}$ are due to the asymmetrical stretching and symmetrical stretching of C-H bond. The asymmetrical stretching gives more electrical dipole exchange and the intensity in the spectrum is higher. The peaks at 2357 $cm^{-1}$ and 2336 $cm^{-1}$ are created by the asymmetrical stretching and symmetrical stretching of C-N triple (nitrile) bond. The peaks at 3856 $cm^{-1}$, 3750 $cm^{-1}$ and 3613 $cm^{-1}$ are attributed to the existence of carboxylic acid (broad at room temperature, liquid nitrogen is used

for us). The absorption value of nitrile is higher than the accumulative signal of C-H stretching.

The ATR-FTIR spectrum SAM of thioacetate based push-pull chromophore on gold showed a lot of information in figure 23. The peaks at 2936 $cm^{-1}$ and 2857 $cm^{-1}$ are due to the asymmetrical stretching and symmetrical stretching of C-H bond. The peaks at 2361 $cm^{-1}$ is created by the asymmetrical stretching and symmetrical stretching of CN(nitrile) triple bond. Also, carboxylic acid can be seen from 3500 $cm^{-1}$ to 4000 $cm^{-1}$ (broad at room temperature, liquid nitrogen is used for us). The peak at 1590 $cm^{-1}$ is attributed to the carbonyl group of thioacetate. The absorption value of nitrile is weaker than the accumulative signal of C-H stretching. There are several differences between the spectrum in figure 22 and the spectrum in figure 23. The specific signal is at 1708 $cm^{-1}$ for JW88 and 2005 $cm^{-1}$, 2361 $cm^{-1}$ and 2598 $cm^{-1}$ for JW112.

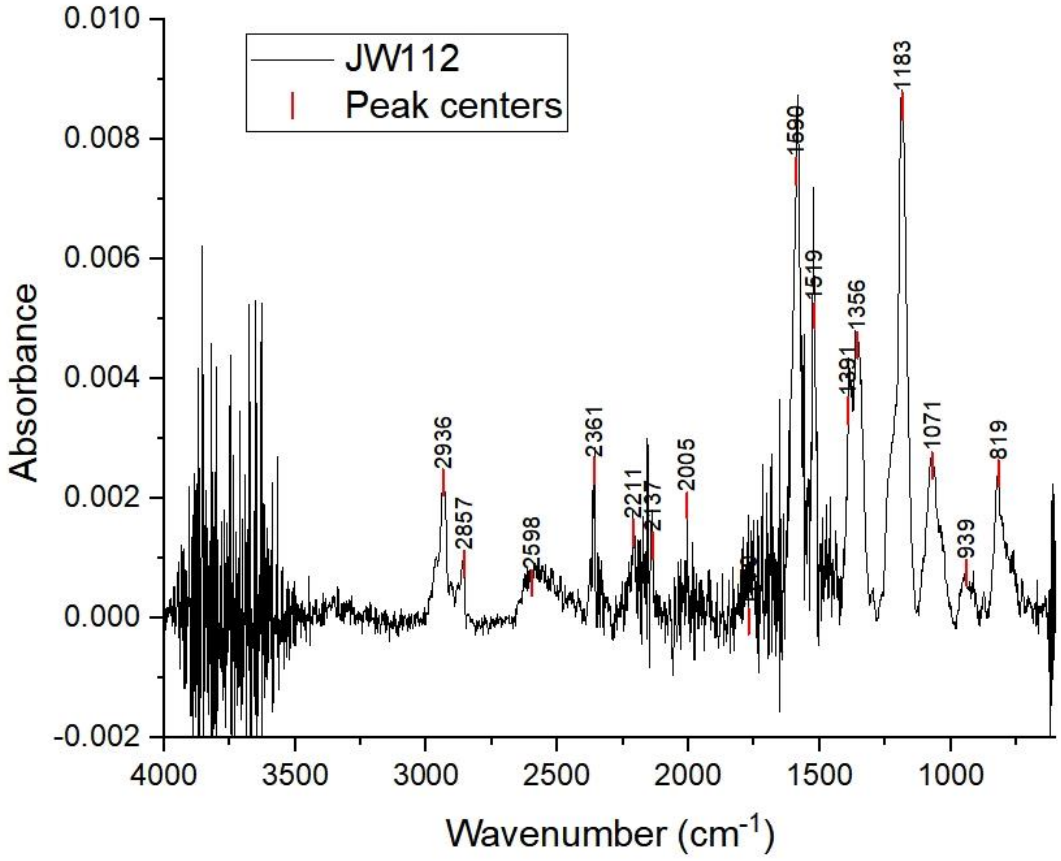


**Figure 23**: the ATR-FTIR spectrum of self-assembled monolayer of thioacetate based push-pull chromophore JW112 on gold

The ATR-FTIR spectrum SAM of rhodanine-N-acetic acid based push-pull chromophore JW58 on gold showed a lot of information in figure 24. The peaks at 2925 $cm^{-1}$ and 2854 $cm^{-1}$ are due to the asymmetrical stretching and symmetrical stretching of C-H bond. Carbonyl stretching is found according to the peak at 1747 $cm^{-1}$ and 1714 $cm^{-1}$. The peaks at 3835 $cm^{-1}$ and 3744 $cm^{-1}$ are attributed to the existence of carboxylic acid (broad at room temperature, liquid nitrogen is used for

us). Also, water molecules caused noise at that position. The signals at 1377 $cm^{-1}$ and 1174 $cm^{-1}$ are common in the spectrum in the figure 23 and the figure 24. The specific signals are 1648 $cm^{-1}$, 1557 $cm^{-1}$, 1511 $cm^{-1}$, 1459 $cm^{-1}$, 1256 $cm^{-1}$, 1114 $cm^{-1}$, 1013 $cm^{-1}$, 947 $cm^{-1}$, 723 $cm^{-1}$ in the spectrum in figure 24.

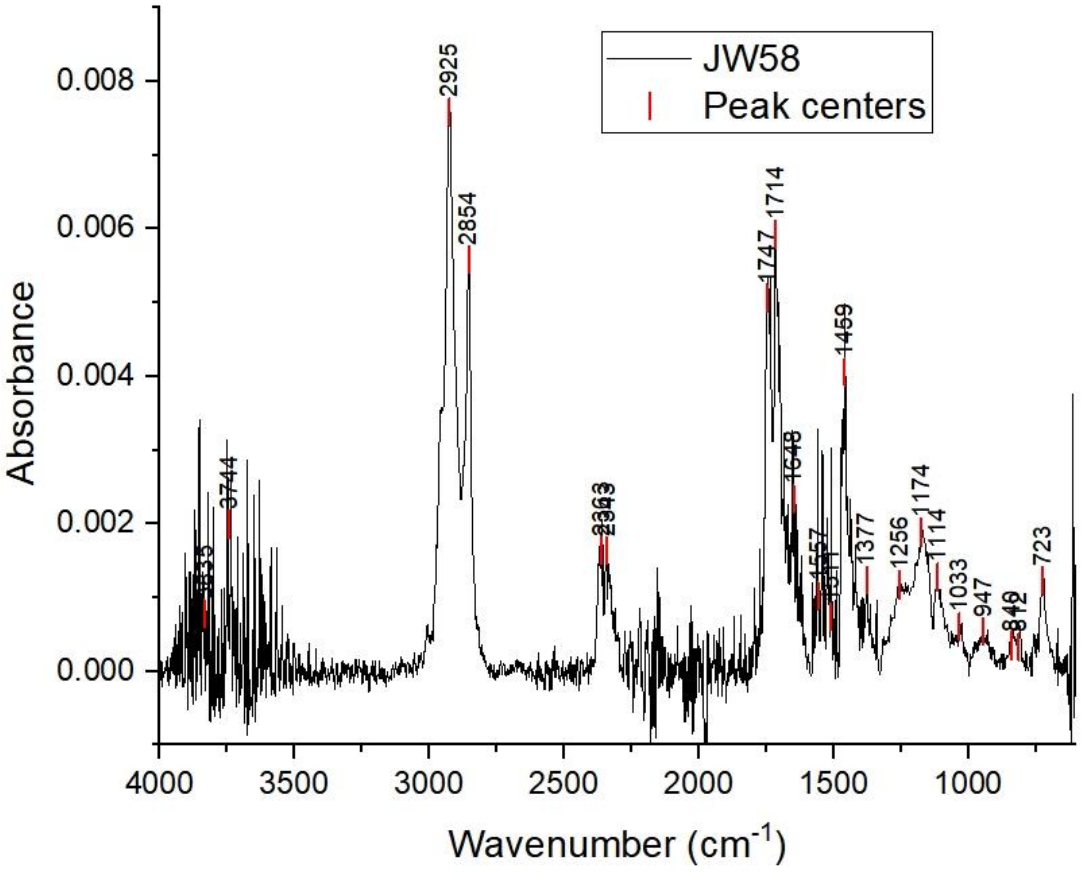


**Figure 24**: the ATR-FTIR spectrum of self-assembled monolayer of rhodanine-N-acetic acid based push-pull chromophore JW58 on gold

# VII. X-ray photoelectron spectroscopy

X-ray photoelectron spectroscopy (XPS) measurements were performed in a SPECS ProvenXPS system equipped with a PHOIBOS 150 2D-CMOS hemispherical analyser and a monochromated X-ray source FOCUS 500. The Al $K_\alpha$ X-ray source (1486.6 eV) running at 400 W is separated from the analyser by an angle of 55°. A medium magnification mode and constant pass energy of the analyser equal to 20 eV were used for analysis. Photoelectron data were recorded at a take-off angle of 90° (normal detection). A flood gun was used for surface charge compensation. The electron binding energies ($E_b$) were calibrated to maximum of the valence band. Binding energies, line widths and areas of the different XPS peaks were obtained by a weighted least-squares fitting of a Gaussian model curve to the experimental data using the Origin. The focus is on the S 2p signal for XPS using the excitation of core electron. The reference of the binding energy is from certain references[194,195].

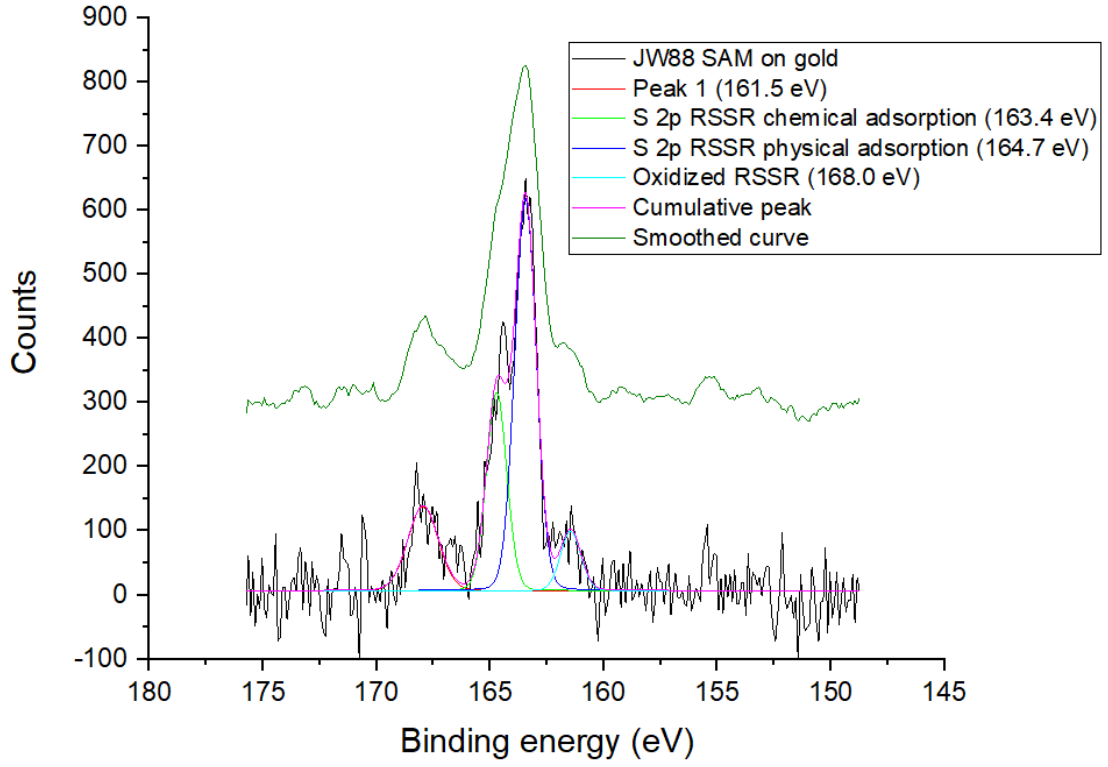


**Figure 25**: the XPS S 2p spectrum of self-assembled monolayer of disulfide based push-pull chromophore JW88 on gold. A curve above is the smoothed spectrum that has been shifted for the sake of the clarity.

A lot of information can be extracted from the XPS S 2p spectra. For disulfide based push-pull chromophore JW88 in figure 25, four peaks can be revelated: 161.5 eV, 163.4 eV, 164.7 eV and 168.0 eV in the spectrum. The main peaks are 163.4 eV, and 164.7 eV caused by the chemical adsorption and the physical adsorption of

push-pull chromophore respectively. The peak at 168.0 eV is for oxidized species on the surface. By looking at the reference value of the binding energy for the sulphur with different oxidation number, a problem is found. The reference value of binding energy for S(-II), S(-I) and S(0) are around 161 eV, 162 eV and 163.5 eV. There is shift towards higher binding energy for a more oxidized state from the experimental result and reference value. The reason to explain this for now is that UV-ozone processing is adopted prior to the SAM preparation and dioxygen molecule is dissociated by UV absorption. The atomic form of oxygen is adsorbed on the substrate, and it is the source to quench hydrogeno ligand after the addition oxidation.

For thioacetate based push-pull chromophore JW112 in figure 26, three peaks can be fitted by Pseudo-Voigt model. 163.5 eV is for chemical adsorption of the thioacetate-based push-pull chromophore. The presence of oxidized species can be seen in the spectrum (168.6 eV). The peak at 164.8 eV is for the physical adsorption. The process is believed to insert the gold atom between the sulphur and the carbon of the carbonyl, and the byproduct is the carboxylate. At the end, a smoothed curve is plotted in figure 26 to better show the allure of the curve.

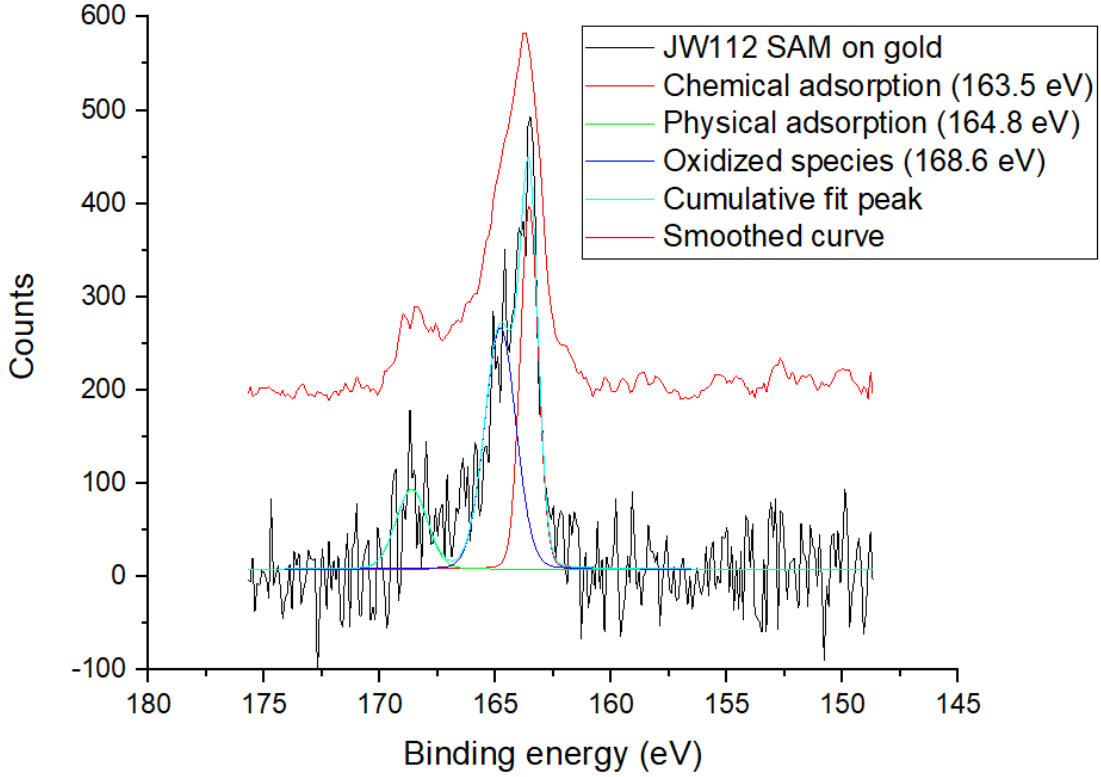


**Figure 26**: XPS S 2p spectrum of self-assembled monolayer of thioacetate based push-pull chromophore JW112 on gold and fits of the curve. The red curve is the smoothed spectrum that has been shifted for the sake of the clarity.

# VIII. Statistical analysis of the I-V curves of the adsorbed push-pull chromophore molecule on the surface

According to the XPS spectra, it seems that the sulphur part is attached on the surface. However, the oxidation state will not change if the thioacetate is adsorbed on the surface. Here we propose a theoretical approach to simulate our system: the preparation of the self-assembled monolayer with well oriented push-pull chromophores on the surface. There are two possible orientations of the push-pull chromophore on the surface. The orientation depends on the electrostatic interaction between the two molecules of the push-pull chromophore, the adsorption and the temperature. We use canonical ensemble to introduce this situation.

For a configuration (C), the probability to find this configuration P(C) in canonical ensemble is:

$$P(C) = \frac{e^{\frac{-E_C}{k_B T}}}{Z}$$

$k_B$: the Boltzmann constant
T: the temperature
Z: the partition function
$E_C$: the energy of the configuration
$\mu$: the chemical potential

The scanning tunnelling microscopy imaging condition is at room temperature. To have better electrical property, it is necessary to either decrease the temperature or lengthen the molecule. Moreover, the scanning tunnelling microscopy imaging condition is not in vacuum, it means that we cannot see the configuration of the molecule by topographical images. The idea is to use the scanning tunnelling spectroscopy function during the scanning tunnelling microscopy imaging. A small statistical analysis can be taken to determine the configuration of the adsorbed push-pull chromophore molecules on the surface via the identification of different allure of the curve. An explanation is presented in the figure 27.

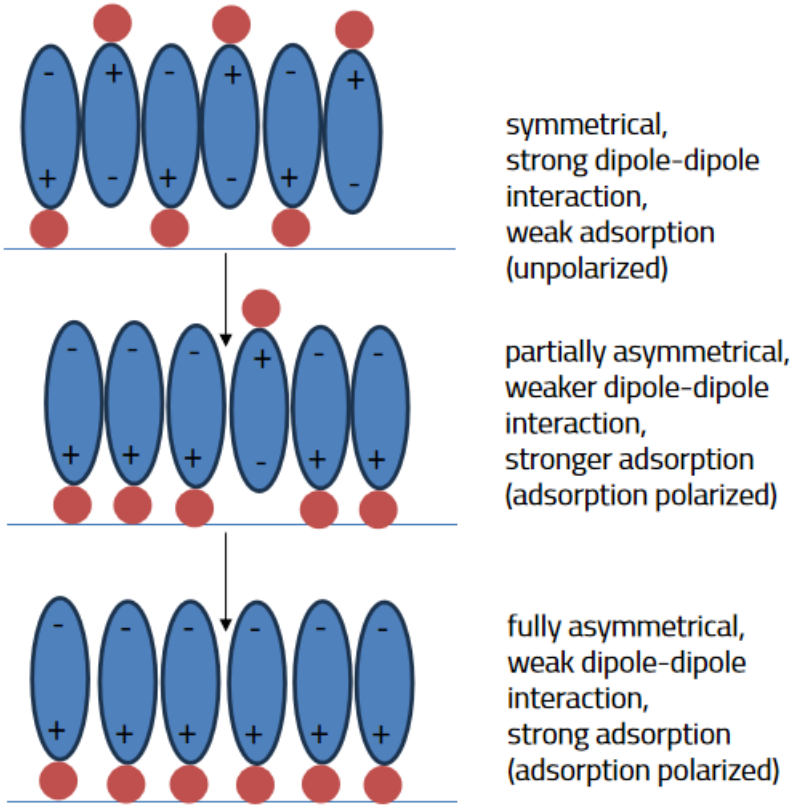


**Figure 27**: Different configuration of the push-pull chromophore molecule in the self-assembled monolayer of the molecule on the surface.

The situation described in the formula can be presented in the figure 27. There are two factors to influence the configuration of the push-pull chromophore molecule on the surface when the temperature is fixed: the intermolecular electrostatic interaction between the dipoles and the adsorption between the surface and the molecule. Without the surface, the push-pull chromophore will form head-tail structure to minimize the total energy of the system. The adsorption of the molecule on the surface is a method to polarize the direction of the electrical dipole possessed by the push-pull chromophore (adsorption polarization). If the adsorption is weak, the direction of the dipole will not be much polarized, and most of the molecule is in the head-tail structure on the surface. If adsorption is comparable with the intermolecular electrostatic interaction, a part of the molecules will have all well-oriented direction for the electrical dipole rather than head-tail structure. If the adsorption is strong enough, all the molecules in the head-tail structure will be changed so that only one direction of the electrical dipole of the push-pull chromophore will be on the surface.

In our experiments, the scanning tunnelling microscopy imaging condition is at room temperature. To have better electrical property, it is necessary to either decrease the temperature or lengthen the molecule. Moreover, the scanning tunnelling microscopy imaging condition is not in vacuum, it means that we cannot see the configuration of the molecule by topographical images.

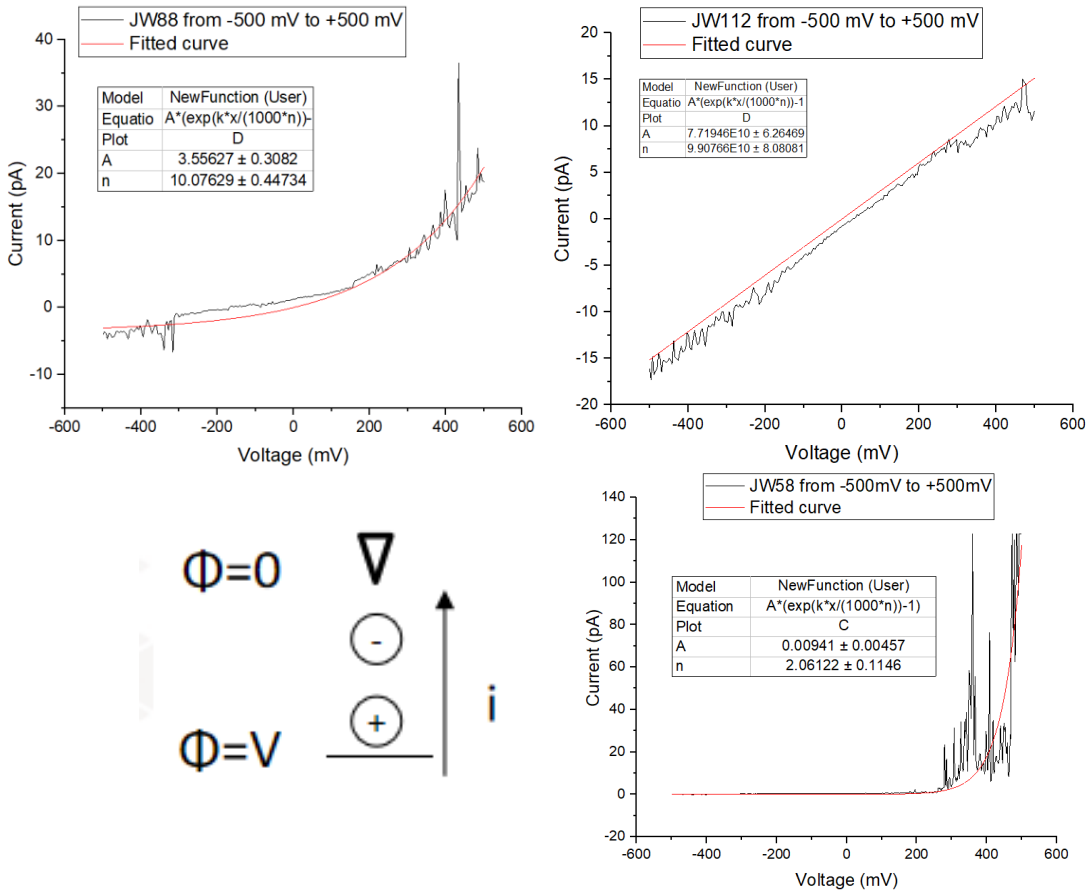


**Figure 28**: Different configuration of the push-pull chromophore molecule in the self-assembled monolayer of the molecule on the surface.

The idea is to use the scanning tunnelling spectroscopy function during the scanning tunnelling microscopy imaging. A small statistical analysis can be taken to determine the orientation of the adsorbed push-pull chromophore molecules on surface.

According to the setup of the scanning tunnelling microscopy, which is presented in figure 28, the shape of the I-V curve with rectification at positive bias (applied to the surface) can confirm the existence of the electrical dipole on the surface with minus on top and plus at bottom. The plus is for the electron-donating group and the minus is for the electron-withdrawing group. Therefore, the molecule of the rhodanine-N-acetic acid-based push-pull chromophore (JW58) is adsorbed on the surface via the lone pair of the nitrogen atom in the part of the N,N-dimethylaniline and the disulfide-based push-pull chromophore (JW88) is adsorbed on the surface via the sulphur atom.

For the self-assembled monolayer of thioacetate-based push-pull chromophore (JW112) on gold prepared in a solution where the concentration of the push-pull chromophore is 1 mM, 11 I-V curves were recorded with the range from -1000 mV to 1000 mV using scanning tunnelling spectroscopy. They are collected at different positions on the surface. Each curve shows some noise due to the

instability of the tip position and the temperature. Therefore, the data were smoothed by the adjacent-smoothing method with 10 points to reduce the noise, and they are plotted in the figure 29. The rectification ratio is calculated by taking the current value at +950 mV and -950 mV. The distribution of the rectification ratio is also plotted in the figure 29. The highest rectification ratio is 2.57 and the lowest rectification ratio is 1.11.

We can make an expectation of rectification ratio using the following formula for determining the rectification ratio in larger area:

$$\langle r \rangle = \sum_i r_i p_i$$

<r>: the average rectification ratio
$r_i$: the rectification ratio of ith value
$p_i$: the probability to find such rectification ratio

An averaged I-V curve is also plotted in figure 29 with a rectification ratio of 1.54. According to the formula, this rectification ratio can be served as a more macroscopic rectification ratio <r>.

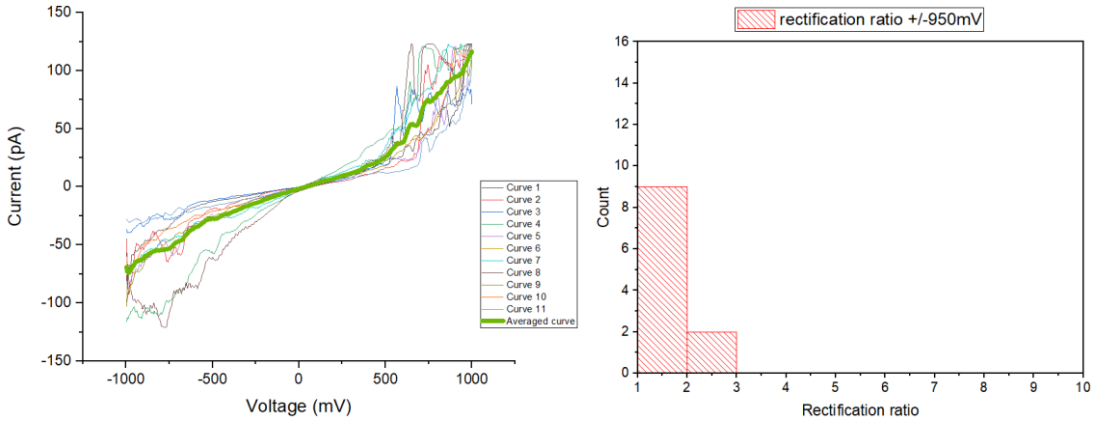


**Figure 29**: (left) Different I-V curves and an average curve during the experiment of scanning tunnelling spectroscopy for the self-assembled monolayer of the thioacetate-based push-pull chromophore molecule JW112 on gold surface in the solution using THF where the concentration of the push-pull chromophore is 1 mM and (right) the histogram for the summary of the rectification ratio distribution of the scanning tunnelling spectroscopy.

For the self-assembled monolayer of disulfide-based push-pull chromophore JW88 on gold, the situation is different. When the self-assembled monolayer on gold is prepared in a solution of DMF where the concentration of the push-pull chromophore is 0.5 mM, 48 I-V curves were recorded with the range from -1000 mV to 1000 mV using scanning tunnelling spectroscopy. Among them, 7 curves have no rectification effect because of the defect, 25 curves have rectification behaviour on negative voltage and 16 curves have rectification behaviour on positive voltage after the same processing. The rectification ratio is calculated by taking the current value at +950 mV and -950 mV.

The I-V curves together with an averaged curve and the histogram of the measured rectification ratio are plotted in figure 30. Among them, 52.1% curves show the rectification effect on negative potential and 33.3% curves show the rectification effect on positive potential. If the push-pull chromophores form always head to tail structure, 66.6 % (33.3×2) of the monolayer is constructed by head to tail structured push-pull chromophores. Therefore, only 18.8 % (52.1-33.3) self-assembled monolayer is constructed with homogeneously oriented push-pull chromophore. This shows the improvement to be done for the preparation of the self-assembled monolayer of push-pull chromophore on gold surface. One of the reasons can be attributed to the unsuccessful breaking of disulfide bond in some cases.

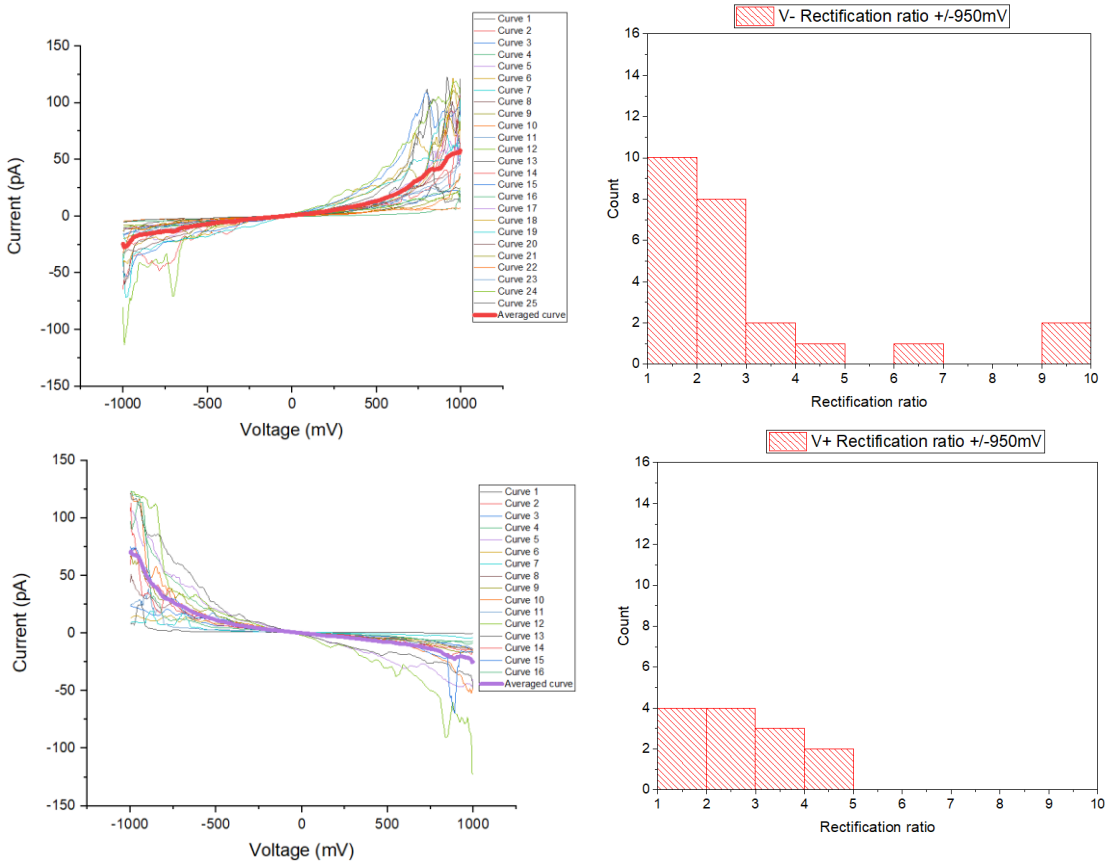


**Figure 30**: (top left) Different negatively rectified I-V curves and an average curve during the experiment of scanning tunnelling spectroscopy for the self-assembled monolayer of the disulfide-based push-pull chromophore molecule JW88 on gold surface in the solution using DMF where the concentration of the push-pull chromophore is 0.5 mM and (top right) the histogram for the summary of the rectification ratio distribution of the scanning tunnelling spectroscopy. (bottom left) Different negatively rectified I-V curves and an average curve during the experiment of scanning tunnelling spectroscopy for the self-assembled monolayer of the disulfide-based push-pull chromophore molecule on gold surface in the solution using DMF where the concentration of the push-pull chromophore is 0.5 mM and (bottom right) the histogram for the summary of the rectification ratio distribution of the scanning tunnelling spectroscopy.

When the solvent becomes EtOH-based solution, 12 I-V curves were recorded with the range from -1000 mV to 1000 mV using scanning tunnelling spectroscopy. Among them, one curve has no rectification effect because of the defect, 8 curves have rectification effect on negative potential and 3 curves have rectification effect on positive potential.

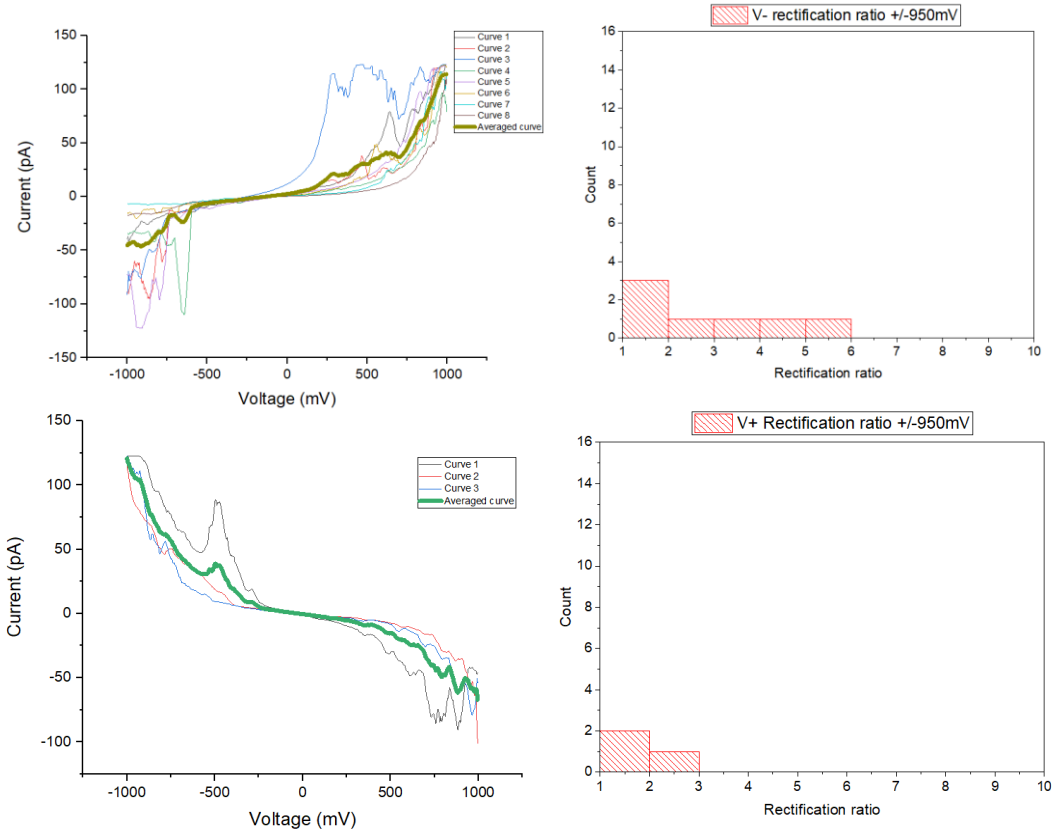


**Figure 31**: (top left) Different negatively rectified I-V curves and an average curve during the experiment of scanning tunnelling spectroscopy for the self-assembled monolayer of the disulfide-based push-pull chromophore molecule JW88 on gold surface in the solution using EtOH where the concentration of the push-pull chromophore is 0.5 mM and (top right) the histogram for the summary of the rectification ratio distribution of the scanning tunnelling spectroscopy. (bottom left) Different negatively rectified I-V curves and an average curve during the experiment of scanning tunnelling spectroscopy for the self-assembled monolayer of the disulfide-based push-pull chromophore molecule on gold surface in the solution using EtOH where the concentration of the push-pull chromophore is 0.5 mM and (bottom right) the histogram for the summary of the rectification ratio distribution of the scanning tunnelling spectroscopy.

The I-V curves and averaged I-V curves together with the histogram of the measured rectification ratio are plotted in figure 31. 25 % I-V curves have rectification effect on positive potential and 66.7 % I-V curves have rectification effect on negative potential. Therefore, approximately 50 % (25×2) self-assembled monolayer of the push-pull chromophore is constituted with head to tail structured push-pull chromophore if the push-pull chromophore forms always and only head

to tail structure. 41.7 % (66.7-25) self-assembled monolayer is constructed with homogeneously oriented push-pull chromophore, which shows the improvement to be done for the preparation of the self-assembled monolayer of push-pull chromophore on gold surface.

In terms of the best solvent to prepare the homogenously oriented self-assembled monolayer of disulfide-based push-pull chromophore on gold, EtOH is better than DMF because of less content of head-tail structured push-pull chromophore in the self-assembled monolayer on gold (41.7%>18.8%).

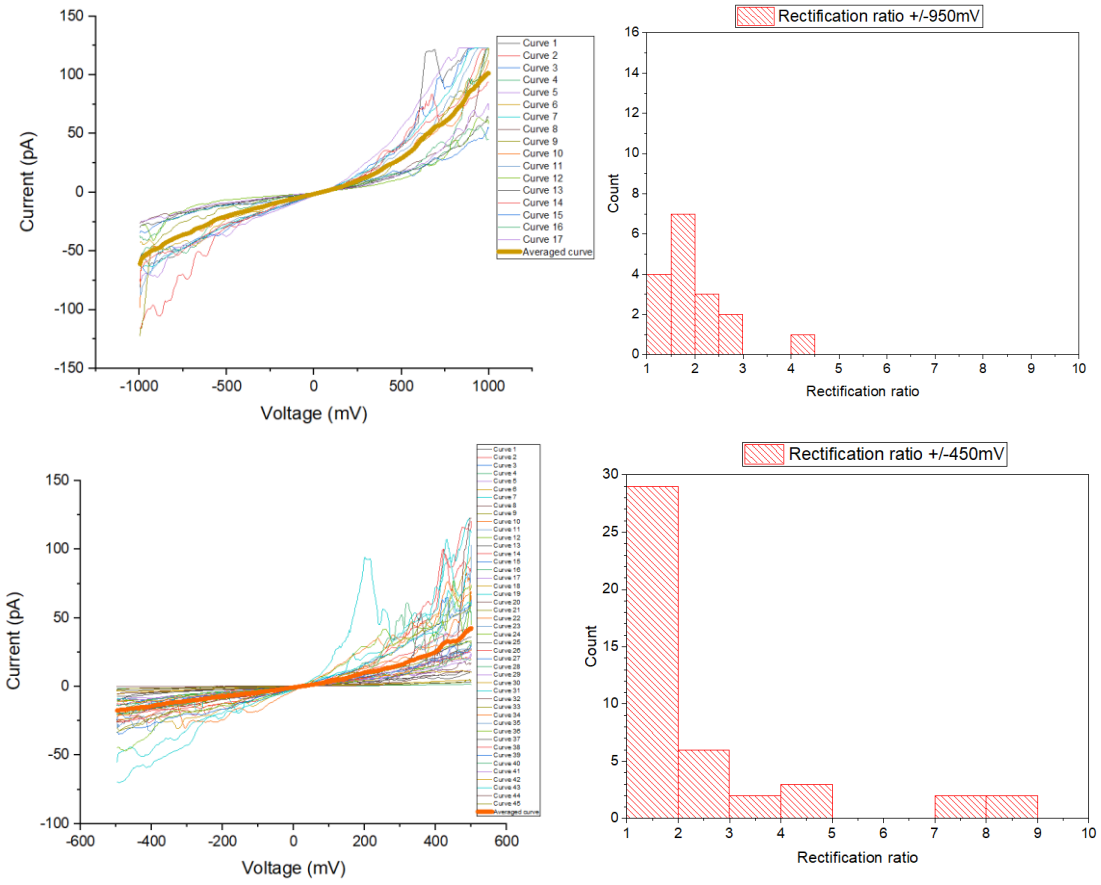


**Figure 32**: (top left) the different I-V curves and an average curve in the range from -1000 mV to +1000 mV during the experiment of scanning tunnelling spectroscopy for the self-assembled monolayer of the rhodanine-N-acetic acid-based push-pull chromophore molecule JW58 on gold surface in the solution using THF where the concentration of the push-pull chromophore is 10 mM; (top right) the rectification ratio distribution at +/-950 mV; (bottom left) the different I-V curves and an average curve in the range from -500 mV to +500 mV during the experiment of scanning tunnelling spectroscopy for the same self-assembled monolayer on gold; (bottom right) the rectification ratio distribution at +/-450 mV.

Finally, for the self-assembled monolayer of rhodanine-N-acetic acid-based push-pull chromophore (JW58) on gold prepared in a solution where the concentration of the push-pull chromophore is 10 mM, 19 I-V curves were recorded with the range from -1000 mV to 1000 mV (2 curves have no rectification ratio) and 55 I-V curves were recorded with the range from -500 mV to 500 mV (10 curves

have no rectification ratio) using scanning tunnelling spectroscopy. They are collected at different positions on the surface. The data was smoothed by the adjacent-smoothing method with 10 points to reduce the noise, and they are plotted in the figure 32. The rectification ratio is calculated by taking the current value at +950 mV and -950 mV and the current value at +450 mV and -450 mV. The distribution of the rectification ratio is also plotted in the figure 32. The highest rectification ratio is 4.20 and the lowest rectification ratio is 1.20 for +/- 950 mV. For the +/- 450 mV, the highest rectification ratio is 251 and the lowest rectification ratio is 1.01.

Averaged I-V curve is also plotted in figure 32 with a rectification ratio of 1.84 for +/- 950 mV and 2.12 for +/- 450 mV. According to the formula, this rectification ratio can be served as a more macroscopic rectification ratio <r>.

# IX. Conclusion

Three synthesized push-pull chromophores (JW58, JW88 and JW112) were used to prepare the self-assembled monolayer on gold. By varying the concentration of the push-pull chromophore and the solvent, the best parameters are determined by several methods: the contact angle measurement, the scanning tunnelling microscopy, atomic force microscopy and surface-enhanced Raman spectroscopy. More information of the chemical composition on the surface is recorded by attenuated total reflection-Fourier transform infrared spectroscopy to determine the types of the chemical bond and the oxidation state of the element. The criterion is to find the set of parameters to have the highest rectification ratio at +/-950 mV using scanning tunnelling spectroscopy and to compare. Due to unsuccessful breaking of S-S disulfide bond, the content of head-tail structured push-pull chromophore is high for the self-assembled monolayer of disulfide push-pull chromophore JW88 on gold. For the self-assembled monolayer of thioacetate-based push-pull chromophore JW112, the S-Au bond is formed for the adsorption. I-V curves proved the uniform orientation of the electrical dipole of the push-pull chromophore on the surface. A macroscopic rectification ratio of 1.54 is obtained at +/-950mV on 100nm*100nm surface. In terms of the self-assembled monolayer of rhodanine-N-acetic acid-based push-pull chromophore JW58, the lone-pair on the nitrogen atom is responsible for the adsorption. I-V curves proved the uniform orientation of the electrical dipole of the push-pull chromophore on the surface. A macroscopic rectification ratio of 1.84 is obtained at +/-950mV on 100nm*100nm surface.

# B. Self-assembled monolayer of thiol based on the chain of oligo(ethylene glycol) and oligopeptide on gold

The goal of this prospective study is to insert the push-pull chromophore between the substrate and the electro-responsive ω-poly-L-lysine to study the influence of the electrical dipole of the push-pull chromophore on the activation potential enabling motion of the oligopeptide. For this purpose, we have firstly to create such interfaces and characterized them. In fact, the oligopeptide is used to see its chain extension and retraction process because the chain is dressed by positive charge at physiological condition. The use of thiol based on the chain of oligo(ethylene glycol) mPEG12SH as an inert self-assembled inert matrix is to avoid the non-specific adsorption of the biomolecule on the surface. Therefore, in this section, the self-assembled monolayers of ω-poly-L-lysine called 4KC and mPEG12SH were prepared and analysed. Their structures are presented in figure 33.

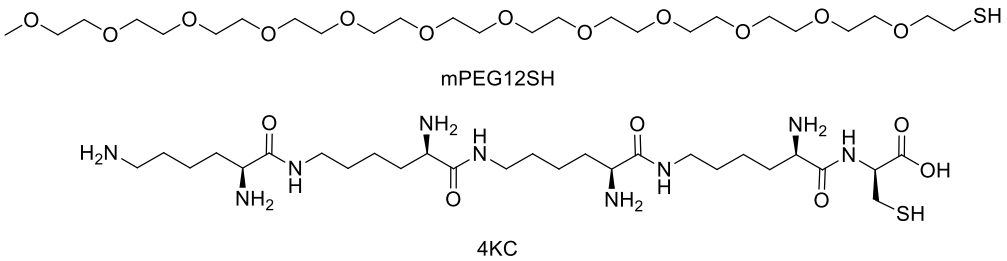


**Figure 33**: (top) the structure of the mPEG12SH and (bottom) the structure of the 4KC

## I. Self-assembled monolayer preparation

For surface functionalization, mPEG12SH comes from Sigma Aldrich; ω-poly-L-lysine comes from Peptide Protein Research Ltd with the sequence (ϵ-K)-(ϵ-K)-(ϵ-K)-(ϵ-K)-C. In the group in the structure of the L-lysine. Since the peptide bond is formed between the carboxylic acid and the amino group at the α-position in the natural peptide and protein, it is necessary to emphasize that the peptide bond is made between the carboxylic acid and the amino group at the ϵ-position for the L-lysine. The gold substrate for the contact angle measurement was made by the evaporation of gold under vacuum on a gallium arsenide substrate. All solvents were bought from Fisher and the deionized water is produced by the distilled water after the filtering of Barnstead Easy Pure system. In the sequence, the C means the L-cysteine and K means the L-lysine.

Prior to the functionalization of a thiol monolayer, the Au electrode surface was rinsed by absolute ethanol, UV-ozone (in air) processed for 10 min as detailed before, rinsed by absolute ethanol and dried using nitrogen gas. The surface functionalization was formed by immersing the precleaned Au electrode for a certain time in a freshly prepared solution at room temperature. Then, the samples

are rinsed by water and absolute ethanol, and dried using nitrogen gas after the functionalization.

The self-assembled monolayers of mPEG12SH were prepared from a solution of 1 mM mPEG12SH and 1 mM sodium hydroxide in absolute ethanol and distilled water. The self-assembled monolayers of oligopeptide 4KC were obtained from a solution of 0.79 mM oligopeptide 4KC and 0.79 mM sodium hydroxide in absolute ethanol and distilled water.

## II. Kinetics study of the formation of the self-assembled monolayer of mPEG12SH on gold using atomic force microscopy

The result is summarized from figure 34 to figure 39. The first attempt is to follow the kinetics of the grafting of the molecule on the surface by AFM. For the self-assembled monolayer of mPEG12SH to monitor the process of the grafting of the molecule on the surface. The solution is $10^{-5}$ M mPEG12SH in absolute EtOH. Different times of the immersion for the gold substrate in the solution have been set to record different stages of the grafting process of the molecule on the surface and of the formation of the self-assembled monolayer. When the immersion time is 30s, several white round spots can be seen on the surface of the gold. This kind of change of the topography and the phase of the surface is not caused by the substrate but the molecule. It is believed that each smaller spot may be caused by only one (or very few for the larger) molecule of mPEG12SH with a contracted conformation.

When the immersion time is set to 1 min, no white spots are on the surface anymore and the surface is full of dark cracks. Due to the contrast of the height on the topography image and the contrast in the phase image, it is believed that the cracks are the uncovered region by the molecule and at this stage, the surface coverage by the molecule is about 80%. When the immersion time is 2 min, the cracks on the image disappeared and the relatively flat surface is full of the mPEG12SH molecules. However, some bundles are visible. It is believed that the topographical and phase variations on the surface is caused by the mPEG12SH molecules with different conformations. When the immersion time is set to 5 min, the AFM image shows a much flatter surface. It is believed that within 5 min, the formation of the self-assembled monolayer is very rapid as the gold surface is fully covered by the molecule and the organization of the molecular chain begins to find the thermodynamic equilibrium.

Rundqvist et al. followed the formation of the self-assembled monolayer with mPEG12SH on gold in liquid phase[227]. They found the same process of the evolution of the formation of the self-assembled monolayer with a better resolution. The roughness of the surface is also recorded with the attention to

minimize the effect caused by the gold substrate. The $R_q$ value is 0.217 nm when the immersion time is 30s, 0.217 nm when the immersion time is 1 min, 0.447 nm when the immersion time is 2 min, 0.205 nm when the immersion time is 5 min, 0.236 nm when the immersion time is 1h and 0.212 nm when the immersion time is 4h.

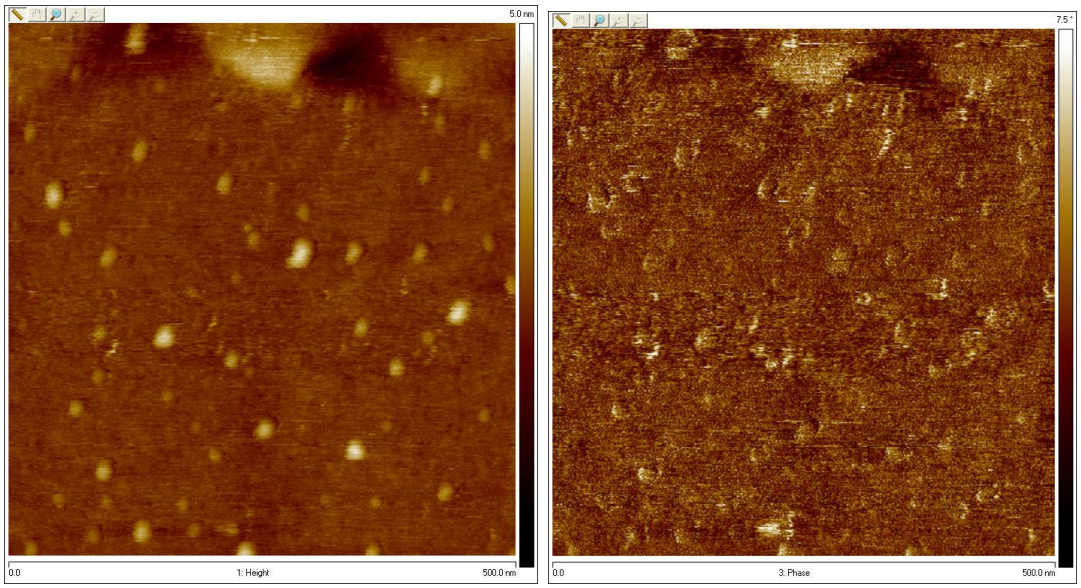


**Figure 34**: AFM (left) topography and (right) phase image of mPEG12SH/Au(111)/mica after 30s immersion in the 0.01mM mPEG12SH solution in absolute ethanol (5nm z scale).

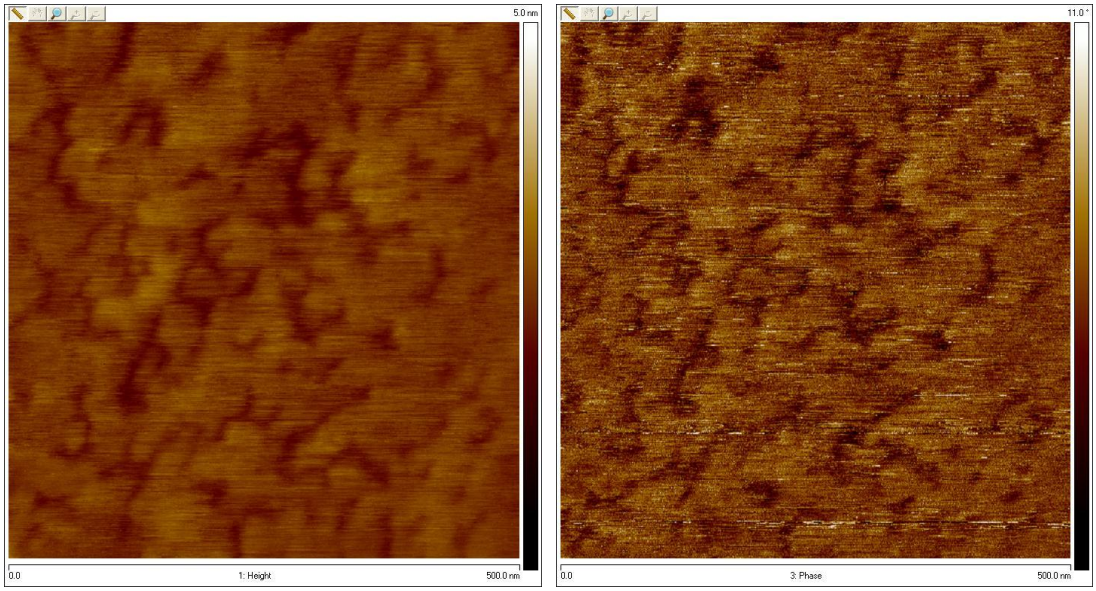


**Figure 35**: AFM (left) topography and (right) phase image of mPEG12SH/Au(111)/mica after 1min immersion in the 0.01mM mPEG12SH solution in absolute ethanol (5nm z scale).

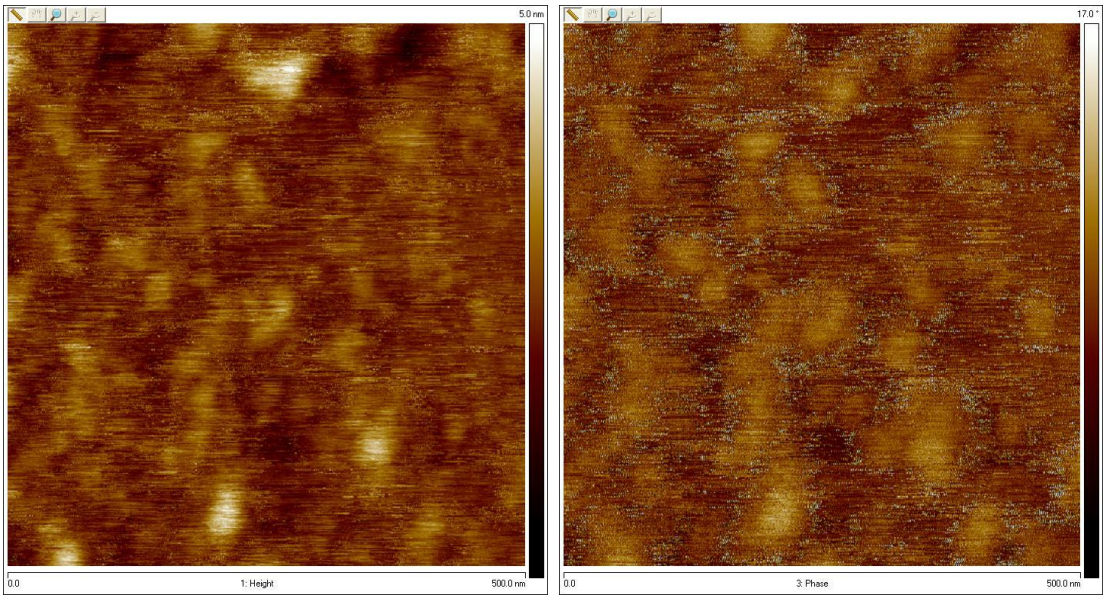


**Figure 36**: AFM (left) topography and (right) phase image of mPEG12SH/Au(111)/mica after 2min immersion in the 0.01mM mPEG12SH solution in absolute ethanol (5nm z scale).

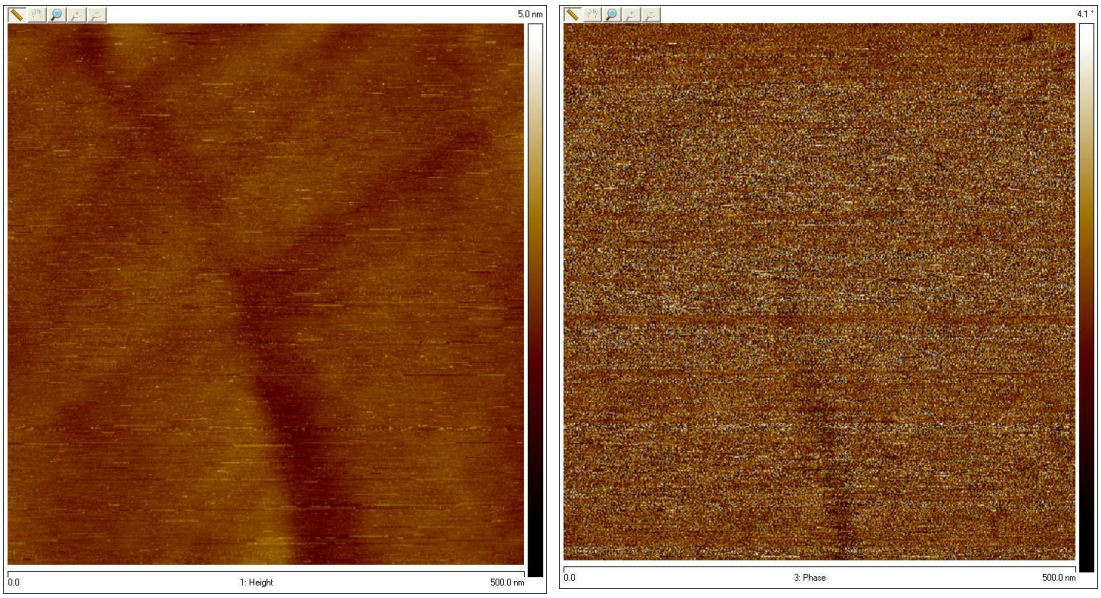


**Figure 37**: AFM (left) topography and (right) phase image of mPEG12SH/Au(111)/mica after 5min immersion in the 0.01mM mPEG12SH solution in absolute ethanol (5nm z scale).

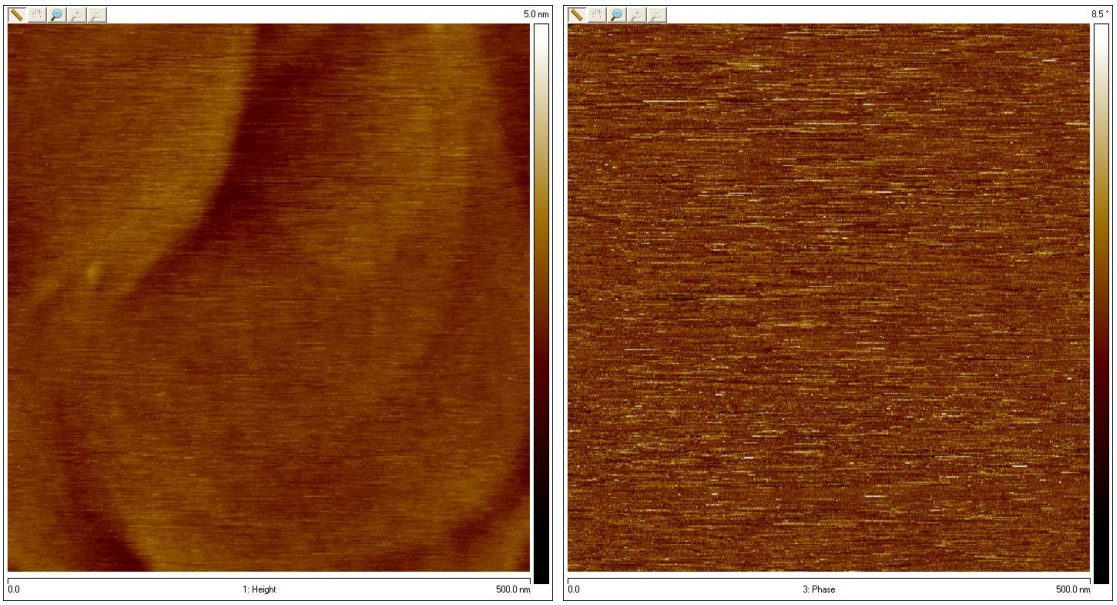


**Figure 38**: AFM (left) topography and (right) phase image of mPEG12SH/Au(111)/mica after 1h immersion in the 0.01mM mPEG12SH solution in absolute ethanol (5nm z scale).

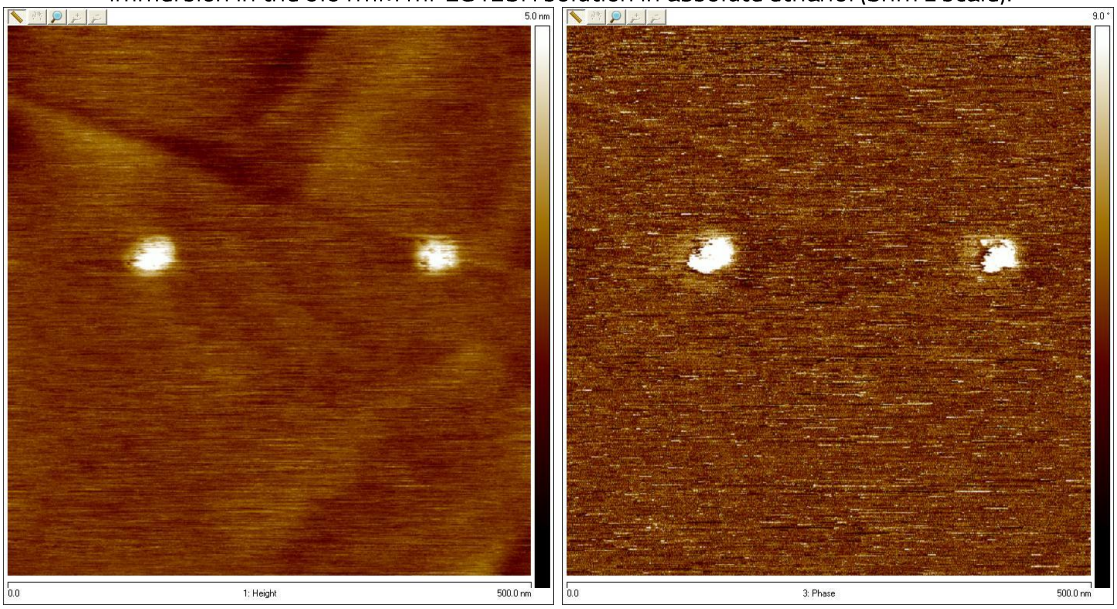


**Figure 39**: AFM (left) topography and (right) phase image of mPEG12SH/Au(111)/mica after 4h immersion in the 0.01mM mPEG12SH solution in absolute ethanol (5nm z scale).

## III. Scanning tunnelling microscopy

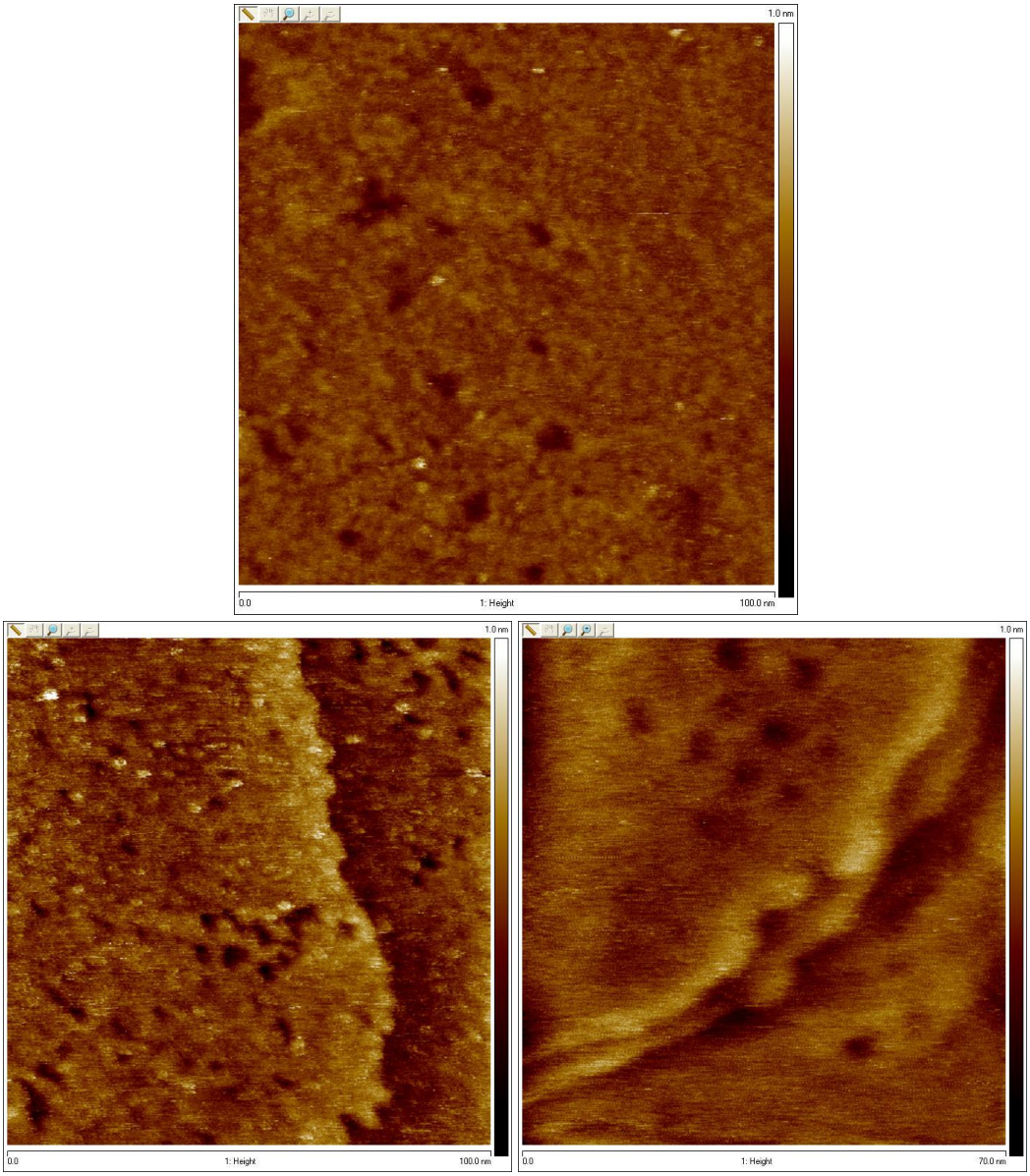


**Figure 40**: (top) the STM (5pA, -200mV) image (100*100 $nm^2$) of Au(111)/mica; (bottom left) the STM (5pA, -200mV) image (100*100 $nm^2$) of mPEG12SH self-assembled monolayer on Au(111)/mica; (bottom right) the STM (3pA, -50mV) image (70*70 $nm^2$) of 4KC self-assembled monolayer on Au(111)/mica. The z scale is always 1 nm.

After the preparation of the self-assembled monolayer of mPEG12SH on gold and the self-assembled monolayer of 4KC on gold, the samples are characterized by scanning tunnelling microscope to have an insight on the organisation and morphology of the self-assembled monolayer at the molecular scale.

From figure 40, the STM image of the bare Au(111)/mica showed very flat structure with several holes on the image. The self-assembled monolayer of mPEG12SH form also a very flat structure on the surface despite the existence of

holes in the image. It is quite surprising to see the fact that rearrangement of the conformation of the larger molecules like mPEG12SH is fast enough to be done within 24h. However, there are not too much similar works in the literature. Kang et al.[228] reported the STM image on the self-assembled monolayer of shorter mPEG2SH. The self-assembled monolayer of mPEG12SH is also characterized by atomic force microscopy[229,230]. Similarly, 4KC molecule can also form a flat structure on the gold substrate within 24h. It is worthy to emphasize that the 4KC is charged in the ethanol before being grafted on the surface. It means that a flat stable self-assembled monolayer of molecules can be formed for a small oligomer whether the molecules are charged or not. In the literature, there are similar works[231,232], however, no similar work used the L-cysteine as the grafting unit. The self-assembled monolayer of oligopeptide is also characterized by atomic force microscopy in the literature[233,234].

## IV. Attenuated total reflection-Fourier transform infrared spectroscopy

The self-assembled monolayer of mPEG12SH was also checked by the ATR-FTIR spectroscopy. The result is in the figure 41. The characteristic peaks are found at 2928 $cm^{-1}$ and 2852 $cm^{-1}$ for C-C stretching and 1160 $cm^{-1}$ and 1104 $cm^{-1}$ for C-O stretching in the ATR-FTIR spectroscopy, showing the existence of the mPEG12SH.

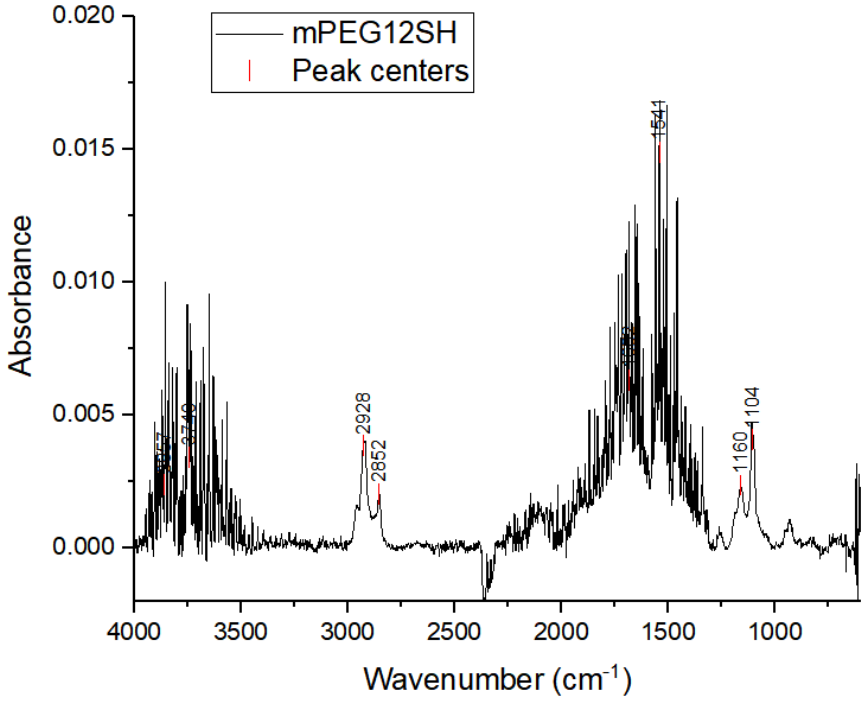


**Figure 41**: (right) the ATR-FTIR spectrum of self-assembled monolayer of mPEG12SH

Vanderah et al.[235] recorded RAIRS spectra without ATR crystal of the mPEG6SH SAM from absolute ethanol from 1800 to 900 $cm^{-1}$ and from 3100 to 2700 $cm^{-1}$, respectively. The strong absorption bands at 2893 $cm^{-1}$ band in the 3100-2700 $cm^{-1}$ region and 1118 $cm^{-1}$ in the 1800 to 900 $cm^{-1}$ in the spectra from the ethanolic solvents. The work of Heeb et al.[236] recorded PM-IRRAS spectra without ATR crystal but with polarization modulation of the mPEG7SH SAM from absolute ethanol from 1600 to 900 $cm^{-1}$ and from 3200 to 2600 $cm^{-1}$, respectively. The strong absorption bands are located at 2893 $cm^{-1}$, in the 3200-2600 $cm^{-1}$ region and 1118 $cm^{-1}$ in the 1600 to 900 $cm^{-1}$ in the spectra from the ethanolic solvents. With this evidence, the formation of mPEG12SH on gold can be ensured by ATR-FTIR spectra.

# V. Conclusion

In this chapter, we successfully prepared the self-assembled monolayer of mPEG12SH and oligopeptide 4KC on the Au(111) on mica substrate. The quality was characterized by atomic force microscopy, scanning tunnelling microscopy and attenuated total reflection – Fourier Transform Infrared spectroscopy. This shows evidence of the molecule deposition with the possibility to functionalize the surface by bigger oligomer molecule.

# C. Surface functionalization of the gold surface by binary self-assembled monolayer of the molecule on the surface

To be able to achieve the final application of this study, it is mandatory to obtain active molecular site in an inert matrix made of thiol with the chain of oligo(ethylene glycol). For this purpose, in this section we deal with binary self-assembled monolayer of push-pull chromophore or oligopeptide isolated in an inert environment.

There are two ways to make binary self-assembled monolayer: the coadsoption[237] and the desorption-adsorption exchange reaction[238]. The grafting process is not an irreversible process, and the grafted molecule can desorb from the surface by capturing a gold atom. Thus, the grafting process is a reversible process in dynamic equilibrium. It is the principle to make binary self-assembled monolayer on gold. The self-assembled monolayer of dodecanethiol is one of the fundamental bases in the field of self-assembled monolayer and it is used firstly in the next section as a model inert matrix. To our knowledge, there are no articles reporting the binary self-assembled monolayer of alkanethiol and push-pull chromophore but the binary self-assembled monolayer with alkanethiol and ferrocene-based molecules[202,226] or molecules based on bipyridine-based metal-ligand complex[239].

## I. Binary self-assembled monolayer preparation

For surface functionalization, dodecanethiol (CAS 112-55-0) comes from Acros Organics, anhydrous sodium hydroxide pellets (CAS 1310-73-2) come from Carlo Erba. All solvents were bought from Fisher and the deionized water is produced by the distilled water after the filtering of Barnstead Easy Pure system.

Prior to the functionalization of a thiol monolayer, the Au electrode surface was cleaned by UV-ozone (in air) processed for 10 min. The surface functionalization was formed by immersing the precleaned Au electrode for a certain time in a freshly prepared solution for 24h at room temperature. The solution for the self-assembled monolayer as the matrix is made with a concentration of 1mM dodecanethiol and sodium hydroxide in absolute ethanol and distilled water. For exchange process, the concentration of the solution is 0.5 mM of push-pull chromophore JW88 in absolute ethanol. The substrate is then rinsed by tetrahydrofuran, water, ethanol, and dichloromethane and dried using nitrogen gas after the surface functionalization.

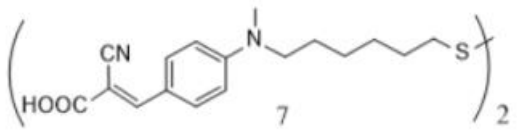


**Figure 42**: the molecular structure of the push-pull chromophore JW88 to prepare the binary self-assembled monolayer

Then, the same process is done by inserting the push-pull chromophore (figure 42) in the matrix of the hydroxyundecanethiol matrix and inserting the hydroxyundecanethiol in the matrix of the push-pull chromophore. The reason to choose the hydroxyundecanethiol is that it is more hydrophilic and more suitable for the application in the biology. Here is the procedure to make the mixed self-assembled monolayer using hydroxyundecanethiol as the matrix by the insertion of the push-pull chromophore. The solution for this self-assembled monolayer is 1mM of hydroxyundecanethiol and 1mM of sodium hydroxide in absolute ethanol and distilled water. The preparation is at room temperature and the deposition duration is 24h. The self-assembled monolayer showed a very crystalline structure. For exchange process, the solution is prepared with 0.5 mM of push-pull chromophore JW88 in absolute ethanol. After the deposition, the substrate is rinsed by tetrahydrofuran, water, and ethanol, and dried using nitrogen gas after the surface functionalization.

The binary self-assembled monolayer of mPEG12SH and push-pull chromophore is prepared in the following way. The solution for this self-assembled monolayer is 10 mL 1mM mPEG12SH and 1mM sodium hydroxide in absolute ethanol and distilled water. The preparation is at room temperature and the time is 24h. For exchange process, the solution is 0.5 mM push-pull chromophore JW88 in absolute ethanol for a certain time. The substrate will be rinsed by tetrahydrofuran, water, and ethanol, and dried using nitrogen gas after the surface functionalization.

The binary self-assembled monolayer of mPEG12SH and 4KC is prepared in the following way. The solution for this self-assembled monolayer is 1mM mPEG12SH and 1mM sodium hydroxide in absolute ethanol and distilled water. The preparation is at room temperature and the deposition duration is 24h. For exchange process, the solution is 0.79 mM oligopeptide 4KC and 0.79 mM sodium hydroxide in absolute ethanol and distilled water. The desorption-adsorption reaction is for 24h. The substrate is rinsed by tetrahydrofuran, water, and ethanol, and dried using nitrogen gas after the surface functionalization.

## II. Contact angle measurement

| | 0h exchange | 6h exchange | 24h exchange | Push-pull chromophore |
|---|---|---|---|---|
| | 109.4±3.05° | 90.4±4.80° | 86.4±2.02° | 76.4±2.06° |
| Dodecanethiol content | 100% | 42.7% | 30.3% | 0% |
| Push-pull chromophore content | 0% | 57.3% | 69.7% | 100% |

**Table 1**: the value of the water contact angle for different self-assembled monolayers and the content of different components

The exchange process is also monitored by the contact angle measurement by applying the Cassie's law (see Chap. 2). For the result of the preparation of binary

self-assembled monolayer of dodecanethiol and push-pull chromophore, the result is satisfying. By using the Cassie's law, the content of the push-pull chromophore increases from 0 to 57.3% after 6 hours of exchange and 69.7% after 24 hours of exchange.

## III. Scanning tunnelling microscopy

The exchange process has been firstly studied with the insertion of the push-pull chromophore in the matrix of the dodecanethiol. We can see that the structure does not change after the exchange, and we can see the appearance of white spots. This is the evidence of the exchange process. STM was used to analyse the result of the exchange process of push-pull chromophore in the matrix of the dodecanethiol on the surface (figure 43), push-pull chromophore in the matrix of the hydroxyundecanethiol (figure 44) and the reverse (figure 44), and push-pull chromophore in the matrix of mPEG12SH (figure 45). The self-assembled monolayer of dodecanethiol and the self-assembled monolayer of hydroxyundecanethiol showed a very crystalline structure systematically. By increasing the insertion time of the push-pull chromophore in the self-assembled monolayer of dodecanethiol, more and more brighter spots appear on the STM image. It shows that the exchange undergoes since the length of the push-pull chromophore is longer than dodecanethiol. The roughness is also recorded. Without desorption-adsorption exchange, the roughness is 0.072 nm. This value becomes 0.134 nm after 6 hours and 0.208 nm after 24 h. The longer the time for the desorption-adsorption process, the higher the roughness. Such change of the roughness is correlated to the number of inserted molecules. We counted 6 for 6h and 19 for 24 h in a 70×70 $nm^2$ image. Hobara et al.[240] prepared self-assembled monolayer of 1-hexadecanethiol and 3-mercaptopropanoic acid. The phase separation can be easily identified due to big length difference of the two molecules.

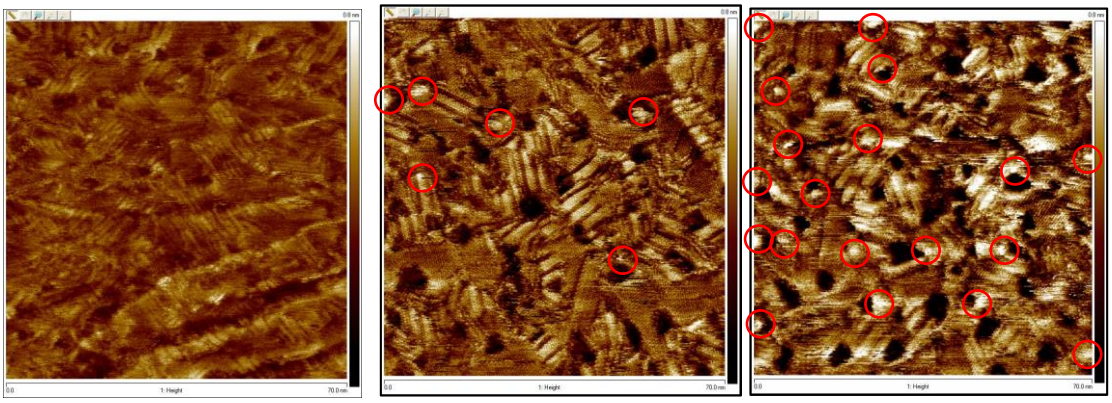

**Figure 43**: (left) the STM image of self-assembled monolayer of dodecanethiol before the exchange process (I = 2 pA, V = -200 mV, 70nm*70 nm); (middle) the STM image of self-assembled monolayer of dodecanethiol after 6h exchange process using push-pull chromophore JW88 (I = 2 pA, V = -200 mV, 70nm*70 nm); (right) the STM image of self-assembled monolayer of dodecanethiol after 24h exchange process using push-pull chromophore JW88 (I = 2 pA, V = -200 mV, 70nm*70 nm). Red circles represent the location of the push-pull chromophore inserted in the dodecanethiol matrix. The z scale is 0.8 nm

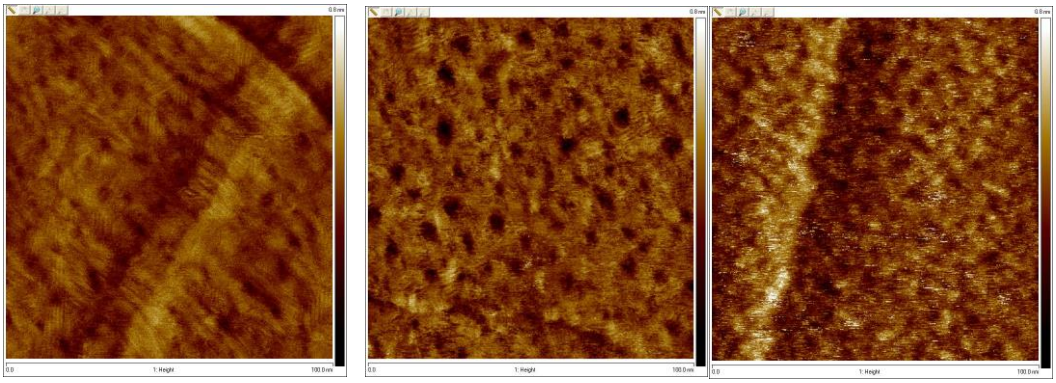

**Figure 44**: (left) the STM image of self-assembled monolayer of hydroxyundecanethiol before the exchange process (I = 2 pA, V = -200 mV, 100nm*100 nm); (middle) the STM image of self-assembled monolayer of hydroxyundecanethiol after 24h exchange process using push-pull chromophore JW88 (I = 2 pA, V = -200 mV, 100nm*100 nm); (right) the STM image of self-assembled monolayer of push-pull chromophore JW88 after 24h exchange process using hydroxyundecanethiol (I = 2 pA, V = -200 mV, 100nm*100 nm). The z scale is always 0.8 nm.

According to the result of the image of the scanning tunnelling microscope, it appears better to choose the insertion of the push-pull chromophore in the matrix of hydroxyundecanethiol due to the better order. Comparing figure 43 right and figure 44 middle for 24 h of push-pull chromophore insertion, it seems that the insertion of the push-pull chromophore inside the matrix of hydroxyundecanethiol is slower than the same attempt with dodecanethiol as the matrix. The reason for this is that the hydroxy terminal group is more polar and the interaction between the alkane chains are hampered. The same reason to explain why it is better to insert push-pull chromophore in the hydroxyundecanethiol matrix not the opposite way because the terminal group of push-pull chromophore is even more polar. The attempt was also done by inserting the push-pull chromophore in the matrix of the

mPEG12SH in figure 45. However, the change of the height in the topographical image is not obvious. Nevertheless, some white spots can be distinguished after two hours and even after three hours of insertion. The difficulty of the insertion may be due to the bad interaction between the non-polar alkyl chain and polar chain constituted by ethylene glycol.

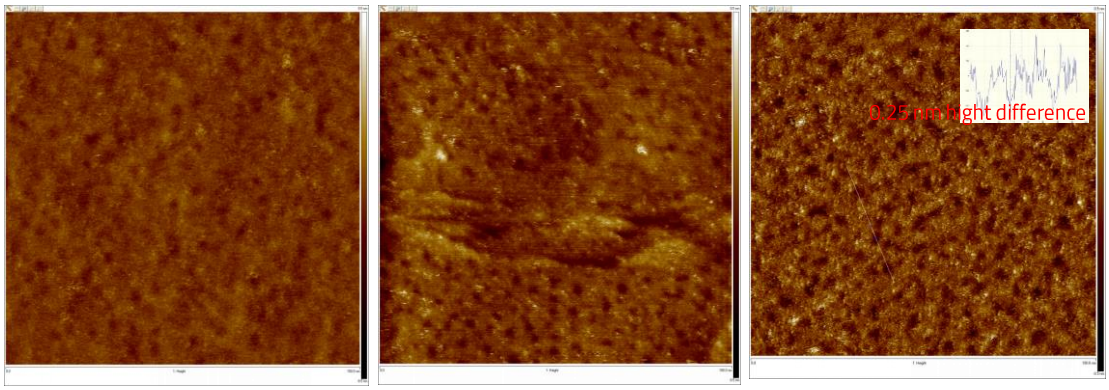


**Figure 45**: (left) the STM topography image of self-assembled monolayer of oligomer of mPEG12SH before the exchange process (I = 5 pA, V = -200 mV, 100nm*100 nm); (middle) the STM topography image of self-assembled monolayer of oligomer of mPEG12SH after 2h exchange process using push-pull chromophore (I = 5 pA, V = -200 mV, 100nm*100 nm); (right) the STM topography image of self-assembled monolayer of oligomer of mPEG12SH after 3h exchange process using push-pull chromophore (I = 5 pA, V = -200 mV, 100nm*100 nm). The z scale is always 0.5 nm.

## IV. Electrostatic force microscopy

The attempt was also done by inserting the oligopeptide 4KC in the matrix of mPEG12SH monitored by electrostatic force microscopy, which is more specialized for the analysis of charged 4KC on the surface. The change of the height in the topographical image (figure 46) is obvious by finding more and more round spots after the insertion. The roughness $R_q$ of the images is also calculated and recorded. For the self-assembled monolayer of 4KC, the roughness is 0.105 nm. For the result of the binary self-assembled monolayer mPEG12SH/4KC, the value is 0.250 nm when the desorption-adsorption process time is 6 h. When the time is extended to 24 h, the value of the roughness is however 0.242 nm. In terms of the amplitude image (figure 47), the lift mode is used by adding the distance between the surface and the tip (30 nm). The voltage is always at 0 V. The Van der Waals forces vanishes more rapidly than the electrostatic force. The height in the topography image is caused by electrostatic force and the Van der Waals forces. However, the shape of the substate becomes less clear in the amplitude image because the tip is lifted 30 nm. However, we cannot use the phase image because it is not useful to distinguish the part caused by mPEG12SH and the part caused by 4KC unless the lift mode is used (figure 48). The group of Mendes had published a

number of article of binary self-assembled monolayer of thiol with the chain of oligo(ethylene glycol) and oligopeptide for the bio-application[7,241–243], however, no scanning probe microscopy images have been done for this system.

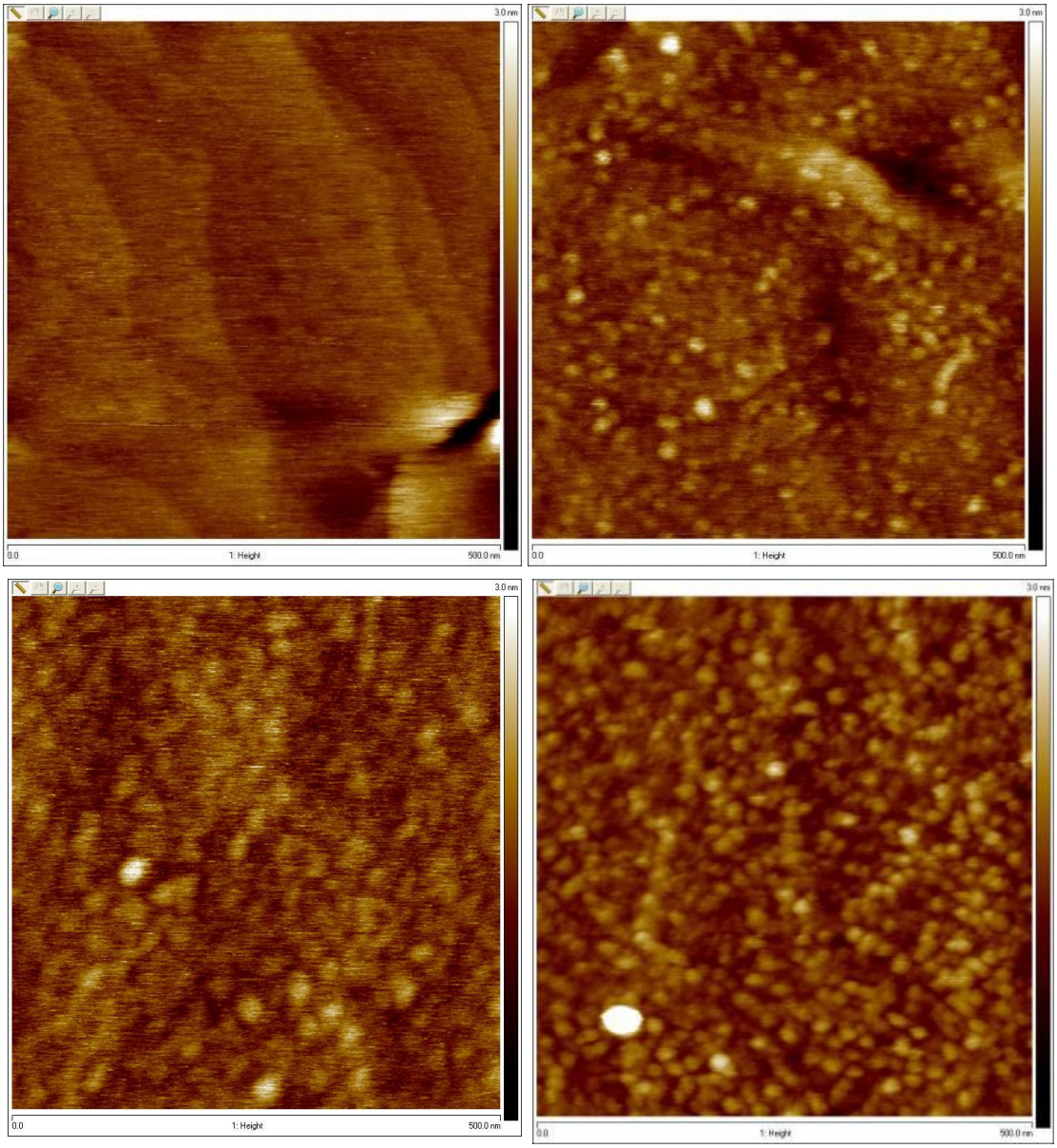

**Figure 46**: (top left) the EFM topography image of self-assembled monolayer of oligomer of mPEG12SH (500nm*500 nm); (top right) the EFM topography image of self-assembled monolayer of oligomer of mPEG12SH after 6h exchange process using oligopeptide 4KC (500nm*500 nm); (bottom left) the EFM topography image of self-assembled monolayer of oligomer of mPEG12SH after 24h exchange process using oligopeptide 4KC (500nm*500 nm); (bottom right) the EFM topography image of self-assembled monolayer of oligopeptide 4KC (500nm*500 nm)

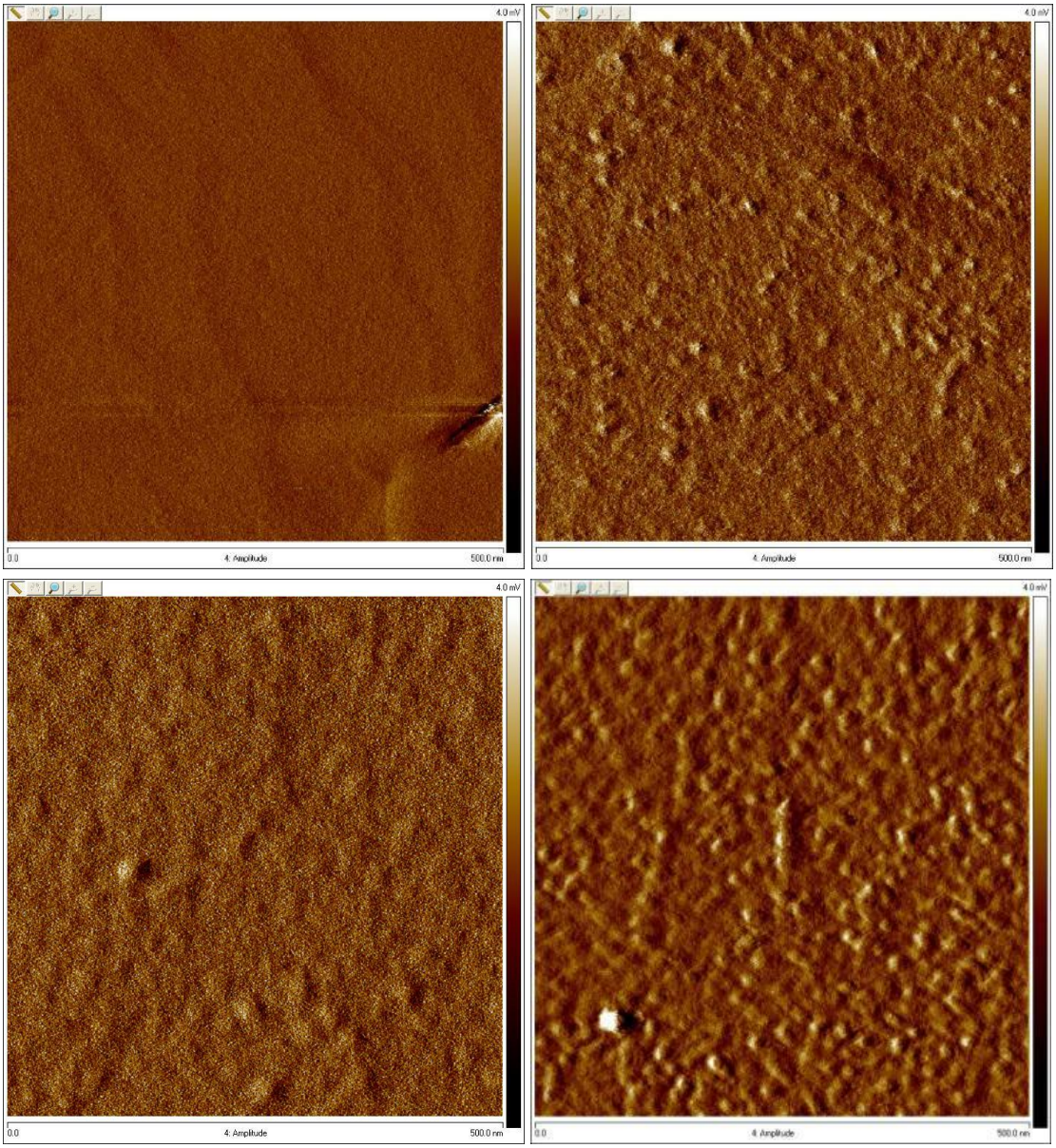

**Figure 47**: (top left) the EFM amplitude image of self-assembled monolayer of oligomer of mPEG12SH (500nm*500 nm); (top right) the EFM amplitude image of self-assembled monolayer of oligomer of mPEG12SH after 6h exchange process using oligopeptide 4KC (500nm*500 nm); (bottom left) the EFM amplitude image of self-assembled monolayer of oligomer of mPEG12SH after 24h exchange process using oligopeptide 4KC (500nm*500 nm); (bottom right) the EFM amplitude image of self-assembled monolayer of oligopeptide 4KC (500nm*500 nm)

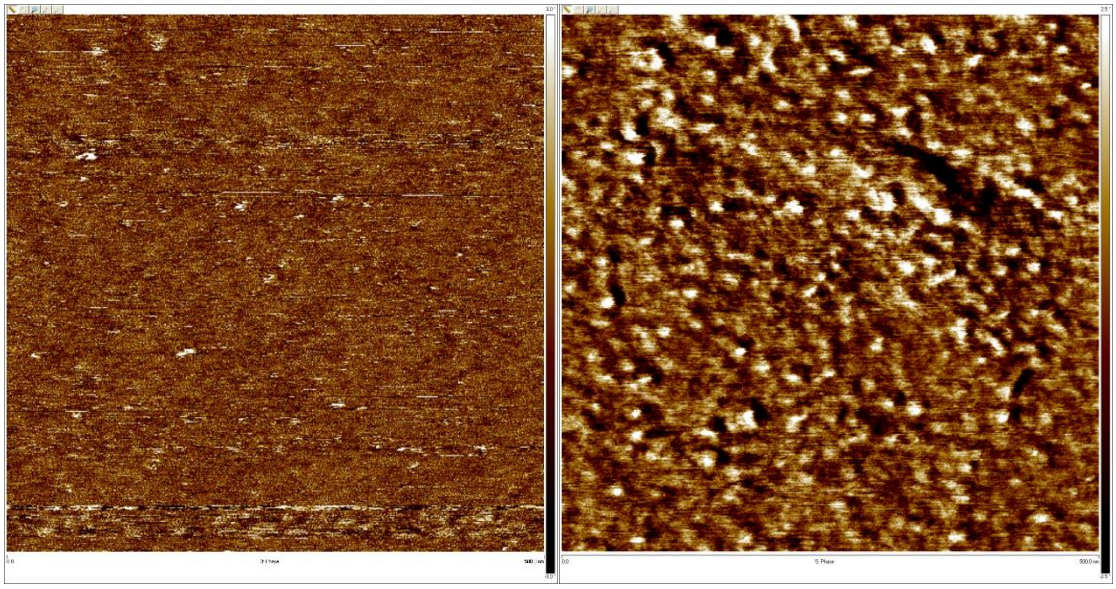

**Figure 48**: (left) the EFM phase image of self-assembled monolayer of thiol based on oligomer of mPEG12SH after 6h exchange process using oligopeptide 4KC (500nm*500 nm); (right) the EFM phase image of self-assembled monolayer of thiol based on oligomer of mPEG12SH after 6h exchange process using oligopeptide 4KC in the lift mode (500nm*500 nm)

# V. Conclusion

In this chapter, the binary self-assembled monolayer was prepared successfully by desorption-adsorption exchange reaction. The push-pull chromophore + dodecanethiol system shows that binary self-assembled monolayer on the gold substrate can be prepared by desorption-adsorption exchange reaction. The push-pull chromophore + hydroxyundecanethiol system demonstrated that it is better to insert push-pull chromophore into inert matrix. The push-pull chromophore + mPEG12SH system illustrated that the polarity of the chain is important for the preparation of the self-assembled monolayer on the substrate. The mPEG12SH + oligopeptide system tells that the desorption-adsorption exchange reaction is also valid for longer chains. The two binary systems described above are important. The dodecanethiol-push-pull chromophore system is essential for the development of organic electronics and the mPEG12SH-4KC system is crucial for the development of biosensor.

# D. Conclusion

In this chapter, we summarized all the self-assembled monolayer prepared using active molecules to achieve the final goal of my PhD project. Three synthesized push-pull chromophores (JW58, JW88 and JW112) were used to prepare the self-assembled monolayer on gold. The self-assembled monolayer of push-pull chromophore on gold can be made using direct adsorption in the liquid phase after the immersion of the substrate. The criterion is to find the set of parameters during the preparation of the self-assembled monolayer to have the strongest asymmetrical electrical behaviour and to compare. A much significant asymmetrical behaviour is seen for JW58 due to higher asymmetrical ratio within narrow voltage range. The self-assembled monolayer of mPEG12SH and oligopeptide 4KC on the Au(111) on mica substrate shows the possibility to functionalize the surface by bigger oligomer molecule. It is also the beginning of the development of the biosensor. Binary self-assembled monolayer was prepared successfully by desorption-adsorption exchange reaction (push-pull chromophore + dodecanethiol, push-pull chromophore + hydroxyundecanethiol, push-pull chromophore + mPEG12SH and 4KC + mPEG12SH), and it is beneficial for the development of organic electronics and biosensor.

# 6. Conclusion and perspectives

In this work, I was interested in new push-pull chromophores and their self-assembled monolayers to use their dipole to modulate the potential of a layer deposited on top.

During my bibliographic research, I focused especially on how self-assembled monolayer of push-pull chromophores can be applied to solar cell, nanodielectrical material and biosensors, which had not been addressed deeply in the literature, enabling to be published as a review article.

Then, to provide a model system, the self-assembled monolayer of cysteamine, para-aminothiophenol and 3-amino-5-mercapto-1,2,4-triazole were prepared as the layer for the charge transport and potential modulation. In addition, 3-ferrocenoylpropanoic acid were added for the post-functionalization as an active component in the cyclic voltammetry. The quality of the self-assembled monolayer was checked by contact angle measurement, atomic force microscopy, scanning tunnelling microscopy, X-ray photoelectron spectroscopy and surface-enhanced Raman spectroscopy. The effect of potential modulation was tested and confirmed by cyclic voltammetry of self-assembled monolayers of 3-ferrocenoylpropanoic acid adsorbed on top of the self-assembled monolayer of cysteamine and para-aminothiophenol. Indeed, the effect of the potential modulation was evidenced through the shift of the potential of the electrochemical reaction in the cyclic voltammetry.

Then the idea is to replace such interfacial layers by the self-assembly of push-pull chromophore that had to be synthesized. We successfully synthesized a novel bifunctional push-pull chromophore with disulfide grafting unit to replace the aminothiol as the molecular electrical dipole. The synthesis was terminated by two push-pull chromophores with cyanoacetic acid, a push-pull chromophore with disulphide and a push-pull chromophore using rhodanine-N-acetic acid. The novel push-pull chromophore is synthesized with innovative structure with potential for many fields. Then a thorough chemical analysis was done to determine the structure of the push-pull chromophore and the photophysical properties of the push-pull chromophore with several characterization methods. Our novel push-pull chromophore attained all the requirements to be considered as a push-pull chromophore for the functionalization for the next stage of the PhD.

The three synthesized push-pull chromophores were used to prepare the self-assembled monolayer on gold. They were thoroughly characterized by a variety of the methods: contact angle measurement, scanning tunnelling microscopy, atomic force microscopy, surface-enhanced Raman spectroscopy, attenuated total reflection-Fourier transform infrared spectroscopy and X-ray photoelectron spectroscopy. A much significant asymmetrical behaviour was seen for rhodanine-N-acetic-based push-pull chromophore due to higher rectification ratio, lower dark current and narrow voltage range. Self-assembled monolayers of mPEG12SH and

oligopeptide 4KC on gold show a good start for the preparation of the biosensor platform and the possibility to functionalize the surface by bigger oligomer molecules. The result is examined using scanning tunnelling microscopy, atomic force microscopy, attenuated total reflection-Fourier transform infrared spectroscopy and X-ray photoelectron spectroscopy. Binary self-assembled monolayers were prepared successfully by desorption-adsorption exchange reaction. The result is checked by contact angle measurement, scanning tunnelling microscopy, atomic force microscopy and electric force microscopy. It is beneficial for the development of organic electronics (dodecanethiol + push-pull chromophore) and biosensor (mPEG12SH + oligopeptide).

The perspectives of this work are numerous:

1. In terms of the self-assembled monolayer preparation, the temperature, the atmospheric environment and the annealing condition should be considered as important parameters to be tested.
2. In terms of the push-pull chromophore, new push-pull chromophores could be synthesized with other dipole properties for their electrical and optical property with the procedure presented in the PhD thesis. For this purpose, I have begun to modify the studied push-pull chromophore with an extended π-conjugated spacer to enhance the electrical dipole, which is presented below. The recent work is done after the Wittig reaction.

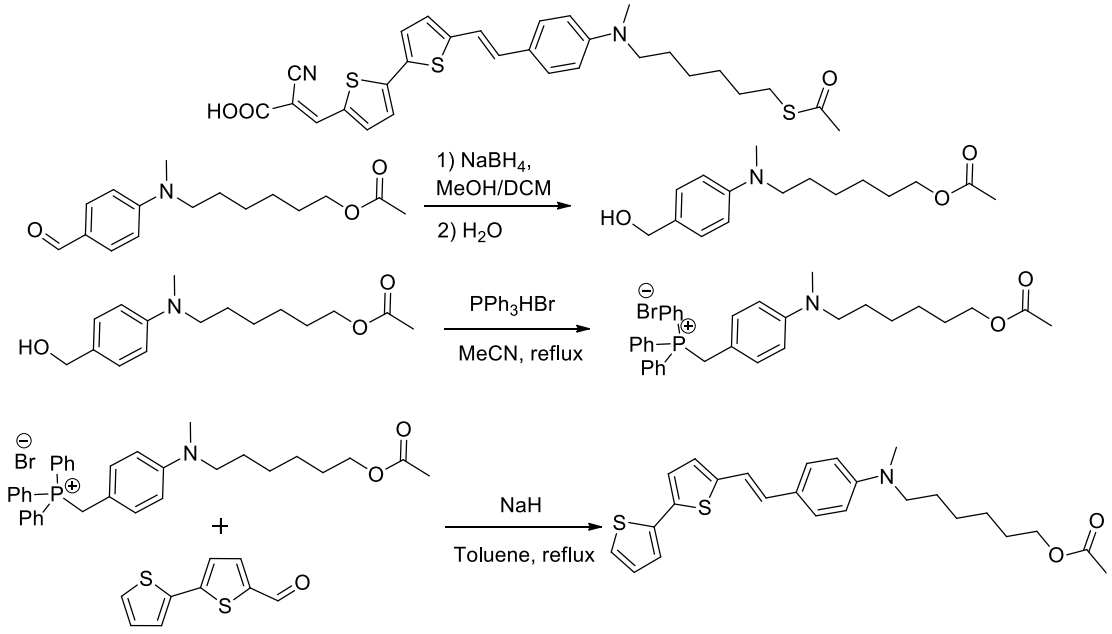

3. Grafting the oligopeptide on top of the push-pull chromophores. An idea to do this is to use the activated ester using N-hydroxysuccinimide and carbodiimide (like DCC, dicyclohexylcarbodiimide) to change the carboxylic acid on the surface. Then amine can be adopted to form amide bond.

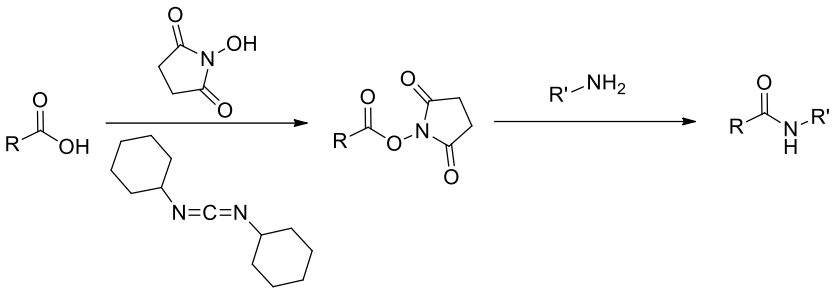


4. Testing the effect of potential to polarize the direction of the electrical dipole to have better orientation of the electrical dipole on the surface.
5. Testing the effect of potential on the oligopeptide unfolding with/without the push-pull chromophore.
6. As a goal, in collaboration with biologists we could consider the biosensor activity by grafting a sensing moiety and trying to detect the complementary moiety in a solution.

# References:


(1) Malytskyi, V.; Simon, J.-J.; Patrone, L.; Raimundo, J.-M. Thiophene-Based Push–Pull Chromophores for Small Molecule Organic Solar Cells (SMOSCs). *RSC Adv.* **2015**, *5* (1), 354–397. https://doi.org/10.1039/C4RA11664J.

(2) Roncali, J.; Leriche, P.; Blanchard, P. Molecular Materials for Organic Photovoltaics: Small Is Beautiful. *Adv. Mater.* **2014**, *26* (23), 3821–3838. https://doi.org/10.1002/adma.201305999.

(3) Ha, Y.; Facchetti, A.; Marks, T. J. Push–Pull π-Electron Phosphonic-Acid-Based Self-Assembled Multilayer Nanodielectrics Fabricated in Ambient for Organic Transistors. *Chem. Mater.* **2009**, *21* (7), 1173–1175. https://doi.org/10.1021/cm8031187.

(4) Zhu, Y.; Ma, C.; Han, H.; Sun, R.; Liao, X.; Xie, M. Azobenzene-Functionalized Polymers by Ring-Opening Metathesis Polymerization for High Dielectric and Energy Storage Performance. *Polym. Chem.* **2019**, *10* (19), 2447–2455. https://doi.org/10.1039/C9PY00151D.

(5) Ulman, A. *An Introduction to Ultrathin Organic Films: From Langmuir--Blodgett to Self--Assembly*.

(6) Malytskyi, V.; Gadenne, V.; Ksari, Y.; Patrone, L.; Raimundo, J.-M. Synthesis and Characterization of Thiophene-Based Push-Pull Chromophores for Tuning the Electrical and Optical Properties of Surfaces with Controlled SAM Formation. *Tetrahedron* **2017**, *73* (39), 5738–5744. https://doi.org/10.1016/j.tet.2017.08.004.

(7) Santos Gomes, B.; Cantini, E.; Tommasone, S.; Gibson, J. S.; Wang, X.; Zhu, Q.; Ma, J.; McGettrick, J. D.; Watson, T. M.; Preece, J. A.; Kirkman-Brown, J. C.; Publicover, S. J.; Mendes, P. M. On-Demand Electrical Switching of Antibody–Antigen Binding on Surfaces. *ACS Appl. Bio Mater.* **2018**, *1* (3), 738–747. https://doi.org/10.1021/acsabm.8b00201.

(8) Bureš, F. Fundamental Aspects of Property Tuning in Push–Pull Molecules. *RSC Adv.* **2014**, *4* (102), 58826–58851. https://doi.org/10.1039/C4RA11264D.

(9) Liu, J.; Ouyang, C.; Huo, F.; He, W.; Cao, A. Progress in the Enhancement of Electro-Optic Coefficients and Orientation Stability for Organic Second-Order Nonlinear Optical Materials. *Dyes and Pigments* **2020**, *181*, 108509. https://doi.org/10.1016/j.dyepig.2020.108509.

(10) Forrest, S. R.; Thompson, M. E. Introduction: Organic Electronics and Optoelectronics. *Chem. Rev.* **2007**, *107* (4), 923–925. https://doi.org/10.1021/cr0501590.

(11) Miller, R. D.; Chandross, E. A. Introduction: Materials for Electronics. *Chem. Rev.* **2010**, *110* (1), 1–2. https://doi.org/10.1021/cr900384b.

(12) Bredas, J.-L.; Durrant, J. R. Organic Photovoltaics. *Acc. Chem. Res.* **2009**, *42* (11), 1689–1690. https://doi.org/10.1021/ar900238j.
(13) Wu, Y.; Zhu, W. Organic Sensitizers from D–π–A to D–A–π–A: Effect of the Internal Electron-Withdrawing Units on Molecular Absorption, Energy Levels and Photovoltaic Performances. *Chem. Soc. Rev.* **2013**, *42* (5), 2039–2058. https://doi.org/10.1039/C2CS35346F.
(14) Hains, A. W.; Liang, Z.; Woodhouse, M. A.; Gregg, B. A. Molecular Semiconductors in Organic Photovoltaic Cells. *Chem. Rev.* **2010**, *110* (11), 6689–6735. https://doi.org/10.1021/cr9002984.
(15) Duan, C.; Huang, F.; Cao, Y. Recent Development of Push–Pull Conjugated Polymers for Bulk-Heterojunction Photovoltaics: Rational Design and Fine Tailoring of Molecular Structures. *J. Mater. Chem.* **2012**, *22* (21), 10416. https://doi.org/10.1039/c2jm30470h.
(16) Ohmori, Y. Development of Organic Light-Emitting Diodes for Electro-Optical Integrated Devices. https://doi.org/10.1002/lpor.200810059.
(17) Allard, S.; Forster, M.; Souharce, B.; Thiem, H.; Scherf, U. Organic Semiconductors for Solution-Processable Field-Effect Transistors (OFETs). https://doi.org/10.1002/anie.200701920.
(18) Kivala, M.; Diederich, F. Acetylene-Derived Strong Organic Acceptors for Planar and Nonplanar Push–Pull Chromophores. *Acc. Chem. Res.* **2009**, *42* (2), 235–248. https://doi.org/10.1021/ar8001238.
(19) Roncali, J. Molecular Engineering of the Band Gap of pi-Conjugated Systems. https://doi.org/10.1002/marc.200700345.
(20) Katz, H. E.; Singer, K. D.; Sohn, J. E.; Dirk, C. W.; King, L. A.; Gordon, H. M. Greatly Enhanced Second-Order Nonlinear Optical Susceptibilities in Donor-Acceptor Organic Molecules. *J. Am. Chem. Soc.* **1987**, *109* (21), 6561–6563. https://doi.org/10.1021/ja00255a079.
(21) Chafin, A. P.; Davis, M. C.; Lai, W. W.; Lindsay, G. A.; Park, D. H.; Herman, W. N. Benzofuran-Terminated Infrared Dyes and Their Electro-Optic Properties in Guest–Host Polymers. *Optical Materials* **2011**, *33* (8), 1307–1315. https://doi.org/10.1016/j.optmat.2011.03.004.
(22) Yang, Y.; He, Z.; He, J.; Jiang, G.; Liu, F. The Influence on Properties with Different Conjugated Direction of Phenoxazine and Phenothiazine-Based Chromophores for Organic Nonlinear Optical Materials. *Dyes and Pigments* **2020**, *176*, 108219. https://doi.org/10.1016/j.dyepig.2020.108219.
(23) Bhuiyan, M. D. H.; Ashraf, M.; Teshome, A.; Gainsford, G. J.; Kay, A. J.; Asselberghs, I.; Clays, K. Synthesis, Linear & Non Linear Optical (NLO) Properties of Some Indoline Based Chromophores. *Dyes and Pigments* **2011**, *89* (2), 177–187. https://doi.org/10.1016/j.dyepig.2010.10.010.
(24) Xu, H.; Wang, H.; Hu, C.; Fu, M.; He, Y.; Liu, J.; Liu, X. The Influence of Different Donor/Acceptor Matches on Chromophore's Nonlinear Optical Activity. *Dyes*

*and Pigments* **2016**, *131*, 215–223. https://doi.org/10.1016/j.dyepig.2016.04.023.
(25) Martínez De Baroja, N.; Garín, J.; Orduna, J.; Andreu, R.; Blesa, M. J.; Villacampa, B.; Alicante, R.; Franco, S. Synthesis, Characterization, and Optical Properties of 4 *H* -Pyran-4-Ylidene Donor-Based Chromophores: The Relevance of the Location of a Thiophene Ring in the Spacer. *J. Org. Chem.* **2012**, *77* (10), 4634–4644. https://doi.org/10.1021/jo300373m.
(26) Marco, A. B.; Andreu, R.; Franco, S.; Garín, J.; Orduna, J.; Villacampa, B.; Alicante, R. Efficient Second-Order Nonlinear Optical Chromophores Based on Dithienothiophene and Thienothiophene Bridges. *Tetrahedron* **2013**, *69* (19), 3919–3926. https://doi.org/10.1016/j.tet.2013.03.027.
(27) Marco, A. B.; Martínez de Baroja, N.; Franco, S.; Garín, J.; Orduna, J.; Villacampa, B.; Revuelto, A.; Andreu, R. Dithienopyrrole as a Rigid Alternative to the Bithiophene π Relay in Chromophores with Second-Order Nonlinear Optical Properties. *Chemistry – An Asian Journal* **2015**, *10* (1), 188–197. https://doi.org/10.1002/asia.201402870.
(28) Marco, A. B.; Burrezo, P. M.; Mosteo, L.; Franco, S.; Garín, J.; Orduna, J.; Diosdado, B. E.; Villacampa, B.; López Navarrete, J. T.; Casado, J.; Andreu, R. Polarization, Second-Order Nonlinear Optical Properties and Electrochromism in 4H-Pyranylidene Chromophores with a Quinoid/Aromatic Thiophene Ring Bridge. *RSC Adv.* **2015**, *5* (1), 231–242. https://doi.org/10.1039/C4RA12791A.
(29) Faux, N.; Caro, B.; Robin-Le Guen, F.; Le Poul, P.; Nakatani, K.; Ishow, E. γ-Methylene Chalcogenapyrans and Benzopyrans as Proaromatic Donors in "Push–Pull" Fischer Type Carbene Complexes: Influences of Chalcogen Atom and Chain Length on the Electronic and N.L.O. Properties of These Molecules. *Journal of Organometallic Chemistry* **2005**, *690* (21–22), 4982–4988. https://doi.org/10.1016/j.jorganchem.2005.07.049.
(30) Solanke, P.; Achelle, S.; Cabon, N.; Pytela, O.; Barsella, A.; Caro, B.; Robin-le Guen, F.; Podlesný, J.; Klikar, M.; Bureš, F. Proaromatic Pyranylidene Chalcogen Analogues and Cyclopenta[ c ]Thiophen-4,6-Dione as Electron Donors and Acceptor in Efficient Charge-Transfer Chromophores. *Dyes and Pigments* **2016**, *134*, 129–138. https://doi.org/10.1016/j.dyepig.2016.07.008.
(31) Liu, F.; Wang, H.; Yang, Y.; Xu, H.; Yang, D.; Bo, S.; Liu, J.; Zhen, Z.; Liu, X.; Qiu, L. Using Phenoxazine and Phenothiazine as Electron Donors for Second-Order Nonlinear Optical Chromophore: Enhanced Electro-Optic Activity. *Dyes and Pigments* **2015**, *114*, 196–203. https://doi.org/10.1016/j.dyepig.2014.11.015.
(32) Čibová, A.; Martinická, A.; Magdolen, P.; Zahradník, P.; Cigáň, M.; Uherek, M.; Chorvát, D. Dicationic and Monocationic Benzobisthiazolium Salts as

Potential NLO Chromophores. *Dyes and Pigments* **2018**, *149*, 597–611. https://doi.org/10.1016/j.dyepig.2017.11.015.
(33) Singer, K. D.; Katz, H. E.; Dirk, C. W.; Sohn, J. E.; King, L. A.; Gordon, H. M. Second-Order Nonlinear-Optical Properties of Donor- and Acceptor-Substituted Aromatic Compounds. *J. Opt. Soc. Am. B* **1989**, *6* (7), 1339. https://doi.org/10.1364/JOSAB.6.001339.
(34) Dörr, M.; Zentel, R.; Dietrich, R.; Meerholz, K.; Bräuchle, C.; Wichern, J.; Zippel, S.; Boldt, P. Reactions on Vinyl Isocyanate/Maleimide Copolymers: NLO-Functionalized Polymers with High Glass Transitions for Nonlinear Optical Applications. *Macromolecules* **1998**, *31* (5), 1454–1465. https://doi.org/10.1021/ma971122n.
(35) Jang, S.-H.; Luo, J.; Tucker, N. M.; Leclercq, A.; Zojer, E.; Haller, M. A.; Kim, T.-D.; Kang, J.-W.; Firestone, K.; Bale, D.; Lao, D.; Benedict, J. B.; Cohen, D.; Kaminsky, W.; Kahr, B.; Brédas, J.-L.; Reid, P.; Dalton, L. R.; Jen, A. K.-Y. Pyrroline Chromophores for Electro-Optics. *Chem. Mater.* **2006**, *18* (13), 2982–2988. https://doi.org/10.1021/cm052861i.
(36) Durand, R. J.; Achelle, S.; Gauthier, S.; Cabon, N.; Ducamp, M.; Kahlal, S.; Saillard, J.-Y.; Barsella, A.; Robin-Le Guen, F. Incorporation of a Ferrocene Unit in the π-Conjugated Structure of Donor-Linker-Acceptor (D-π-A) Chromophores for Nonlinear Optics (NLO). *Dyes and Pigments* **2018**, *155*, 68–74. https://doi.org/10.1016/j.dyepig.2018.03.029.
(37) Kalinin, A. A.; Sharipova, S. M.; Burganov, T. I.; Levitskaya, A. I.; Dudkina, Y. B.; Khamatgalimov, A. R.; Katsyuba, S. A.; Budnikova, Y. H.; Balakina, M. Yu. High Thermally Stable D–π–A Chromophores with Quinoxaline Moieties in the Conjugated Bridge: Synthesis, DFT Calculations and Physical Properties. *Dyes and Pigments* **2018**, *156*, 175–184. https://doi.org/10.1016/j.dyepig.2018.04.002.
(38) Liu, F.; Zhang, H.; Xiao, H.; Xu, H.; Bo, S.; Qiu, L.; Zhen, Z.; Lai, L.; Chen, S.; Wang, J. Structure–Function Relationship Exploration for Enhanced Electro-Optic Activity in Isophorone-Based Organic NLO Chromophores. *Dyes and Pigments* **2018**, *157*, 55–63. https://doi.org/10.1016/j.dyepig.2018.04.036.
(39) Sun, J.; Zheng, M.; Jia, J.; Wang, W.; Cui, Y.; Gao, J. New Coumarin-Benzoxazole Derivatives: Synthesis, Photophysical and NLO Properties. *Dyes and Pigments* **2019**, *164*, 287–295. https://doi.org/10.1016/j.dyepig.2019.01.010.
(40) Raimundo, J.-M.; Blanchard, P.; Gallego-Planas, N.; Mercier, N.; Ledoux-Rak, I.; Hierle, R.; Roncali, J. Design and Synthesis of Push–Pull Chromophores for Second-Order Nonlinear Optics Derived from Rigidified Thiophene-Based π-Conjugating Spacers. *J. Org. Chem.* **2002**, *67* (1), 205–218. https://doi.org/10.1021/jo010713f.
(41) Zhang, C.; Dalton, L. R.; Oh, M.-C.; Zhang, H.; Steier, W. H. Low $V_\pi$ Electrooptic Modulators from CLD-1: Chromophore Design and Synthesis,

Material Processing, and Characterization. *Chem. Mater.* **2001**, *13* (9), 3043–3050. https://doi.org/10.1021/cm010463j.
(42) Yang, Y.; Wang, H.; Liu, F.; Yang, D.; Bo, S.; Qiu, L.; Zhen, Z.; Liu, X. The Synthesis of New Double-Donor Chromophores with Excellent Electro-Optic Activity by Introducing Modified Bridges. *Phys. Chem. Chem. Phys.* **2015**, *17* (8), 5776–5784. https://doi.org/10.1039/C4CP05829A.
(43) Yang, Y.; Liu, J.; Zhang, M.; Liu, F.; Wang, H.; Bo, S.; Zhen, Z.; Qiu, L.; Liu, X. The Important Role of the Location of the Alkoxy Group on the Thiophene Ring in Designing Efficient Organic Nonlinear Optical Materials Based on Double-Donor Chromophores. *J. Mater. Chem. C* **2015**, *3* (16), 3913–3921. https://doi.org/10.1039/C5TC00241A.
(44) Yang, Y.; Bo, S.; Wang, H.; Liu, F.; Liu, J.; Qiu, L.; Zhen, Z.; Liu, X. Novel Chromophores with Excellent Electro-Optic Activity Based on Double-Donor Chromophores by Optimizing Thiophene Bridges. *Dyes and Pigments* **2015**, *122*, 139–146. https://doi.org/10.1016/j.dyepig.2015.06.012.
(45) Zhang, C.; R. Dalton, L.; Oh, M.-C.; Zhang, H.; H. Steier, W. Low V Electrooptic Modulators from CLD-1: Chromophore Design and Synthesis, Material Processing, and Characterization. https://doi.org/10.1021/cm010463j.
(46) Xia, P. F.; Feng, X. J.; Lu, J.; Movileanu, R.; Tao, Y.; Baribeau, J.-M.; Wong, M. S. Triarylamino and Tricyanovinyl End-Capped Oligothiophenes with Reduced Optical Gap for Photovoltaic Applications. *J. Phys. Chem. C* **2008**, *112* (42), 16714–16720. https://doi.org/10.1021/jp805555c.
(47) Zhang, W.; Tse, S. C.; Lu, J.; Tao, Y.; Wong, M. S. Solution Processable Donor–Acceptor Oligothiophenes for Bulk-Heterojunction Solar Cells. *J. Mater. Chem.* **2010**, *20* (11), 2182. https://doi.org/10.1039/b926203b.
(48) Kim, J.; Ko, H. M.; Cho, N.; Paek, S.; Lee, J. K.; Ko, J. Efficient Small Molecule Organic Semiconductor Containing Bis-Dimethylfluorenyl Amino Benzo[b]Thiophene for High Open Circuit Voltage in High Efficiency Solution Processed Organic Solar Cell. *RSC Adv.* **2012**, *2* (7), 2692. https://doi.org/10.1039/c2ra01271e.
(49) Lin, L.-Y.; Chen, Y.-H.; Huang, Z.-Y.; Lin, H.-W.; Chou, S.-H.; Lin, F.; Chen, C.-W.; Liu, Y.-H.; Wong, K.-T. A Low-Energy-Gap Organic Dye for High-Performance Small-Molecule Organic Solar Cells. *J. Am. Chem. Soc.* **2011**, *133* (40), 15822–15825. https://doi.org/10.1021/ja205126t.
(50) Chiu, S.-W.; Lin, L.-Y.; Lin, H.-W.; Chen, Y.-H.; Huang, Z.-Y.; Lin, Y.-T.; Lin, F.; Liu, Y.-H.; Wong, K.-T. A Donor–Acceptor–Acceptor Molecule for Vacuum-Processed Organic Solar Cells with a Power Conversion Efficiency of 6.4%. *Chem. Commun.* **2012**, *48* (13), 1857–1859. https://doi.org/10.1039/C2CC16390J.
(51) Chen, Y.-H.; Lin, L.-Y.; Lu, C.-W.; Lin, F.; Huang, Z.-Y.; Lin, H.-W.; Wang, P.-H.; Liu, Y.-H.; Wong, K.-T.; Wen, J.; Miller, D. J.; Darling, S. B. Vacuum-Deposited Small-Molecule Organic Solar Cells with High Power Conversion Efficiencies

by Judicious Molecular Design and Device Optimization. *J. Am. Chem. Soc.* **2012**, *134* (33), 13616–13623. https://doi.org/10.1021/ja301872s.
(52) Deng, D.; Yang, Y.; Zhang, J.; He, C.; Zhang, M.; Zhang, Z.-G.; Zhang, Z.; Li, Y. Triphenylamine-Containing Linear D-A-D Molecules with Benzothiadiazole as Acceptor Unit for Bulk-Heterojunction Organic Solar Cells. *Organic Electronics* **2011**, *12* (4), 614–622. https://doi.org/10.1016/j.orgel.2011.01.013.
(53) Lin, Y.; Li, Y.; Zhan, X. Small Molecule Semiconductors for High-Efficiency Organic Photovoltaics. *Chem. Soc. Rev.* **2012**, *41* (11), 4245. https://doi.org/10.1039/c2cs15313k.
(54) Liu, Q.; Du, Z.; Chen, W.; Sun, L.; Chen, Y.; Sun, M.; Yang, R. Low HOMO Isoindigo Based Small Molecule for High Open-Circuit Voltage 1.0V Solution Processed Organic Solar Cells. *Synthetic Metals* **2013**, *178*, 38–43. https://doi.org/10.1016/j.synthmet.2013.06.024.
(55) Ying, W.; Guo, F.; Li, J.; Zhang, Q.; Wu, W.; Tian, H.; Hua, J. Series of New D-A-π-A Organic Broadly Absorbing Sensitizers Containing Isoindigo Unit for Highly Efficient Dye-Sensitized Solar Cells. https://doi.org/10.1021/am300925e.
(56) Song, S.; Kim, T.; Park, H.; Jin, Y.; Kim, I.; Kim, J. Y.; Suh, H. Low Bandgap Small Molecules Based on 2,2-Bithiophene-3,3-Dicarboximide for Soluble-Processed Solar Cells. *Synthetic Metals* **2013**, *183*, 16–23. https://doi.org/10.1016/j.synthmet.2013.09.001.
(57) Loser, S.; Bruns, C. J.; Miyauchi, H.; Ortiz, R. P.; Facchetti, A.; Stupp, S. I.; Marks, T. J. A Naphthodithiophene-Diketopyrrolopyrrole Donor Molecule for Efficient Solution-Processed Solar Cells. *J. Am. Chem. Soc.* **2011**, *133* (21), 8142–8145. https://doi.org/10.1021/ja202791n.
(58) Loser, S.; Miyauchi, H.; Hennek, J. W.; Smith, J.; Huang, C.; Facchetti, A.; Marks, T. J. A "Zig-Zag" Naphthodithiophene Core for Increased Efficiency in Solution-Processed Small Molecule Solar Cells. *Chem. Commun.* **2012**, *48* (68), 8511. https://doi.org/10.1039/c2cc32646a.
(59) Gadenne, V.; Grenier, B.; Praveen, C.; Marsal, P.; Valmalette, J. C.; Patrone, L.; Raimundo, J. M. Combined SERS/DFT Studies of Push–Pull Chromophore Self-Assembled Monolayers: Insights into Their Surface Orientation. *Phys. Chem. Chem. Phys.* **2019**, *21* (46), 25865–25871. https://doi.org/10.1039/C9CP04008K.
(60) Marco, A. B.; Martínez De Baroja, N.; Andrés-Castán, J. M.; Franco, S.; Andreu, R.; Villacampa, B.; Orduna, J.; Garín, J. Pyranylidene/Thienothiophene-Based Organic Sensitizers for Dye-Sensitized Solar Cells. *Dyes and Pigments* **2019**, *161*, 205–213. https://doi.org/10.1016/j.dyepig.2018.09.035.
(61) Unny, D.; Kandregula, G. R.; Sivanadanam, J.; Ramanujam, K. Molecular Engineering of Pyrene Carbazole Dyes with a Single Bond and Double Bond

as the Mode of Linkage. *New J. Chem.* **2020**, *44* (38), 16511–16525. https://doi.org/10.1039/D0NJ03228J.
(62) Paul, A.; Biswas, A.; Sinha, S.; Shah, Sk. S.; Bera, M.; Mandal, M.; Singh, N. D. P. Push–Pull Stilbene: Visible Light Activated Photoremovable Protecting Group for Alcohols and Carboxylic Acids with Fluorescence Reporting Employed for Drug Delivery. *Org. Lett.* **2019**, *21* (9), 2968–2972. https://doi.org/10.1021/acs.orglett.9b00124.
(63) Robello, D. R. Linear Polymers for Nonlinear Optics. I. Polyacrylates Bearing Aminonitro-Stilbene and -Azobenzene Dyes. *J. Polym. Sci. A Polym. Chem.* **1990**, *28* (1), 1–13. https://doi.org/10.1002/pola.1990.080280101.
(64) Dieck, H. A.; Heck, R. F. Organophosphinepalladium Complexes as Catalysts for Vinylic Hydrogen Substitution Reactions. *J. Am. Chem. Soc.* **1974**, *96* (4), 1133–1136. https://doi.org/10.1021/ja00811a029.
(65) Götzinger, A. C.; Michaelis, C. S.; Müller, T. J. J. 3-Phenothiazinyl Propiolates – Fluorescent Electrophores by Sonogashira Coupling of Ethyl Propiolate. *Dyes and Pigments* **2017**, *143*, 308–316. https://doi.org/10.1016/j.dyepig.2017.04.049.
(66) Justin Thomas, K. R.; Velusamy, M.; Lin, J. T.; Chuen, C.-H.; Tao, Y.-T. Chromophore-Labeled Quinoxaline Derivatives as Efficient Electroluminescent Materials. *Chem. Mater.* **2005**, *17* (7), 1860–1866. https://doi.org/10.1021/cm047705a.
(67) Shinotsuka, R.; Oba, T.; Mitome, T.; Masuya, T.; Ito, S.; Murakami, Y.; Kagenishi, T.; Kodama, Y.; Matsuda, M.; Yoshida, T.; Wakamori, M.; Ohkura, M.; Nakai, J. Synthesis of Quinolyl-Pyrrole Derivatives as Novel Environment-Sensitive Fluorescent Probes. *Journal of Photochemistry and Photobiology A: Chemistry* **2019**, *382*, 111900. https://doi.org/10.1016/j.jphotochem.2019.111900.
(68) Han, L.; Wu, H.; Cui, Y.; Zu, X.; Ye, Q.; Gao, J. Synthesis and Density Functional Theory Study of Novel Coumarin-Type Dyes for Dye Sensitized Solar Cells. *Journal of Photochemistry and Photobiology A: Chemistry* **2014**, *290*, 54–62. https://doi.org/10.1016/j.jphotochem.2014.06.001.
(69) Kumar, R. J.; Churches, Q. I.; Subbiah, J.; Gupta, A.; Ali, A.; Evans, R. A.; Holmes, A. B. Enhanced Photovoltaic Efficiency via Light-Triggered Self-Assembly. *Chem. Commun.* **2013**, *49* (58), 6552. https://doi.org/10.1039/c3cc43841d.
(70) Aissaoui, N.; Bergaoui, L.; Landoulsi, J.; Lambert, J.-F.; Boujday, S. Silane Layers on Silicon Surfaces: Mechanism of Interaction, Stability, and Influence on Protein Adsorption. *Langmuir* **2012**, *28* (1), 656–665. https://doi.org/10.1021/la2036778.
(71) Tanaka, M.; Sawaguchi, T.; Kuwahara, M.; Niwa, O. Surface Modification of Silicon Oxide with Trialkoxysilanes toward Close-Packed Monolayer

Formation. *Langmuir* **2013**, *29* (21), 6361–6368. https://doi.org/10.1021/la4009834.
(72) Arndt, N. B.; Schlüter, F.; Böckmann, M.; Adolphs, T.; Arlinghaus, H. F.; Doltsinis, N. L.; Ravoo, B. J. Self-Assembled Monolayers of Arylazopyrazoles on Glass and Silicon Oxide: Photoisomerization and Photoresponsive Wettability. *Langmuir* **2022**, *38* (2), 735–742. https://doi.org/10.1021/acs.langmuir.1c02651.
(73) Cicero, R. L.; Linford, M. R.; Chidsey, C. E. D. Photoreactivity of Unsaturated Compounds with Hydrogen-Terminated Silicon(111). *Langmuir* **2000**, *16* (13), 5688–5695. https://doi.org/10.1021/la9911990.
(74) Langner, A.; Panarello, A.; Rivillon, S.; Vassylyev, O.; Khinast, J. G.; Chabal, Y. J. Controlled Silicon Surface Functionalization by Alkene Hydrosilylation. *J. Am. Chem. Soc.* **2005**, *127* (37), 12798–12799. https://doi.org/10.1021/ja054634n.
(75) Liu, Y.; Yamazaki, S.; Yamabe, S.; Nakato, Y. A Mild and Efficient Si (111) Surface Modification via Hydrosilylation of Activated Alkynes. *J. Mater. Chem.* **2005**, *15* (46), 4906. https://doi.org/10.1039/b511535c.
(76) Zhong, Y. L.; Bernasek, S. L. Mild and Efficient Functionalization of Hydrogen-Terminated Si(111) via Sonochemical Activated Hydrosilylation. *J. Am. Chem. Soc.* **2011**, *133* (21), 8118–8121. https://doi.org/10.1021/ja2020839.
(77) Bain, C. D.; Troughton, E. B.; Tao, Y. T.; Evall, J.; Whitesides, G. M.; Nuzzo, R. G. Formation of Monolayer Films by the Spontaneous Assembly of Organic Thiols from Solution onto Gold. *J. Am. Chem. Soc.* **1989**, *111* (1), 321–335. https://doi.org/10.1021/ja00183a049.
(78) Yokota, Y.; Mino, Y.; Kanai, Y.; Utsunomiya, T.; Imanishi, A.; Wolak, M. A.; Schlaf, R.; Fukui, K. Comparative Studies of Photoelectron Spectroscopy and Voltammetry of Ferrocene-Terminated Self-Assembled Monolayers Possessing Different Electron-Donating Abilities. *J. Phys. Chem. C* **2014**, *118* (20), 10936–10943. https://doi.org/10.1021/jp5023899.
(79) Walczak, M. M.; Chung, C.; Stole, S. M.; Widrig, C. A.; Porter, M. D. Structure and Interfacial Properties of Spontaneously Adsorbed N-Alkanethiolate Monolayers on Evaporated Silver Surfaces. *J. Am. Chem. Soc.* **1991**, *113* (7), 2370–2378. https://doi.org/10.1021/ja00007a004.
(80) Porter, M. D.; Bright, T. B.; Allara, D. L.; Chidsey, C. E. D. Spontaneously Organized Molecular Assemblies. 4. Structural Characterization of n-Alkyl Thiol Monolayers on Gold by Optical Ellipsometry, Infrared Spectroscopy, and Electrochemistry. *J. Am. Chem. Soc.* **1987**, *109* (12), 3559–3568. https://doi.org/10.1021/ja00246a011.
(81) Nuzzo, R. G.; Fusco, F. A.; Allara, D. L. Spontaneously Organized Molecular Assemblies. 3. Preparation and Properties of Solution Adsorbed Monolayers

of Organic Disulfides on Gold Surfaces. *J. Am. Chem. Soc.* **1987**, *109* (8), 2358–2368. https://doi.org/10.1021/ja00242a020.
(82) Bain, C. D.; Biebuyck, H. A.; Whitesides, G. M. Comparison of Self-Assembled Monolayers on Gold: Coadsorption of Thiols and Disulfides. *Langmuir* **1989**, *5* (3), 723–727. https://doi.org/10.1021/la00087a027.
(83) Strong, L.; Whitesides, G. M. Structures of Self-Assembled Monolayer Films of Organosulfur Compounds Adsorbed on Gold Single Crystals: Electron Diffraction Studies. *Langmuir* **1988**, *4* (3), 546–558. https://doi.org/10.1021/la00081a009.
(84) Chidsey, C. E. D.; Bertozzi, C. R.; Putvinski, T. M.; Mujsce, A. M. Coadsorption of Ferrocene-Terminated and Unsubstituted Alkanethiols on Gold: Electroactive Self-Assembled Monolayers. *J. Am. Chem. Soc.* **1990**, *112* (11), 4301–4306. https://doi.org/10.1021/ja00167a028.
(85) Alves, C. A.; Smith, E. L.; Porter, M. D. Atomic Scale Imaging of Alkanethiolate Monolayers at Gold Surfaces with Atomic Force Microscopy. *J. Am. Chem. Soc.* **1992**, *114* (4), 1222–1227. https://doi.org/10.1021/ja00030a015.
(86) Sellers, H.; Ulman, A.; Shnidman, Y.; Eilers, J. E. Structure and Binding of Alkanethiolates on Gold and Silver Surfaces: Implications for Self-Assembled Monolayers. *J. Am. Chem. Soc.* **1993**, *115* (21), 9389–9401. https://doi.org/10.1021/ja00074a004.
(87) Nuzzo, R. G.; Dubois, L. H.; Allara, D. L. Fundamental Studies of Microscopic Wetting on Organic Surfaces. 1. Formation and Structural Characterization of a Self-Consistent Series of Polyfunctional Organic Monolayers. *J. Am. Chem. Soc.* **1990**, *112* (2), 558–569. https://doi.org/10.1021/ja00158a012.
(88) Sabatani, E.; Cohen-Boulakia, J.; Bruening, M.; Rubinstein, I. Thioaromatic Monolayers on Gold: A New Family of Self-Assembling Monolayers. *Langmuir* **1993**, *9* (11), 2974–2981. https://doi.org/10.1021/la00035a040.
(89) Fenter, P.; Eisenberger, P.; Liang, K. S. Chain-Length Dependence of the Structures and Phases of CH 3 ( CH 2 ) n – 1 SH Self-Assembled on Au(111). *Phys. Rev. Lett.* **1993**, *70* (16), 2447–2450. https://doi.org/10.1103/PhysRevLett.70.2447.
(90) Dai, J.; Li, Z.; Jin, J.; Cheng, J.; Kong, J.; Bi, S. Study of the Solvent Effect on the Quality of Dodecanethiol Self-Assembled Monolayers on Polycrystalline Gold. *Journal of Electroanalytical Chemistry* **2008**, *624* (1–2), 315–322. https://doi.org/10.1016/j.jelechem.2008.07.001.
(91) Delamarche, E.; Michel, B.; Kang, H.; Gerber, Ch. Thermal Stability of Self-Assembled Monolayers. *Langmuir* **1994**, *10* (11), 4103–4108. https://doi.org/10.1021/la00023a033.
(92) Doudevski, I.; Schwartz, D. K. Concentration Dependence of Self-Assembled Monolayer Island Nucleation and Growth. *J. Am. Chem. Soc.* **2001**, *123* (28), 6867–6872. https://doi.org/10.1021/ja0042783.

(93) Azizian, S.; Eris, S.; Wilson, L. D. Re-Evaluation of the Century-Old Langmuir Isotherm for Modeling Adsorption Phenomena in Solution. *Chemical Physics* **2018**, *513*, 99–104. https://doi.org/10.1016/j.chemphys.2018.06.022.
(94) Breslow, R.; Belvedere, S.; Gershell, L.; Leung, D. The Chelate Effect in Binding, Catalysis, and Chemotherapy. *Pure and Applied Chemistry* **2000**.
(95) Davydova, E. I.; Sevastianova, T. N.; Timoshkin, A. Y.; Suvorov, A. V.; Frenking, G. Chelate Effect: The Importance of Reorganization Energy. *Int J of Quantum Chemistry* **2004**, *100* (4), 419–425. https://doi.org/10.1002/qua.20094.
(96) Ulman, A. Formation and Structure of Self-Assembled Monolayers. *Chem. Rev.* **1996**, *96* (4), 1533–1554. https://doi.org/10.1021/cr9502357.
(97) Hudalla, G. A.; Murphy, W. L. Using "Click" Chemistry to Prepare SAM Substrates to Study Stem Cell Adhesion. *Langmuir* **2009**, *25* (10), 5737–5746. https://doi.org/10.1021/la804077t.
(98) Irving, D. L.; Brenner, D. W. Diffusion on a Self-Assembled Monolayer: Molecular Modeling of a Bound + Mobile Lubricant. *J. Phys. Chem. B* **2006**, *110* (31), 15426–15431. https://doi.org/10.1021/jp0609840.
(99) Alagta, A.; Felhösi, I.; Bertoti, I.; Kálmán, E. Corrosion Protection Properties of Hydroxamic Acid Self-Assembled Monolayer on Carbon Steel. *Corrosion Science* **2008**, *50* (6), 1644–1649. https://doi.org/10.1016/j.corsci.2008.02.008.
(100) Chaki, N. K.; Vijayamohanan, K. Self-Assembled Monolayers as a Tunable Platform for Biosensor Applications. *Biosensors and Bioelectronics* **2002**, *17* (1–2), 1–12. https://doi.org/10.1016/S0956-5663(01)00277-9.
(101) Xiang, H. Y.; Li, W. G. Electrochemical Sensor for *Trans* -Resveratrol Determination Based on Indium Tin Oxide Electrode Modified with Molecularly Imprinted Self-Assembled Films. *Electroanalysis* **2009**, *21* (10), 1207–1210. https://doi.org/10.1002/elan.200804488.
(102) Chinwangso, P.; Jamison, A. C.; Lee, T. R. Multidentate Adsorbates for Self-Assembled Monolayer Films. *Acc. Chem. Res.* **2011**, *44* (7), 511–519. https://doi.org/10.1021/ar200020s.
(103) Nuzzo, R. G.; Allara, D. L. Adsorption of Bifunctional Organic Disulfides on Gold Surfaces. *J. Am. Chem. Soc.* **1983**, *105* (13), 4481–4483. https://doi.org/10.1021/ja00351a063.
(104) Bruening, M.; Cohen, R.; Guillemoles, J. F.; Moav, T.; Libman, J.; Shanzer, A.; Cahen, D. Simultaneous Control of Surface Potential and Wetting of Solids with Chemisorbed Multifunctional Ligands. *J. Am. Chem. Soc.* **1997**, *119* (24), 5720–5728. https://doi.org/10.1021/ja964434z.
(105) Lee, Y. J.; Jeon, I. C.; Paik, W.; Kim, K. Self-Assembly of 1,2-Benzenedithiol on Gold and Silver: Fourier Transform Infrared Spectroscopy and Quartz Crystal Microbalance Study. *Langmuir* **1996**, *12* (24), 5830–5837. https://doi.org/10.1021/la9603131.

(106) Kim, C. H.; Han, S. W.; Ha, T. H.; Kim, K. *O* -Xylene-α,α'-Dithiol Monolayer Film on Gold: Fourier Transform Infrared Spectroscopy, Quartz Crystal Microbalance, and Atomic Force Microscopy Study. *Langmuir* **1999**, *15* (24), 8399–8404. https://doi.org/10.1021/la981397b.
(107) Garg, N.; Lee, T. R. Self-Assembled Monolayers Based on Chelating Aromatic Dithiols on Gold. *Langmuir* **1998**, *14* (14), 3815–3819. https://doi.org/10.1021/la980238p.
(108) Garg, N.; Friedman, J. M.; Lee, T. R. Adsorption Profiles of Chelating Aromatic Dithiols and Disulfides: Comparison to Those of Normal Alkanethiols and Disulfides. *Langmuir* **2000**, *16* (9), 4266–4271. https://doi.org/10.1021/la991100p.
(109) Tao, Y.-T.; Wu, C.-C.; Eu, J.-Y.; Lin, W.-L.; Wu, K.-C.; Chen, C. Structure Evolution of Aromatic-Derivatized Thiol Monolayers on Evaporated Gold. *Langmuir* **1997**, *13* (15), 4018–4023. https://doi.org/10.1021/la9700984.
(110) Karpovich, D. S.; Blanchard, G. J. Direct Measurement of the Adsorption Kinetics of Alkanethiolate Self-Assembled Monolayers on a Microcrystalline Gold Surface. *Langmuir* **1994**, *10* (9), 3315–3322. https://doi.org/10.1021/la00021a066.
(111) Garg, N.; Carrasquillo-Molina, E.; Lee, T. R. Self-Assembled Monolayers Composed of Aromatic Thiols on Gold: Structural Characterization and Thermal Stability in Solution. *Langmuir* **2002**, *18* (7), 2717–2726. https://doi.org/10.1021/la0115278.
(112) Colorado, R.; Villazana, R. J.; Lee, T. R. Self-Assembled Monolayers on Gold Generated from Aliphatic Dithiocarboxylic Acids. *Langmuir* **1998**, *14* (22), 6337–6340. https://doi.org/10.1021/la9804381.
(113) Lee, T.-C.; Hounihan, D. J.; Colorado, R.; Park, J.-S.; Lee, T. R. Stability of Aliphatic Dithiocarboxylic Acid Self-Assembled Monolayers on Gold. *J. Phys. Chem. B* **2004**, *108* (8), 2648–2653. https://doi.org/10.1021/jp0370066.
(114) Park, T.-H.; Therien, M. J. Carbodithioate-Terminated Oligo(Phenyleneethynylene)s: Synthesis and Surface Functionalization of Gold Nanoparticles. *Org. Lett.* **2007**, *9* (15), 2779–2782. https://doi.org/10.1021/ol070789j.
(115) Shon, Y.-S.; Lee, T. R. Chelating Self-Assembled Monolayers on Gold Generated from Spiroalkanedithiols. *Langmuir* **1999**, *15* (4), 1136–1140. https://doi.org/10.1021/la981568c.
(116) Whitesell, J. K.; Chang, H. K. Directionally Aligned Helical Peptides on Surfaces. *Science* **1993**, *261* (5117), 73–76. https://doi.org/10.1126/science.261.5117.73.
(117) Creager, S. E.; Collard, D. M.; Fox, M. A. Mediated Electron Transfer by a Surfactant Viologen Bound to Octadecanethiol on Gold. *Langmuir* **1990**, *6* (10), 1617–1620. https://doi.org/10.1021/la00100a017.

(118) Kittredge, K. W.; Minton, M. A.; Fox, M. A.; Whitesell, J. K. α-Helical Polypeptide Films Grown From Sulfide or Thiol Linkers on Gold Surfaces. *HCA* **2002**, *85* (3), 788. https://doi.org/10.1002/1522-2675(200203)85:3<788::AID-HLCA788>3.0.CO;2-R.
(119) Kitagawa, T.; Idomoto, Y.; Matsubara, H.; Hobara, D.; Kakiuchi, T.; Okazaki, T.; Komatsu, K. Rigid Molecular Tripod with an Adamantane Framework and Thiol Legs. Synthesis and Observation of an Ordered Monolayer on Au(111). *J. Org. Chem.* **2006**, *71* (4), 1362–1369. https://doi.org/10.1021/jo051863j.
(120) Dubois, L. H.; Nuzzo, R. G. Synthesis, Structure, and Properties of Model Organic Surfaces. *Annu. Rev. Phys. Chem.* **1992**, *43* (1), 437–463. https://doi.org/10.1146/annurev.pc.43.100192.002253.
(121) Katano, S.; Kim, Y.; Matsubara, H.; Kitagawa, T.; Kawai, M. Hierarchical Chiral Framework Based on a Rigid Adamantane Tripod on Au(111). *J. Am. Chem. Soc.* **2007**, *129* (9), 2511–2515. https://doi.org/10.1021/ja065893v.
(122) Kitajgorodskij, A. I.; Kitajgorodskij, A. I. *Molecular Crystals and Molecules*; Physical chemistry; Acad. Press: New York, NY, 1973.
(123) Mei, B. C.; Oh, E.; Susumu, K.; Farrell, D.; Mountziaris, T. J.; Mattoussi, H. Effects of Ligand Coordination Number and Surface Curvature on the Stability of Gold Nanoparticles in Aqueous Solutions. *Langmuir* **2009**, *25* (18), 10604–10611. https://doi.org/10.1021/la901423z.
(124) Mei, B. C.; Susumu, K.; Medintz, I. L.; Delehanty, J. B.; Mountziaris, T. J.; Mattoussi, H. Modular Poly(Ethylene Glycol) Ligands for Biocompatible Semiconductor and Gold Nanocrystals with Extended pH and Ionic Stability. *J. Mater. Chem.* **2008**, *18* (41), 4949. https://doi.org/10.1039/b810488c.
(125) Stewart, M. H.; Susumu, K.; Mei, B. C.; Medintz, I. L.; Delehanty, J. B.; Blanco-Canosa, J. B.; Dawson, P. E.; Mattoussi, H. Multidentate Poly(Ethylene Glycol) Ligands Provide Colloidal Stability to Semiconductor and Metallic Nanocrystals in Extreme Conditions. *J. Am. Chem. Soc.* **2010**, *132* (28), 9804–9813. https://doi.org/10.1021/ja102898d.
(126) Stine, K. J.; Andrauskas, D. M.; Khan, A. R.; Forgo, P.; D'Souza, V. T. Electrochemical Study of Self-Assembled Monolayers of a b-Cyclodextrin Methyl Sulfide Covalently Linked to Anthraquinone. *Journal of Electroanalytical Chemistry* **1999**.
(127) Nelles, G.; Weisser, M.; Back, R.; Wohlfart, P.; Wenz, G.; Mittler-Neher, S. Controlled Orientation of Cyclodextrin Derivatives Immobilized on Gold Surfaces. *J. Am. Chem. Soc.* **1996**, *118* (21), 5039–5046. https://doi.org/10.1021/ja9539812.
(128) Labonté, A. P.; Tripp, S. L.; Reifenberger, R.; Wei, A. Scanning Tunneling Spectroscopy of Insulating Self-Assembled Monolayers on Au(111). *J. Phys. Chem. B* **2002**, *106* (34), 8721–8725. https://doi.org/10.1021/jp025626l.
(129) Thoden Van Velzen, E. U.; Engbersen, J. F. J.; De Lange, P. J.; Mahy, J. W. G.; Reinhoudt, D. N. Self-Assembled Monolayers of Resorcin[4]Arene

Tetrasulfides on Gold. *J. Am. Chem. Soc.* **1995**, *117* (26), 6853–6862. https://doi.org/10.1021/ja00131a007.
(130) Huijser, A.; Savenije, T. J.; Kroeze, J. E.; Siebbeles, L. D. A. Exciton Diffusion and Interfacial Charge Separation in *m Eso* -Tetraphenylporphyrin/$TiO_2$ Bilayers: Effect of Ethyl Substituents. *J. Phys. Chem. B* **2005**, *109* (43), 20166–20173. https://doi.org/10.1021/jp053265e.
(131) Knupfer, M. Exciton Binding Energies in Organic Semiconductors. *Appl. Phys. A* **2003**, *77* (5), 623–626. https://doi.org/10.1007/s00339-003-2182-9.
(132) Jono, R.; Sumita, M.; Tateyama, Y.; Yamashita, K. Redox Reaction Mechanisms with Non-Triiodide Mediators in Dye-Sensitized Solar Cells by Redox Potential Calculations. *J. Phys. Chem. Lett.* **2012**, *3* (23), 3581–3584. https://doi.org/10.1021/jz301589a.
(133) Yanagida, S.; Yu, Y.; Manseki, K. Iodine/Iodide-Free Dye-Sensitized Solar Cells. *Acc. Chem. Res.* **2009**, *42* (11), 1827–1838. https://doi.org/10.1021/ar900069p.
(134) Cong, J.; Yang, X.; Kloo, L.; Sun, L. Iodine/Iodide-Free Redox Shuttles for Liquid Electrolyte-Based Dye-Sensitized Solar Cells. *Energy Environ. Sci.* **2012**, *5* (11), 9180. https://doi.org/10.1039/c2ee22095d.
(135) Hamann, T. W.; Ondersma, J. W. Dye-Sensitized Solar Cellredox Shuttles. *Energy Environ. Sci.* **2011**, *4* (2), 370–381. https://doi.org/10.1039/C0EE00251H.
(136) Daeneke, T.; Mozer, A. J.; Uemura, Y.; Makuta, S.; Fekete, M.; Tachibana, Y.; Koumura, N.; Bach, U.; Spiccia, L. Dye Regeneration Kinetics in Dye-Sensitized Solar Cells. *J. Am. Chem. Soc.* **2012**, *134* (41), 16925–16928. https://doi.org/10.1021/ja3054578.
(137) Hamann, T. W.; Farha, O. K.; Hupp, J. T. Outer-Sphere Redox Couples as Shuttles in Dye-Sensitized Solar Cells. Performance Enhancement Based on Photoelectrode Modification via Atomic Layer Deposition. *J. Phys. Chem. C* **2008**, *112* (49), 19756–19764. https://doi.org/10.1021/jp807395g.
(138) Hattori, S.; Wada, Y.; Yanagida, S.; Fukuzumi, S. Blue Copper Model Complexes with Distorted Tetragonal Geometry Acting as Effective Electron-Transfer Mediators in Dye-Sensitized Solar Cells. *J. Am. Chem. Soc.* **2005**, *127* (26), 9648–9654. https://doi.org/10.1021/ja0506814.
(139) Feldt, S. M.; Wang, G.; Boschloo, G.; Hagfeldt, A. Effects of Driving Forces for Recombination and Regeneration on the Photovoltaic Performance of Dye-Sensitized Solar Cells Using Cobalt Polypyridine Redox Couples. *J. Phys. Chem. C* **2011**, *115* (43), 21500–21507. https://doi.org/10.1021/jp2061392.
(140) Yella, A.; Lee, H.-W.; Tsao, H. N.; Yi, C.; Chandiran, A. K.; Nazeeruddin, Md. K.; Diau, E. W.-G.; Yeh, C.-Y.; Zakeeruddin, S. M.; Grätzel, M. Porphyrin-Sensitized Solar Cells with Cobalt (II/III)–Based Redox Electrolyte Exceed 12

Percent Efficiency. *Science* **2011**, *334* (6056), 629–634. https://doi.org/10.1126/science.1209688.
(141) The Chemical Record - 2016 - Chowdhury - Prospects of Graphene as a Potential Carrier-Transport Material in.Pdf.
(142) Ye, J.; Li, X.; Zhao, J.; Mei, X.; Li, Q. Efficient and Stable Perovskite Solar Cells Based on Functional Graphene-Modified P3HT Hole-Transporting Layer. *RSC Adv.* **2016**, *6* (43), 36356–36361. https://doi.org/10.1039/C6RA03466G.
(143) Zhang, Y.; Elawad, M.; Yu, Z.; Jiang, X.; Lai, J.; Sun, L. Enhanced Performance of Perovskite Solar Cells with P3HT Hole-Transporting Materials via Molecular p-Type Doping. *RSC Adv.* **2016**, *6* (110), 108888–108895. https://doi.org/10.1039/C6RA21775C.
(144) Yang, F.; Kamarudin, M. A.; Hirotani, D.; Zhang, P.; Kapil, G.; Ng, C. H.; Ma, T.; Hayase, S. Melamine Hydroiodide Functionalized $MAPbI_3$ Perovskite with Enhanced Photovoltaic Performance and Stability in Ambient Atmosphere. *Solar RRL* **2019**, *3* (1), 1800275. https://doi.org/10.1002/solr.201800275.
(145) Elawad, M.; John, K. I.; Idris, A. M.; Yang, L.; Gao, Y. An Organic Hole-Transporting Material Spiro-OMeTAD Doped with a Mn Complex for Efficient Perovskite Solar Cells with High Conversion Efficiency. *RSC Adv.* **2021**, *11* (52), 32730–32739. https://doi.org/10.1039/D1RA05906H.
(146) Liu, C.; Fang, Z.; Sun, J.; Shang, M.; Zheng, K.; Yang, W.; Ge, Z. Donor-Acceptor-Donor Type Organic Spacer for Regulating the Quantum Wells of Dion-Jacobson 2D Perovskites. *Nano Energy* **2022**, *93*, 106800. https://doi.org/10.1016/j.nanoen.2021.106800.
(147) Kouki, H.; Pitié, S.; Torkhani, A.; Mamèche, F.; Decorse, P.; Seydou, M.; Kouki, F.; Lang, P. Tailor-Made Amino-Based Self-Assembled Monolayers Grafted on Electron Transport ZnO Layers: Perovskite Solar Cell Performance and Modified Interface Relationship. *ACS Appl. Energy Mater.* **2022**, *5* (2), 1635–1645. https://doi.org/10.1021/acsaem.1c03050.
(148) Alagumalai, A.; Venu Rajendran, M.; Ganesan, S.; Sudhakaran Menon, V.; Raman, R. K.; Chelli, S. M.; Muthukumar Vijayasayee, S.; Gurusamy Thangavelu, S. A.; Krishnamoorthy, A. Interface Modification with Holistically Designed Push–Pull D–π–A Organic Small Molecule Facilitates Band Alignment Engineering, Efficient Defect Passivation, and Enhanced Hydrophobicity in Mixed Cation Planar Perovskite Solar Cells. *ACS Appl. Energy Mater.* **2022**, *5* (6), 6783–6796. https://doi.org/10.1021/acsaem.2c00400.
(149) Liu, C.; Su, H.; Pu, Y.; Guo, M.; Zhai, P.; Liu, L.; Fu, H. 3D Polydentate Complexing Agents for Passivating Defects and Modulating Crystallinity for High-Performance Perovskite Solar Cells. *Adv Funct Materials* **2023**, *33* (17), 2212577. https://doi.org/10.1002/adfm.202212577.

(150) Zhang, Z.; Gao, Y.; Li, Z.; Qiao, L.; Xiong, Q.; Deng, L.; Zhang, Z.; Long, R.; Zhou, Q.; Du, Y.; Lan, Z.; Zhao, Y.; Li, C.; Müllen, K.; Gao, P. Marked Passivation Effect of Naphthalene-1,8-Dicarboximides in High-Performance Perovskite Solar Cells. *Advanced Materials* **2021**, *33* (31), 2008405. https://doi.org/10.1002/adma.202008405.
(151) Yoon, M.-H.; Facchetti, A.; Marks, T. J. σ-π Molecular Dielectric Multilayers for Low-Voltage Organic Thin-Film Transistors. *Proc. Natl. Acad. Sci. U.S.A.* **2005**, *102* (13), 4678–4682. https://doi.org/10.1073/pnas.0501027102.
(152) Everaerts, K.; Emery, J. D.; Jariwala, D.; Karmel, H. J.; Sangwan, V. K.; Prabhumirashi, P. L.; Geier, M. L.; McMorrow, J. J.; Bedzyk, M. J.; Facchetti, A.; Hersam, M. C.; Marks, T. J. Ambient-Processable High Capacitance Hafnia-Organic Self-Assembled Nanodielectrics. *J. Am. Chem. Soc.* **2013**, *135* (24), 8926–8939. https://doi.org/10.1021/ja4019429.
(153) Ting, G. G.; Acton, O.; Ma, H.; Ka, J. W.; Jen, A. K.-Y. Study on the Formation of Self-Assembled Monolayers on Sol–Gel Processed Hafnium Oxide as Dielectric Layers. *Langmuir* **2009**, *25* (4), 2140–2147. https://doi.org/10.1021/la802944n.
(154) Jung, Y.; Kline, R. J.; Fischer, D. A.; Lin, E. K.; Heeney, M.; McCulloch, I.; DeLongchamp, D. M. The Effect of Interfacial Roughness on the Thin Film Morphology and Charge Transport of High-Performance Polythiophenes. *Adv. Funct. Mater.* **2008**, *18* (5), 742–750. https://doi.org/10.1002/adfm.200701089.
(155) Huang, W.; Yu, X.; Zeng, L.; Wang, B.; Takai, A.; Di Carlo, G.; Bedzyk, M. J.; Marks, T. J.; Facchetti, A. Ultraviolet Light-Densified Oxide-Organic Self-Assembled Dielectrics: Processing Thin-Film Transistors at Room Temperature. *ACS Appl. Mater. Interfaces* **2021**, *13* (2), 3445–3453. https://doi.org/10.1021/acsami.0c20345.
(156) Wang, B.; Di Carlo, G.; Turrisi, R.; Zeng, L.; Stallings, K.; Huang, W.; Bedzyk, M. J.; Beverina, L.; Marks, T. J.; Facchetti, A. The Dipole Moment Inversion Effects in Self-Assembled Nanodielectrics for Organic Transistors. *Chem. Mater.* **2017**, *29* (23), 9974–9980. https://doi.org/10.1021/acs.chemmater.7b03397.
(157) Leech, D. Affinity Biosensors. *Chem. Soc. Rev.* **1994**, *23* (3), 205. https://doi.org/10.1039/cs9942300205.
(158) Andrade, J. D.; Hlady, V. Protein Adsorption and Materials Biocompatibility: A Tutorial Review and Suggested Hypotheses. In *Biopolymers/Non-Exclusion HPLC*; Benoit, H., Cantow, H.-J., Dall'Asta, G., Dušek, K., Fujita, H., Gordon, M., Henrici-Olivė, G., Heublein, G., Höcker, H., Kausch, H.-H., Kennedy, J. P., Ledwith, A., Okamura, S., Olivé, S., Overberger, C. G., Ringsdorf, H., Saegusa, T., Schrag, J. L., Schulz, G. V., Slichter, W. P., Stille, J. K., Series Eds.; Advances in Polymer Science; Springer Berlin Heidelberg: Berlin, Heidelberg, 1986; Vol. 79, pp 1–63. https://doi.org/10.1007/3-540-16422-7_6.

(159) Mrksich, M.; Grunwell, J. R.; Whitesides, G. M. Biospecific Adsorption of Carbonic Anhydrase to Self-Assembled Monolayers of Alkanethiolates That Present Benzenesulfonamide Groups on Gold. *J. Am. Chem. Soc.* **1995**, *117* (48), 12009–12010. https://doi.org/10.1021/ja00153a029.
(160) Huang, Y.; Dong, X.; Shi, Y.; Li, C. M.; Li, L.-J.; Chen, P. Nanoelectronic Biosensors Based on CVD Grown Graphene. *Nanoscale* **2010**, *2* (8), 1485. https://doi.org/10.1039/c0nr00142b.
(161) Gross, J. H. *Mass Spectrometry: A Textbook*, Corr. 2nd printing.; Springer: Berlin, 2011.
(162) Kebarle, P.; Tang, L. From Ions in Solution to Ions in the Gas Phase - the Mechanism of Electrospray Mass Spectrometry. *Anal. Chem.* **1993**, *65* (22), 972A-986A. https://doi.org/10.1021/ac00070a001.
(163) Ridgway, J. P. Cardiovascular Magnetic Resonance Physics for Clinicians: Part I. *J Cardiovasc Magn Reson* **2010**, *12* (1), 71. https://doi.org/10.1186/1532-429X-12-71.
(164) Rankin, N. J.; Preiss, D.; Welsh, P.; Burgess, K. E. V.; Nelson, S. M.; Lawlor, D. A.; Sattar, N. The Emergence of Proton Nuclear Magnetic Resonance Metabolomics in the Cardiovascular Arena as Viewed from a Clinical Perspective. *Atherosclerosis* **2014**, *237* (1), 287–300. https://doi.org/10.1016/j.atherosclerosis.2014.09.024.
(165) Grasse, E. K.; Torcasio, M. H.; Smith, A. W. Teaching UV–Vis Spectroscopy with a 3D-Printable Smartphone Spectrophotometer. *J. Chem. Educ.* **2016**, *93* (1), 146–151. https://doi.org/10.1021/acs.jchemed.5b00654.
(166) Ojeda, J. J.; Dittrich, M. Fourier Transform Infrared Spectroscopy for Molecular Analysis of Microbial Cells. In *Microbial Systems Biology*; Navid, A., Ed.; Methods in Molecular Biology; Humana Press: Totowa, NJ, 2012; Vol. 881, pp 187–211. https://doi.org/10.1007/978-1-61779-827-6_8.
(167) Blum, M.; John, H. Historical Perspective and Modern Applications of Attenuated Total Reflectance – Fourier Transform Infrared Spectroscopy (ATR-FTIR). *Drug Testing and Analysis* **2012**, *4* (3–4), 298–302. https://doi.org/10.1002/dta.374.
(168) *Practical Raman Spectroscopy: With 11 Tables*; Gardiner, D. J., Bowley, H. J., Graves, P. R., Eds.; Springer: Berlin Heidelberg, 1989.
(169) Pluchery, O.; Bryche, J.-F. An Introduction to Plasmonics.
(170) *Electroanalytical Methods*; Scholz, F., Bond, A. M., Compton, R. G., Fiedler, D. A., Inzelt, G., Kahlert, H., Komorsky-Lovrić, Š., Lohse, H., Lovrić, M., Marken, F., Neudeck, A., Retter, U., Scholz, F., Stojek, Z., Eds.; Springer Berlin Heidelberg: Berlin, Heidelberg, 2010. https://doi.org/10.1007/978-3-642-02915-8.
(171) Dickinson, E. J. F.; Limon-Petersen, J. G.; Rees, N. V.; Compton, R. G. How Much Supporting Electrolyte Is Required to Make a Cyclic Voltammetry Experiment Quantitatively "Diffusional"? A Theoretical and Experimental

Investigation. *J. Phys. Chem. C* **2009**, *113* (25), 11157–11171. https://doi.org/10.1021/jp901628h.
(172) Hiemenz, P. C.; Rajagopalan, R. *Principles of Colloid and Surface Chemistry*, 3. ed., ev.expanded.; CRC, Taylor & Francis: Boca Raton, Fla., 1997.
(173) Cricenti, A.; Colonna, S.; Girasole, M.; Gori, P.; Ronci, F.; Longo, G.; Dinarelli, S.; Luce, M.; Rinaldi, M.; Ortenzi, M. Scanning Probe Microscopy in Material Science and Biology. *J. Phys. D: Appl. Phys.* **2011**, *44* (46), 464008. https://doi.org/10.1088/0022-3727/44/46/464008.
(174) Baláž, P.; Choi, W. S.; Fabián, M. Mechanochemistry in the Preparation of Advanced Materials. **2006**.
(175) Li, B.; Zhang, Y.; Wang, J.; Jia, Z.; Shi, C.; Ma, Y.; Ma, L. Fabricating Ultra-Sharp Tungsten STM Tips with High Yield: Double-Electrolyte Etching Method and Machine Learning. *SN Appl. Sci.* **2020**, *2* (7), 1246. https://doi.org/10.1007/s42452-020-3017-4.
(176) García, R. Dynamic Atomic Force Microscopy Methods. *Surface Science Reports* **2002**, *47* (6–8), 197–301. https://doi.org/10.1016/S0167-5729(02)00077-8.
(177) Ashwell, G. J.; Tyrrell, W. D.; Whittam, A. J. Molecular Rectification: Self-Assembled Monolayers in Which Donor–(π-Bridge)–Acceptor Moieties Are Centrally Located and Symmetrically Coupled to Both Gold Electrodes. *J. Am. Chem. Soc.* **2004**, *126* (22), 7102–7110. https://doi.org/10.1021/ja049633u.
(178) Pokharel, U. R.; Daigle, D. P.; Naquin, S. D.; Engeron, G. S.; Lo, M. A.; Fronczek, F. R. Synthesis, Crystal Structure, and Electrochemistry of Mono- and Bis-Homoannular Ferrocene Derivatives. *Crystals* **2024**, *14* (2), 141. https://doi.org/10.3390/cryst14020141.
(179) Hauser, A.; Enachescu, C.; Daku, M. L.; Vargas, A.; Amstutz, N. Low-Temperature Lifetimes of Metastable High-Spin States in Spin-Crossover and in Low-Spin Iron(II) Compounds: The Rule and Exceptions to the Rule. *Coordination Chemistry Reviews* **2006**, *250* (13–14), 1642–1652. https://doi.org/10.1016/j.ccr.2005.12.006.
(180) Kumar, P.; De Coene, Y.; Clays, K.; Kaur, P.; Singh, K. Size Economy and First Hyperpolarizability: Synthesis and Nonlinear Optical Behavior of Ferrocene-Based Donor–Acceptor Chromophores Lacking π-Linkers. *Dalton Trans.* **2023**, *52* (34), 12130–12142. https://doi.org/10.1039/D3DT01897K.
(181) Cheema, H.; Baumann, A.; Loya, E. K.; Brogdon, P.; McNamara, L. E.; Carpenter, C. A.; Hammer, N. I.; Mathew, S.; Risko, C.; Delcamp, J. H. Near-Infrared-Absorbing Indolizine-Porphyrin Push–Pull Dye for Dye-Sensitized Solar Cells. *ACS Appl. Mater. Interfaces* **2019**, *11* (18), 16474–16489. https://doi.org/10.1021/acsami.8b21414.
(182) Milan, R.; Singh Selopal, G.; Cavazzini, M.; Orlandi, S.; Boaretto, R.; Caramori, S.; Concina, I.; Pozzi, G. Zinc Phthalocyanines as Light Harvesters for SnO2-

Based Solar Cells: A Case Study. *Sci Rep* **2020**, *10* (1), 1176. https://doi.org/10.1038/s41598-020-58310-1.
(183) Viswanathan, T.; David, E.; Prabu, S.; Mishra, K.; Prakash, M.; Shanmugan, S.; Palanisami, N. Effect of the Phenyl Group on the Non-Linear Optical (NLO) and Aggregation Induced Emission (AIE) Properties of Ferrocene Conjugated Linear D–π–A/D–π–A–π–A Chromophores. *New J. Chem.* **2024**, *48* (23), 10717–10729. https://doi.org/10.1039/D4NJ01199F.
(184) Ansar, S. M.; Perera, G. S.; Jiang, D.; Holler, R. A.; Zhang, D. Organothiols Self-Assembled onto Gold: Evidence for Deprotonation of the Sulfur-Bound Hydrogen and Charge Transfer from Thiolate. *J. Phys. Chem. C* **2013**, *117* (17), 8793–8798. https://doi.org/10.1021/jp312836q.
(185) Yu, H. Z.; Zhao, J. W.; Wang, Y. Q.; Cai, S. M.; Liu, Z. F. Fabricating an Azobenzene Self-Assembled Monolayer via Step-by-Step Surface Modification of a Cysteamine Monolayer on Gold. *Journal of Electroanalytical Chemistry* **1997**, *438* (1–2), 221–224. https://doi.org/10.1016/S0022-0728(97)00055-7.
(186) Ouerghi, O.; Diouani, M. F.; Belkacem, A.; Elsanousi, A.; Jaffrezic-Renault, N. Adjunction of Avidin to a Cysteamine Self-Assembled Monolayer for Impedimetric Immunosensor. *JBNB* **2016**, *07* (01), 1–12. https://doi.org/10.4236/jbnb.2016.71001.
(187) Sun, J.-J.; Su, H.-S.; Yue, H.-L.; Huang, S.-C.; Huang, T.-X.; Hu, S.; Sartin, M. M.; Cheng, J.; Ren, B. Role of Adsorption Orientation in Surface Plasmon-Driven Coupling Reactions Studied by Tip-Enhanced Raman Spectroscopy. *J. Phys. Chem. Lett.* **2019**, *10* (10), 2306–2312. https://doi.org/10.1021/acs.jpclett.9b00203.
(188) Fontanesi, C.; Como, E. D.; Vanossi, D.; Montecchi, M.; Cannio, M.; Mondal, P. C.; Giurlani, W.; Innocenti, M.; Pasquali, L. Redox-Active Ferrocene Grafted on H-Terminated Si(111): Electrochemical Characterization of the Charge Transport Mechanism and Dynamics. *Sci Rep* **2019**, *9* (1), 8735. https://doi.org/10.1038/s41598-019-45448-w.
(189) Yokota, Y.; Mino, Y.; Kanai, Y.; Utsunomiya, T.; Imanishi, A.; Fukui, K. Electronic-State Changes of Ferrocene-Terminated Self-Assembled Monolayers Induced by Molecularly Thin Ionic Liquid Layers: A Combined Atomic Force Microscopy, X-Ray Photoelectron Spectroscopy, and Ultraviolet Photoelectron Spectroscopy Study. *J. Phys. Chem. C* **2015**, *119* (32), 18467–18480. https://doi.org/10.1021/acs.jpcc.5b05682.
(190) Fischer, A. B.; Wrighton, M. S.; Umana, M.; Murray, R. W. An X-Ray Photoelectron Spectroscopic Study of Multilayers of an Electroactive Ferrocene Derivative Attached to Platinum and Gold Electrodes. *J. Am. Chem. Soc.* **1979**, *101* (13), 3442–3446. https://doi.org/10.1021/ja00507a003.
(191) Fujii, S.; Kurokawa, S.; Murase, K.; Lee, K.-H.; Sakai, A.; Sugimura, H. Self-Assembled Mixed Monolayer Containing Ferrocenylthiol Molecules: STM

Observations and Electrochemical Investigations. *Electrochimica Acta* **2007**, *52* (13), 4436–4442. https://doi.org/10.1016/j.electacta.2006.12.026.
(192) Sun, Q.-W.; Murase, K.; Ichii, T.; Sugimura, H. Anionic Effect of Ionic Liquids Electrolyte on Electrochemical Behavior of Ferrocenylthiol/Alkanethiol Binary SAMs. *Journal of Electroanalytical Chemistry* **2010**, *643* (1–2), 58–66. https://doi.org/10.1016/j.jelechem.2010.03.008.
(193) Watcharinyanon, S.; Moons, E.; Johansson, L. S. O. Mixed Self-Assembled Monolayers of Ferrocene-Terminated and Unsubstituted Alkanethiols on Gold: Surface Structure and Work Function. *J. Phys. Chem. C* **2009**, *113* (5), 1972–1979. https://doi.org/10.1021/jp808938d.
(194) Yang, W.; Chai, L.; Yang, Z.; Zhao, F.; Liao, Q.; Si, M. Mechanism of Chemical Reduction of Cr(VI). In *Remediation of Chromium-Contaminated Soil: Theory and Practice*; Environmental Science and Engineering; Springer Nature Singapore: Singapore, 2023; pp 171–255. https://doi.org/10.1007/978-981-99-5463-6_4.
(195) Li, H.; Meng, R.; Guo, Y.; Chen, B.; Jiao, Y.; Ye, C.; Long, Y.; Tadich, A.; Yang, Q.-H.; Jaroniec, M.; Qiao, S.-Z. Reversible Electrochemical Oxidation of Sulfur in Ionic Liquid for High-Voltage Al–S Batteries. *Nat Commun* **2021**, *12* (1), 5714. https://doi.org/10.1038/s41467-021-26056-7.
(196) Zhang, Q.; Wang, H. Mechanistic Insights on Plasmon-Driven Photocatalytic Oxidative Coupling of Thiophenol Derivatives: Evidence for Steady-State Photoactivated Oxygen. *J. Phys. Chem. C* **2018**, *122* (10), 5686–5697. https://doi.org/10.1021/acs.jpcc.8b00660.
(197) Wirde, M.; Gelius, U.; Nyholm, L. Self-Assembled Monolayers of Cystamine and Cysteamine on Gold Studied by XPS and Voltammetry. *Langmuir* **1999**, *15* (19), 6370–6378. https://doi.org/10.1021/la9903245.
(198) Merlen, A.; Gadenne, V.; Romann, J.; Chevallier, V.; Patrone, L.; Valmalette, J. C. Surface Enhanced Raman Spectroscopy of Organic Molecules Deposited on Gold Sputtered Substrates. *Nanotechnology* **2009**, *20* (21), 215705. https://doi.org/10.1088/0957-4484/20/21/215705.
(199) Huege, R. The Laser-Raman Spectrum of Ferrocene. 3.
(200) Delafosse, G.; Merlen, A.; Clair, S.; Patrone, L. A Surface Enhanced Raman Spectroscopy Study of Aminothiophenol and Aminothiophenol-C60 Self-Assembled Monolayers: Evolution of Raman Modes with Experimental Parameters. *The Journal of Chemical Physics* **2012**, *136* (19), 194704. https://doi.org/10.1063/1.4717720.
(201) Auletta, T.; van Veggel, F. C. J. M.; Reinhoudt, D. N. Self-Assembled Monolayers on Gold of Ferrocene-Terminated Thiols and Hydroxyalkanethiols. *Langmuir* **2002**, *18* (4), 1288–1293. https://doi.org/10.1021/la011474u.
(202) Lee, L. Y. S.; Sutherland, T. C.; Rucareanu, S.; Lennox, R. B. Ferrocenylalkylthiolates as a Probe of Heterogeneity in Binary Self-

Assembled Monolayers on Gold. *Langmuir* **2006**, *22* (9), 4438–4444. https://doi.org/10.1021/la053317r.
(203) Lee, H. J.; Jamison, A. C.; Yuan, Y.; Li, C.-H.; Rittikulsittichai, S.; Rusakova, I.; Lee, T. R. Robust Carboxylic Acid-Terminated Organic Thin Films and Nanoparticle Protectants Generated from Bidentate Alkanethiols. *Langmuir* **2013**, *29* (33), 10432–10439. https://doi.org/10.1021/la4017118.
(204) Hoang, J.; Park, C. S.; Lee, H. J.; Marquez, M. D.; Zenasni, O.; Gunaratne, P. H.; Lee, T. R. Quaternary Ammonium-Terminated Films Formed from Mixed Bidentate Adsorbates Provide a High-Capacity Platform for Oligonucleotide Delivery. *ACS Appl. Mater. Interfaces* **2018**, *10* (47), 40890–40900. https://doi.org/10.1021/acsami.8b12244.
(205) Jiao, L.; Yu, C.; Li, J.; Wang, Z.; Wu, M.; Hao, E. β-Formyl-BODIPYs from the Vilsmeier–Haack Reaction. *J. Org. Chem.* **2009**, *74* (19), 7525–7528. https://doi.org/10.1021/jo901407h.
(206) Baert, F.; Cabanetos, C.; Allain, M.; Silvestre, V.; Leriche, P.; Blanchard, P. Thieno[2,3-*b*]Indole-Based Small Push–Pull Chromophores: Synthesis, Structure, and Electronic Properties. *Org. Lett.* **2016**, *18* (7), 1582–1585. https://doi.org/10.1021/acs.orglett.6b00438.
(207) Fauvel, S.; Riquelme, A. J.; Andrés Castán, J.-M.; Mwalukuku, V. M.; Kervella, Y.; Challuri, V. K.; Sauvage, F.; Narbey, S.; Maldivi, P.; Aumaître, C.; Demadrille, R. Push-Pull Photochromic Dyes for Semi-Transparent Solar Cells with Light-Adjustable Optical Properties and High Color-Rendering Index. *Chem. Sci.* **2023**, *14* (32), 8497–8506. https://doi.org/10.1039/D3SC02328A.
(208) Kang, M. S.; Kang, S. H.; Kim, S. G.; Choi, I. T.; Ryu, J. H.; Ju, M. J.; Cho, D.; Lee, J. Y.; Kim, H. K. Novel D–π–A Structured Zn(Ii)-Porphyrin Dyes Containing a Bis(3,3-Dimethylfluorenyl)Amine Moiety for Dye-Sensitised Solar Cells. *Chem. Commun.* **2012**, *48* (75), 9349. https://doi.org/10.1039/c2cc31384g.
(209) Lu, J.; Xu, X.; Cao, K.; Cui, J.; Zhang, Y.; Shen, Y.; Shi, X.; Liao, L.; Cheng, Y.; Wang, M. D–π–A Structured Porphyrins for Efficient Dye-Sensitized Solar Cells. *J. Mater. Chem. A* **2013**, *1* (34), 10008. https://doi.org/10.1039/c3ta11870c.
(210) Hine, J.; Thomas, C. H.; Ehrenson, S. J. The Effect of Halogen Atoms on the Reactivity of Other Halogen Atoms in the Same Molecule. V. The SN2 Reactivity of Methylene Halides [1]. *J. Am. Chem. Soc.* **1955**, *77* (14), 3886–3889. https://doi.org/10.1021/ja01619a061.
(211) Wallace, T. P.; Stauffer, C. H. Reactivity of 1-Bromoalkanes with Thiocyanate. *J. Phys. Chem.* **1967**, *71* (7), 2083–2085. https://doi.org/10.1021/j100866a017.
(212) Mandal, B.; Basu, B. Recent Advances in S–S Bond Formation. *RSC Adv.* **2014**, *4* (27), 13854. https://doi.org/10.1039/c3ra45997g.

(213) Avhad, K.; Jadhav, M.; Patil, D.; Chowdhury, T. H.; Islam, A.; Bedja, I.; Sekar, N. Rhodanine-3-Acetic Acid Containing D-π-A Push-Pull Chromophores: Effect of Methoxy Group on the Performance of Dye-Sensitized Solar Cells. *Organic Electronics* **2019**, *65*, 386–393. https://doi.org/10.1016/j.orgel.2018.11.041.
(214) Fernandes, S. S. M.; Herbivo, C.; Aires-de-Sousa, J.; Comel, A.; Belsley, M.; Raposo, M. M. M. Theoretical and Experimental Studies of Aryl-Bithiophene Based Push-Pull π-Conjugated Heterocyclic Systems Bearing Cyanoacetic or Rhodanine-3-Acetic Acid Acceptors for SHG Nonlinear Optical Applications. *Dyes and Pigments* **2018**, *149*, 566–573. https://doi.org/10.1016/j.dyepig.2017.10.001.
(215) Ricci, R. W.; Ditzler, M.; Nestor, L. P. Discovering the Beer-Lambert Law. *J. Chem. Educ.* **1994**, *71* (11), 983. https://doi.org/10.1021/ed071p983.
(216) Swinehart, D. F. The Beer-Lambert Law.
(217) Gadde, S.; Batchelor, E. K.; Weiss, J. P.; Ling, Y.; Kaifer, A. E. Control of H- and J-Aggregate Formation via Host–Guest Complexation Using Cucurbituril Hosts. *J. Am. Chem. Soc.* **2008**, *130* (50), 17114–17119. https://doi.org/10.1021/ja807197c.
(218) Würthner, F.; Kaiser, T. E.; Saha-Möller, C. R. J-Aggregates: From Serendipitous Discovery to Supramolecular Engineering of Functional Dye Materials. *Angew Chem Int Ed* **2011**, *50* (15), 3376–3410. https://doi.org/10.1002/anie.201002307.
(219) Pudlak, M.; Pincak, R. Energy Gap between Highest Occupied Molecular Orbital and Lowest Unoccupied Molecular Orbital in Multiwalled Fullerenes. *Phys. Rev. A* **2009**, *79* (3). https://doi.org/10.1103/physreva.79.033202.
(220) Da Silva, R. R.; Ramalho, T. C.; Santos, J. M.; Figueroa-Villar, J. D. On the Limits of Highest-Occupied Molecular Orbital Driven Reactions: The Frontier Effective-for-Reaction Molecular Orbital Concept. *J. Phys. Chem. A* **2006**, *110* (3), 1031–1040. https://doi.org/10.1021/jp054434y.
(221) Büchel, R. C.; Rudolph, D. A.; Frank, I. Deterministic Quantum Mechanics: The Role of the MAXWELL–BOLTZMANN Distribution. *Int J of Quantum Chemistry* **2021**, *121* (7). https://doi.org/10.1002/qua.26555.
(222) Koudriavtsev, A.; Jameson, R. F.; Linert, W. *The Law of Mass Action*; Springer Berlin Heidelberg: Berlin, Heidelberg, 2001. https://doi.org/10.1007/978-3-642-56770-4.
(223) Ahn, M.; Kim, M.-J.; Cho, D. W.; Wee, K.-R. Electron Push–Pull Effects on Intramolecular Charge Transfer in Perylene-Based Donor–Acceptor Compounds. *J. Org. Chem.* **2021**, *86* (1), 403–413. https://doi.org/10.1021/acs.joc.0c02149.
(224) Zhu, H.; Wang, X.; Ma, R.; Kuang, Z.; Guo, Q.; Xia, A. Intramolecular Charge Transfer and Solvation of Photoactive Molecules with Conjugated Push–Pull

Structures. *ChemPhysChem* **2016**, *17* (20), 3245–3251. https://doi.org/10.1002/cphc.201600674.
(225) Ashwell, G. J.; Mohib, A. Improved Molecular Rectification from Self-Assembled Monolayers of a Sterically Hindered Dye. *J. Am. Chem. Soc.* **2005**, *127* (46), 16238–16244. https://doi.org/10.1021/ja054699q.
(226) Khalid, H.; Opodi, E. M.; Song, X.; Wang, Z.; Li, B.; Tian, L.; Yu, X.; Hu, W. Modulated Structure and Rectification Properties of a Molecular Junction by a Mixed Self-Assembled Monolayer. *Langmuir* **2022**, *38* (35), 10893–10901. https://doi.org/10.1021/acs.langmuir.2c01751.
(227) Rundqvist, J.; Hoh, J. H.; Haviland, D. B. Poly(Ethylene Glycol) Self-Assembled Monolayer Island Growth. *Langmuir* **2005**, *21* (7), 2981–2987. https://doi.org/10.1021/la0471792.
(228) Kang, H.; Han, S.; Seong, S.; Son, Y. J.; Ito, E.; Hara, M.; Noh, J. Unique Mixed Phases and Structures of Self-Assembled Monolayers on Au(111) Derived from Methoxy-Terminated Mono(Ethylene Glycol)Ethanethiols. *J. Phys. Chem. C* **2017**, *121* (33), 18021–18029. https://doi.org/10.1021/acs.jpcc.7b05817.
(229) Li, L.; Chen, S.; Zheng, J.; Ratner, B. D.; Jiang, S. Protein Adsorption on Oligo(Ethylene Glycol)-Terminated Alkanethiolate Self-Assembled Monolayers: The Molecular Basis for Nonfouling Behavior. *J. Phys. Chem. B* **2005**, *109* (7), 2934–2941. https://doi.org/10.1021/jp0473321.
(230) Rundqvist, J.; Hoh, J. H.; Haviland, D. B. Substrate Effects in Poly(Ethylene Glycol) Self-Assembled Monolayers on Granular and Flame-Annealed Gold. *Journal of Colloid and Interface Science* **2006**, *301* (1), 337–341. https://doi.org/10.1016/j.jcis.2006.05.012.
(231) *Peptide Self-Assembly and Engineering: Fundamentals, Structures, and Applications*; Yan, X., Ed.; Wiley-VCH: Weinheim, 2024.
(232) Gatto, E.; Venanzi, M. Self-Assembled Monolayers Formed by Helical Peptide Building Blocks: A New Tool for Bioinspired Nanotechnology. *Polym J* **2013**, *45* (5), 468–480. https://doi.org/10.1038/pj.2013.27.
(233) Petroff, C. A.; Cassone, G.; Šponer, J.; Hutchison, G. R. Intrinsically Polar Piezoelectric Self-Assembled Oligopeptide Monolayers. *Advanced Materials* **2021**, *33* (17), 2007486. https://doi.org/10.1002/adma.202007486.
(234) Guo, Y.; Li, M.; Mylonakis, A.; Han, J.; MacDiarmid, A. G.; Chen, X.; Lelkes, P. I.; Wei, Y. Electroactive Oligoaniline-Containing Self-Assembled Monolayers for Tissue Engineering Applications. *Biomacromolecules* **2007**, *8* (10), 3025–3034. https://doi.org/10.1021/bm070266z.
(235) Vanderah, D. J.; Valincius, G.; Meuse, C. W. Self-Assembled Monolayers of Methyl 1-Thiahexa(Ethylene Oxide) for the Inhibition of Protein Adsorption. *Langmuir* **2002**, *18* (12), 4674–4680. https://doi.org/10.1021/la025720t.
(236) Heeb, R.; Lee, S.; Venkataraman, N. V.; Spencer, N. D. Influence of Salt on the Aqueous Lubrication Properties of End-Grafted, Ethylene Glycol-Based Self-

Assembled Monolayers. *ACS Appl. Mater. Interfaces* **2009**, *1* (5), 1105–1112. https://doi.org/10.1021/am900062h.
(237) Tian, H.; Xiang, D.; Shao, H.; Yu, H.-Z. Electrochemical Identification of Molecular Heterogeneity in Binary Redox Self-Assembled Monolayers on Gold. *J. Phys. Chem. C* **2014**, *118* (25), 13733–13742. https://doi.org/10.1021/jp5040745.
(238) Kong, G. D.; Song, H.; Yoon, S.; Kang, H.; Chang, R.; Yoon, H. J. Interstitially Mixed Self-Assembled Monolayers Enhance Electrical Stability of Molecular Junctions. *Nano Lett.* **2021**, *21* (7), 3162–3169. https://doi.org/10.1021/acs.nanolett.1c00406.
(239) Park, J.; Belding, L.; Yuan, L.; Mousavi, M. P. S.; Root, S. E.; Yoon, H. J.; Whitesides, G. M. Rectification in Molecular Tunneling Junctions Based on Alkanethiolates with Bipyridine–Metal Complexes. *J. Am. Chem. Soc.* **2021**, *143* (4), 2156–2163. https://doi.org/10.1021/jacs.0c12641.
(240) Hobara, D.; Ota, M.; Imabayashi, S.; Niki, K.; Kakiuchi, T. Phase Separation of Binary Self-Assembled Thiol Monolayers Composed of 1-Hexadecanethiol and 3-Mercaptopropionic Acid on Au(111) Studied by Scanning Tunneling Microscopy and Cyclic Voltammetry. *Journal of Electroanalytical Chemistry* **1998**, *444* (1), 113–119. https://doi.org/10.1016/S0022-0728(97)00553-6.
(241) Mendes, P. M. Stimuli-Responsive Surfaces for Bio-Applications. *Chem. Soc. Rev.* **2008**, *37* (11), 2512. https://doi.org/10.1039/b714635n.
(242) Yeung, C. L.; Wang, X.; Lashkor, M.; Cantini, E.; Rawson, F. J.; Iqbal, P.; Preece, J. A.; Ma, J.; Mendes, P. M. Modulation of Biointeractions by Electrically Switchable Oligopeptide Surfaces: Structural Requirements and Mechanism. *Adv. Mater. Interfaces* **2014**, *1* (2), 1300085. https://doi.org/10.1002/admi.201300085.
(243) Pranzetti, A.; Davis, M.; Yeung, C. L.; Preece, J. A.; Koelsch, P.; Mendes, P. M. Direct Observation of Reversible Biomolecule Switching Controlled By Electrical Stimulus. *Adv Materials Inter* **2014**, *1* (5), 1400026. https://doi.org/10.1002/admi.201400026.